Late Quaternary ice dynamics of the Monte San Lorenzo ice cap, Patagonia

Julian Rodney Victor Martin

Department of Geography

Royal Holloway, University of London

Thesis submitted for the degree of Doctor of Philosophy (PhD)

Royal Holloway, University of London

September 2019

Declaration

ROYAL HOLLOWAY

Declaration of Authorship for Co-Authored Work

If you are presenting partly co-authored work, please indicate below your individual contribution to the thesis.

Name of candidate: JULIAN RODNEY VICTOR MARTIN

Thesis title: LATE QUATERNARY ICE DYNAMICS OF THE MONTE SAN LORENZO ICE CAP, PATAGONIA

I confirm that the thesis that I am presenting has been co-authored with:

BETHAN DAVIES and VARYL THORNDYCRAFT

Within this partly co-authored work, I declare that the following contributions are entirely my own work:

(Here you should indicate, in précis style, the datasets that you gathered, interpreted and discussed; methods that you developed; complete first drafts that you wrote; content that is entirely your own work; etc. It is often appropriate to organise this statement by chapter)

Chapter 4 and Chapter 1.5 of this thesis have been adapted from Martin et al. 2019 (See Appendices) I wrote the manuscript and drew the figures. All authors assisted with fieldwork, contributed ideas and edited the manuscript.

Chapter 2.1.3 and 2.1.4 have in part been adapted from an unedited draft of material I wrote as a contribution towards Davies et al. submitted (See Appendices).
Davies and Thorndycraft assisted with fieldwork and data collection in the field.
I undertook the modelling, data processing and calculations, and produced the figures and maps unless otherwise stated.
I wrote the contents of the thesis with discussion with Davies and Thorndycraft.

Signed: ..... Date: 26/09/2019
(Candidate)

Signed: ..... Date: 26/09/2019
(Supervisor)

This form should be signed by the candidate and the candidate's supervisor and returned to Student Administration, Royal Holloway, Egham, Surrey TW20 0EX with the copies of the thesis.

Acknowledgements

First and foremost, I would like to thank my supervisors Bethan Davies and Varyl Thorndycraft. Their support, help, guidance and patience has been invaluable and their commitment to teaching and enthusiasm for the subject has provided much needed encouragement and energy. From their support with fieldwork, to day to day queries, to their final assistance bringing this thesis together, I am very thankful to have had Bethan and Varyl as supervisors.

I would like to acknowledge Dr Richard Jones for his invaluable assistance in setting up, initialising and running PISM. Dr Jan Leanarts is gratefully thanked for processing the RAMCO 2.3 climatic dataset for use in PISM. Dr Nick Golledge is thanked for his assistance in running PISM.

I am very grateful to all the academic, technical and administrative staff within the Department of Geography, who welcomed me into the department and have always been available and keen to help with any questions or problems. The close, friendly, encouraging community within the department has really made the last four years. Likewise, I am extremely grateful to the fantastic group of PhD students past and present who made PhD life so enjoyable. I have had a great time and great laugh with more people than I can name, but in particular to Rachel and Dave who have been there on the DTP since day one. To Rhys, Jacob, Paul and Ash who made my first months in EMU, and the years since, so much fun. Richard, Lizzy, Angharad, Simon, Alice, Josh, Amy, Jen and many more who I spent so many days with. All those on the DTP, too many to mention, who made the first 6 months of my PhD a time I will always look back on so fondly. I am grateful to have had this group of people around me. To Rachael whose constant support, motivation and laughter I will be forever grateful.

Finally, to my parents and brother George, thank you for your unending support and unconditional willingness to do whatever you can to help and support me.

This thesis was supported by a Natural Environment Research Council award NE/ L002485/1, as well as numerous organisations including the Quaternary Research Association (QRA), Geologists Association (GA), British Society for Geomorphology (GSB) and INQUA, for funding fieldwork and supporting conference attendance. Cosmogenic nuclide ages were supported by NERC Cosmogenic Isotope Analysis Facility (CIAF), grant number 9174/0417.

Abstract

Glaciers of small ice caps have short response times and high climate sensitivity, making them a useful proxy for understanding palaeoclimate. Past changes in climate and glacier dynamics can provide an analogue for present-day and future rapid climate and glacier change. Land-terminating glaciers are of particular interest, since their extent is largely a function of temperature and precipitation. Constraining the past behaviour of these glaciers from the geological record and glacier mass-balance sensitivities from numerical modelling can yield insights into past climate change. This is of particular interest in Patagonia to help elucidate the behaviour of the precipitation bearing Southern Westerly Winds, which are changed dynamically during the Late Pleistocene and Holocene. Key climatic constraints on glaciers east of the Northern Patagonian Icefield are also poorly understood, complicated by a lack of understanding of interactions between glaciers and ice-dammed palaeolakes. This study presents a new reconstruction of the deglaciation of the northern Monte San Lorenzo ice cap, southern South America, during a period of accelerated warming following the Antarctic Cold Reversal. Detailed geomorphological mapping of the valleys north of Monte San Lorenzo reveals 14 primary ice limits, two of which were dated to 12.5 ± 0.4 ka and 12.1 ± 0.4 ka by cosmogenic nuclide dating. Glacial landsystem analysis enables and formalises the reconstruction of Antarctic Cold Reversal and Holocene glacier dynamics and glacier-lake interactions. This work underpins a numerical model (PISM) of the ice cap to evaluate palaeoclimate drivers. Climatic and physical parameter sensitivity experiments and climatic response time tests provide, for the first time, an important insight into the controls of glacier change and the response of temperate Patagonian glaciers to rapidly-warming climate. Forcing the model using temperature and precipitation combinations to match reconstructed ice limits provides estimates of past climate conditions following the Antarctic Cold Reversal.

Contents

List of Figures

List of Tables

1. Introduction

1.1. Rationale

Patagonian glaciers are among the most climatically sensitive glaciers found anywhere on Earth (Mackintosh et al., 2017) and have been receding and losing mass in recent decades (Braun et al., 2019; Dussaillant et al., 2019). Their annual specific volume loss, in excess of 1 m water equivalent (w.e.), is the highest observed globally (Zemp et al., 2019). This has important implications for sea level rise, with Patagonian glaciers contributing 0.06 mm a year, over 10% of global glacier contribution (Dussaillant et al., 2019). With ongoing warming and ice-mass loss through the 21st century, some of the largest reductions in glacier runoff are predicted to occur in South America as a result of glacier shrinkage (Huss and Hock, 2018). It is therefore vital that the glacier-climate interactions, dynamics and drivers of changes of these ice masses are well understood, in order to predict future glacier change and its wider impacts. Past changes in glacier dynamics during periods of rapid climatic transitions within Patagonian and the Southern Hemisphere can provide an analogue for understanding present-day and future rapid climate and glacier change (Anderson and Mackintosh, 2006; Mackintosh et al., 2017).

Patagonia sits in the path of precipitation bearing Southern Westerly Winds (SWW) (Garreaud et al., 2009). These winds are a key part of the Southern Hemisphere ocean-climate system, bringing precipitation to South America and other southern land masses (Gilli et al., 2005; Moy et al., 2008), driving Southern Ocean surface currents (Shulmeister et al., 2004) and influencing ocean upwelling which in turn controls CO_2 fluxes from the deep ocean to the atmosphere (Anderson et al., 2009; Russell et al., 2006). Past latitudinal variations in the SWW may have driven glacier fluctuations in Patagonia during the last glacial-interglacial transition (Boex et al. 2013; Bertrand et al., 2012; Douglass et al., 2005; Glasser et al., 2012) and indeed there is evidence in Patagonia for a dramatic reduction in ice extent during this time and through the Holocene (Caldenius, 1932; Mercer, 1976; Hubbard et al., 2005; Hein et al., 2010), punctuated by readvances during the Antarctic Cold Reversal (ACR) (14.5 ka - 12.8 ka) (García et al., 2012, 2018; Nimick et al., 2016; Davies et al., 2018; Sagredo et al., 2018) and during multiple Holocene neoglaciations (Bertrand et al., 2012; Aniya, 2013; Sagredo et al., 2018; Reynout et al., in press). Well chronologically constrained reconstructions of past glacier change could therefore provide insights into the evolution of Southern Hemisphere ocean-atmosphere systems, including the latitudinal migration of the SWW, during periods of rapid climatic transition.

Further understanding of past and present-day glacier-climate interactions can be obtained through glacier numerical modelling, providing quantitative insights into glacier-climate sensitivities, mass balance and ice flow dynamics. Matching the output of a glacier model to

geologically constrained ice reconstructions can also yield quantitative insights into past climate conditions (Golledge et al., 2012; Patton et al., 2017; Ely et al., 2019). Therefore, there is a need for improved understanding of past glacier-climate interactions and the timing and characteristics of past glacier fluctuations.

Small ice caps in Patagonia, such as Monte San Lorenzo (MSL, Monte Cochrane) (Figure 1.1), have short response times and high climate sensitivity, making them a particularly useful proxy for understanding rapid changes in palaeoclimate and resulting glacier response (Bahr et al., 1998). Due to the strong west-east precipitation gradient across the Patagonian Andes (Warren and Sugden, 1993) and their location further inland, these smaller ice caps located in the cordillera (72 – 73°W) to the east of the Patagonian Icefields (e.g., Araos et al., 2018; Sagredo et al., 2018) may also be particularly sensitive to changes in precipitation and therefore act as a proxy for phasing of the Southern Annual Mode (SAM) and evolution of the interrelated SWW (Moreno et al., 2018b).

This study investigates the dynamics, timing, environments, processes and drivers of the deglaciation of the MSL ice cap (47.5°S; Figure 1.1) during the climatic transition following the ACR through to the present-day. Geomorphological mapping, sedimentology and ^{10}Be cosmogenic nuclide surface exposure dating are used to produce a new, temporally and spatially well constrained record of deglaciation and landsystem change in Salto, Tranquilo and Pedregoso valleys to the north of the ice cap (Figure 1.1). Calluqueo Glacier is reconstructed at stages of stabilisation and moraine formation based upon geomorphological interpretation, from which palaeoglacier Equilibrium Line Altitudes (ELAs) are calculated and quantitative estimates of past precipitation obtained. Numerical modelling using the Parallel Ice Sheet Model (PISM) is applied for the first time in Patagonia to create a simulation of the present-day ice cap, providing insights into mass-balance distribution, flow dynamics and glacier thermal regime. This model is then used to test the sensitivity of the ice cap to precipitation and temperature, as well as providing estimates of palaeoclimate conditions during the Last Glacial-Interglacial Transition (LGIT), mid-Holocene and Little Ice Age (LIA), constrained by the new empirical palaeoglacier reconstructions. This work provides important insights into the climate sensitivity of the MSL ice cap, and drivers of deglaciation during a period of rapid climate change.

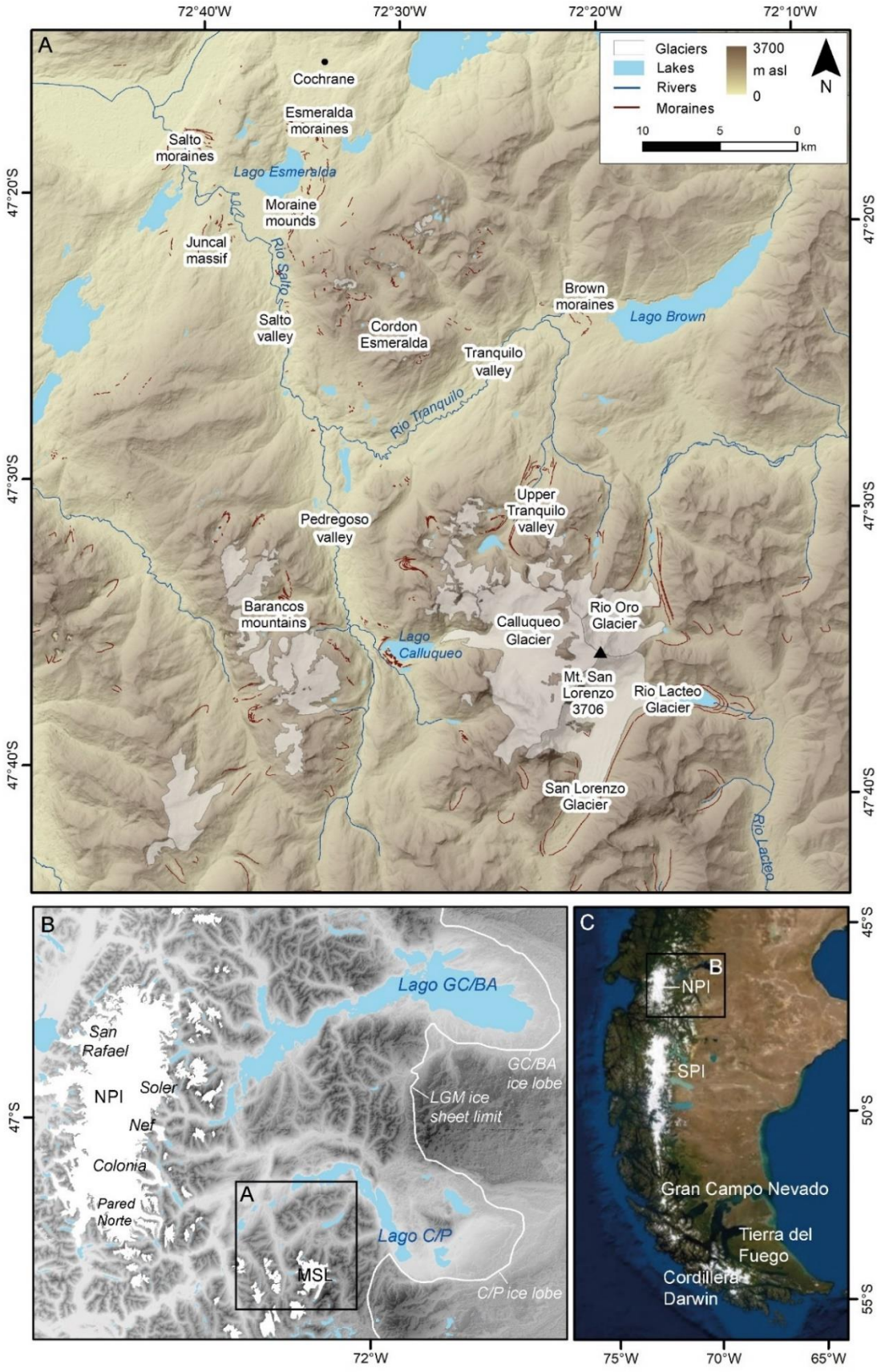

Figure 1.1. (A) Map of the study area north of the MSL Ice cap with major place names and features labelled. (B) Maps showing the location of the study area within the context of the region east of the NPI, with selected NPI outlet glaciers and Lago General Carrera/Buenos Aires (GCBA) and Lago Cochrane/Pueyrredón (CP) labelled. (C) Study region within the context of southern South America.

1.2. Previous work and gaps in knowledge

Deglaciation in Patagonia left a range of ice-marginal glacial (Glasser and Jansson, 2005; Glasser et al., 2008; Bendle et al., 2017b; Darvill et al., 2017) and palaeolake landforms (Turner et al., 2005; Bell, 2008, 2009; Hein et al., 2010; Bourgois et al., 2016; Glasser et al., 2016; Davies et al., 2018; Thorndycraft et al., 2019) in valleys to the east of the Northern Patagonian Icefield (NPI) as ice receded westwards. These features have been used to formalise glacial, glaciofluvial, glaciolacustrine and paraglacial processes in the form of glaciolacustrine, fjord-terminating and land-terminating glacier landsystems (Glasser et al., 2009; Davies et al., 2018). However, work investigating the temporal evolution and interaction between landsystems, notably those in complex interlinked valleys in the cordillera east of the Patagonian icefields, is lacking. This includes the valleys immediately north of the MSL ice cap. The geomorphology of these valleys have been mapped only by remote sensing (Glasser and Jansson, 2005; Glasser et al., 2009; Bendle et al., 2017b) apart from recent field mapping in the northern Salto valley (Davies et al., 2018), Upper Tranquilo valley (Sagredo et al., 2018) and far-eastern section of the Tranquilo valley (Araya et al., 2014) (Figure 1.1A). Detailed field mapping and sedimentological data needed to reconstruct processes and landforms north of the MSL ice cap are therefore largely missing. Hence, further work is needed to understand of the controls on sediment-landform assemblage formation and the timing of landsystem evolution.

The mapped geomorphological record and currently available chronological data have allowed for an increasingly detailed reconstruction of deglaciation of the Patagonian Ice Sheet (Davies et al., submitted and references therein), however there are few detailed high-resolution sequences of glacier recession (e.g. Strelin et al., 2014; Sagredo et al., 2018) with which to study deglaciation during rapid climatic changes. This is also the case north of MSL, where chronological constraint is limited to moraine complexes marking the ACR limit of Calluqueo Glacier in the northern Salto valley (Davies et al., 2018), a single post-ACR moraine inset of this (Glasser et al., 2012). The most complete sequence of moraines are that found in the Upper Tranquilo valley marking an ACR ice limit and post-ACR deglaciation of Tranquilo Glacier (Sagredo et al., 2018). The evidence for multiple moraines down valley of Calluqueo Glacier (Glasser et al., 2012; Bendle et al., 2017b) provides an opportunity to quantify the timing and rates of recession of this glacier from its ACR limit (Davies et al., 2018) during a period of rapid climate warming.

Our understanding of Patagonian paleoclimate through the last deglaciation has been improved by the use of climate proxy records, such as pollen, charcoal and palaeolake level modelling

(Moreno, 2004; Elbert et al., 2013; Iglesias et al., 2016; Moreno and Videla, 2016; Quade and Kaplan, 2017; Moreno et al., 2018a), providing insights in to local and hemispheric climate and ocean-atmosphere systems (Lamy et al., 2010; Björck et al., 2012; Fletcher and Moreno, 2012; Darvill et al., 2016) Quantifiable estimates of temperature and precipitation from terrestrial proxy records however are limited (Tonello et al., 2009; Massaferro and Larocque-Tobler, 2013; Schäbitz et al., 2013; Sagredo et al., 2018). Obtaining such estimates is key to understanding climate and atmospheric-system change, including the migration and variations in intensity of the SWW, during periods of rapid climate change and complex hemispheric-wide reorganisation of the ocean-atmosphere system (Bendle et al., 2019).

To understand glacier-climate relationships during these periods it is important to understand glacier mass balance distribution and present-day active glacier dynamics. There is little work of this nature in Patagonia, in part due to an absence of empirical field data, climate data and only a few modelling studies focusing on the NPI (Schaefer et al., 2013), San Rafael Glacier (Koppes et al., 2011), the SPI (Schaefer et al., 2015; Bravo et al., 2019), Chico Glacier (Rivera, 2004) and Glaciar Perito Morano (Stuefer et al., 2007). Our understanding of the MSL ice cap is limited to records of recession, surface elevation and mass change over recent decades based on remote sensing (Falaschi et al., 2016). Its detailed mass balance distribution and mass turnover, key physical behaviours and physical and climatic sensitivities are unclear, hence the need for numerical modelling.

1.3. Research questions

From the key gaps in our current understanding of past and present Patagonian glaciers and climate, we devise five key research questions to target in this work, expanded upon in the following chapters.

RQ 1) What were the key processes and landsystems that operated during the deglaciation of the valleys to the north of Monte San Lorenzo and what controlled these? *(Chapter 4)*

RQ 2) What was the timing and rate of deglaciation of Calluqueo Glacier following the Antarctic Cold Reversal? *(Chapters 5, 6 and 8)*

RQ 3) What are the mass balance distribution, physical properties and behaviours and sensitivities of glaciers at the Monte San Lorenzo ice cap? *(Chapter 7)*

RQ 4) Quantitatively, how different was precipitation and temperature at periods of glacier readvance and stillstand following the Antarctic Cold Reversal and through the Holocene compared to today? *(Chapters 6 and 7)*

RQ 5) What were the key drivers of deglaciation of the Monte San Lorenzo ice following the Antarctic Cold Reversal? *(Chapter 8)*

1.4. Aims & objectives

1.4.1. Aims

Aim 1. To elucidate the timing and nature of deglaciation of outlet valleys north of the Monte San Lorenzo ice cap through the Late Pleistocene and Holocene, and reveal glacier dynamics, processes, land systems and climate which operated during this time, alongside the primary controls on sediment-landform associations and landsystem development. *(Chapters 4, 5 and 6)*

Aim 2. To quantify present-day physical glacier properties, ice dynamics and sensitivities of the Monte San Lorenzo ice cap. *(Chapter 7)*

Aim 3. To determine the controls on deglaciation of the Monte San Lorenzo ice cap within the context of the Southern Hemisphere climate system. *(Chapter 7 and 8)*

1.4.2. Objectives

Obj. 1. Determine sediment-landform assemblages, through remote sensing and field mapping, across a spectrum of palaeoglacial and glacial environments, from which landsystem models are then generated. *(Chapter 4)*

Obj. 2. Date glacially-transported boulders found on moraine ridge crests using ^{10}Be cosmogenic nuclide surface exposure dating to obtain ages for the formation of moraine ridge complexes. *(Chapter 5)*

Obj. 3. Produce a chronologically-constrained palaeoglaciological reconstruction of Calluqueo Glacier and landsystem evolution during deglaciation. *(Chapter 6)*

Obj. 4. Use the new reconstructions of Calluqueo Glacier to reconstruct palaeo-ELAs at periods of glacier stillstand and readvance using the AABR method, from which palaeoprecipitation can be quantified using the WAIS Divide ice core temperature record as a relative temperature difference input. *(Chapter 6)*

Obj. 5. Numerical modelling (using the Parallel Ice Sheet Model) to produce a simulation of the present-day Monte San Lorenzo ice cap, tuned to empirical data and conduct model sensitivity experiments to investigate physical, mass balance and climate parameters. *(Chapter 7)*

Obj. 6. Drive model simulations using precipitation and temperature scenarios to match new empirical reconstructions of Calluqueo Glacier, obtaining estimates of past climate conditions. *(Chapter 7)*

Obj. 7. Synthesise the geomorphological, geochronological, ELA and modelling data to evaluate glacier response to Southern Hemisphere palaeoclimate. *(Chapter 8)*

1.5. Study area

MSL (47°35'S, 72°18'W) is an isolated granodioritic to granitic massif (Ramos et al., 1982), located 70 km east of the of the main Andean Chain(Figure 1.1**Error! Reference source not found.**B). It experiences a temperate climate with mean annual air temperature of 8.4°C and average annual precipitation of 750 mm w.e. (Direccion Meteologica de Chile, 2001) recorded at the nearest meteorological station in the town of Cochrane 40 km to the north (47°14'S, 72°33'W; 182 m asl) (Figure 1.1A).

At the Last Glacial Maximum (LGM), ice from glaciers on the western and northern flanks of MSL discharged into the Salto and Tranquilo valleys, coalescing with the Cochrane-Pueyrredón (CP) outlet lobe from the NPI (Wenzens, 2002). The CP and General Carrera-Buenos Aires (GCBA) outlet lobes reached the Argentinian lowlands (Figure 1.1B) forming large moraine sequences (Caldenius, 1932; Mercer, 1976; Douglass et al., 2006; Hein et al., 2010; Bendle et al., 2017a; Mendelova et al., 2017). Upon ice recession, large ice-dammed lakes formed in the Lago GCBA and Lago CP valleys, draining to the Atlantic (Turner et al., 2005; Bell, 2008; García et al., 2014). Subsequent punctuated drops in lake level occurred as lower elevation drainage pathways opened and drainage switched to the Pacific (Turner et al., 2005; Bell, 2008, 2009; Hein et al., 2010; Bourgois et al., 2016; Glasser et al., 2016; Davies et al., 2018; Thorndycraft et al., 2019). During this period, the large unified palaeolake Lago Chelenko occupied the Cochrane and Lago GCBA valleys at 340-350 m asl, dammed by Pared Norte Glacier to the east (Davies et al., 2018; Thorndycraft et al., 2019) (Figure 1.2).

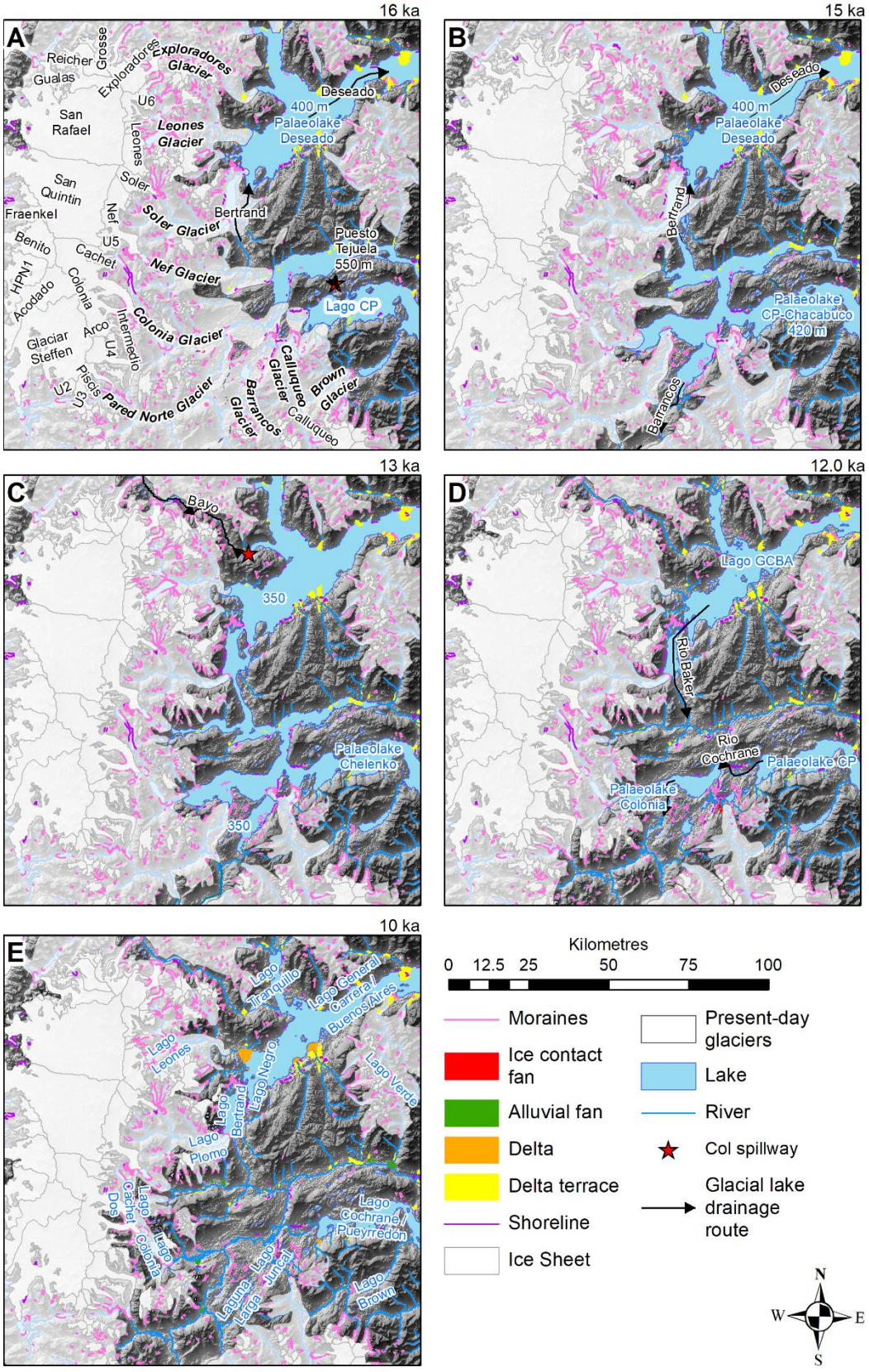

Figure 1.2. Evolution of glaciers and lakes east of the Northern Patagonian Icefield, from 16 – 5 ka. From Davies et al. (2018).

Ice discharging from MSL and the eastern Barrancos Mountains (Figure 1.1A) contributed to large glaciers in the Salto and Tranquilo valleys (Davies et al., 2018). Ice in the Salto valley coalesced to terminate in Lago Chelenko, forming the ACR Esmeralda moraines at 13.4 ± 0.2 ka

(Davies et al., 2018; Thorndycraft et al., 2019; Figure 1.2C)). Recession of ice formed a series of inset moraines, including the "Moraine Mounds" (Figure 1.2D) dated to 12.7 ± 0.4 ka (Glasser et al., 2012).

Today, small-scale glaciers occupy high ground on Cordon Esmeralda (Figure 1.1A). MSL supports a small ice cap with an area of 207 km^2, with the largest outlet glacier, Calluqueo Glacier descending to 520 m asl (Falaschi et al., 2013). There is asymmetry in the snowline attributed to regional precipitation gradients: 1700 - 1750 m asl in the wetter western sectors and 1800 m asl in the drier eastern sectors (Falaschi et al., 2013).

1.6. Thesis structure and results

Chapter 2 introduces present and past glaciation and climate in Patagonia and specifically the MSL ice cap, identifying gaps in current understanding, before outlining the key physical concepts behind glacier flow dynamics and mass balance that form the fundamental theoretical basis for this thesis. Chapter 3 provides a broad overview of the methods and approaches used in this thesis. Chapters 4, 5, 6, and 7 outline data collection and results obtained from this work, before these findings are discussed within the broader Southern Hemisphere and global glaciological and climatic context in Chapter 8. Chapter 9 presents the conclusions of this work.

1.6.1. Chapter 4: Sediment-landform assemblages and landsystems of the northern MSL region

Chapter 4 targets **Obj. 1**, detailing newly mapped sediment-landform assemblages in the Salto, Tranquilo and Pedregoso valleys north of the MSL ice cap, obtained from detailed remote sensing, field-based geomorphological mapping and sedimentological investigation. Work identified seven new moraine sets, ground truthing a further seven within a recessional sequence, and revealed a complex evolution between glaciolacustrine, land-terminating glacial, mountain valley and paraglacial landsystems and processes during deglaciation. Climate, topography and ice-dammed lakes are found to be key controls on sediment-landform associations and landsystem development.

1.6.2. Chapter 5: Glacier chronology and post-ACR recession

Chapter 5 targets **Obj. 2**, detailing the results of new ^{10}Be surface exposure dating of ten glacially-transported boulders found on moraine ridges across two moraine complexes within the Salto and Predrogoso valleys, giving new uncertainty weighed mean (UWM) ages to these complexes of 12.5 ± 0.4 ka and 12.1 ± 0.4 ka respectively. These new dates are then added to existing, recalculated surface exposure ages and newly acquired geomorphological information from Chapter 4.

1.6.3. Chapter 6: Palaeoglacier and ELA reconstruction

Chapter 6 targets **Obj. 3 and 4**, synthesizing the sediment-landform assemblage and landsystem findings from Chapter 4 with the newly obtained and existing chronological data presented in Chapter 5, to provide a new palaeoglaciological reconstruction of the northern flank of the MSL ice cap from the ACR to present day. The new temporally constrained reconstructions of ice extent are then used to reconstruct palaeo-ELAs at periods of glacier stillstand/readvance at ca. 12.1 ka, 5.6 ka and the LIA, using the AABR method. Using the relationship between precipitation and temperature at the ELA, and the WAIS Divide palaeotemperature reconstruction, precipitation is quantified at these points in time. Relative to present day, these reconstructions show 1.1°C cooling and 33% to 37% higher precipitation at ca. 12.1 ka, 0.3°C cooling and 24% to 33% higher precipitation at ca. 5.6 ka and 0.7°C cooling and 19% to 29% higher precipitation at the LIA. These values provide a hypothesis for past climate conditions, tested with a glacier numerical model in Chapter 7.

1.6.4. Chapter 7: Numerical modelling of the MSL ice cap

Chapter 7 targets **Obj. 5 and 6**, presenting a new present-day simulation of the MSL ice cap, using the Parallel Ice Sheet Model (PISM). Temperature and precipitation datasets, obtained from climate models (WorldClim2 and RACMO2.3) and empirical data are first evaluated for their suitability to force the model, before the model is tuned to match present-day ice extent, thickness and velocity. Experiments testing the model's sensitivity to physical parameters (ice rheology and bed strength), mass balance parameters (positive degree day melt factors) and climate (temperature and precipitation) are described and results presented. The present-day ice cap is found to be composed of largely temperate ice, flowing up to 330 m yr^{-1} primarily through basal sliding, with a high surface mass flux. Surface mass balance ranges across the ice cap from +4.8 m w.e. a^{-1} to -6.5 m w.e. a^{-1}.

1.6.5. Chapter 8: Discussion

Chapter 8 first evaluates the landsystems and processes operating north of the MSL ice cap, as revealed in chapter 4, within the context of temperate glacial landsystems and processes globally. **RQ 5 and Obj. 7** are then targeted, evaluating the chronology of recession of Calluqueo Glacier from Chapters 5 and 6 and results of model climate sensitivity experiments from chapter 7 within the context of Patagonian and wider Southern Hemisphere deglaciation, climate and ocean-atmosphere system change following the ACR. It is found that while temperature is the dominant control on glacier mass balance and glacier change, glaciers at MSL have among the highest sensitivity to precipitation relative to temperature of glaciers throughout Patagonia and New Zealand. It is concluded that deglaciation of Calluqueo Glacier following the ACR was

primarily driven by rapid Southern Hemisphere atmospheric warming, but was also likely to be significantly impacted by reduction in precipitation following the southward migration of the SWW during this time.

2. Literature review

This chapter will firstly introduce Patagonia and then focus on the area of Monte San Lorenzo, with a description of the physiography, palaeoclimate and present and past glaciology. Next a review of previous work will highlight gaps in existing knowledge to set up the foundation of research upon which this thesis builds. Finally, the chapter introduces the physical concepts behind how and why glaciers flow, advance and recede. This chapter therefore forms the fundamental theoretical basis for the thesis.

2.1. Study area

2.1.1. Regional setting

South America is dominated on its western flank by the Andes which extend for 68° in latitude from their northmost point in tropical Colombia (12°N) to their temperate southernmost extent in Chile and Argentina (56°S) (Rodbell et al., 2009). Between 40°S and 55°S a complex fjord system sits to the west (Glasser and Ghiglione, 2009), while overdeepened lake basins extend into the plains of the Argentine steppe to the east (Turner et al., 2005). South America's primary ice masses are the NPI and larger SPI (46.5°S to 51°S) which cover 4365 km^2 and 13,219 km^2 respectively (Davies and Glasser, 2012), Gran Campo Nevado (53°S) and Cordillera Darwin (54.5°S) (Figure 2.1).

Patagonia intersects the path of the moisture-bearing mid-latitude SWW, bringing precipitation to the Patagonian Andes and its major ice masses, as well as other southern continents (Trenberth, 1991; Gilli et al., 2005; Moy et al., 2008). Patagonia experiences a temperate climate, with a strong precipitation gradient from west to east caused by the Andean orographic divide. Between 5000 mm and 10000 mm mean annual precipitation west of the Andes decreases to less than 300 mm in the rain shadow east of the continental divide (Garreaud et al., 2013). The core of the SWW circulate above the southern ocean, situated between 48°S and 50°S (Moreno et al. 2009). They are primarily driven by the strong temperature and pressure gradients between the pole and equator and are a major driver of the Antarctic Circumpolar Current (Shulmeister et al. 2004). The SWW are therefore strongly interconnected with broader oceanic and atmospheric systems, driving ocean upwelling and in turn controlling CO_2 fluxes from the deep ocean to the atmosphere (Russell et al., 2006; Anderson et al., 2009).

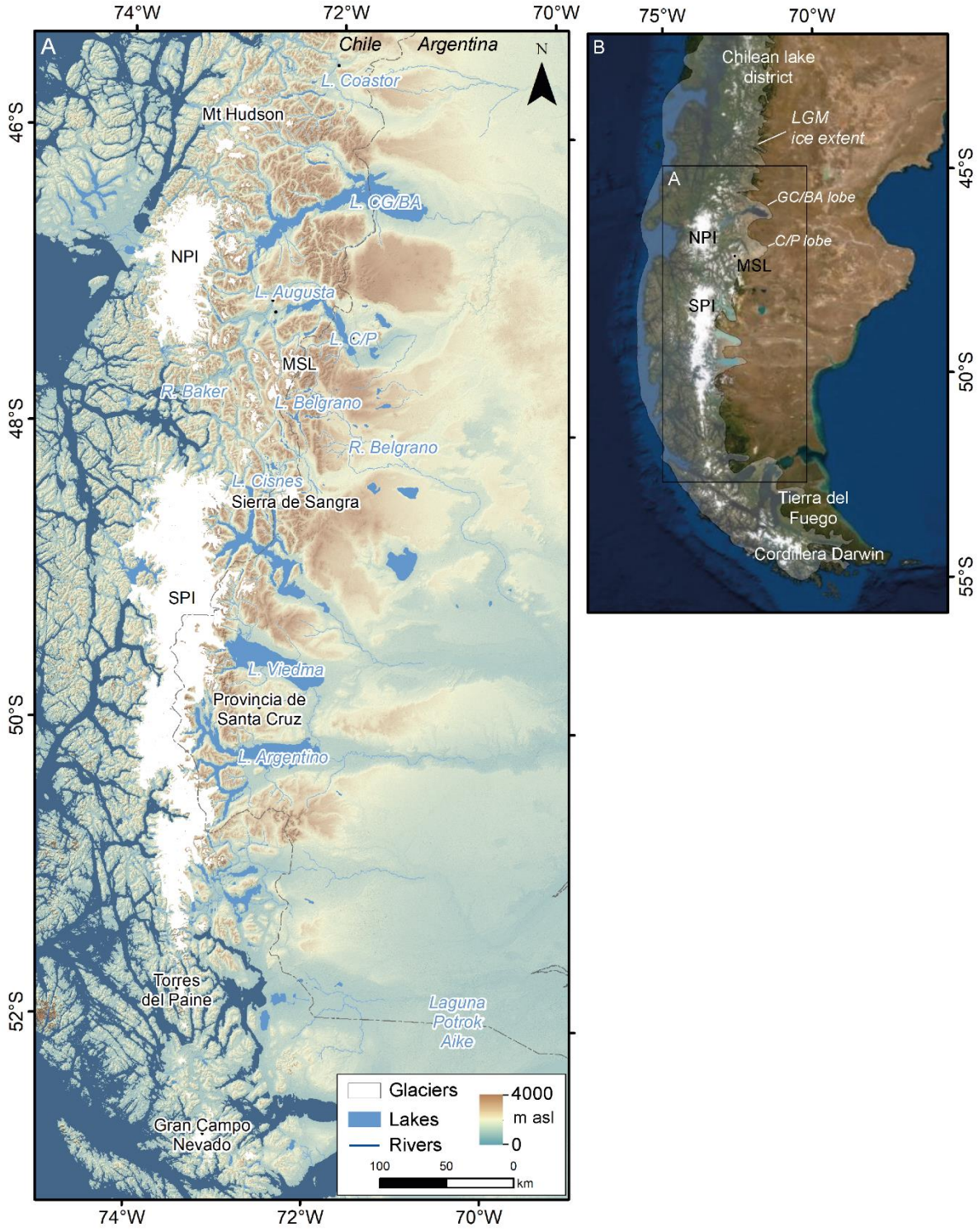

Figure 2.1. (A) Map of the region surrounding the NPI and SPI in Patagonia with selected lake, river and place names labelled. (B) NPI and SPI within the wider context of southern South America, with the extent of the Patagonian Ice Sheet at the LGM shown.

The MSL ice cap (47˚35'S, 72˚18'W, 3706 m asl) is the third highest peak in the Patagonian Andes (Masiokas et al., 2009). Up to 102 ice bodies have been mapped on MSL, covering an area of 207 km^2 (Falaschi et al., 2013). Alongside Sierra de Sangra to the south, these represent the major ice masses to the east of the Patagonian Ice Fields (Figure 2.1A). The four largest glaciers at San Lorenzo are the valley glaciers Rio Oro, Rio Lacteo, San Lorenzo Sur and Calluqueo.

Calluqueo is the largest at 45.3 km^2 (Falaschi et al., 2013), extending to 6oo m asl. (Figure 1.1A; Chapter 1). Rio Lacteo Glacier to the east and San Lorenzo Glacier are largely debris covered and terminate in proglacial lakes. The meltwater of the Rio Lacteo glacier discharges into Rio Lacteo river, which alongside meltwater from San Lorenzo Glacier, feeds into Lago Belgrano to the south. Calluqueo glacier to the west terminates on bedrock but supplies a large, 3.5 km long, proglacial lake, which discharges into Rio Salto to the north. Meltwater from Rio Oro glacier feeds into Lago CP to the northeast. 130 active rock glaciers have also been identified at MSL and the immediately surrounding area (Falaschi et al., 2015).

MSL experiences a temperate climate with a mean annual temperature of 8.4 °C as measured between 2013 and 2016 at the meteorological station in Cochrane (47° 24'S, 72° 59'W). Recent precipitation records from Cochrane are intermittent, however a more complete record exists for the period 1980 to 2000, during which average annual precipitation was 750 mm (Dirección Meteorológica de Chile). A 0°C isotherm for MSL is located at approximately 1725 m asl (Falaschi et al., 2015), concordant with a visible snowline between 1700 and 1800 m asl (Falaschi et al., 2013). With the majority of the glaciated area at low elevations, these glaciers also have low accumulation area ratios (Falaschi et al., 2013, 2016) and are hence sensitive to small changes in ELA.

Study of MSL outlet glaciers is limited. Falaschi et al. (2016) used SRTM and SPOT5 DEM differencing to derive glacier surface elevation changes between 2000 and 2012. This revealed concentrated zones of surface lowering in the lower ablation areas of Calluqueo, Rio Oro, Rio Lacteo and San Lorenzo Glaciers of greater than 5 m a^{-1}, and between 0 m a^{-1} and 5 m a^{-1} in the accumulation area, with values > 2 m a^{-1} only at the highest elevations. However, the understanding of glacier mass balance magnitude and distribution and mass turnover at the glaciers is still unknown. In the absence of field studies, glacier flow dynamics and velocity are also unclear, with only patchy surface velocity records available from the Global Land Ice Velocity Extraction Landsat 8 (GoLIVE) Version 1 dataset (Fahnestock et al., 2016; Scambos et al., 2016). The distribution of temperate and cold-based ice is also unknown. Records show that glaciers at MSL have reduced in size during recent warming, with the glaciated area decreasing by 0.8% a^{-1} between 1985 and 2008 (Falaschi et al., 2013). However, the degree to which glaciers are sensitive to temperature and precipitation and the relative importance of these climate variables for glacier change is unknown.

2.1.2. Palaeoclimate of Patagonia

Patagonia has experienced complex changes in climate following the LGM, a period defined as 27 to 21 ka (Clark et al., 2009; Hughes et al., 2013). During the Last Glacial-Interglacial Transition

(LGIT) (*ca* 18 ka to 8 ka), a period of atmospheric warming occurred in the Patagonia, punctuated by the ACR cooling event (14.5 ka to 12.8 ka) (Blunier et al., 1997; Lemieux-Dudon et al., 2010; Pedro et al., 2016). From the WAIS Divide ice core record, a rapid *ca* 2.5°C increase in temperature can be seen following the ACR until the onset of the Holocene (11.7 ka) after which warming became more gradual (Buizert et al., 2015; Cuffey et al., 2016).

Indications of the palaeoclimate of Patagonia have been established from numerous proxy records. The locations of proxy sites is dictated by the natural requirements of their formation (e.g. glaciated regions, lakes, peat bogs etc.) and ease of accessibility, resulting in most records being found to the east of the ice fields (Kilian and Lamy, 2012). Numerous publications have sought to compile such records (e.g. Mancini et al., 2005; Kilian and Lamy, 2012; Iglesias et al., 2016) from which inferences about broad scale atmospheric circulation and systems have been made (Lamy et al., 2010; Björck et al., 2012; Fletcher and Moreno, 2012). Using these records in combination provides the best opportunity to gain the most comprehensive insight into past regional climate.

Between 16 and 11 ka, pollen records in the Chilean Lake District (Figure 2.1B) reflect long term cool and wet conditions in the region, with enhanced variability in the LGIT (Moreno, 2004; Moreno and Videla, 2016). Particular cold periods have been identified during the ACR and Huelmo–Mascardi Cold Reversal (13.5 to 11.6 ka) (Hajdas et al., 2003; Massaferro et al., 2014; Moreno and Videla, 2016). South of 45°S, temporal oscillations in the isotope and pollen record indicate low but variable levels of moisture during this time (Iglesias et al., 2016), with other records contrasting slightly, suggesting increased precipitation in a cold climate with particular precipitation variations between 13.4 and 11.8 ka (Villa-Martínez et al., 2012). To the south of the SPI, palynological records and transfer functions suggest a dry Late Glacial period (*ca* 15 ka to 11.5 ka) (Schäbitz et al., 2013), with precipitation increasing into the Holocene (Tonello et al., 2009). Temperatures were broadly warm, but with a colder period coeval with the ACR (Mansilla et al., 2016), as at sites to the north.

The Holocene began with an extended warm and dry period between 11.3 and 7 ka in the Chilean Lake District, before cooler and wetter periods with reduced fire activity, climaxing at 5 ka at the time glaciers reaching the first Neoglacial maximum (Moreno, 2004; Moreno and Videla, 2016). A similar early to mid-Holocene sequence is apparent at 44°S at Lago La Pava (Iglesias et al., 2016), with increased fire activity followed by cooler and wetter conditions after 8.5 ka, a signature also seen at records on both sides of the Andes at latitudes between 41°S and 45°S (Iglesias et al., 2016). Again a similar sequence is seen in central Patagonia (47°S) where pollen, spore and charcoal records to east of the NPI at Lago Augusta also suggest a warm start to the Holocene between 11.8 ka and 9.8 ka, followed by a precipitation increase (Villa-Martínez

et al., 2012). Warmer conditions moving into the Holocene are also reflected in a marine core off the Chilean Taitao Peninsula at 46°S, established through clay mineralogy and major element geochemistry (Siani et al., 2010). In southern Patagonia at marine (Caniupán et al., 2011) and pollen sites with continued *Nothofagus* development (Mansilla et al. 2016) at 52°S indicate a warm climate up to *ca* 8 ka. Contrary to sites further north, southern Patagonia pollen, charcoal and lake level records provide evidence for a dry, low precipitation period in the mid Holocene (Kilian and Lamy, 2012; Schäbitz et al., 2013; Mansilla et al., 2016), although this is not the case at all sites (Tonello et al., 2009).

The late Holocene saw alternating, centennial phases of cold and wet and warm and dry conditions in the Chilean Lake District with a significant drought at 2.5 ka (Moreno and Videla, 2016) in the middle of a prolonged warm-dry phase between 2.9 ka and 1.8 ka, after which modern climate conditions become apparent (Moreno, 2004). Further south, air temperature reconstructions from Lago Coastor (45°S) sediment cores reveals a colder than present period *ca* 1.5 ka, followed by a warmer period *ca* 1.4 ka to 0.9 ka, with a notable onset of colder conditions from *ca* 0.8 ka onwards (Elbert et al., 2013). $\delta^{18}O$ mollusc records from Lago Cisnes (47°S) point towards a dry late Holocene period between 1.7 ka and 1.1 ka, with a more recent humid period between 0.75 and 0.17 ka (Alvarez et al., 2015). Quantitative reconstructions from pollen transfer functions at Lago Argentino (52°S) (Tonello et al., 2009) and Laguna Potrok Aike (52°S) (Schäbitz et al., 2013) indicate a general increase in precipitation continuing into the late Holocene, albeit with short term fluctuations. Within this increase, Ca/Ti records at Laguna Potrok Aike (Haberzettl et al., 2009) are able to pick out a notable dry period during the Medieval Climate Anomaly (Schäbitz et al., 2013). Data from this site also indicates a drier last 1000 years (Tonello et al., 2009).

Due to the strong relationship between the SWW and precipitation in southern South America (Garreaud, 2007), precipitation proxies have primarily been used to make inferences about the timing and nature of the past latitudinal shifts, expansion, contraction and changes in the intensity of the SWW belt. Although, as with temperature and precipitation inferences, there are discrepancies between reconstructions (see e.g. Kilian and Lamy, 2012), some broad patterns can be found across proxies and sites. During the Lateglacial, SWW strength was generally low, but increased during the ACR and Younger Dryas at sites in the Chilean Lake District and across Patagonia, and the belt migrated southwards during this time (Fletcher and Moreno, 2012; Mayr et al., 2013; Oehlerich et al., 2015; Vanneste et al., 2015; Moreno and Videla, 2016). This was followed by a general decrease in wind strength into the early Holocene before an increase into the middle Holocene, coinciding with the onset of Holocene neoglaciations (Fletcher and Moreno, 2012; Villa-Martínez et al., 2012; Oehlerich et al., 2015;

Van Daele et al., 2016). A broad increase in wind strength in central Patagonia supports the theory that the SWW belt broadened during the early and middle Holocene (Van Daele et al., 2016). In the late Holocene the SWW reduced in intensity towards conditions similar to present (Lamy et al., 2010; Oehlerich et al., 2015). Sites to the west of the Andes suggest an anti-phasing between the winds' core and northern margin during the Holocene, with a stronger core and weaker northern margin during the early Holocene and the opposite occurring in the late Holocene (Lamy et al., 2010). The range of proxy records discussed here provide a key indication of changes in Patagonian climate through the last deglaciation, however quantifiable estimates of temperature and particularly precipitation are limited in number and spatial extent (Tonello et al., 2009; Massaferro and Larocque-Tobler, 2013; Schäbitz et al., 2013b).

2.1.3. Deglaciation of the Patagonian Icefields and Monte San Lorenzo

During the climate variations of the Quaternary, the Patagonian Icefield has grown and receded multiple times (Kaplan et al., 2004, 2005; Glasser et al., 2012). Large moraines to the east of the current NPI and SPI show the extent of outlet glaciers during Pleistocene maxima (Caldenius 1932). These vary in distance from the current extent of the icefield, from approximately 200 km in the north to 80 km in the south (Wenzens, 2002). At 30 ka the Patagonian Ice Sheet (PIS) covered 497.6 x 10^3 km^2, extending to the continental shelf in the west (Hubbard et al., 2005; Davies et al, submitted) and as large outlet lobes into the Argentinian lowlands to the east (Glasser et al., 2005). East of the NPI, the Lago GCBA and Lago CP lobes extended over 160 km from the present-day ice field to their LGM extent delineated by major arcuate moraine complexes (Caldenius, 1932; Kaplan et al., 2004; Glasser et al., 2005; Hein et al., 2010; Bendle et al., 2017b). The Lago GCBA lobe formed the Fenix moraines, dated to between approximately 21 ka and 29 ka (Kaplan et al., 2004; Douglass et al., 2006; Davies et al., submitted). To the south the Río Blanco Moraines mark an LGM extent of the Lago CP lobe between approximately 21 ka and 30 ka (Hein et al., 2009, 2010; Smedley et al., 2016). Based on a varve record, the onset of deglaciation of the Lago GCBA lobe has been dated to 18.1 ± 0.21 ka (Bendle et al., 2017a), with deglaciation occurring regionally after between 18 ka and 19 ka (Davies et al., submitted). Deglaciation east of the Northern Patagonian Icefield was accompanied by the development of large regional and smaller localised ice-dammed lakes, which underwent complex evolution, and drainage reversal events, as ice receded and new drainage pathways opened to the Pacific (Figure 2.2) (Turner et al., 2005; Bell, 2008; Hein et al., 2010; García et al., 2014; Bourgois et al., 2016; Carrivick et al., 2016; Davies et al., 2018; Martin et al., 2019; Thorndycraft et al., 2019).

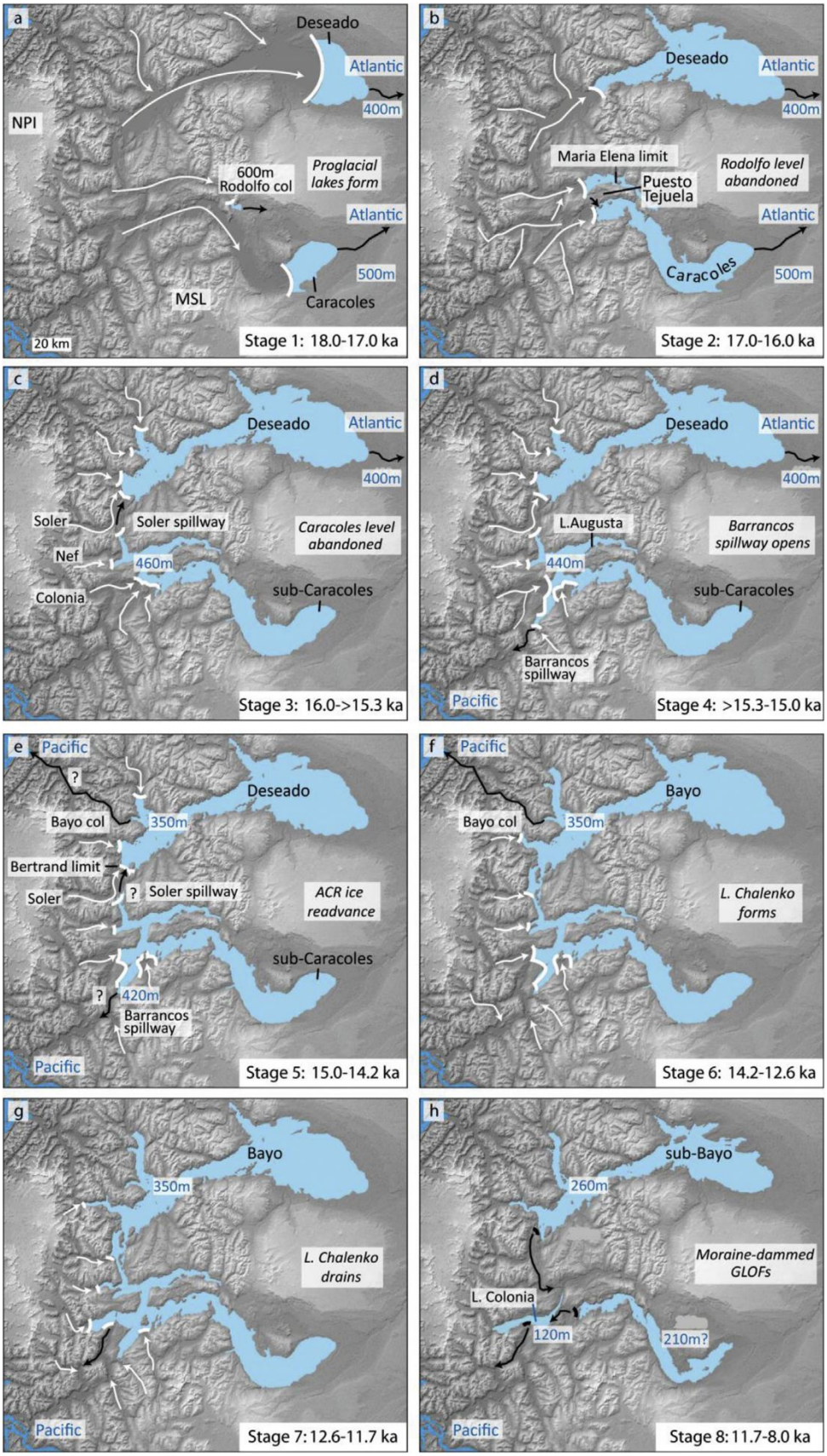

Figure 2.2. Evolution of large regional ice-dammed palaeolakes east of the NPI (46-48°S) during deglaciation. White and black arrows indicate ice flow and meltwater drainage pathways respectively. White and black lines delineate glacier-lake margins and moraine dam positions respectively (Thorndycraft et al., 2019).

At the LGM, outlet glaciers to the southeast of MSL converged in Rio Belgrano valley, extending *ca* 70 km from the massif (Mendelová et al., 2020). To the north and west, glaciers fed into the Tranquilo, and Pedergoso and Salto valleys respectively (Davies et al., 2018), before becoming part of the larger Colonia ice lobe, draining towards Lago Cochrane (Wenzens, 2002). Moraines mapped around MSL show frontal positions during the late Pleistocene and Holocene (Mercer, 1968; Wenzens, 2005; Glasser et al., 2012; Garibotti and Villalba, 2017; Davies et al., 2018). The large Lago Esmeralda terminal moraine (Figure 1.1A, Chapter 1) set to the east of the Lago Esmeralda has been dated to the ACR to mark the furthest readvance of ice from the Calluqueo glacier since the LGM (Davies et al., 2018). Subsequent inset moraines mark periodic recession of Calluqueo glacier (Glasser et al., 2012; Davies et al., 2018; Martin et al., 2019). The chronology of deglaciation of the Monte San Lorenzo ice cap is discussed further in Chapter 5 and Chapter 8. In the northern Salto valley, mapping of palaeoshorelines, the ice-contact fan Juncal fan, and subaqueous morainal banks revealed a glaciolacustrine landsystem and associated processes following recession of Calluqueo glacier from its ACR limit (Davies et al., 2018). Our current understanding of the environments, landsystems and processes with operated north of the MSL during deglaciation are otherwise unknown.

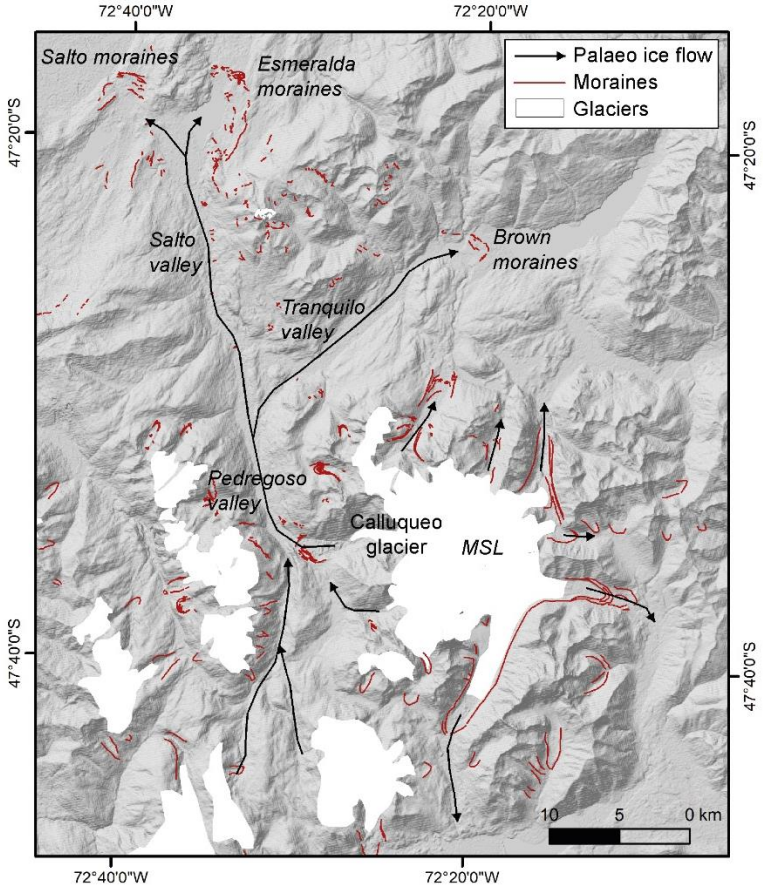

Figure 2.3. Palaeo ice-flow routes of the outlet glaciers of the Monte San Lorenzo ice cap

2.2. Physical glaciology and controls on glacier change

2.2.1. Glacier mass balance and mass balance processes

Glaciers are an active system, with processes constantly exchanging mass between the glacier and the surrounding environment (Figure 2.4). The summed product of these processes over time determines the glacier's total change in mass, its mass balance (Cuffey and Paterson, 2010).

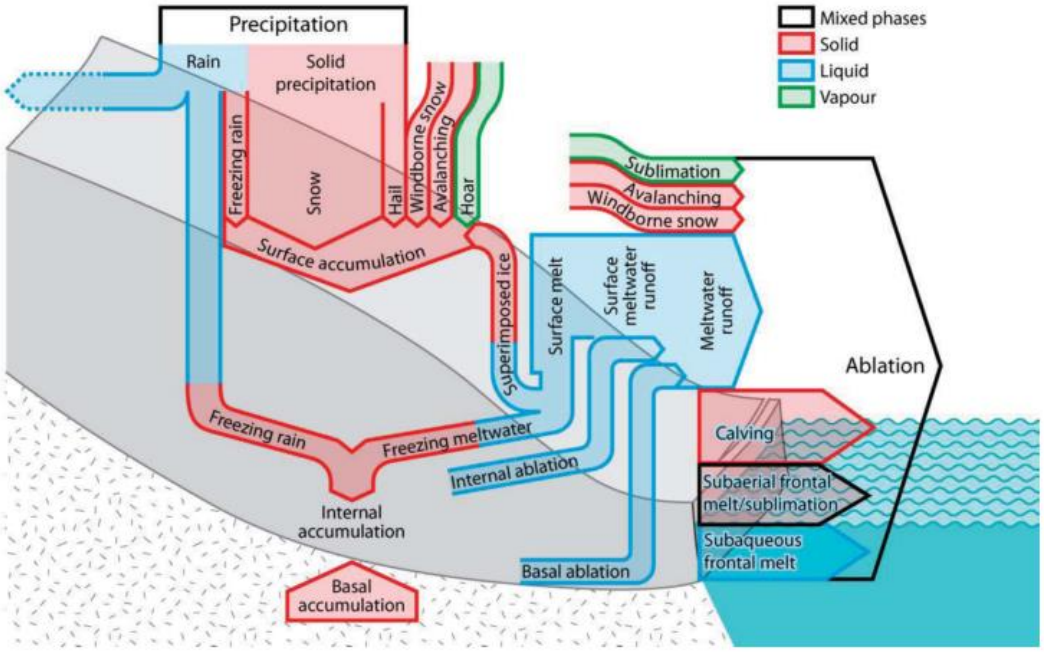

Figure 2.4. Schematic diagram showing processes of mass exchange between the glacier and surrounding environment which determine the glacier's mass balance. Arrow widths do not indicate magnitudes of the movement of mass (Cogley et al., 2011).

Each year a glacier gains mass (accumulation) predominantly by the addition of snow and ice on the surface and by the refreezing of meltwater in the glacier's upper layers. Mass is lost (ablation) through the melting and breakaway of ice during summer and through the change of water direct from the solid to liquid phase (sublimation). If the glacier has a net gain of mass (the input of ice is greater than the loss), the mass balance is positive. If the glacier is losing more ice than is being input into the system, the mass balance is negative (Benn and Evans, 2010). The net change in mass over an annual cycle controls the size of the glacier from one year to the next, whether it grows or shrinks (Cogley et al., 2011). Glacier mass balance is therefore an indication of the 'health' of a glacier.

The mass balance of a glacier can change during a year, depending on when periods of accumulation and ablation occur. This is in turn a product of the seasonal variation in air temperature and precipitation which themselves vary globally, leading to different mass balance cycles in different regions (Ageta and Higuchi, 1984). Air temperature is important as a warm

climate can result in precipitation falling as rain rather than snow, therefore decreasing effective accumulation (e.g. at the Antarctic Peninsula (Davies et al., 2014)).

In mid to high-latitude regions such as those of Patagonia, Europe and North America, a winter accumulation cycle occurs, where accumulation dominates in the winter and ablation dominates in the summer (Benn and Evans, 2010; Cuffey and Paterson, 2010) (Figure 2.5a). Such a pattern is also seen in the western Himalaya (Karakoram, Ladakh etc) (Benn et al., 2005). Where the summer climate is influenced by monsoons and contrasted by a cold and dry winter season (e.g. at the high altitudes of the Tibetan Platea (Fujita and Ageta, 2000) and Nepal (Ageta, 1983) in the eastern Himalaya) accumulation and ablation happen simultaneously in the summer months (Figure 2.2b). Mass balance therefore does not fluctuate significantly between seasons. If there is little variation in temperature between seasons (e.g. in East Africa (Hastenrath, 1984)) accumulation and ablation remains relatively constant throughout the year (Figure 2.5c).

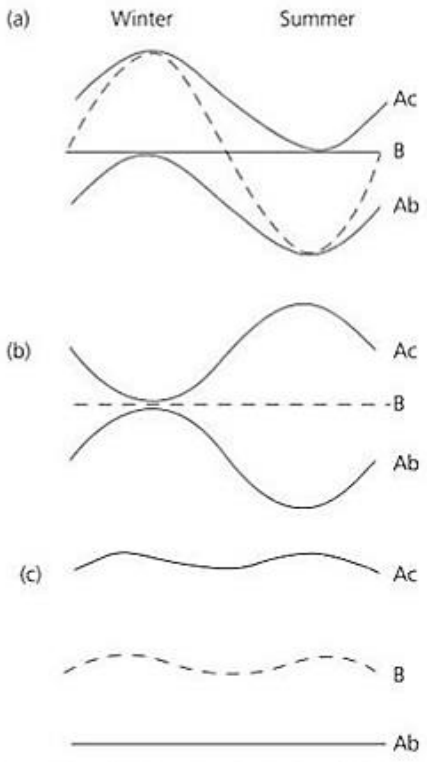

Figure 2.5. Annual mass balance cycles with different patterns of accumulation (Ac), ablation (Ab) and resulting mass balance (B) for winter accumulation type (a), summer accumulation type (b), and year-round ablation type (c). Modified from Ageta & Higuchi 1984 in Benn & Evans 2010.

It is important to measure and record glacier mass balance in light of the role glaciers play in wider interconnected systems, and their strong connection to the Earth's climate. Glacier mass balance has been shown to be controlled by large scale atmospheric circulation, pressure and related weather systems (Alt, 1978; McCabe and Fountain, 1995; Dowdeswell et al., 1997). In southern South America, large glacier mass balance variations through the Holocene have been attributed to the behaviour of the moisture bearing SWW wind system (Douglass et al., 2005;

Glasser et al., 2012; Boex et al., 2013) which dictates the location and volume of precipitation in the region (Trenberth, 1991; McCulloch et al., 2000) especially along the west of the Andes (Lamy et al., 2010). Because mass balance is a key aspect of glacier dynamics, it forms the link between climate and glacier behaviour (Benn & Evans 2010). Based upon this link, details of paleoclimate variations on millennial timescales can be reconstructed from evidence of past glacier fluctuations (e.g. Svendsen & Mangerud 1992; McCulloch et al., 2000). Over a more recent time period, a better understanding of the relationship between glacier mass balance and climate can be gained by comparing how both of these records have changed over past decades (Dowdeswell et al., 1997; Braithwaite et al., 2013). This is particularly important when monitoring how climate is changing in the present day (Haeberli et al., 2007) and when trying to predict how glaciers will behave given projections of future climate change (Collins et al., 2013).

Glaciers form an important part of the hydrological system, storing water as solid snow and ice, and in liquid form in subglacial, supraglacial, englacial and proglacial lakes (Benn & Evans 2010). Mass lost from glaciers accounts for approximately 30% of current sea level rise (Gardner et al., 2013). Estimates like this have been produced from mass balance records since the mid-20th century (Meier 1984; Meier et al., 2007; Marzeion et al., 2012; Gardner et al., 2013), including from those in Patagonia (Rignot et al., 2003). Glacier snow and ice also provides an important mechanism for sustaining water supplies and hydroelectric power generation during seasonal periods of low rainfall (Fountain and Tangborn, 1985; Immerzeel et al., 2010), contributing most to water availability in very arid regions (Kaser et al., 2010). By supplying rivers, glacier meltwater supports biodiversity, which has been impacted negatively by reductions in glacier mass (Brown et al., 2007; Jacobsen et al., 2012). Glacier retreat has also been proposed to increase the risk of glacier lake outburst flooding through the growth of moraine-dammed lakes such as in the Himalayas (Richardson and Reynolds, 2000) and Patagonia (Harrison et al., 2006; Dussaillant et al., 2010). Because of the wider role and impact glaciers have, measuring mass balance is key to monitor and predict potential knock on effects of glacier mass balance change.

2.2.1.1. Methods for determining glacier mass balance

Mass balance has been monitored since the late 19th century (Mercanton et al., 1916) by taking measurements directly from the glacier surface using the glaciological method (stake readings, snow pits and snow probing) (Østrem and Stanley, 1969). Continuous annual measurements however were not regularly taken until 1946 when a study began at Storglaciären, Sweden (Schytt, 1962). The glaciological method has been widely implemented (e.g. Thorarinsson 1940; Hagen & Liestøl 1990) and was used when the first mass balance estimates of a Patagonian glacier were made by Popovnin and others in 1999.

Other methods to determine mass balance change have since been developed. Hydrological models determine mass balance by subtracting the output of water from a glacier from the input (e.g. Soruco et al., 2009). The gravitational method calculates mass balance based on measurements of small changes in the gravitational field of the earth at a glacier, using the Gravity Recovery and Climate Experiment (GRACE) satellite (e.g. Luthcke et al., 2008). The geodetic method uses temporal changes in the altitude of points on the glaciers surface (Cuffey and Paterson, 2010), a method that has been applied to, amongst others, the Patagonian ice fields. A Digital Elevation Model (DEM) created with data from the NASA Shuttle Radar Topography Mission (SRTM) has been compared to historical mapping and DEMs to determine mass change and equivalent contribution to sea level rise (Rignot et al., 2003).

Over millennial time scales, geological methods such as geomorphological mapping combined with cosmogenic nuclide dating of glacial transported boulders can be used to recreate past glacier extent and mass balance (e.g. Balco, 2011). This concept will be used in this study, with mass balance inherently linked to the past dynamics of the Calluqeuo glacier which will be reconstructed and modelled. Discrepancies have been found to occur to varying extents between different methods of glacier mass balance measurements (Tangborn et al., 1971; Cox and March, 2004; Hagg et al., 2004) so a degree of caution should be taken when comparing studies which have used different data collection methods. Since 1986 global glacier mass balance data has been collated and made freely available by the World Glacier Monitoring Service (e.g. Figure 2.6) (Zemp et al., 2009).

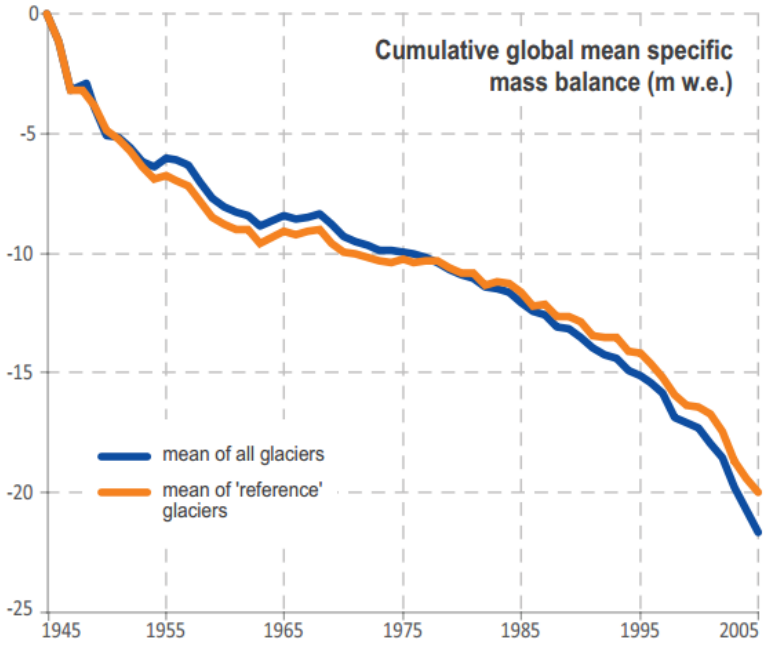

Figure 2.6. Example of global glacier mass balance data compiled by the World Glacier Monitoring Service, showing increasing negative mass balance for glaciers globally compared to 30 'reference' glaciers (World Glacier Monitoring Service, 2008)

2.2.1.2. Mass balance processes

The main components of ablation and accumulation that determine the mass balance of a glacier are shown in Figure 2.4. At the glacier surface, mass is added by snowfall, avalanche deposition, wind deposition and refreezing of melt water. Mass is lost by wind scour, melting of ice and sublimation (Cuffey and Paterson, 2010).

The surface mass balance rate ($\dot{b}_s$) is equal to:

$$\dot{b}_s = \dot{c}_s + \dot{c}_a - \dot{a}_m + \dot{c}_r - \dot{a}_{sub} + \dot{c}_w \qquad (2.1)$$

$\dot{c}_s$ = snowfall, $\dot{c}_a$= avalanche deposition, $\dot{a}_m$ = melt, $\dot{c}_r$ = refreezing of water, $\dot{a}_{sub}$ = sublimation, $\dot{c}_w$ = wind deposition (Cuffey and Paterson, 2010).

If the annual snowfall on a glacier's surface is greater than the local loss of snow by ablation processes, layers of snow will accumulate. After surviving one ablation season, snow is defined as firn (Cogley et al., 2011). Those layers compact, undergo recrystallization, and the volume of voids decreases, leading to an increase in density of the material., The densities of materials formed by these processes are listed in Table 2.1. The processes involved in the transformation of snow to ice and the time taken for this transformation to occur differs between cold polar regions and high altitudes and mid-latitude low altitude temperate regions. These differences are due to the role of melt water in the latter setting (Benn & Evans 2010).

Table 2.1 Densities of various forms of solid water. 1. Seligman & Douglas 1936 and others; 2. Cuffey & Paterson 2010 3. Cogley et al., 2011. 'Depth hoar' is a low density, porous layer of ice crystals, shaped as prisms, pyramids or cups ranging in size from 2 to 5 mm formed and found beneath the snow surface (Cuffey and Paterson, 2010; Cogley et al., 2011).

Material	*Density (kg m^{-3})*
New snow (immediately after falling in calm conditions)[1,2]	50-70
Newly fallen snow near freezing point[3]	100-300
Depth hoar[2]	100-300
Settled snow[1,2,3]	200-300
Wind-packed snow[1,2,3]	350-400
Firn[1,2,3]	400-830
Glacier ice[1,2]	830-923

.

In a cold region, dry processes dominate. "Newtonian sliding" of grains past one another occurs upon compaction (Alley, 1987), followed by sintering of ice particles, whereby material is transferred to the space between particles forming bonds (Hobbs and Mason, 1964; Maeno and

Eblnuma, 1983). Recrystallization and deformation then become the primary processes further reducing poor space (Cuffey and Paterson, 2010) before glacier ice is formed through deformation by creep (Wilkinson, 1988). In low to mid-latitude temperate regions such as in Patagonia, meltwater percolating through the snow accelerates the process of transformation to ice (Figure 2.7, in this example at the Upper Seward Glacier, Alaska) (Benn & Evans 2010). With water present, ice bonds form between grains, which grow thicker until the pore space is significantly reduced, and glacier ice forms (Wakahama, 1975). The process of packing is accelerated as meltwater acts to lubricate the grains and pull the grains together by surface tension, creating a higher maximum density than in a dry zone (Cuffey and Paterson, 2010).

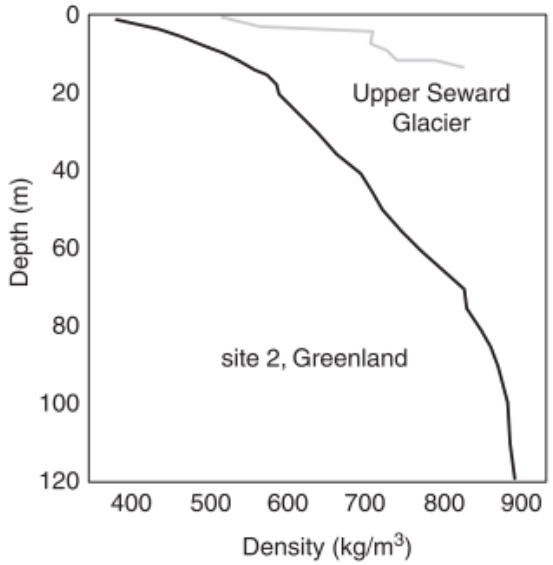

Figure 2.7. A comparison between density profiles of a very wet glacier (Upper Seward Glacier from coastal Alaska) and a very dry glacier (site from Greenland) (after Paterson, 1994 in Anderson & Anderson, 2010)

Melting is commonly the main process of ablation on glaciers, particularly in those regions where temperatures are above freezing during parts of the annual cycle, such as Patagonia. In cold, dry continental settings such as in the high latitudes of Antarctica, sublimation plays a greater role (Benn & Evans 2010). Both processes are driven by the net flux of energy from the atmosphere to the glacier surface, most importantly by radiation and turbulent mixing of heat and water vapour in the air adjacent to the glacier surface (Cuffey and Paterson, 2010). Wind scour can also remove mass from the surface of a glacier, depending on the surrounding topography (Benn & Evans 2010).

The increase of mass within a glacier occurs by the freezing of water which enters the englacial system either by percolation of rain or surface water through snow or fern, movement of surface water into crevasses and moulines or by injection of water into basal fractures (Cuffey and

Paterson, 2010). The first of these processes in particular varies systematically along a glacier as described in the classification of glacier zones. Ablation within the glacier, like elsewhere, occurs by melting; this requires energy in the form of heat. Closer to the ice surface, this can come from solar radiation. At greater depths, energy is provided by the geothermal heat flux, deformation of ice and the flow of water through the glaciers internal hydrological system. As ice moves it releases energy known as strain heating, in particular where the ice deforms. (Cuffey and Paterson, 2010).

The addition of mass at the base of the glacier occurs by subglacial water freezing to the underside of the glacier. This occurs due to the relationship between melting temperature and pressure. When subglacial water under high hydrostatic pressure moves into an area of low pressure, the melting point increases, resulting in water being supercooled by the overlying ice unless it warms sufficiently before this can occur (Cuffey and Paterson, 2010). This process often occurs when water flows up a steep slope out of an over-deepening (Alley et al., 1998). Basal ablation occurs by melting. Heat energy transferred to the system is either geothermal from the underlying bed or produced by friction because the ice is flowing. A typical geothermal heat flux of 0.05 W m^{-2} produces a mass balance rate of -5 mm a^{-1}. A glacier sliding at 10 m a^{-1} results in an extra 3 mm of melt per year (Cuffey and Paterson, 2010). If the glacier flows significantly faster, frictional heat will dominate melting.

Where glaciers terminate in an aqueous environment, mass is also lost by calving at the glacier terminus. Blocks of ice break off the glacier at its margin, forming icebergs if the glacier is lake or marine terminating. Rarely, calving also occurs onto dry land by dry calving if the glacier is land terminating. Melting also occurs at the glacier front which can contribute to the break off of ice masses by aiding the growth of crevasses (Cogley et al., 2011). Aqueous calving is a significant process in southern South America. For the period between 2000 and 2011, 61.3 km^3 of ice was lost through calving from the SPI, approximately twice as much as was lost through surface melting (Schaefer et al., 2015). At the SPI all but two outlet glaciers calve into fjords (to the west of the icefield) and proglacial lakes (predominantly on the eastern flank) (Aniya et al., 1996; Warren and Aniya, 1999). At the NPI three quarters of glaciers terminate in water, predominantly in freshwater lakes (Warren and Aniya, 1999; Lopez et al., 2010) with the exception of the tidewater terminating glacier San Rafael (Warren et al., 1995). Mass loss due to calving from NPI and SPI outlet glaciers increased during the period between 1975 and 2011, and upon retreat, previously non-calving glaciers have transitioned to calve into newly formed pro-glacial lakes (Warren and Aniya, 1999; Schaefer et al., 2013).

Calving is controlled by non-climatic variables, such as variations in strain rate and stress imbalances (Benn et al., 2007) and tidal flexure, buoyancy forces, water depth, water

temperature and topography (Warren 1992). Calving glaciers have shown to oscillate out of phase with past climate changes in Patagonia (Warren and Rivera, 1994). Of particular relevance to this study is the decoupling from climate which occurs upon the transition of a glacier from land terminating to calving into a growing proglacial lake (Kirkbride, 1993; Chinn, 1996). It is therefore difficult to make inferences about past climatic conditions based on the glaciological record of calving glaciers. It is a similar case for surge-type and debris covered glaciers whose link to climate either does not exist or is impaired (Yde and Paasche, 2010).

2.2.1.3. Mass balance terminology

Anonymous (1969) and the IHD (International Hydrological Decade) (1970) have been the widely accepted source of mass balance terminology over recent decades, however with improved understanding of glacier mass balance and measurement technologies, further complexities and inconsistencies in terminology have developed (Cogley, 2010; Cuffey and Paterson, 2010; Cogley et al., 2011). Resolving these inconsistencies was the reasoning behind the publication of Cogley et al., 2011, which contains the most recent widely accepted definitions of mass balance terminology.

Glacier-wide mass balance is the mass balance measured or estimated over the entire glacier. This is used as opposed to the term point mass balance which is the mass balance for a specific location on the glacier. The point is at the top of a vertical column through the glacier (Figure 2.8). In conventional notation, point mass balances are written in lower-case (e.g. b_w) and glacier-wide mass balances are indicated by upper-case (e.g. B_w). Mass balance at different depths through the glacier can also be communicated. The surface, englacial and basal mass balances refer to the sum of accumulation and ablation caused by exchanges of mass occurring at the respective depths through the glacier. Since surface mass balance includes internal accumulation (water refreezing within the glacier) which is not detected by measuring surface mass balance, Cogley et al. (2011) suggest that the term climatic mass balance should be used, which is the sum of the surface and englacial mass balance. Climatic-basal mass balance can be used to communicate changes in mass not caused by flow dynamics.

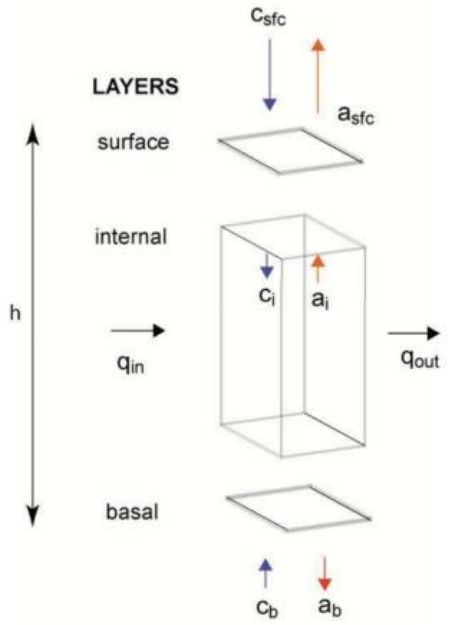

Figure 2.8. The mass balance of a column of glacier ice with height (h), ablation (a) and accumulation (c) processes at the surface (sfc), internally (i) and at the base (b) and ice discharge through the column (q). Cogley et al.,2011

The stratigraphic and fixed date systems for classifying mass balance temporally were initially defined by Anonymous (1969), and have not changed when discussed in subsequent publications (e.g. IHD 1970; Benn & Evans 2010; Cogley et al.,2011). The stratigraphic system uses successive summer surfaces in the stratigraphy of the upper layer of the glacier to determine boundaries from one mass balance year to the next (Anonymous, 1969), equivalent to two successive annual minima of glacier mass (t_1 and t_2 in Figure 2.9) (Cogley et al., 2011). Anonymous (1969) further divides the mass balance year into winter and summer mass balances, covering the period from the start of the mass balance year (mass minimum at t_1) to the time of maximum glacier mass (t_m) and the time between the end of the winter season (t_m) to the end of the mass-balance year (t_2) respectively. The period from t_m to t_2 is the summer season. When a fixed-date system is used, fixed calendar dates define the periods over which mass balance is measured (Anonymous, 1969), from 1st October to 30th September for mid to high latitude glaciers (Benn and Evans, 2010). This method is preferred when applying data practically, for example for estimating the contribution of melt water to hydro-electric facilities (Kaser et al., 2003). Mayo et al. (1972) created a system which combined data from the stratigraphic and fixed date systems to remove unrepresentative results when extrapolating over a whole glacier and to allow for more direct relation of data to hydrological and meteorological applications.

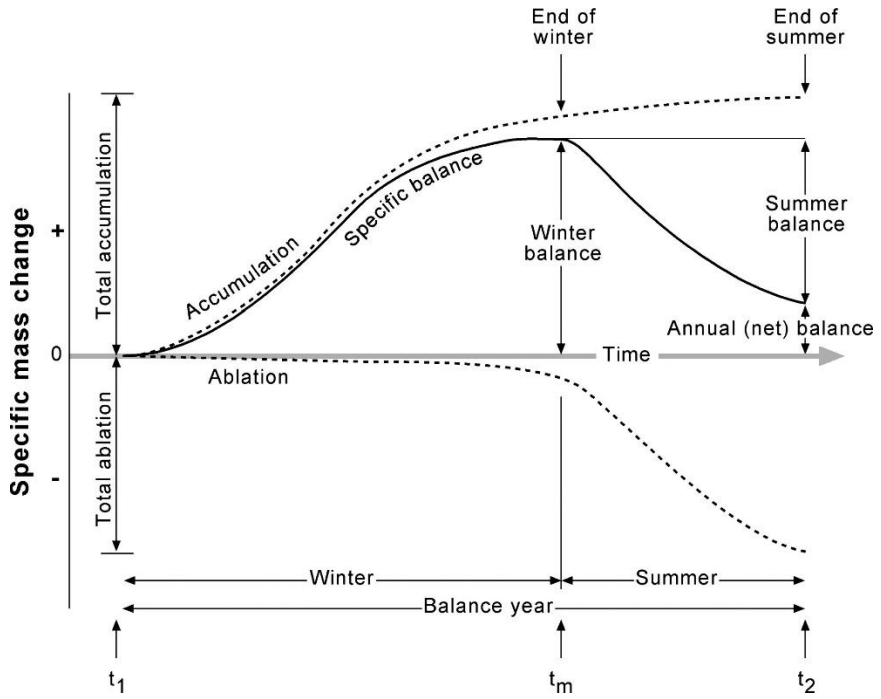

Figure 2.9. Definitions used to distinguishing mass balance temporally in relation to the changing specific balance during an annual cycle (Cogley et al., 2011).

The dimension of mass balance is simply mass (M). When expressed per unit area, the dimension is ML^{-2}. This is called the specific mass balance, which is often referred to simply as mass balance (Cuffey and Paterson, 2010). When specific mass balance is expressed as a rate, per unit time, it has the dimension $ML^{-2}T^{-1}$. Specific mass balance is commonly expressed as meters water equivalent (m w.e.; see equation 2.2 where ρ_w is the density of water). This is the height a certain volume of water (based on its mass) would reach when distributed over a given area, usually 1 m^2.

$$0.001 \text{ m w.e.} = 1 \text{ kg m}^{-2} / \rho_w \qquad (2.2)$$

When reporting mass balance, the area over which the mass balance was calculated should be given to allow for data to be converted between units (e.g. specific units to mass or volume) and mass balances to be compared across different glaciers. Mass conservation in a column through the glacier (Figure 2.8), is expressed by the continuity equation (Eq. 2.3). $\dot{H}$ is the rate of change of thickness of the column, $\dot{b}$ is the specific mass balance rate, or here for clarity to distinguish from the inclusion of changes due to flow dynamics, the climatic-basal mass balance. $\vec{q}$ is the flow vector. As the density of ice is constant, any change in H is due to a change in mass (Cogley et al., 2011).

$$\dot{H} = \dot{b} - \nabla \cdot \vec{q} \qquad (2.3)$$

Mass balance can be subdivided through the vertical column (Eq. 2.4) depending on where the exchange of mass occurs, either on the surface (*s*), internally (*i*), or at the base (*b*) (Cuffey and Paterson, 2010).

$$\dot{b} = \dot{b}_s + \dot{b}_i + \dot{b}_b \quad (2.4)$$

This division with depth through the glacier is necessary as different mass exchange processes happen at different sections of the glacier (Figure 2.4). Generally however, mass exchange on the surface of the glacier dominates (Cuffey and Paterson, 2010). The rate of change of ice thickness at a certain depth (z) can be given by including the ice discharge through the column (Eq. 2.5) where *H* = ice thickness, *W* = glacier length, *q* = (in this context) ice discharge per unit width (L^2/T), *z* = elevation, *b* = local mass balance.

$$\frac{dH}{dt} = b(z) - \frac{1}{W(z)}\frac{dq}{dx} \quad (2.5)$$

By spatially integrating the local mass balance over the total depth of the column and taking into account the hypsometry ((the distribution of area with altitude) height of the valley above sea level), the total mass balance (*B*) can be calculated (Eq. 2.6) (Anderson & Anderson, 2010).

$$B = \int_0^{Zmax} b(z)W(z)dz \quad (2.6)$$

Figure 2.10 shows the mass balance and ice discharge profiles along the length of a glacier. The mass balance is positive at higher altitudes in the top section of the glacier. This area where the cumulative mass balance is positive relative to the start of the mass balance year is defined as the accumulation zone (Cogley et al., 2011). With decreasing elevation along the glacier length, surface mass balance begins to decrease. The point where the surface mass balance is zero is defined by the Equilibrium Line Altitude (ELA). At elevations below this line and continuing progressively along the glacier, mass balance becomes negative and continues to decrease. The area with a negative cumulative mass balance relative to the start of the mass balance year is defined as the ablation zone (Cogley et al., 2011). Along the glacier profile ice discharge increases as mass and ice flow builds, peaks at the ELA, and then drops off in the ablation zone as mass is lost. The ice discharge is zero at the glacier terminus.

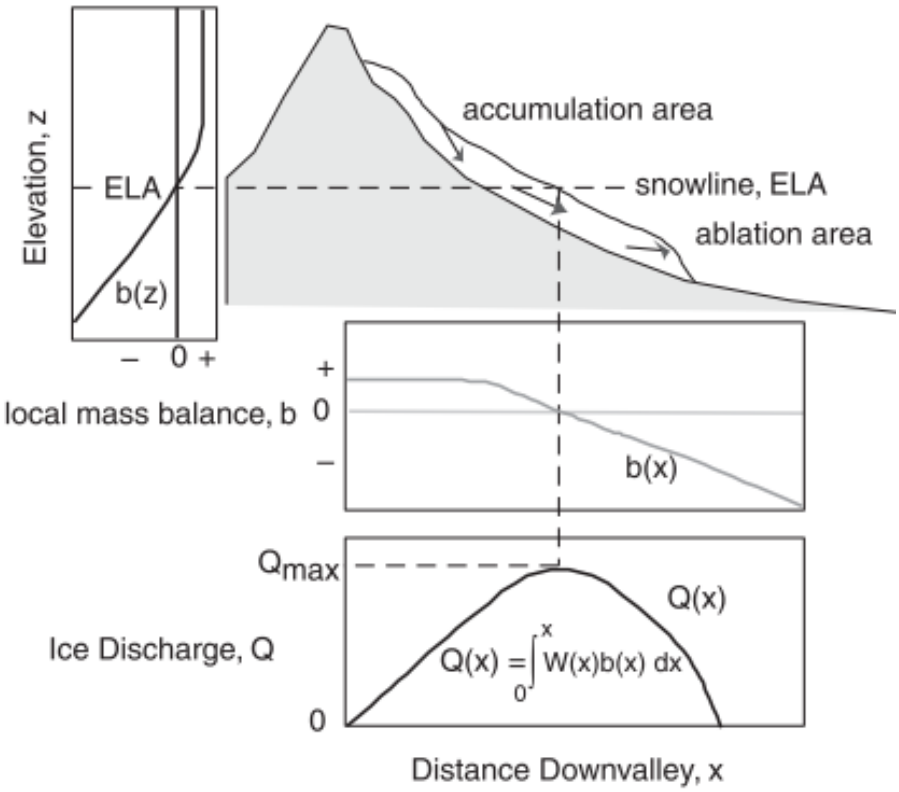

Figure 2.10. Schematic diagrams of a glacier showing accumulation and ablation areas on either side of the equilibrium line, and how the respective mass balance and ice discharge profiles differ over these two zones (from Anderson and Anderson, 2010).

Different locations on a glacier experience different local climatic conditions, primarily because the altitude of the glacier surface changes along its length. Insolation, the aspect of the glacier surface and the transportation of snow by wind are also important spatially variable factors. Surface mass balance is strongly related to climate, with the aforementioned processes of ablation and accumulation predominately controlled by temperature, and also precipitation.

As outlined by Cuffey & Paterson (2010), if air temperature rises:

- Precipitation reaching the ground turns from snow to rain in non-polar environments
- The ice surface is at the melting point for longer
- Melt rates increase strongly if air temperature rises past the melting point

These products of temperature rise have negative effect on mass balance. For colder climates however (mean annual air temperature below -15°C), surface mass balance is controlled primarily by precipitation, as little melting occurs. Temperature still plays a key role, as the water content in the air increases with higher temperatures, leading to increased precipitation.

A glacier can be split into zones based upon which particular mass balance processes are occurring in that area of the glacier (Figure 2.11) (Cogley et al., 2011). This concept and the definitions of zones were first developed by Benson (1961) and Muller (1962) based upon field

data. Benson (1961) undertook pit surveys and Rammsonde (measurement of resistance to penetration) over a 1100-mile traverse in western Greenland, and found four diagenetic facies: ablation, soaked, percolation and dry-snow. This was built upon by Muller (1962) who studied glaciers on Axel Heiberg Island, Canada, and defined five zones: superimposed ice, slush zone, percolation zone B, percolation zone A and dry-snow zone. The main difference between the classifications is that the latter divides Benson's soaked facies into a slush zone and percolation zone B.

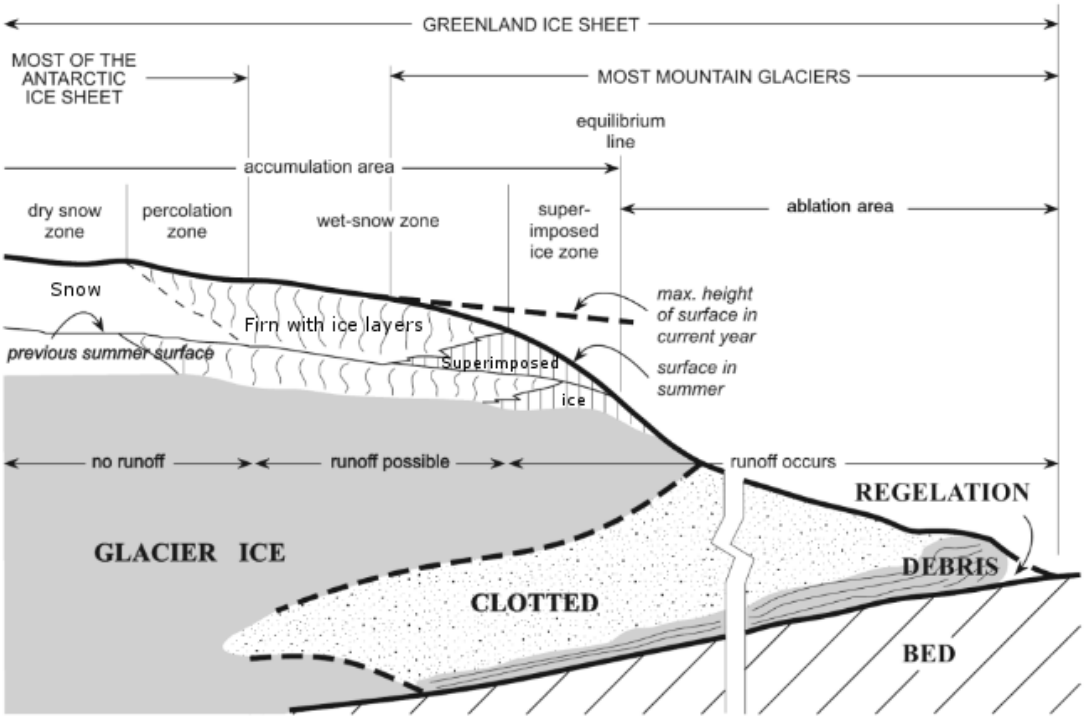

Figure 2.11. Idealised glacier split into zones (Benn & Evans 2010).

In the percolation zone, where water from the surface percolates into the subsurface, the important process of warming by re-freezing of meltwater occurs. Freezing of 1 g of water produces sufficient latent heat to raise the temperature of 160 g of snow by 1 degree. Meltwater can freeze within the firn, forming horizontal lenses and vertical glands (Benn & Evans, 2010). In the wet snow zone, all the snow reaches the melting point during the ablation season, aided by an increase in meltwater with decreasing elevation. The upper boundary of the wet snow zone at the summer surface marks the 0°C isotherm at the end of the summer. With a further decrease in elevation, there is so much meltwater that a continuous mass of ice forms, in the superimposed ice zone. Below the superimposed ice zone is the ELA.

2.2.1.4. Thermal regime

The thermal regime of a glacier is a product of the balance between heat input at base and heat transfer through the overlying ice (Bennett and Glasser, 2009). Cold glaciers sit well below the

freezing point throughout their vertical profile (Figure 2.12a), temperate glaciers sit almost entirely at the pressure melting point (the temperature at which ice melts at a given pressure) (Figure 2.12b) and polythermal glaciers sit below the pressure melting point apart from a basal layer of finite thickness which is at the pressure melting point (Figure 2.12c). With spatial variations in climate and altitude, thermal regimes are distributed in different regions globally; temperate glaciers at the mid latitudes of the European Alps, New Zealand and Patagonia, cold glaciers at high latitudes of Antarctica and the Antarctic Peninsula and polythermal glaciers in Svalbard, northern Sweden and the Himalayas (Glasser and Hambrey, 2001; Hambrey and Glasser, 2012; Davies et al., 2013). The presence of temperate ice in Patagonia's icefields and glaciers has been confirmed by cores taken during field surveys (e.g. of the San Rafael Glacier, Northern Patagonian Icefield (Yamada, 1987), the Pío XI glacier, Southern Patagonian Icefield (Schwikowski et al., 2013) and from the Southern Patagonian Icefield itself (Aristarain and Delmas, 1993)). Measurements of seismic wave speeds also confirms a temperate ice classification in the region (e.g. at Perito Moreno Glacier, Southern Patagonian Icefield (Stuefer et al., 2007)).

The thermal regime dictates glacier movement and in turn erosion, sediment yield and deposition (Boulton, 1972; Hallet et al., 1996; Kleman and Glasser, 2007). This controls the resultant geomorphology such that certain landform assemblages relate to thawed bed conditions below temperate and polythermal glaciers, favourable for subglacial bed erosion, and others to the frozen bed conditions of cold glaciers, with no erosion (Kleman and Borgstrom, 1994). Past thermal regimes, their change through time and to some extent an indication of palaeoclimate, can therefore be reconstructed from glacial geomorphology (Boulton, 1972; Glasser and Hambrey, 2001; Hambrey and Glasser, 2012).

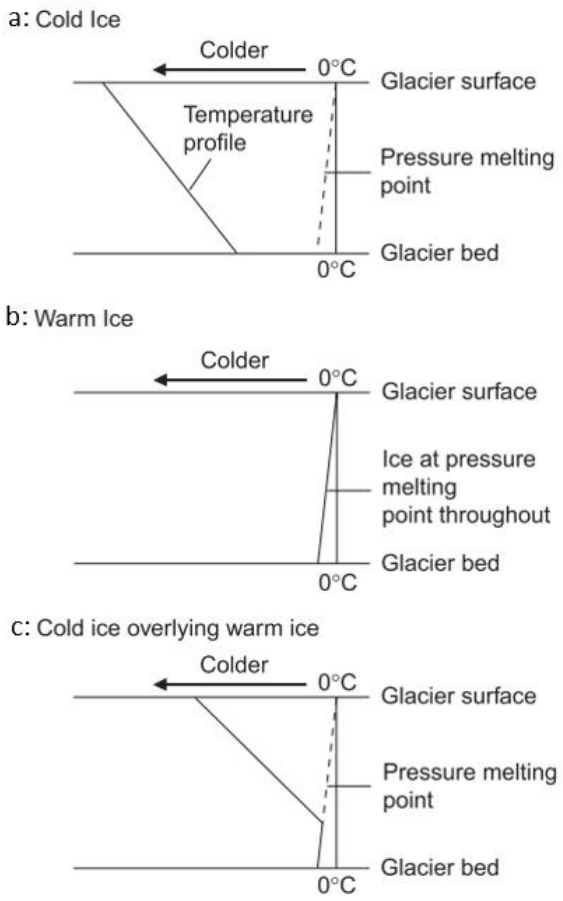

Figure 2.12. Idealised temperature profiles through three glaciers: A: cold based, B:warm based, C: cold ice overlying warm ice at the base (Bennett and Glasser, 2009).

2.2.2. Glacier dynamics

2.2.2.1. Glacier flow

A glacier flows under its own weight due to gravity, transporting snow, ice and debris from high altitude areas of accumulation to the lower altitude ablation zone (Benn & Evans 2010). This movement of ice is fundamental in eroding the landscape and forming glacial landforms. Gravity acts vertically downwards on a glacier with a force (its weight) equal to $\rho g H$ where is the ice density ρ, g is the acceleration due to gravity and H is the ice thickness. Because of either a pressure gradient in the glacier (caused by a change in mass with distance along a glacier profile or because the glacier sits on an angled bed), glaciers flow horizontally. The component of the force acting on the glacier which causes this flow is the driving stress, the force acting per unit area (Cuffey and Paterson, 2010). Taking a simple model of a glacier on a sloping bed (Figure 2.13), the driving stress is the component of the weight parallel to the surface slope, $\rho g H \sin \alpha$. When the glacier is in static equilibrium, this force is balanced by a resistive force, the shear stress at the base of the glacier, the basal drag (τ_b) (Eq. 2.7), which acts in the opposite direction to the driving stress (Cuffey and Paterson, 2010). For a glacier flowing over bedrock, typical values for shear stress are between 50 and 100 kPa (Bennett and Glasser, 2009).

$$\tau = -\rho g H \sin\alpha \qquad (2.7)$$

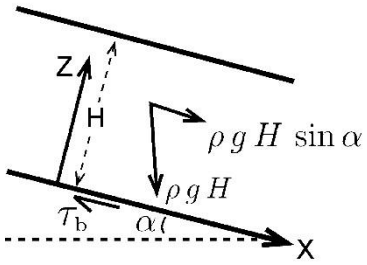

Figure 2.13. Schematic diagram representing a block of ice on a sloped bed, showing the orientation of the principle driving stress (Cuffey and Paterson, 2010).

A thickening of snow and ice in the accumulation zone will cause a steepening of the glacier surface increasing the basal shear stress (Eq. 2.7) until the ice eventually deforms and flows (Bennett and Glasser, 2009). As mass balance dictates glacier thickness and slope, and the shear stress is a factor both of these terms, glacier dynamics and mass balance are strongly interlinked. A positive mass balance causes thickening and steepening of the glacier, increasing the weight of the glacier and the force component down slope, increasing flow (Cuffey and Paterson, 2010). A change in H also has a feedback effect on mass balance by moving the glacier surface into a different local climate. For example, as a glacier thickens, the surface may move into cooler air temperatures, which could result in greater snowfall and accumulation. This would create a positive mass balance feedback. Depending on the properties of the glacier ice and subglacial bed, a glacier can move by internal deformation (creep), by sliding over the bed or by subglacial bed deformation. The latter two processes often can occur together so are collectively termed basal motion (Cuffey and Paterson, 2010).

2.2.2.2. *Creep*

Glacier ice is a polycrystalline, thick viscous fluid, made up of individual crystals whose interaction determines how ice behaves under an applied stress. Under an applied stress ice continuously deforms, a process known as creep (Cuffey and Paterson, 2010). The equation most commonly used to describe the relationship between stress and strain rate is Glen's flow law (Glen, 1955):

$$\dot{\epsilon} = A\tau^n \qquad (2.8)$$

Where $\dot{\epsilon}$ is the strain rate, τ is the stress, A is the flow parameter and n is the creep exponent. n is a constant found by experimental and field data to be approximately equal to 3 (Hooke, 1981). This value results in a nonlinear stress – strain rate relationship, defining ice as a nonlinear

fluid. A fluid with a linear relationship between stress and strain rate is defined as a linear or Newtonian fluid. Increased non-linearity produces a higher mean of ice velocity through the depth of the glacier and the speed which can be measured at the surface becomes a better proxy for mean velocity. A has been found experimentally to be strongly dependent on temperature (Barnes et al., 1971):

$$A = A_o e^{-\frac{Q}{RT_k}} \quad (2.9)$$

Where A_o is the reference flow parameter, Q is the low temperature activation energy for creep, R is the universal gas constant and T_k is the temperature in Kelvin (Cuffey and Paterson, 2010).

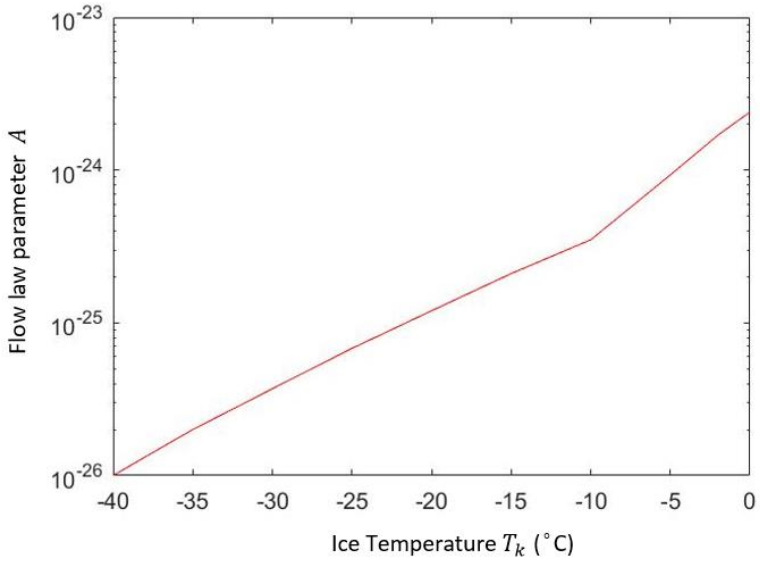

Figure 2.14. Plot showing the relationship between the flow law parameter A and ice temperature Tk. Data from (Budd and Jacka, 1983).

Over the range of temperatures found in terrestrial ice, A varies significantly (Figure 2.14). Up to -10°C, the relationship follows Equation 2.8. Moving closer to the melting point, A increases more rapidly for a given step in temperature, resulting in a more rapid softening of ice as ice approaches the melting point (Cuffey and Paterson, 2010). This is thought to be due to water forming at grain boundaries and grain boundary sliding (Barnes et al., 1971). The impact of temperature on A has implications for the velocity profile through an ice body. With height above the bed, temperature and in turn A decreases rapidly and the ice stiffens. Strain rate, effectively the velocity gradient, decreases moving up away from the bed as a result of Glen's flow law (Anderson and Anderson, 2010). These relationships cause the strain rate and velocity profiles for ice to be notably different from those for a linear fluid (Figure 2.15a and b). Because temperature has such an impact on A it is important that ice temperature is well known when modelling glacier dynamics. As well as for glaciers this is especially the case when studying ice

sheets which have larger temperature ranges from the bed to the surface (Cuffey and Paterson, 2010). Assuming a constant value of A is appropriate for temperate glaciers which are close to the pressure melting point throughout their depth (Figure 2.15b) but this assumption breaks down in polar glaciers and the aforementioned ice sheets (Anderson and Anderson, 2010).

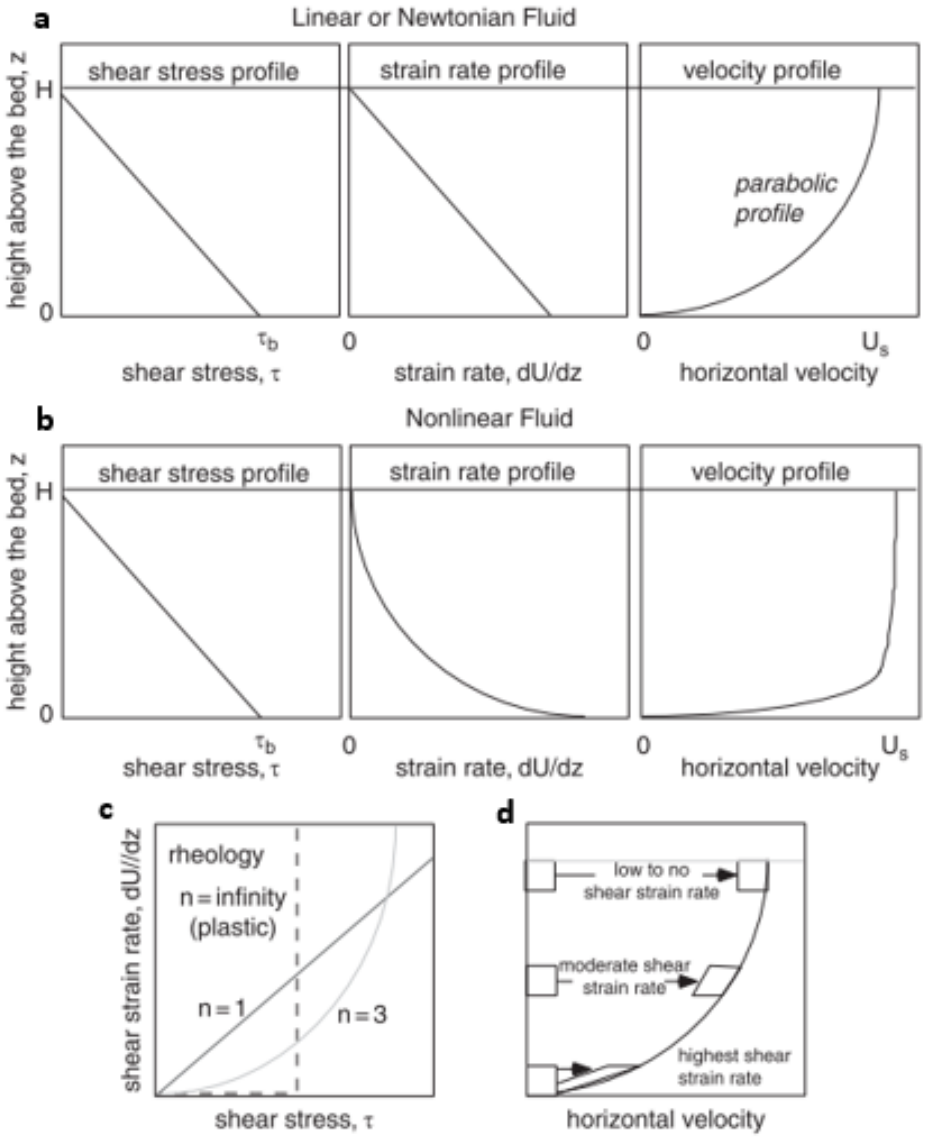

Figure 2.15. Graphs of shear stress, strain rate and velocity profiles through both linear (a) and non-linear fluids (b), strain rate with shear stress for linear (n = 1) and nonlinear (n = 3) fluids (c) and the relationship between ice velocity and shear strain rate shown graphically (d) (Anderson and Anderson, 2010).

To better understand the deformation of ice, equations can be derived from the relationships surrounding shear stress (Eq. 2.7) and Glen's flow law (Eq. 2.8) to give strain rate and velocity profiles with depth through an ice body (Figure 12). Combining equations 2.8 and 2.9 gives the shear strain rate profile:

$$\frac{dU}{dz} = A[\rho g \sin\alpha]^3 \ (H - z)^3 \qquad (2.10)$$

Equation 2.10 can then be integrated to give the velocity profile through the ice:

$$U(z) = A(\rho g \sin\alpha)^3 \left[H3z - \frac{3z2H2}{2} + z3H - \frac{z4}{4} \right] \quad (2.11)$$

2.2.2.3. Basal sliding

To stop temperate and polythermal glaciers from sliding indefinitely over a smooth sloped bed, there must be factors increasing friction at the ice-bed interface to reduce the sliding velocity. These include basal ice debris, bed roughness, and adhesion. If the basal ice contains fragments of rock, and this rock is in contact with the bed, a frictional drag force will act against the force driving sliding (Benn & Evans 2010). Adhesion occurs when basal ice freezes to the bed, supporting the stress at the ice-bed interface imposed upon it by the weight of the ice above (Benn & Evans 2010). The ice therefore will not slide, and movement will occur by creep. The bed below the glacier often contains bumps and irregularities of different sizes and dimensions which the glacier must pass to move down the slope (Benn & Evans 2010). Weertman (1957) developed two theories of how ice masses can move past such obstacles. One of these is regelation. As ice approaches an irregularity on the bed, the pressure in the ice increases as it comes up against an obstacle (Figure 2.16). This decreases the melting point of the ice and if it is at the pressure melting point, the ice on the stoss side melts. Meltwater flows from the area of high pressure at the stoss side to the area of low pressure on the lee side, where it refreezes. Refreezing of the water releases latent heat which is conducted through the obstacle to the stoss side, aiding melting. The energy required to feed this cycle is provided by the shear stress at the base of the glacier.

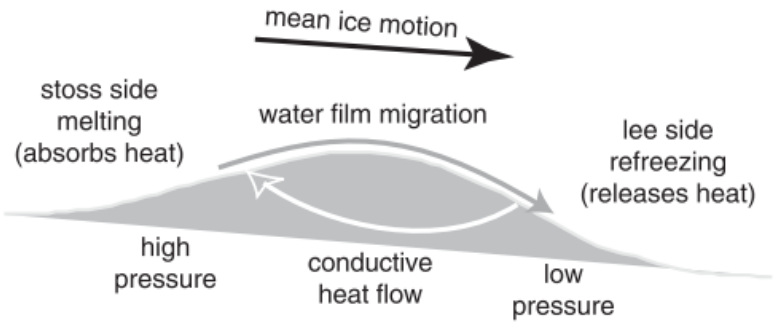

Figure 2.16. Schematic diagram showing the process of regelation (Anderson and Anderson, 2010).

Weertman (1957) however highlights that, if regelation alone is the process facilitating ice flow, sliding would be controlled by the movement of heat through the obstacle. With bodies greater than 1m in length, heat transfer and thus sliding would be limited. It is therefore proposed that

regelation operates alongside a process of enhanced basal creep, where the average creep rate of the ice near the glacier bed is increased by a concentration of stress. From Glen's Flow Law (Eq. 2.8), the strain rate of ice varies with the third power of the shear stress. A relative local increase in stress on the stoss side therefore increases the strain rate and hence the rate of deformation, causing the ice to accelerate around the irregularity (Benn & Evans 2010). Enhanced basal creep facilitates constant deformation. This is observed as bending of foliation planes, in places above regelation layers where bump sizes range from 3 to 50 cm, and exclusively over larger objects greater than a meter in length (Kamb and LaChapelle, 1964). Evidence for regelation can also be seen in the field in the form of isolated deposits of calcite, formed from precipitation of calcium carbonate on the lee side of an obstacle, dissolved from limestone bedrock at the stoss side (Hallet, 1976). Weertman's theories were later built upon by Nye (1969, 1970) and Kamb (1970) to include a more realistic bed model, allowing an estimate of sliding rate to be measured from bed topography (Cuffey and Paterson, 2010).

3. Methods

3.1. Introduction

This chapter outlines the methodological approach and techniques applied to this study. I apply geomorphological mapping and sedimentological analysis techniques within a landsystems framework to establish the sediment-landform assemblages found in the study region and through this reconstruct past glacial environments and processes. This approach is used together with cosmogenic nuclide surface exposure dating of boulders found on moraine ridge crests to quantify the age of moraine formation and to generate a new chronology of ice recession and landsystem evolution in the Salto, Tranquilo and Pedregoso valleys (Figure 1.1A; Chapter 1). New glacier reconstructions are used to calculate palaeo-ELAs using the AABR method, from which palaeoprecipitation is calculated. Finally, I apply glacier numerical modelling using PISM (Bueler and Brown, 2009; Winkelmann et al., 2011) to investigate the present-day physical glacier properties, ice dynamics and sensitivities of the MSL ice cap to changes in physical and climatic parameters. Finally the model is used to explore past glacier-climate scenarios at well-dated and established palaeo ice-limits.

3.2. Landsystems study: geomorphological mapping and sedimentological techniques

3.2.1. Landsystems approach

Studies of past glacial environments, including reconstructions and chronological investigations, must be built upon a detailed understanding of the geomorphology of a study region, including the relationship between landforms and their genesis (Boston et al., 2015; Bickerdike et al., 2018; Chandler et al., 2018; Hedding et al., 2018). This is commonly achieved through combining both geomorphological and detailed sedimentological studies of a landform's internal composition, and through this, establishing sediment-landform assemblages (Fookes et al., 1975; Evans, 2003a; Glasser et al., 2009; Evans et al., 2017; Malecki et al., 2018). We combine these assemblages within a 'landsystems' approach, to provide an effective way of investigating and formalising the nature of these past environments, dynamics and processes. Such an approach is based upon the principle that landscapes with common features can be identified and differentiated, and through a uniformitarian approach be attributed in combination to the processes which lead to their formation (Eyles, 1983; Evans and Twigg, 2002; Evans, 2014). Process-based, sediment-landform studies enable landsystems to be defined by investigating a glaciated setting in a holistic manner, evaluating geomorphology and sedimentology in combination through their genesis (Figure 3.1) (Evans, 2013).

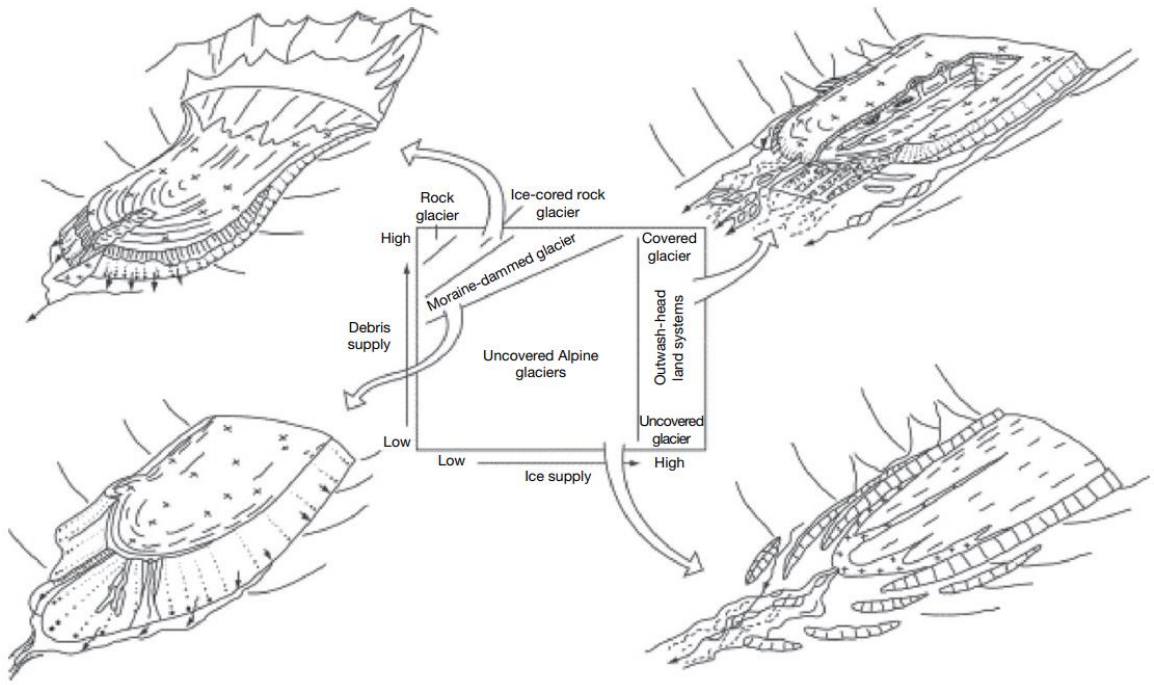

Figure 3.1. Active temperate valley glacier landsystem models and constraints on landsystem development. Reproduced from Benn et al. (2003), (Evans, 2013).

Early work undertaken by Clayton and Moran (1982), Eyles (1983) and Fookes et al. (1975) evolved and applied the previously developed landsystem concept to glaciated landscapes. Numerous subsequent studies have produced sediment-landform association for different landsystems (subglacial, supraglacial, glaciated valley, paraglacial, plateau icefield etc), thermal regimes and geographic regions (e.g. Bennett et al., 2010; Darvill et al., 2017; Evans et al., 2017, 2012, 2009; Glasser et al., 2009 and references therein). For this sediment-landform landsystem study, we therefore undertake initial geomorphological mapping of the study area by remote sensing to determine the landforms present and their spatial interrelationships before subsequent field verification where possible. The availability of sections afforded by numerous road cuttings enables these interpretations to be tested and expanded upon using sedimentological study alongside the detailed remotely sensed and field mapping to develop sediment-landform assemblages.

3.2.2. Geomorphological mapping

The geomorphological mapping of landforms has long been used as a powerful tool to reveal the history of landscape evolution and earth-surface processes (Goodchild, 1875; Caldenius, 1932; Ballantyne, 1989; Smith, 2011; Chandler et al., 2018). It has evolved from an entirely field-based method during the late 19th and early to mid-20th centuries to work alongside desk-based mapping through the use of remotely sensed data, for example, from aerial photographs (early 20th century onwards) (Benn and Ballantyne, 2005; Boston, 2012), satellites (1970s onwards) (Smith et al., 2006; García et al., 2014; Bendle et al., 2017b) and most recently, unmanned aerial

vehicles (UAVs) (Evans et al., 2016; Tonkin et al., 2016; Ely et al., 2017). This holistic approach to mapping, as is adopted in this study in Chapter 4, enables the advantages of each method and dataset to be combined to facilitate accurate landform identification, and where required, the most comprehensive and detailed map possible (e.g. Boston, 2012; Darvill et al., 2014; Everest et al., 2017). This allows process-based and palaeoglaciological studies to be undertaken to create landsystem models (Benn and Lukas, 2006; Golledge, 2007; Glasser et al., 2009; Boston et al., 2015; Chandler et al., 2018; Davies et al., 2018).

For example, Davies et al. (2018) use detailed remote sensing and field geomorphological mapping to develop a process-based glaciolacustine landsystem for the termination of ice from MSL into the ice-dammed Palaeolake Chelenko, including the formation of a subaqueous ice-contact fan and morainal bank. Detailed geomorphological mapping has also been used extensively to reconstruct former mass extents, dynamics, flow patterns and thermal regimes, including reconstructing ice limits directly through mapping of moraines (Lukas and Bradwell, 2010; Barrell, 2011; Clark et al., 2012; Ó Cofaigh et al., 2014; Darvill et al., 2017).

The compilation of extensive geomorphological mapping from across the British Isles has allowed for a detailed reconstruction of the glacial history of the British-Irish Ice Sheet through the BRITICE project (Clark et al., 2012). Over 26,000 features are mapped and geospatially referenced. Features range from large-scale elements such as mega-scale glacial lineations, drumlin fields and meltwater channels to smaller moraines, cirques and eskers. This has since increased to over 170,000 (Clark et al., 2018), with an updated reconstruction of the last British-Irish Ice Sheet expected shortly. Such geomorphological data is used to infer palaeo-ice sheet extent and processes through landscape inversion (Stokes and Clark, 1999, 2002; Stokes et al., 2015) and may be combined into theoretical models to formalise the use of the landform record to reconstruct ice sheets (e.g. Kleman et al., 1994; Kleman and Borgstrom, 1994). Greenwood (2007) effectively used meltwater channel records from the BRITICE database to reconstruct palaeo ice sheet margins and flow patterns, while Kleman et al. (1997) and (2006) used classifications of wet-based deglaciation fans, frozen-bed deglaciation fans, synchronous fans and surge fans within an inversion model to reconstruct the configuration and flow pattern of the palaeo-Fennoscandian ice sheet (Figure 3.2).

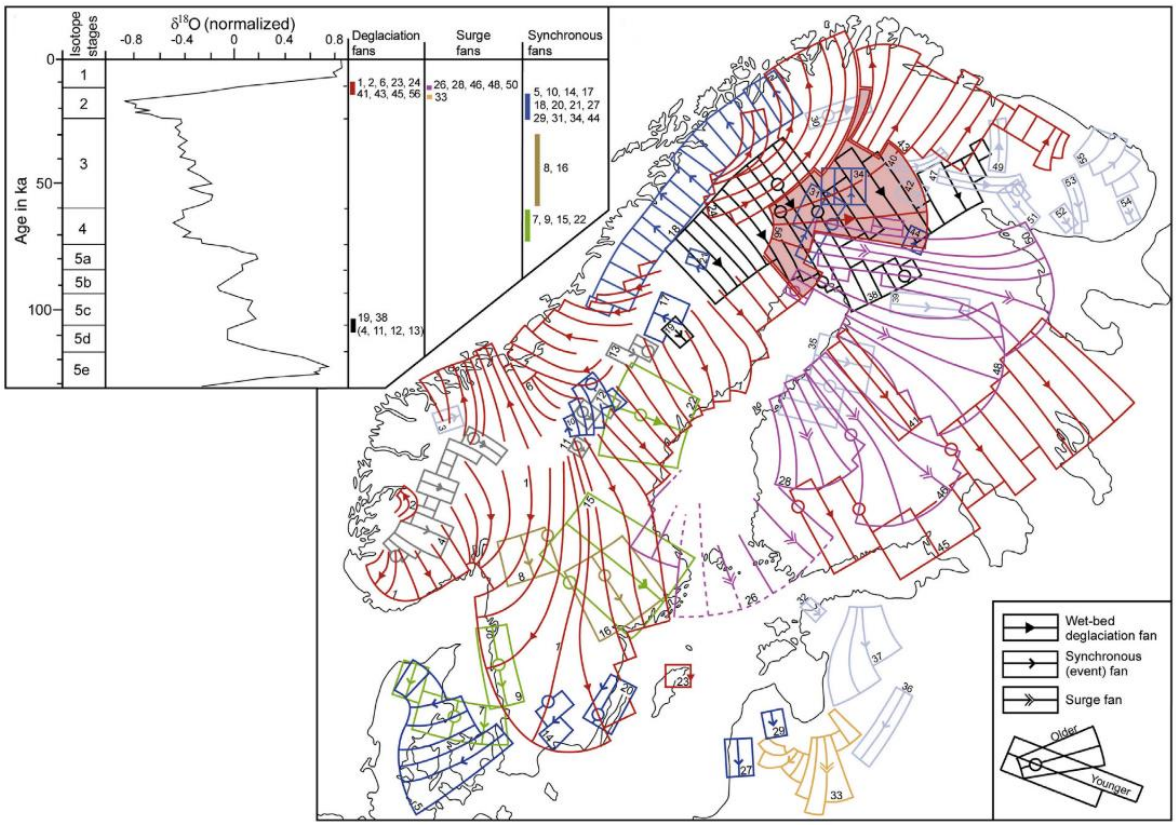

Figure 3.2. Application of glacier inversion on fans mapped to reconstruct the Fennoscandian Ice Sheet. The different overlapping fan types are identified to time-step sequence of ice sheet development (Kleman et al., 2006; in Stokes et al., 2015).

Mapping and the resulting reconstruction of glacial landsystems and morphostratigraphy is also vital when targeting features for dating and for interpreting existing chronological data (e.g. García et al., 2014; Lowe and Walker, 2014; Fogwill et al., 2015; Thorndycraft et al., 2019). A lack of understanding to this end can result in conflicting interpretations of the chronological data (e.g. Gheorghiu et al., (2012) in Boston et al., (2015)). In another example, through the comprehensive mapping of ice limits and palaeoshorelines east of the Northern Patagonian icefield, Thorndycraft et al., (2019) revealed that ^{10}Be cosmogenic nuclide surface exposure ages of glacially transported boulders, which had previously been interpreted as being deposited subaerially and hence dated a past ice margin position (Glasser et al., 2012a), where in fact deposited subaqueously. The ages were hence reinterpreted as providing a date for the drop in level of a palaeo ice-dammed lake.

3.2.2.1. Mapping by remote sensing

Remote mapping of surface landscapes began in the mid to late 20th century though the use of aerial photography. This was found to be an effective tool for the description, classification and mapping of landforms, in particular when combined with topographic maps and field surveys (Smith 1941). Such methods were applied to mapping of the Quaternary landscape in Britain (e.g. Price, 1963; Sugden, 1970) and glacial geomorphological mapping in Canada (Prest, 1968).

The high resolution of aerial photography made it an effective tool, and the technique is still used (Hambrey et al., 2009; Evans, 2010; Boston, 2012; Davies et al., 2013). It has been applied to photogrammetry to create high resolution digital elevation models (Carrivick et al., 2016; Ely et al., 2017). However, mapping from aerial surveys is often limited to a small region of interest. It was not until the development of satellite-based remote sensing in the 1970s and 1980s that large glaciated regions could be mapped quickly and efficiently, on ice sheet scale, and viewed in their entirety (Sugden, 1978; Punkari, 1995; Chandler et al., 2018). Technological advances have since made global satellite imagery widely and freely available, with Landsat (30 m), ASTER (15 m), SPOT-5 (2.5 m) and DigitalGlobal (1 to 2 m) imagery commonly used (Figure 3.3) (Bendle et al., 2017b). Such images are also now pre-processed, mosaiced and made freely available in programmes such as Google Earth Pro™ and ArcMap via the Esri™ World Imagery. Satellite imagery provides the benefit of widespread mapping over large areas and of those areas not accessible on foot such as high mountain valleys. Aerial imagery generally provides a perspective otherwise not available in the field.

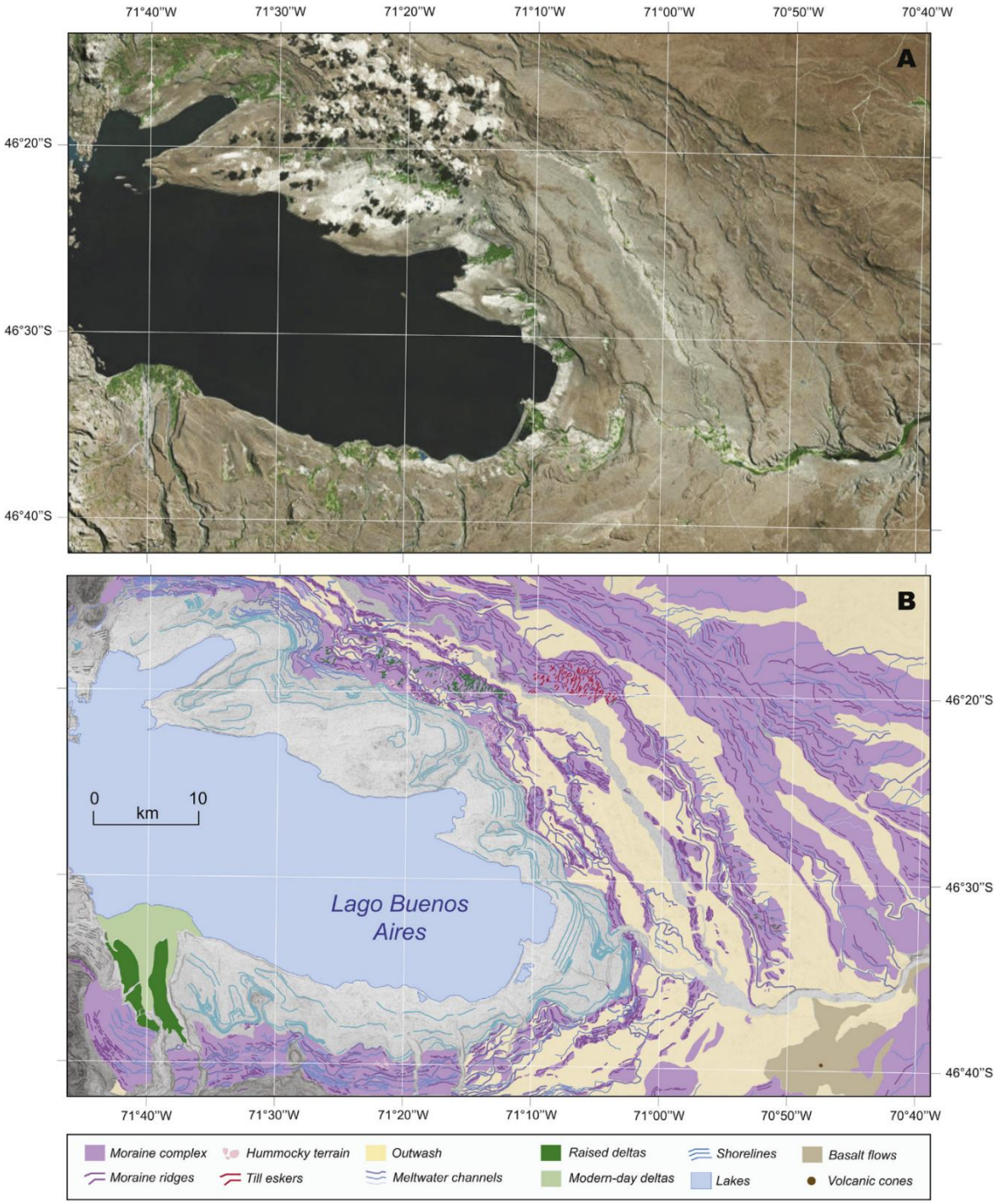

Figure 3.3. Example of geomorphological mapping using on-screen visualisation from satellite imagery (Chandler et al., 2016; Bendle et al., 2017b).

For this study (Chapter 4) geomorphological mapping of the 900 km^2 study region (Figure 4.1; Chapter 4) was initially undertaken through the interpretation of true-colour 0.5 m resolution DigitalGlobe satellite imagery, part of the Esri™ World Imagery, taken between January 2015 and February 2016. Google Earth Pro™ v7.3 (DigitalGlobe imagery) was used in conjunction to this, alongside Google Earth's digital elevation model to view landforms from an oblique, three-dimensional perspective, aiding identification. Additional elevation data were taken from an ASTER G-DEM with 20 m vertical and 30 m horizontal resolution at 95% confidence; cf. (ASTER

GDEM Validation Team, 2011). Landforms were digitised in ArcMap v10.3 at 1:5000 scale using the WGS-1984 UTM-Zone 18S coordinate system. In addition to true colour satellite imagery and ASTER G-DEM, slope-gradient shaded and relief shaded ("hillshade") models were created in ArcMap v10.3 from the ASTER G-DEM. To obtain a comprehensive perspective of the topography and reduce bias, hillshade models were created using multiple azimuths and low angles of illumination (30^{o}) following Smith and Clark (2005).

Using widely available, high-resolution satellite imagery enabled the majority of land area within the extensive study region, including high altitude valleys and steep valley sides inaccessible on foot, to be mapped efficiently. The "top-down" perspective that such imagery provides also enables mapping of extensive areas of surficial sediment, bedrock and large-scale landforms, which would otherwise be difficult to identify or unfeasible to map on foot. However, significant areas of dense woodland make mapping landforms (e.g. moraine ridges) in such vegetated areas difficult and often impossible. These often-extensive landforms must be mapped in the field providing there is sufficient accessibility. The lack of higher resolution DEMs (e.g. LiDAR) also limits the confidence with which some landforms can be identified and interpreted (e.g. distinguishing fluvial terraces separated by < 20 m in elevation), further highlighting the importance of field mapping.

3.2.2.2. Field mapping

The pioneers of field mapping in the late 19^{th} and early 20^{th} centuries undertook their work solely through extensive field surveys, traversing the landscape and recording landforms on topographic base maps (Goodchild, 1875; Wright, 1912; Caldenius, 1932; Williams, 1936; Farrington and Mitchell, 1951). More recent advances in handheld GPS technology have improved the geospatial accuracy of this mapping. Despite the ease of access to remotely sensed data, field based geomorphological mapping is still the only method to ground truth interpretations and determine landform composition. Despite the ever improving resolution of freely available satellite imagery, field mapping should be considered when mapping at small scales and especially when meter scale resolution imagery is not available (Smith et al., 2006).

In this study, I used field mapping (over a period of 6 weeks fieldwork during Nov-Dec 2016 and Dec 2017) to ground-truth remotely sensed mapping, obtain detail on sedimentary associations, and improve landform identification and mapping detail. Landforms in the field were mapped using handheld GPS (Garmin GPSMAP 64) with a documented accuracy of ± 10 m. Areas were targeted that had previously been identified remotely, as well as those suspected to be covered by dense vegetation and therefore unidentifiable from remote sensing alone. For example, lateral moraine ridges which trace from areas of exposed valley-side into areas of dense

vegetation may be mapped on foot along the moraine ridge for kilometres. Alongside ground-truthing, improving the accuracy of landforms identified remotely and discovering new landforms not previously identified highlights the importance of field mapping alongside remote mapping (Roering et al., 2013).

3.2.3. Landform identification criteria

Well-established criteria for landform identification, both by remote sensing and in the field, were used (e.g. Glasser et al., 2005, 2008; Bendle et al., 2017b; Darvill et al., 2017; Chandler et al., 2018) and adapted to account for the specific characteristics of landforms found in the study area (Table 3.1). A key limitation was in the mapping of moraine ridges on the steep, well-vegetated sides of lower-altitude valleys. The dense vegetation both obscured valley-side surface features when observed on remotely sensed imagery, and alongside the steep nature of the valley sides, made mapping on foot unfeasible. Where sections of sparely-vegetated moraine ridges were exposed, these could be traced in the field into well-vegetated areas, and their extent mapped further. The identification of palaeoshorelines may also be difficult and ambiguous where the features are laterally-restricted on the valley side, well-vegetated or there is limited diamictic material into which a shoreline could be carved. Their identification could be supported by being at the same elevation as other shorelines in the same and neighbouring valleys, however this alone should not be used as confirmatory evidence.

Table 3.1. Landform identification criteria used in this study, after Glasser et al. (2005, 2008), Bendle et al. (2017b), Darvill et al. (2017), Chandler et al. (2018).

Landform	Morphology	ID criteria from imagery	ID criteria in field	Uncertainties	Typical sediments	Significance
Moraine ridges	Linear, arcuate, curvilinear or saw-tooth shaped ridges of positive relief, orientated parallel, subparallel or perpendicular to the valley side. Ridges may project only part way across the valley from the valley side.	Smooth texture different from rough bare bedrock. Pale brown in colour where sparsely vegetated. Lighter/darker shading on opposite flanks indicates ridge crest.	Prominent feature of positive relief. Morphology as described. Often found in association with glacially-transported boulders.	Unidentifiable from satellite images in well vegetated areas. Ridges of low relief may be difficult to detect. Possible confusion with trimlines.	Diamicton with stratified massive and laminated sands and gravels.	Mark position of former ice margin. Can be dated to provide temporal context.
Ice-contact slope	Gently-sloping surface, from valley floor up to morainic deposit (e.g. terminal-moraine ridge). Slope commonly orientated along valley.	Uniform surface texture and colour. May show steep break in slope at top, or grade smoothly onto morainic deposit surface.	Visible as extensive area of sloping, uniform terrain.	May be difficult to identify on a low-resolution DEM if change in elevation across slope is small.		Marks terminal position of ice margin.
Morainal bank	Wedge-shaped positive topography over a km scale with one very gently-sloping ice-proximal side and one more steeply-sloping ice-distal side, separated by a crest marked by horse-shoe shaped crescentic scars.	Extensive area of well-vegetated, uniform texture. May show sinuous, linked palaeochannels.	Visible as extensive area of very gently-sloping, uniform vegetated terrain.	May not be obvious in field if well-vegetated and due to the very gently-sloping surface.	Bedded gravelly sands. May be found in association with glaciolacustrine sediments.	Marks terminal position of ice margin. May indicate subaqueous deposition and lacustrine glacier termination.
Kettle hole	Rounded depression within area of morainic or glaciofluvial material (e.g. kame terrace).	Often filled with water but can also be dry. May be vegetated. Contrast in colour from surrounding terrain. Rounded form, associated with morainic complexes or glaciofluvial deposits.	Rounded depression visible from a position of higher topography. May be able to walk into depression if not filled with water.	More obvious from satellite imagery. Can be confused with small lakes formed in bedrock or non-ice related depressions.		Indicates previously-glaciated area and area of deposition of morainic or glaciofluvial material.

Ice-scoured bedrock	Areas of bare or sparsely-vegetated bedrock with visible inherent structures.	Dark brown to grey to pink. Rough and irregular surface texture with visible joints, faults and fractures, distinctive from neighbouring sediment cover.	Rough texture and inherent structures evident. Distinctive in colour. Spatially extensive. Not practical to map in detail in the field.	May be difficult to distinguish from areas of thin/sparse sediment cover over bedrock, where boundary is gradational.		Shows areas of extensive ice at its pressure melting point.
Glacial diamicton	Gently-mounded material deposited on bedrock, ranging in extent, often on valley sides.	Yellow/pale brown in colour, with smooth texture in contrast to often neighbouring rough bedrock. Can be found in association with small channel gorges with clear breaks in slope. Often vegetated.	Where accessible and exposed (e.g. road cuttings) material can be identified as diamicton. Often difficult to identify due to inaccessibility and/or vegetation cover.	May be difficult to distinguish where cover is thin and boundary with bedrock is unclear	Diamicton rich in faceted boulders and faceted striated stone. May be interbedded with planar bedded gravels and sands.	Indicates area of glacier deposition.
Flutes	Linear, elongated, parallel features formed in sediment	Occur in groups, often aligned differently to any inherent bedrock structure. May appear dark and light on opposite sides indicating positive relief. Commonly found in high-mountain areas in this study region, close to glacier cirques, and recently exposed (inside Little Ice Age moraines).	May be visible from distance although best identified from satellite imagery as spatially-extensive and can be partly obscured locally by vegetation or hidden in high-mountain areas.	Potential confusion with bedrock structures or medial moraines. Difficult to identify if short in length.	Fine to coarse gravels with sporadic faceted boulders.	Indicative of former flow direction of warm-based ice and fast ice flow when laterally-extensive and highly-attenuated.
Raised deltas	Flat-topped, steep-sided surface extending along and out from valley side, above valley floor, at the opening of a ravine. Often found in stepped sequence, incised by a palaeo or active river channel.	Uniform smooth-textured surface, in contrast to often adjoining rough bedrock. Light/dark contrast indicates breaks of slope at former delta front and incised channel.	Levels above the valley floor, in stepped sequence with an incised channel is often clearly visible from distance/opposite side of valley.	May be misidentified as a shoreline or kame terrace due to its planar nature at the valley side.	Well-defined, alternating dipping beds of gravels, coarse gravelly sands and hyper-concentrated cobbles.	Height at the delta front at break of slope indicates former lake level.

Ice contact fan	Surfaces sloping to the valley floor from a flat/more gently-sloping top surface, the two separated by a slight break in slope.	Uniform smooth-texture surface may be vegetated. Contains sinuous lines of light/dark contrast indicating palaeochannels, which may also be wider and densely-vegetated with light/dark breaks in slope at their edge.	Prominent feature of positive, sloping relief above the valley floor. Large channels cut into the feature may be visible in the field.	May be misidentified as a raised delta due to its similar sloping morphology, although distinctively lacks a clear valley sediment source (ravine).	Stone-rich, sandy diamicton with abundant fine to coarse gravel.	Indicates the frontal ice position of a marine or lacustrine-terminating glacier.
Palaeoshorelines	Narrow terrace surface on valley side with break in slope away from the valley side.	Approximate constant-elevation surface locally along valley. Light/dark contrast either side of break in slope. May be contrast in vegetation cover. Distinctive from exposed bedrock.	Often visible in the field as a distinctive flat surface on the valley side elevated above the valley floor. Especially identifiable when laterally extensive.	May be misidentified as a kame terrace, although such a feature would be expected to gently slope down valley. Difficult to identify if discontinuous and/or well-vegetated	Carved into diamicton on the valley sides. Well-rounded gravels pebbles and sands may be present. May be associated with far travelled boulders on the terrace surface.	Indicates the former lake level.
Outwash plain	Large, gently-sloping flat plain cut by palaeochannels. Grades from former ice limit (e.g. a moraine ridge).	Large, smooth surface, uniform in texture and colour, and in contrast to surrounding topography. Palaeochannels on surface identifiable by light/dark colour change indicating negative relief. Also highlighted by vegetation change.	Extensive, flat, gently-sloping plains are visible in the field. Palaeochannel depressions can also be visible when looking across the plain's surface.	Exact limits of outwash plain may be difficult to distinguish.	Well-rounded gravels, sands and silt. Sands may be laminated. Larger boulders and cobbles may be found closer to the former ice margin.	Indicates major meltwater outflow pathways.
Fluvial terraces	Terraces running extensively along the valley side, extending out into the valley, sloping gently down valley and often stepped, separated by breaks in slope.	Uniformly-textured, vegetated surface. Break in slope is often unvegetated and lighter in colour. Often occur next to an active river system.	Visible in the field as terraces running extensively along the valley side above the valley floor, with steep	May be mistaken for raised deltas, kame terraces or shorelines, although are distinctively stepped	Bedded, laminated sands and gravels.	Indicate the former floodplain of a river and subsequent down cutting. May be indicative of a drop in

			scarp slopes visible along their edge.	and may be more laterally extensive away from the valley side.		base level and/or decrease in sediment supply.
Palaeochannels	Linear channels forming shallow depressions or deeper incisions. May have gently or steeply-sloping slides with scarps. Incised into fluvial, glaciofluvial, or glacial deposits.	Often appear darker than surrounding sediment and preferentially vegetated. May be sinuous, braided and extensive over valley-fill flood and outwash plains.	Visible in field as deep gorges or shallow laterally-extensive channels.	May be mistaken for breaks of slope at edge of outwash plain. Shallow palaeochannels often not visible in satellite imagery and certainly not on widely-available low-resolution DEMs.		Indicative of former path of river/stream flow. Deep incision may indicate drop of base level.
Kame terrace	Flat-topped surface above valley floor, gently-sloping down valley, extending from valley side. Pitted surface with steep ice-contact face.	Uniform surface texture and colour. Sharp break at ice-contact edge and surrounding terrain shown by shadowing/change in colour and texture. May be well-vegetated. Often associated with moraine ridges extending cross valley from terrace at valley side. No clear valley-side sediment source or catchment	Visible in field as large flat-topped feature, steep-sided, extending down valley, abruptly placed against steep valley-side bedrock in places.	May be confused with shorelines or raised deltas. Raised deltas have clear valley-side sediment source. Shorelines may be found more extensively, spanning multiple valleys. May not have a pitted surface.	Dipping beds of coarse sands an gravels, with faceted and edge-rounded stones. Gravel lenses and shallow scours of gravels and sands also found	Marks position of former lateral or frontal ice-margin and indicates ice thickness. Suggestive of high meltwater discharge and sediment transport.
Boulder bar	Elongated, positive relief, valley-floor feature with tapered ends. 100s m in length.	Uniformly textured, apparently-flat surface that appears speckled with vegetation.	Visible in the field as an isolated, large feature in the valley floor. Boulders present on the surface.	Possible confusion with a point bar.	Reworked diamicton, topped with sporadic boulders on the surface	Often indicative of a large-hydrological-erosion and sediment-transport event, such as a flood. May form as a result of a glacier

						lake outburst flood in a glaciated region.
Alluvial fans	Sloping fans from valley sides fed by a small river or stream.	Smooth surface, splaying out in fan shape from valley side on to valley floor. Sharp boundary with surrounding topography through change in vegetation cover.	Distinct morphology identifiable from enough distance to provide context within valley. Cobble/gravel texture may be identifiable from distance.	Possible to misidentify as palaeo-delta or ice-contact deposit although unlikely.	Course gravels and some small boulders found proximal to the valley side, grading to a greater proportion of finger gravels, sand and silt in the distal portion of the fan.	Reworking of unconsolidated material by meltwater channels and streams.
Debris slopes	Steeply-sloping surface of sediment at the valley side, accumulating and sloping gently at valley floor. Can be laterally-extensive or more locally-confined.	Grey/pale brown in colour depending on composition. Smooth texture, may contain series of cone forms. Largely unvegetated. Common in high-mountain settings above upper vegetation line but also found as shattered bedrock and remobilised moraines in low valleys.	May be visible from valley floor. Texture, colour, morphology and composition clear when visible and/or accessible. Likely to be inaccessible and not visible in high-mountain settings.	Limits of extent in high-mountain areas above upper vegetation line may be difficult to identify.	Angular boulders to cobbles in high valleys. Gravels and sands where associated with reworked morainic material.	Indicates paraglacial processes.
Floodplain	Sediment accumulated in valley floor often cut by a braided river system and found in association with channel bars.	Flat surface in valley floor cut by river system. Densely vegetated in places, often between braided active or palaeochannels.	Visible from valley side and on surface if accessible.	Possible confusion with outwash plain although more densely-vegetated and clearly associated with an established fluvial system.	Sands and gravels	When abandoned, may indicate area of past paraglacial activity. May contain active glaciofluvial system.

3.3. Sedimentology

Sedimentological and stratigraphical studies were undertaken at exposures through landforms (e.g. road cuttings and quarry sites) along the Salto, Pedregoso and Tranquilo valleys. At sections, a lithofacies approach was adopted to describe and interpret the observed record (Eyles et al., 1983; Walker, 1992). A sediment facies is a unit of sediment with distinctive properties (geometry, composition, particle size, structure, colour and fossil content), such that it is formed under distinct conditions and processes of sedimentation and can be cross-referenced with modern analogues and process-based experiments to guide interpretations (Reading, 1978; Hooyer and Iverson, 2000; Evans, 2003b; Evans and Benn, 2004). Such an approach has been applied widely for the description, classification and interpretation of sediments and landforms (e.g. Bennett et al., 2002; Glasser and Hambrey, 2002; Golledge and Phillips, 2008; Longhitano, 2008). With an understanding of the processes of sedimentation and methods of landform formation, it is possible to produce a broad scale stratigraphy of the interrelationship of landforms in time and space (Lee, 2017).

In this study (Chapter 4), vertical logs were taken to provide a representative section and illustrate stratigraphical trends (Jones et al., 1999). These logs accompanied scale photographs and drawings of sections showing major units, boundaries and structures such as faulting, cross cutting relationships and bedding. Sedimentary units were described using established sedimentological techniques, notations and facies codes (Evans and Benn, 2004). This aids in determining the environment and processes of sediment deposition and landform formation. However the complex nature of glacial environments can make interpreting sedimentary sections and stratigraphic correlation difficult (Rose and Menzies, 1996). Glacial systems can contain a range of sediments with high heterogeneity which often experience post-depositional non-glacial modification. Glacial systems also experience a range of mechanisms and rates of deposition over a small area, and hence a range of complex sediments are often found juxtaposed in close proximity. Locally, glaciers can also respond differently to climate forcing depending on elevation, valley morphology and aspect, adding to the complexity of correlating features in time.

Clast morphology data (shape and roundness) were collected from representative facies, following Benn (2004), to investigate particle transportation and erosion histories. Clast-shape analysis has been applied to both present-day and formerly-glaciated mountain settings to define and distinguish lithofacies, reveal sediment transport pathway histories and distinguish between lithofacies found at different glacier thermal regimes (Goodsell et al., 2005; Mills et al., 2009; Brook and Lukas, 2012; Hambrey and Glasser, 2012). Hambrey and Ehrmann (2004)

examined sedimentary facies associated with glaciers in New Zealand's Southern Alps. They were able to identify and distinguish between angular gravels, cobbles and boulders derived from rock fall sources transported supraglacially and more rounded debris at the glacier snouts, transported and reworked by englacial and proglacial streams. This information, helping to reveal sediment transport pathways, can in turn be used as an element to assign glacial landsystems and thermal regimes (section 4.4.1).

Shape data (length of the a, b and c axes) were plotted on a general shape ternary diagram (Sneed and Folk, 1958; Benn and Ballantyne, 1993) to analyse the distribution of samples amongst possible orthorhombic clast shapes and from this C_{40} indices (percentage of clasts with c/a axial ratios ≤ 0.4) (Benn and Ballantyne, 1993) were calculated. Roundness was measured using a semiquantitative approach. Clasts were matched to a comparison chart (Figure 3.4) in order to assign a numerical value to each clast representing its degree of roundness (Krumbein, 2003; Evans and Benn, 2004; Benn and Andrews, 2007). Due to this being a somewhat subjective process, attempting to divide what is a continuous gradation of roundness into defined categories, I undertook the classifications of sample at all sites to achieve consistency and eliminate operator bias where possible.

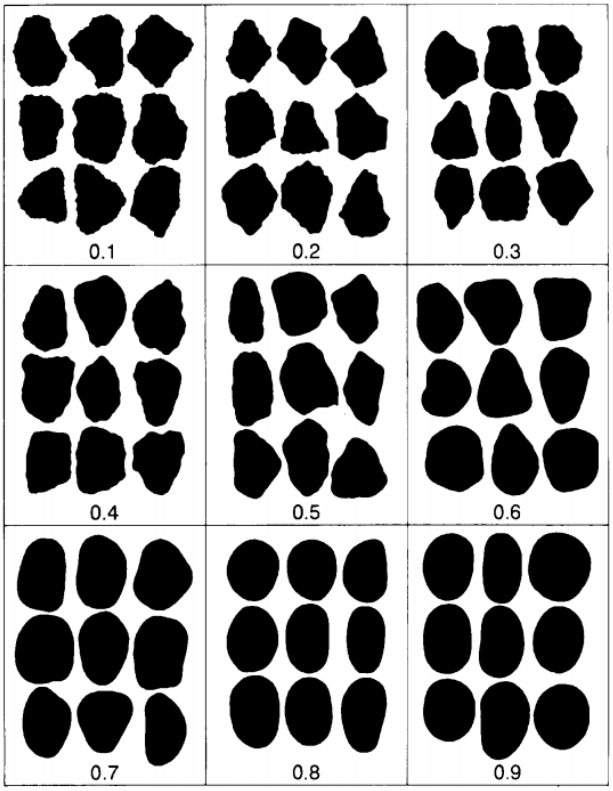

Figure 3.4. Comparison chart for stone shape roundness classification (Krumbein, 2003).

Data were plotted as histograms and analysed using RA (% of angular and very angular clasts) and RWR (% rounded and well-rounded clasts) indices (Evans and Benn, 2004). We use RWR

indices alongside RA to mitigate for the influence of glaciofluvial reworking on the effectiveness of the RA index to distinguish transport pathways (Evans et al., 2010, 2013; Lukas et al., 2013). Due to the impact of lithological variability on clast shape, the mixing of clast lithologies within catchments can reduce the power of the method to distinguish transport pathways (Lukas et al., 2013) and ideally clasts should be separated by lithology and studied independently. However, the collection of clast morphology data is time consuming, and may not always be possible or may have to be undertaken on a limited scale, when time constraints exist.

3.4. Cosmogenic nuclide surface exposure dating

The pioneering work of Davies and Schaffer (1955) showed that terrestrial cosmogenic nuclides (cosmogenic nuclides produced in minerals of rocks at the earth's surface) could be used to directly date rock surfaces and help answer geomorphological research questions. Following the development of Accelerator Mass Spectrometry (AMS) in the early 1980s (Klein et al., 1982; Elmore and Phillips, 1987) and the ability this gave to measure very low isotopic ratios, the terrestrial cosmogenic nuclide surface exposure dating method advanced further (Gosse and Phillips, 2001). The number of radionuclides nuclides available (^{10}Be, ^{14}C, ^{26}Al, and ^{36}Cl) alongside the stable noble gases (^{3}He and ^{21}Ne) enables almost every mineral and lithology to be analysed (Ivy-Ochs and Kober, 2008). The technique now provides a powerful tool to date a range of terrestrial landforms and surfaces of previously unexposed geological material (e.g. Wells et al., 1995; Repka et al., 1997; Van der Woerd et al., 1998; Kelly et al., 2004; Owen et al., 2011).

Cosmogenic nuclide surface exposure dating is now widely used to provide chronological constraints of Quaternary glacier change (Balco, 2011; Ivy-Ochs and Briner, 2014). This is commonly done in two ways: firstly, by dating the surface exposure time of glacially transported boulders (e.g. Owen et al., 2005; Benn and Lukas, 2006; Kong et al., 2009; Glasser et al., 2012) and secondly by dating the exposure time of glacially eroded bedrock (e.g. Brook et al., 1996; Ballantyne, 2010; Glasser et al., 2012b)**.** Measuring the surface exposure time of a glacially deposited boulder provides an approximate date for when this boulder was deposited at an ice margin. A boulder, previously transported within the ice or at the ice-bed interface, will have been eroded, leaving a freshly exposed surface with which to accumulate cosmogenic nuclides upon its deposition and exposure to cosmic rays. When such boulders are deposited on a moraine ridge, the surface exposure ages can be used to obtain the timing of moraine formation, and crucially the time at which the ice margin was at this location.

Dating multiple moraines in this way can provide a chronology of ice recession (Shulmeister et al., 2005; Putnam et al., 2013; Sagredo et al., 2018). For example, on the northern side of the MSL ice cap, Sagredo et al. (2018) dated a sequence of seven moraine limits in the Upper

Tranquilo valley, taking samples from 24 boulders across 12 moraine ridges. This revealed a major ice limit at the ACR, followed by minor glacier fluctuations as marked by three inset moraines which also dated to this period. Two further inset moraines revealed minor readvances or periods of glacier stability at the onset of the Holocene and later in the mid Holocene.

A chronology of ice thinning can also be obtained through surface exposure dating, by dating glacial erratics at different altitudes. This method has, for example, been applied to Antarctica at sites at Marie Byrd Land to reconstruct the timing and rate of thinning of the West Antarctic Ice Sheet (Stone et al., 2003). A similar 'dip stick' method has also been applied to the Framnes Mountains in Mac. Robertson Land in East Antarctica to determine the magnitude and timing of recession of the East Antarctic Ice Sheet. A similar principle can also be applied to freshly exposed bedrock surfaces. As temperate ice moves over underlying bedrock, the bedrock surface is eroded by abrasion and quarrying (Glasser and Bennett, 2004) revealing a fresh rock surface when ice recedes. Measuring the exposure age of such a surface therefore provides a timing for ice recession past this location. For example, Brook et al. (1996) used ^{10}Be and ^{26}Al exposure dating of bedrock samples from a vertical transect at Skåla, western Norway, to reveal the record of thinning of the Fennoscandian ice sheet.

This study (Chapter 5) uses the former application of surface exposure dating, sampling boulders on moraine ridge crests to obtain an approximate age for moraine formation and date of ice marginal position.

3.4.1. ^{10}Be cosmogenic nuclide production

How long a rock surface has been newly exposed to the atmosphere can be determined using surface exposure dating based on the principle that the longer a rock has been exposed to the atmosphere, the more of the cosmogenic nuclide there will be in the rock's upper surface. This is because the amount of cosmogenic nuclide in the rock builds up over time when exposed to cosmic radiation. Cosmic radiation entering into the earth's atmosphere undergoes spallation reactions with atmospheric gas nuclei producing secondary cosmic rays composed of high energy protons, neutrons and mesons in a process (Figure 3.5) (Gosse and Phillips, 2001; Darvill, 2013).

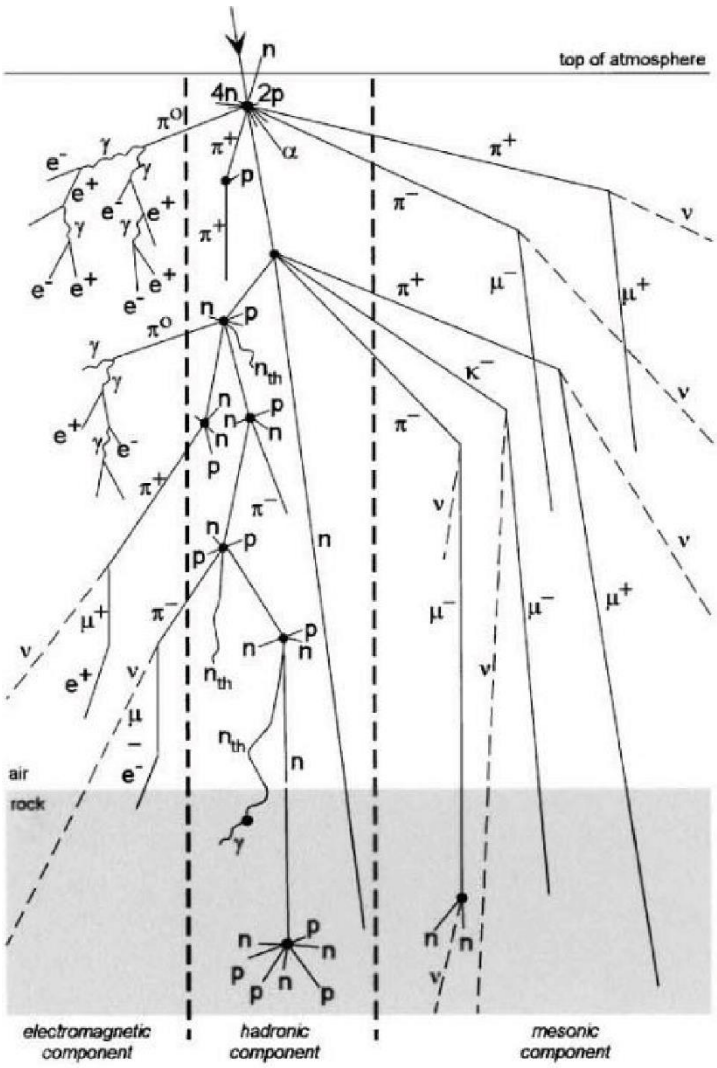

e^+	positron
e^-	electron
κ	kaon
n	neutron
p	proton
μ	muon
π	pion
γ	gamma ray or photon
ν	neutrino

Figure 3.5. Demonstrating secondary particle production in the atmosphere and rock as a result of spallation reactions (Gosse and Phillips, 2001).

As these secondary neutrons collide with target minerals in the surface of rocks, lighter particles are split off from the elements in the mineral lattice. A cosmogenic nuclide is left in the place of the original element as a result of this spallation reaction, further spallation reactions occur and lighter particles are split off from the elements which make up the mineral lattice, leaving a cosmogenic nuclide in place of the original element (Ivy-Ochs and Kober, 2008). In the case of

silicon and oxygen in quartz, the collision causes spallation and muon reactions (Figure 3.5) (Gosse and Phillips, 2001) producing ^{10}Be at a rate of ca. 4 atoms g^{-1} quartz yr^{-1} (Balco et al., 2008; Borchers et al., 2016; Corbett et al., 2016). As the exposure to cosmic radiation is approximately constant over geological time, ^{10}Be builds up predictably. The concentration of ^{10}Be in the rock can be measured, and because the half-life of ^{10}Be is known (1.39 million years (Chmeleff et al., 2010; Korschinek et al., 2010)), the length of time the rock surface has been exposed to the atmosphere can be calculated (Gosse and Phillips, 2001; Ivy-Ochs and Kober, 2008; Dunai, 2010). The precise rate of nuclide production however is site specific, depending on site altitude and latitude. Higher altitude sites experience higher production rates. This is because the radiation passes through less of the earth's atmosphere so there is therefore less attenuation and the site receives a greater amount of radiation (Ivy-Ochs and Kober, 2008). High latitude sites experience higher production rates due to a lower cut-off rigidity (the degree to which primary rays' momentum is deflected by the Earth's magnetic field, which must be overcome in order to pass into the atmsophere) (Dunai, 2010; Darvill, 2013). The amount of rays that penetrate also depends upon variations in long-term primary ray production (Dunai 2001; Darvill 2013). These factors are taken into account during exposure age calculation (section 3.4.3) (Balco et al., 2008).

3.4.2. Production rates and scaling

In order to calculate an age from a concentration of ^{10}Be atoms, the production rate at the particular site needs to be estimated, as the rate at which the nuclide is produced varies with latitude, altitude and time, as well as sample thickness and density (Lal, 1991; Stone, 2000). Site specific production rates are estimated based upon a regionally, or globally derived production rate. These reference production rates are calculated and averaged from samples with independently dated exposure ages, using techniques such as varve records, radiocarbon dating or tree-ring chronologies (Kubik et al., 1998; Balco and Schaefer, 2006; Kaplan et al., 2011; Darvill, 2013). An average global ^{10}Be reference production rate can be derived from samples selected from sites in the USA, Scotland, Peru, Iceland, New Zealand, Norway and southern Argentina (Borchers et al., 2016). Data sets were strictly selected based upon the quality and completeness of data from a given site, with little uncertainty in parameters such as location, independent age constraints, erosion rate or degree of post depositional shielding.

Due to the location dependent nature of nuclide production rates, using reference samples from the region of interest to derive a regional production rate may provide final exposure ages more representative of the true exposure age. To obtain such a regionally derived rate for Patagonia, Kaplan et al., (2011) presents high-precision ^{10}Be measurements from samples taken from the surface of boulders on the Herminitia and Puerto Bandera moraines adjacent to Lago Argentino, alongside maximum- and minimum-limiting ^{14}C ages for the moraines. During the exposure age

calculation, a reference production rate is deduced, which when the chosen scaling factor is applied (to scale the production rate for location and time), best fits the production rates observed at the independently dated sites (Balco et al., 2008).

The global or regional production rates can be scaled for latitude and altitude to create an estimate of the site-specific production rate. Six primary scaling schemes exist: St (Lal, 1991; Stone, 2000), De (Desilets et al., 2006), Du (Dunai, 2001), Li (Lifton et al., 2005), Lm (Nishiizumi et al., 1989; Lal, 1991; Stone, 2000) and LSDn (Lifton et al., 2014), which differ slightly in the way that the effect of atmospheric pressure, the geomagnetic field and solar variability are calculated (Balco et al., 2008; Darvill, 2013). Ages produced using the different scaling methods and production rates vary slightly, meaning that it is important to ensure the same scaling method and production rate is used when comparing ages from multiple samples and sites.

This reference production rate is taken as the representative regional production rate. Using the Lm scaling method, an in-situ ^{10}Be production rate between 3.60 and 3.82 atoms/g/yr (Kaplan et al., 2011) is required to produce ^{10}Be surface-exposure ages compatible with the ^{14}C ages. This range also encompasses the rate derived from samples from the New Zealand's Southern Alps (3.74 ± 0.08 atoms/g/yr based on Lm scaling) (Putnam et al., 2010).

The local production rate can also be affected by shielding of the boulder from incoming cosmic rays by the surrounding topography and more proximal valley side and morphological features. Shielding reduces the local production rate, and if not accounted for in the final age calculation, will lead to an erroneously young sample age. Therefore, the angle of elevation of the horizon from the sample is measured in the field over 360° around the boulder, from which the impact of shielding is calculated when determining the final exposure age (Balco et al., 2008).

The degree of surface erosion of the boulder should also be considered. The process of erosion removes the upper surface of the rock which contains the highest concentration of nuclides, as well as exposing a surface now younger than the age of boulder deposition. These processes produce an anomalously young exposure age for the boulder. The rate of erosion can be estimated at specific sites based upon measuring the degree to which erosion resistant features in the rock, such as quartz veins, protrude from the eroded surface. This erosion rate is included in the final exposure age calculation.

3.4.3. Complicating issues in surface exposure dating

As well as the length of exposure time, a boulder's pre and post-depositional history can affect the amount of ^{10}Be present in its upper surface at the time of sampling. Details of this are given in Gosse and Phillips (2001) and Darvill (2013) and are explained here.

Inheritance

A boulder previously exposed to the atmosphere before its final deposition will carry forward a prior concentration of ^{10}Be, known as inheritance. The measured value of ^{10}Be in the sample would therefore not reflect solely the boulder's most recent period of exposure. Such a sample would give an erroneously old age. Inheritance can be reduced or removed by erosion of the boulder's previously exposed surface during subglacial transport. To mitigate against the effect of inheritance, boulders are selected which show signs of subglacial transport (are faceted, striated, sub-rounded), and therefore have the greatest chance of removal of any previously exposed rock surface.

Post-depositional movement and exhumation

Post-depositional rolling, slumping or exhumation (Figure 3.6) will result in a present-day upper surface of the boulder which may not have been exposed to the atmosphere for the entirety of the moraine's emplacement. Determining the age from such a boulder would give an anomalously young age for the moraine. The effect of post-depositional movement can be mitigated against by selecting boulders which are the least likely to have shifted, rolled or slumped. Boulders on the centre of a ridge crest are selected as they cannot have moved from higher ground following to their current position following initial deposition. To mitigate against potential exhumation of the boulder, large boulders (a b-axis > 1 m) are targeted as it is less likely that their upper surface was covered following deposition.

Post-depositional shielding

Episodic covering of a boulder's upper surface following deposition can periodically reduce the site specific production rate, leading to an erroneously young exposure age. Boulders may be covered by snow, loess or vegetation. 1 m depth of snow of density 0.3 g cm^{-3} covering a boulder's upper surface for four months of the year can produce an exposure age 5 % younger than the true exposure age (Gosse et al., 1995a; Licciardi et al., 1999, Gosse and Phillips 2001). This is mitigated against and its potential impact reduced by sampling large boulders. The windy setting of this region is also likely to act to reduce the build-up of prolonged, deep snow cover. It is therefore not expected that periodic snow cover would impact the exposure age to such an extent as 5 %. A value less than this is within the uncertainty of the exposure ages. Because of this, and because the depth and extent of periodic snow cover is difficult to estimate, no correction is made. To reduce the potential impact of anomalous ages when establishing an age for a geomorphological event, and aid in their identification, it is common practice to sample multiple boulders from the same feature. Putkonen and Swanson (2003) suggest that ideally three to seven boulders should be sampled, favouring smaller moraines which have undergone

less degradation and potential of boulders being exposed after moraine formation due to ridge-crest lowering. With larger datasets it may be possible to distinguish the relative importance of inheritance and moraine degradation for causing skew within sample ages for a moraine, and from this obtain a age estimate that accounts for these processes (Applegate et al., 2010, 2012).

Isostatic uplift

Isostatic changes of the crust change the local production rate by changing the altitude of the site. The effect a 50 m elevation change has on a change in sample age is approximately 0.5% (Gosse and Phillips 2001). Isostatic uplift observed across the NPI is less than 50 m (Thorndycraft et al., 2019). Again considering the effect on the final age is within the larger error of the sample's age, isostatic changes are not taken in to account.

3.4.4. Sample selection criteria and sampling

Considering the aforementioned ways to mitigate potential complicating issues in surface exposure dating, the following sample selection criteria and sampling methodology was used. Boulders were selected for sampling which show no signs of rolling or slumping and were located on the centre of a moraine ridge crest. Selected boulders were faceted and sub-rounded (signs of subglacial transport). Within these criteria, the largest boulders on a moraine were selected where possible, with a b-axis > 1 m.

Given Obj. 3 of this thesis, to produce a chronologically-constrained palaeoglaciological reconstruction of Calluqueo Glacier, moraines were selected which mark the reconstructed frontal ice position at a location where chronological constraint is missing. Moraines which may have formed subaqueous in ice-dammed lakes were therefore avoided. This is explained within the context of the site location and description in section 5.3. Following Putkonen and Swanson (2003), five boulders were sampled from each moraine or moraine complex. Ten boulders were sampled in total across two sites. Five from a single moraine ridge at M9 and five across 5 smaller ridges within the M12 moraine complex (Figure 5.1). The number of boulders sampled was limited by the number of boulders found that met the selection criteria.

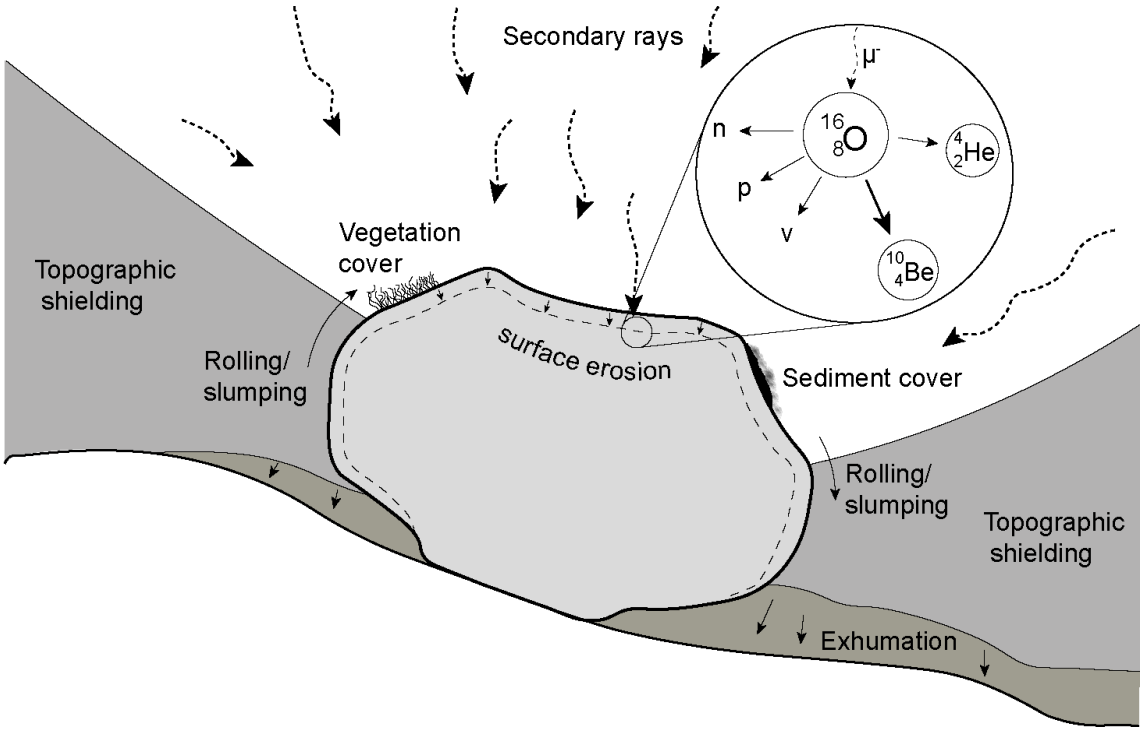

Figure 3.6. Factors affecting boulder shielding and potential post-depositional processes which alter the sampled surface. In part after Darvill 2013. Negative muon capture spallation reaction within the upper surface of the rock shown inset. Letters correspond to table in Figure 3.5.

Samples greater than 1 kg in weight (to ensure sufficient quartz content) were taken from the upper 5 cm of the flat surface of quartz-rich boulders using a hammer and chisel. While rock saws, drills or small explosive charges can also be used to break the surface rock into fragments, the method used is dependent on accessibility to equipment and practically of equipment transport to the sample site. A hammer and chisel are most commonly used due to portability and having the least lasting environmental or aesthetic impact on the boulder. However, this method can be physically demanding and time consuming. Samples from each boulder were collected in separate durable bags and labelled accordingly. Because of the variation in production rate with altitude and latitude (Lal, 1991), the coordinate location and elevation above sea-level of each boulder were recorded. The dimensions of the boulder were measured and records of its lithology, shape, surface texture, slope and weathering, immediate setting on the moraine ridge, surrounding sediments, broader geomorphological setting and angle of elevation to the horizon were taken. Multiple photos were taken of the boulders from all surrounding angles to provide a record of their relative position on the moraine ridge.

3.4.5. Sample processing, age calculation and evaluation

Following sample collection, the whole rock samples were mechanically crushed and sieved to 250-500 µm in the department of Earth Science at Royal Holloway University of London. Sample processing and analysis was done at the Natural Environment Research Council (NERC) Cosmogenic Isotope Analysis Facility (CIAF) at the Scottish Universities Environmental Research

Centre (SUERC). Quartz was isolated by froth floatation and then magnetic mineral separation using a Frantz® iso-dynamic mineral separator, before being treated by hexafluorosilicic acid and undergoing repeated etching in 2% hydrofluoric acid (HF) to remove unwanted particulates. Quartz purity was assayed by ICP-OES. The purified quartz was dissolved in 40% HF with 0.23 mg ^{9}Be carrier solution and Be is chemically isolated following the methods developed by Child et al. (2000). The solution is precipitated as Be(OH)2, baked to BeO in a quartz crucible before being mixed with Nb to prepare the BeO-Nb targets. The ^{10}Be/^{9}Be ratios were measured by the 5 MV NEC Pelletron accelerator mass spectrometer (AMS) at SUERC (Xu et al., 2010), normalised to the NIST SRM4325 standard, ^{10}Be/^{9}Be ratio 2.79 x 10^{-11} (Nishiizumi et al., 2007). The processed blank ratios ranged between 6 and 10 % of the sample ^{10}Be/Be ratios. The uncertainty of this correction is included in the stated standard uncertainties.

Ages are commonly calculated using the CRONUS-Earth online calculator (hess.ess.washington.edu (Balco et al., 2008)). This requires a sample's nuclide concentration and associated 1-standard error analytical uncertainty as measured by AMS, along with the sample's physical properties (thickness and density), location (latitude and longitude), elevation, erosion rate and shielding correction. Ages are calculated by solving equation 3.1 for exposure age (*T*).

$$N = S_{thick} S_G P_{ref,sp,Xx} \int_0^T S_{Xx}(t) \exp(-\lambda t) \exp\left(\frac{-\varepsilon t}{\Lambda_{sp}}\right) \mathrm{d}t + P_\mu \int_0^T \exp(-\lambda t) \exp\left(\frac{-\varepsilon t - z/2}{\Lambda_\mu}\right) \mathrm{d}t \quad (3.1)$$

Table 3.2. Variables in equation 3.1 used to calculate a sample's exposure age. After Balco et al. (2008).

Symbol	Variable	Units
T	Exposure age	years before sample collection date
N	Measured nuclide concentration in the sample	atoms g^{-1}
S_{thick}	Thickness correction	nondimensional
S_G	Geometric shielding correction	nondimensional
$P_{ref,sp,Xx}$	Reference production rate due to spallation for scaling scheme (Xx)	atoms g^{-1} yr^{-1}
$S_{Xx}(t)$	Scaling factor for scaling scheme (Xx)	nondimensional
λ	Nuclide decay constant	yr^{-1}
ε	Externally derived surface erosion rate	g cm^{-2} yr^{-1}
Λ_{sp}	Effective attenuation length for spallogenic production	g cm^{-2}
P_μ	Surface production rate in the sample due to muons	atoms g^{-1} yr^{-1}
Λ_μ	Effective attenuation length for the production by muons	g cm^{-2}

Z	Sample thickness	g cm $^{-2}$

Ages are presented as thousand calendar years that the boulder's surface has been exposed up until the sample date. Samples in this study were collected in December 2016, so the term ka refers to the number of thousand years before December 2016. The CRONUS-Earth online calculator presents dates for multiple scaling methods to allow for easy comparison. Calculated dates are also presented with "internal" and "external" uncertainties. The internal uncertainty is the uncertainty on the measured nuclide concentration, also known as the measurement, or analytical uncertainty. The external uncertainty includes all uncertainties input into the age calculation, and therefore also includes the production rate uncertainty (Balco et al., 2008). Normal kernel density estimate plots can be used to evaluate the ages at each moraine, with the shape of the summed probability distributions used to establish the presence of outliers within the moraine's dataset (e.g. Kelly et al., 2008). Internal uncertainties are used for these plots rather than the external uncertainty. Given that they are taken from the same feature, the samples are exposed to the same production rate uncertainty.

Due to the potential subjectivity of using normal kernel density estimate plots alone to identify outliers, a reduced chi-squared test (equation 3.2) (cf. Jones et al., 2019) can also be used to statistically assess the spread of the data. Such a test measures the fit between the uncertainty weighted mean (UWM) ($\bar{\mu}$) (equation 3.3) and set of individual exposure ages.

$$x_R^2 = \frac{1}{n-1} \sum_{i=1}^{n} \frac{(x_i - \bar{\mu})}{v_i^2} \tag{3.2}$$

$$\bar{\mu} = \sum_i \left(\frac{\frac{1}{v_i}}{\sum_i \frac{1}{v_i}} \right) x_i \tag{3.3}$$

$$k = 1 + 2\sqrt{\frac{2}{n-1}} \tag{3.4}$$

Where v_i is the sample's internal age uncertainty and x_i is the sample's mean age. The UWM ($\bar{\mu}$) is the arithmetic mean of the sample ages, where each age is weighted by the inverse of the sample's internal age uncertainty, such that those with the lower uncertainty have a greater contribution to the final mean value than those with higher uncertainty. A reduced chi-squared test x_R^2 value less than the 2σ envelope criterion k (equation 3.4) indicates a > 95% probability that the data is representative of a single population of ages. In this scenario an UWM is a valid age estimate for the feature (Spencer et al., 2017), and sample dates are presented with the corresponding UWM age and weighted standard deviation ($\bar{\sigma}$) (equation 3.5) for the feature in question. Bayesian age modelling is also used to aid identification of outliers, through examining

the degree of agreement between the modelled and unmodelled ages which is explained in section 3.5.

$$\overline{\sigma} = \sqrt{\sum_i \left(\frac{\frac{1}{v_i}}{\sum_i \frac{1}{v_i}} \right) (x_i - \bar{\mu})^2} \quad (3.5)$$

3.5. Bayesian age modelling

Bayesian age modelling utilises a known order of events, derived from interpretation of sediment-landform assemblages, with independent chronological information to constrain the timing of a phases within a sequence. In Bayesian terminology, a prior model is first built, containing the information about the order of events (e.g. the sequence of ice-margin formation when applied to deglaciation) before any age measurements are considered. A likelihood model is then built incorporating the age data from the given events (e.g. surface exposure ages of moraine boulders) as probability distribution functions representing the likelihood that an event will have a particular age (Bronk Ramsey, 2008, 2009a). Markov Chain Monte Carlo iterations (Gilks et al., 1995) are used, combining both the prior and likelihood probabilities to find possible ages for each event, which are presented as posterior probability densities (Bronk Ramsey, 2008, 2009a). As in this study, the Bayesian method is increasingly used as a tool to constrain the chronological history of deglaciation, reducing the uncertainty range of measured ages based upon their known order of occurrence as well as aiding the identification of outliers (e.g. Bendle et al., 2017a; Chiverrell et al., 2013; Jones et al., 2015; Smedley et al., 2017)

Chapter 5 provides a model for the order of sequential moraine formation in the Salto and Tranquilo valleys, following the ACR, based upon a geomorphological and stratigraphical study. A uniform phase sequence model (Bronk Ramsey, 2008) was utilised in Oxcal v4.3 (https://c14.arch.ox.ac.uk) to produce probability density estimates for each surface exposure age sample, utilising phase and boundary functions to identify and separate the samples by moraine site. The General outlier model (Bronk Ramsey, 2009b), was applied enabling outliers to be identified and retained in the model, but their influence proportionately scaled down. Samples were further assessed for their fit within the wider dataset based upon the agreement index, with a minimum recommended value of 60% (Bronk Ramsey, 2009a).

3.6. ELA and ice surface reconstruction

Due to the relationship between temperature and precipitation at a glacier's Equilibrium-Line Altitude (ELA) (Ohmura et al., 1992; Braithwaite, 2008; Sagredo et al., 2014) it is possible to extract palaeoclimatic information from the ELA of a reconstructed palaeo-glacier (Dahl and Nesje, 1992; Bakke et al., 2005; Bjune et al., 2005; Stansell et al., 2007). If a record of past temperature is available, a quantitative estimation of palaeoprecipitation can be obtained. Such a tool is particularly useful given the difficulty of quantitatively reconstructing palaeoprecipitation from other palaeoclimate proxies. ELAs can be calculated based upon the elevation of glacial landforms, using the maximum elevation of lateral moraines (Lichtenecker, 1938; Andrews, 1975), the altitude of the cirque floor (Reuther et al., 2004) or the concentration of land surface area (Egholm et al., 2009). These methods however have limitations which can introduce errors into the ELA calculation. For example calculating ELA based upon the altitude of the cirque floor requires specific glacier types formed over multiple glaciations (Pellitero et al., 2015). More preferred methods use the geometry of the reconstructed glacier's surface. Of these the Accumulation Area Ratio (AAR) method is most common, based upon the assumption that when glaciers are at equilibrium the ratio between the accumulation and ablation areas is constant. However this method does not take into account glacier mass balance gradient or hypsometry (Osmaston, 2005).

These factors are taken into account in the Accumulation Area Balance Ratio (AABR) method (Osmaston, 1975; Furbish and Andrews, 1984) and is hence taken to be a more robust approach (Pellitero et al., 2015). Such a method is used in this study and reported in Chapter 6. As well as adding greater mass balance weighting to areas further above or below the ELA, a balance ratio is also added to account for differences in mass balance gradients above and below the ELA. Commonly, glacier hypsometry is obtained manually using a cartographic method based upon morphological evidence of a former glacier's extent and best estimates of the palaeo-glacier's surface contours (e.g. Lukas, 2006; Rea and Evans, 2007), before being incorporated into the AABR calculation (Osmaston, 2005). However, morphological features to provide evidence for ice extent are often absent, or landforms have been poorly preserved. A preferable method is to combine available geomorphological evidence with an ice surface derived numerically.

In this study, the GlaRe GIS tool for ArcGIS (Pellitero et al., 2016) is used. This reconstructs a three-dimensional ice surface based upon a given bed topography and an element of the reconstructed ice margin (e.g. lateral or frontal moraine or a trimline). The model produces a two dimensional reconstruction of the glacier's flowline, assuming perfect plasticity rheology (Paterson, 1994), based upon the equation 3.6 for shear stress at the glacier's bed (Nye, 1952):

$$H = \tau/(\rho g \sin\alpha) \quad (3.6)$$

where τ is a uniform basal shear stress, ρ is ice density and α is the ice surface slope, which is then interpolated to produce the 3D surface. This method assumes the present-day topography is the same as that of the palaeo-glacier bedrock topography. If ice is still present this must first be 'removed' (Chapter 7) to produce a best estimate of the palaeo-bedrock surface. This method also assumes the glacier is in equilibrium and is land-terminating. Once a palaeo-ice surface has been reconstructed, this can be used as the input to an automatic calculation of the glacier ELA. Here a GIS tool for ArcGIS developed by Pellitero et al., (2015) is used to produce AABR-derived ELAs, following Osmaston (2005), providing the advantage of rapid ELA calculation based upon the best estimate of the palaeo-ice surface. The newly derived ELAs can be combined with relative temperature offsets from the West Antarctic Ice Sheet (WAIS) Divide surface air temperature reconstruction (Cuffey et al., 2016) to calculate quantitative estimates of precipitation at the ELA for each phase of glacier stillstand (Ohmura et al., 1992).

3.7. Glacier numerical modelling

3.7.1. Ice-sheet and glacier models

Computer-based numerical models of glaciers and ice sheets simulate how ice flows and ice-mass changes based upon key physical ice-flow, energy and mass flux laws. Models range in complexity from the simplest one-dimensional flow-line models to more complex three-dimensional models. One-dimensional flowline models simulate the downward flow of ice along a single line, commonly the centreline of a valley glacier or ice-stream where the mass being modelled is laterally constrained (Oerlemans, 1997; Anderson and Mackintosh, 2006; Gladstone et al., 2012; Davies et al., 2014). A cross-sectional plane such as a trapezoid perpendicular to ice flow may be included to define the lateral geometry of the ice. A width-dependent shape factor may also be applied to account for changes in valley or ice-stream width along the flowline, ensuring conservation of mass. More complex two- and three-dimensional models have been developed to allow for modelling of ice masses containing multiple flow-lines, such as ice sheets, ice caps and bifurcating glaciers, and internal variations in ice dynamics. Two-dimensional models (e.g. Meur and Vincent, 2003) vertically integrate velocity, shear stress and energy flux within the ice, simplifying the model and allowing for shorter computational processing times. Fully three-dimensional models (e.g. SICOPOLIS (Greve et al., 2011), the Glimmer CISM (Rutt et al., 2009), Elmer/Ice (Zwinger et al., 2007) and PISM (Winkelmann et al., 2011)) allow for variations in these variables throughout the ice column. This allows for more complex ice flow processes and environments to be simulated, although wall-clock run times are longer.

This range of glacier and ice-sheet models are typically used to reconstruct past ice masses with the view to better understand present day and future ice behaviour (e.g. Pollard and DeConto,

2009; Jamieson et al., 2012; Golledge et al., 2017). Models are also used to simulate present ice masses under future climate (e.g. Seddik et al., 2012; Joughin et al., 2014), as well as investigating specific glacier or ice sheet processes at the grounding line and calving front, or the development of crevasses and meltwater pathways (Morlighem et al., 2010; Todd and Christoffersen, 2014; Gong et al., 2018). These studies provide key data regarding past ice volume and mass balance, ice mass sensitivity and response times to climatic changes, the role of grounding line and calving processes in ice stream stability, quantitative palaeotemperature and precipitation data and contributions of ice masses to future sea level rise.

The output of glacier models can be constrained by and tested against empirical data. These data are commonly in the form of chronologically constrained ice-mass reconstructions from dated ice limits, but can an also include subglacial landform formation and reconstructed glacial transport pathways (e.g., Golledge et al., 2012; Livingstone et al., 2015; Becker et al., 2016; Jouvet et al., 2017). It is important to obtain a comprehensive understanding of the past glacial landsystems for the environment with which the model is being compared to, in order to take into account in the model where possible all the past glacial processes which operated (e.g. the impact of any ice-dammed lakes), and understand the historical context of available chronological data. PISM has been applied widely to the Greenland Ice Sheet (Langen et al., 2012; Aschwanden et al., 2016; Nielsen et al., 2018), Antarctic Ice Sheets (Fogwill et al., 2016; Golledge et al., 2017; Kingslake et al., 2018) as well as mountainous regions globally (Golledge et al., 2012; Jouvet et al., 2017; Yan et al., 2018) to reconstruct past ice masses and climate and investigate complex ice flow patterns. These studies commonly include model-data comparisons.

In one example, Golledge et al. (2012) applied PISM to New Zealand's Southern Alps to evaluate the accuracy of modelled glaciers between valleys, model sensitivity and to devise an estimate of past climate at the LGM. Modelled ice extent was compared to mapped moraines (Barrell, 2011) to show that a cooling of 6 – 6.5^{o}C combined with a 25% reduction in precipitation from present day is required to produce an ice extent at the LGM limit. Simulations at increasingly fine resolutions (2 km, 1 km, 500 m) illustrated the importance of using high resolution grids to best resolve glacier dynamics in small mountain-valley glaciers. PISM has also been used in a similar manner to investigate precipitation patterns. Becker et al., (2016) used PISM to model ice extent at the LGM, with a LGM ice reconstruction based on geomorphological mapping as a reference (Geologische Bundesanstalt, 2013). Through forcing the model with different temperature and precipitation combinations, it was possible to deduce that a significant decrease in precipitation compared to present day is required in the north of the Alps compared to in the south to match the model to empirically reconstructed LGM ice extent. This suggests a

change in precipitation pattern since the LGM, which the authors attribute to a southward shift of the North Atlantic storm track during the LGM.

3.7.2 The Parallel Ice Sheet Model (PISM)

In this study we apply the Parallel Ice Sheet Model (PISM) to the MSL. PISM is an open source, fully three dimensional, thermodynamically coupled, time-dependent ice sheet model (Bueler and Brown, 2009; Winkelmann et al., 2011). By distributing mass continuity and thermodynamic equations at each grid cell across multiple processor cores, PISM has greater computational efficiency than other numerical ice sheet models (Golledge et al., 2012; The PISM authors, 2017) facilitating higher resolution models (e.g. Aschwanden et al., 2013) and shortening model run times.

PISM operates a non-sliding shallow ice approximation (SIA) (Hutter, 1983) in parallel with a vertically integrated, sliding shallow shelf approximation (SSA) (Weis et al., 1999) forming a 'hybrid' model (Bueler and Brown, 2009). SIA accounts for flow by shear within the ice, neglecting longitudinal and transverse stresses and assuming no sliding at the ice-bed interface. SIA is a simplified version of the Stokes equations for mass continuity (equation 3.7) and stress balance (equation 3.8) which describe the flow of glacier ice.

$$\nabla \cdot u = 0 \tag{3.7}$$

$$-\nabla p + \nabla \cdot \tau_{ij} + \rho g = 0 \tag{3.8}$$

Where u is the 3D ice velocity, p is the ice pressure, τ_{ij} is the deviatoric stress tensor, ρ is the ice density and is the acceleration due to gravity. Complex glacier flow models can solve the Stokes equations for the evolution of ice stress, however this is highly computationally demanding. PISM therefore uses simplified Stokes equations (equations 3.9 and 3.10), which when combined with Glen's flow law (Chapter 2), give the SIA equation for deformation velocity (equation 3.11) (Schmidt, 2019)

$$\frac{\delta \tau}{\delta z} = -\nabla_x p \tag{3.9}$$

$$\frac{\delta p}{\delta z} = -\rho g \tag{3.10}$$

$$u = -2(\rho g)^n \left|\nabla_{Z_s}\right|^{n-1} \left[\int_{Z_b}^{Z_s} A(z_s - \zeta)^n d\zeta\right] \nabla h \tag{3.11}$$

- n Glen's flow law flow exponent (most commonly equal to 3)
- Z_s glacier surface elevation
- Z_b glacier bed elevation

A Ice softness

h Ice thickness

ζ vertical integration variable from the glacier's bed to the glacier's surface

The SIA equation assumes the vertical component of the stress field is negligible given the high width-to-depth ratios of ice sheets. This model therefore works well for the majority of ice in ice sheets, but breaks down in areas of fast flowing ice. In such scenarios an SSA model simulates ice more effectively, accounting for flow through the movement of the ice over a weak substrate or whilst floating. The velocity due to sliding is calculated using the SSA equation (equation 3.12) (Bueler and Brown, 2009)

$$\frac{\delta T_{i,1}}{\delta x_1} + \frac{\delta T_{i,2}}{\delta x_2} + \tau_{b,i} = \rho g h \frac{\delta h}{\delta x_i} \qquad (3.12)$$

where x_i is the coordinates in the horizontal plane and $T_{i,j}$ is the vertically averaged stress tensor. Such a setup that facilitates the modelling of basal sliding through SSA is favourable for simulating fast-flowing grounded ice in the form of ice streams (Schoof, 2006) in Antarctica and Greenland and as well at temperate warm-based outlet glaciers, such as at MSL. By operating a hybrid model, PISM is thus able to model flow through both internal shearing (SIA) and basal sliding (SSA). The resulting modelled velocity field is a weighted average of the SIA model (Hutter, 1983) and plastic till form of the SSA model (Schoof, 2006), with greater weighting towards the SIA if sliding is slow and to the SSA if sliding is fast (Bueler and Brown, 2009).

In PISM, as well as coupling a more complicated climate model, the glacier's mass balance can be determined using a simple positive degree day (PDD) model (Figure 3.7). Such an approach is adopted in Chapter 7. The amount of precipitation that falls as snow and the amount of snow and ice that melts is a product of the ice surface temperature and hence the number of PDDs. F_{snow} and F_{ice} are PDD factors for snow and ice respectively (the thickness of snow and ice melted per degree kelvin per PDD), which can be tuned within PISM. Following melting, water may be refrozen based upon the predetermined refreeze fraction (θ_{refreeze}).

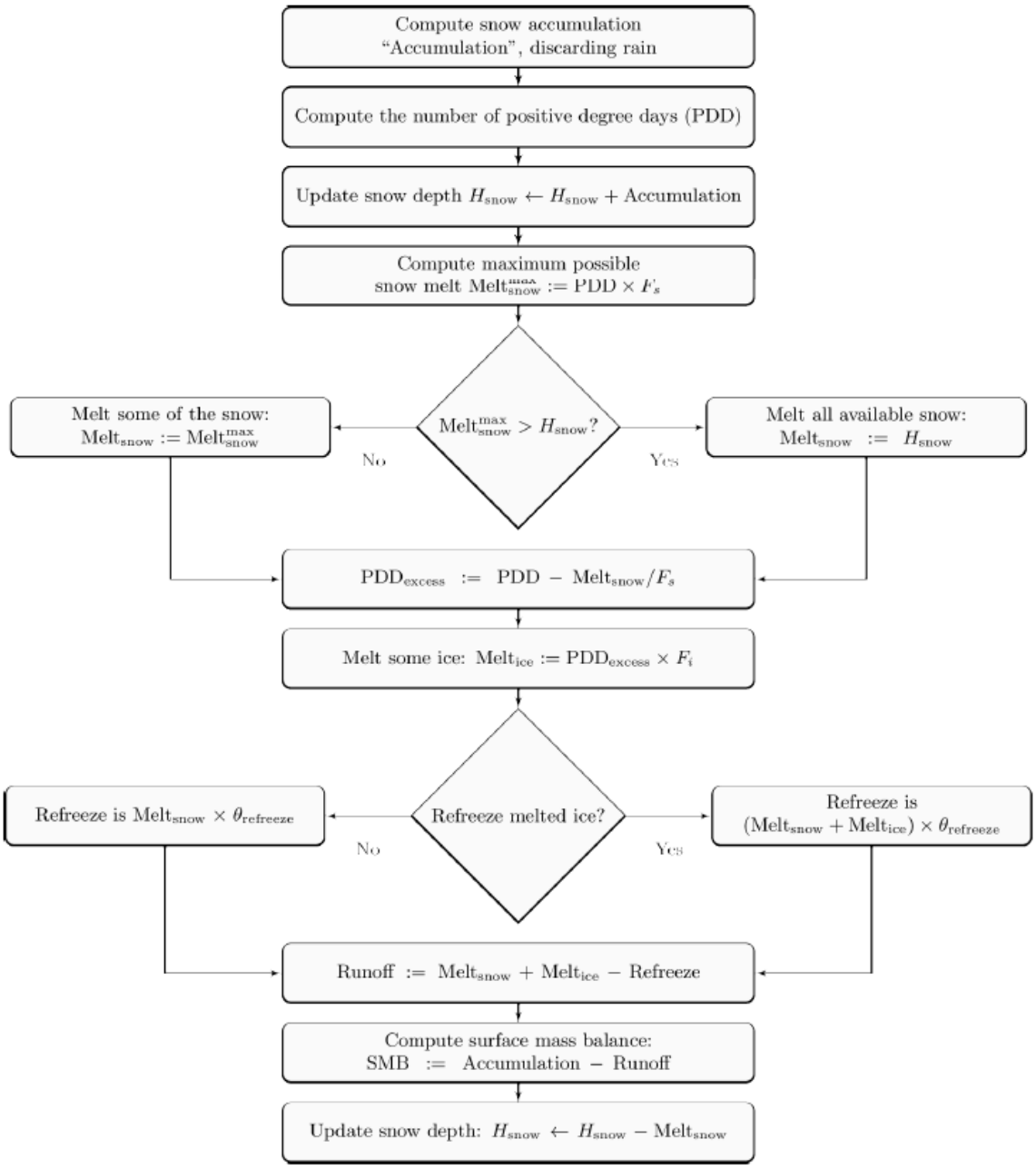

Figure 3.7. Flow chart illustrating the positive degree day model used within PISM to determine the glacier's mass balance (the PISM authors, 2017).

3.7.3. Modelling caveats

Certain caveats must be taken into account when using a numerical ice sheet or glacier model. Validating the model to present day or past conditions can be difficult due to a lack of observations, in particular of ice thickness. A lack of ice thickness data also makes producing a bedrock DEM difficult, or validate an inverse ice thickness model. Ice penetrating radar can be used to determine present day ice thickness of ice sheets such as Greenland, however flight lines often do not cover the entire ice mass (e.g. Bamber et al., 2013). The Patagonian Icefields have been surveyed for ice thickness but like elsewhere, flight lines do not cover the ice mass and outlet glaciers in their entirety, and small ice caps around the periphery of the major icefields,

such as MSL, are not surveyed (Gourlet et al., 2016; Millan et al., 2019). Inverse modelling therefore often must be used to establish ice thickness and generate a bedrock DEM. Golledge et al. (2012) determines ice thickness using the shear stress equation (3.6) to determine ice thickness (*H*) (Nye, 1952). Errors with this model are greatest at glacier margins where the surface slopes are greatest, however it is still favourable to use a bedrock DEM calculated in this way rather than dismissing ice thickness and using a surface DEM for the model's bedrock. A similar ice thickness model for Patagonia derived from the shear stress equation (Carrivick et al., 2016) is used in this study and explained in Chapter 7.

4. Sediment-landform assemblages and landsystems of the northern Monte San Lorenzo region

4.1. Introduction

4.1.1. Rationale

Atmospheric cooling during the ACR resulted in glacier readvance in the Southern Hemisphere mid-latitudes as shown by cosmogenic nuclide dating from moraine systems in Patagonia (García et al., 2012; Nimick et al., 2016; Darvill et al., 2017; Davies et al., 2018; Sagredo et al., 2018) and New Zealand (Putnam et al., 2010). In central Patagonia, the outlet glaciers of the NPI had receded back to the valleys of the Andean Cordillera by the time of the ACR readvance and many were terminating in large proglacial lakes (Davies et al., 2018; Thorndycraft et al., 2019). Antarctic ice core records, such as the WAIS Divide, show that the ACR in the Southern Hemisphere high latitudes was followed by *ca* 4000 years of warming from *ca* 13.0-9.0 ka, with rapid warming of 2 °C between *ca* 13.0-12.0 ka (Buizert et al., 2015). The geomorphic setting and evolution of Patagonian valley glaciers during post-ACR warming make them an interesting analogue for understanding present-day glacial dynamics in rapidly-warming, temperate climatic settings. During this period and the subsequent Holocene, glacier recession and punctuated readvances left behind discrete geomorphological features, revealing past glaciolacustrine, fjord-terminating and land-terminating glacier landsystems (Glasser et al., 2009b; Davies et al., 2018). Little work has been done to investigate the evolution and interaction of these landsystems, in particular those associated with the smaller ice caps located in the Cordillera east of the Patagonian icefields (72-73°W). These localities provide opportunities for elucidating the roles of climatic, topographic and glaciolacustrine controls on the evolution of late Quaternary glaciated valleys found in Patagonia (Glasser et al., 2009). Morphological and sedimentological data from low-altitude, shallowly-sloping, steep-sided

interlinked valleys, are currently limited and furthermore subsequent paraglacial modification has also received little attention in Patagonia.

Herein we establish sediment-landform assemblages and use a landsystems framework to examine the sedimentology and geomorphology of landforms in valleys to the north of the MSL ice cap (Figure 4.1), formed during a period of overall atmospheric warming. The glacial, glaciolacustrine, glaciofluvial and paraglacial landforms and deposits in the Salto, Tranquilo and Pedregoso valleys formed through the late Pleistocene and Holocene make up the basis for our sediment-landform study. These valleys represent contrasting styles of landsystems, including glaciolacustrine, land-terminating and glaciofluvial, but with significant paraglacial modification, and juxtaposed with small-scale mountain glaciers. Comparing these different landsystems will provide a template for understanding the roles different processes play in landscape evolution and modification in Patagonia. This new understanding of glacier landsystem and process change forms the basis for new chronological data presented in Chapter 5 and a temporally constrained palaeoglaciological reconstruction of the northern margin of the MSL ice cap in Chapter 6.

4.1.2. Research questions, aims and objectives

To address the current gaps in understanding surrounding the evolution of landsystems and controls on landsystems development north of the MSL ice cap, this chapter aims to answer the following research questions as part of **RQ 1** of this thesis: **1. Which sediment-landform assemblages are found in the Salto, Tranquilo and Pedregoso valleys, north of the MSL ice cap? 2. Which landsystems are there evidence for in these valleys? 3. What were the primary controls on sediment-landform associations and landsystem development?** The aims of the work presented in this chapter is to elucidate the nature and relative timing of changes in glacial environments, dynamics and processes since the ACR, addressing **Aim 1** of this thesis. Within **Obj. 1** of this thesis, our objectives in this chapter are: 1) to determine sediment-landform assemblages across a spectrum of palaeoglacial and glacial environments; 2) generate

landsystems' models explaining the processes of sediment-landform generation in central Patagonia; and 3) elucidate the influence of ice-dammed lakes and other controls on palaeoglacier dynamics.

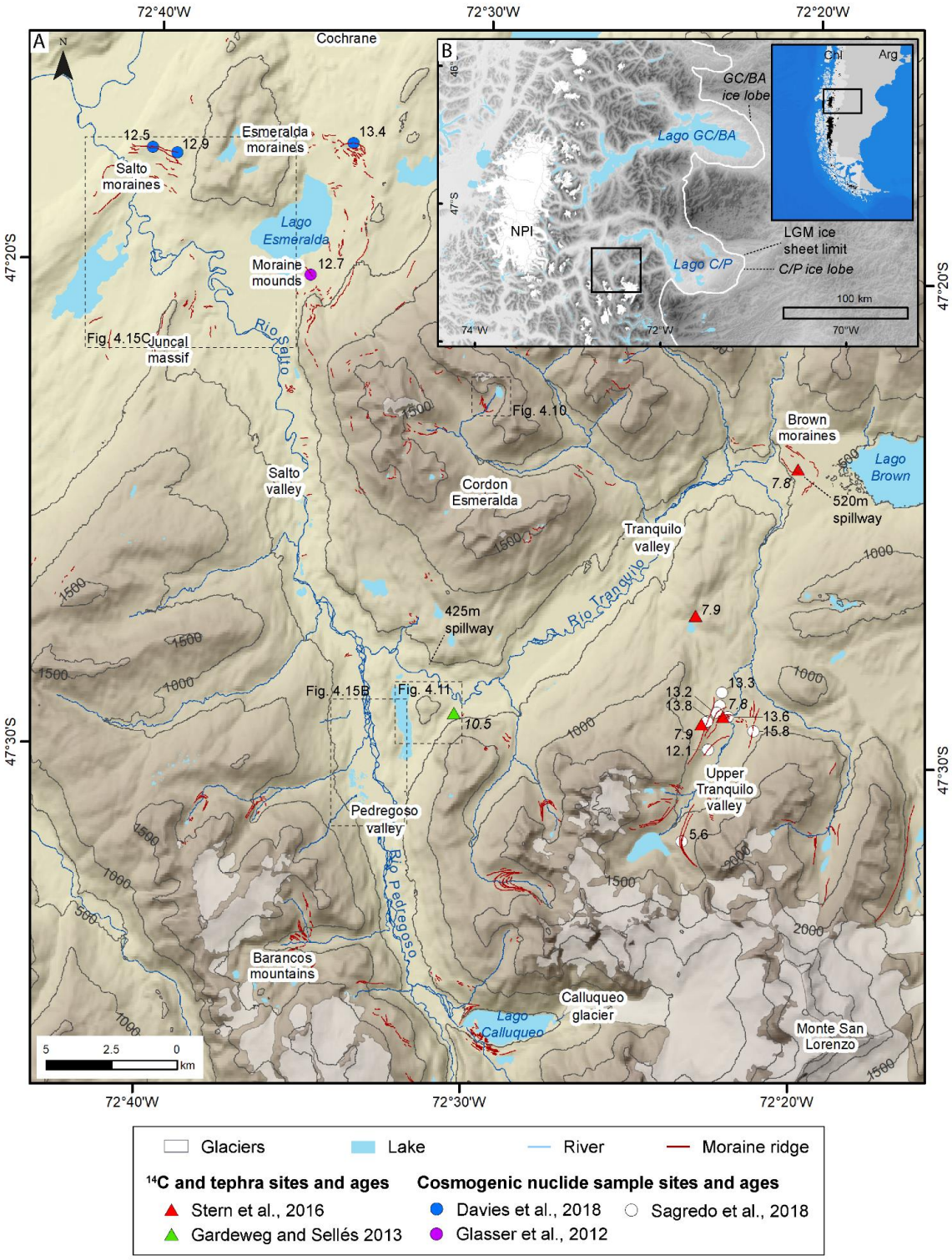

Figure 4.1. (A) Map of the study area north of the MSL Icecap including sites and mean landform ages from the published literature. (B) Maps showing the location of the study area within the context of the region east of the NPI and SPI, including Lago GCBA and Lago CP.

4.2. Methods

The Salto, Tranquilo and Pedregoso valleys were mapped and digitised in ArcMap 10.3 at 1:5000 scale using 1 m resolution DigitalGlobe imagery, part of the Esri™ World Imagery (Chapter 3). Google Earth Pro (DigitalGlobe imagery) was used in conjunction to this, alongside Google Earth's digital elevation model to view landforms from an oblique perspective, aiding identification. Additional elevation data were taken from ASTER GDEM (20 m vertical and 30 m horizontal resolution, 95% confidence; cf. (ASTER GDEM Validation Team, 2011). Field mapping (Nov-Dec 2016 and Dec 2017) was used to ground-truth remotely sensed mapping and improve landform identification and mapping detail. Roadside cuttings along the Salto and Tranquilo valleys provided sediment exposures for landforms. Landforms in the field were mapped using handheld GPS with a documented accuracy of ± 10 m.

Well-established criteria for landform identification, both by remote sensing and in the field, were used (Glasser et al., 2005, 2008; Bendle et al., 2017; Darvill et al., 2017; Chandler et al., 2018) and adapted to account for the specific characteristics of landforms found in the study area (Chapter 3.2.3, Table 3.1). Moraine ridges were grouped into 'sets' based upon their relative position within a valley to delineate a period of ice-marginal stability. Frontal and lateral moraines which could be traced to one another, or lateral moraines at the same altitude on opposite valley sides, were grouped into the same set. We group landforms into 5 sediment-landform associations that we outline in sections 4.3.2. to 4.3.6: ice-marginal, subglacial, glaciolacustrine, glaciofluvial and paraglacial.

Sedimentological and stratigraphical studies were undertaken at exposures through landforms (road cuttings and quarry sites) along the Salto and Tranquilo valleys using standard procedures (Evans and Benn, 2004). Clast morphology data (shape and roundness) were collected from representative facies, following Benn (2004), to investigate transportation and erosion histories. Shape data were plotted on a general shape ternary diagram (Sneed and Folk, 1958; Benn and Ballantyne, 1993) and from this C_{40} indices (Benn and Ballantyne, 1993) were calculated.

Roundness data were plotted as histograms and analysed statistically using RA (percentage of angular and very angular clasts in the sample) and RWR (percentage of rounded and well-rounded clasts in the sample) indicies (Evans and Benn, 2004). We use RWR indices alongside RA to mitigate for the influence of glaciofluvial reworking on the effectiveness of the RA index to distinguish transport pathways (Evans et al., 2010, 2013; Lukas et al., 2013). Cosmogenic nuclide surface exposure ages were recalculated (Figure 4.1) using version 3 of the online exposure age calculator formerly known as the CRONUS-Earth online exposure age calculator (Balco et al., 2008) with a regional Patagonian production rate calculated from the Kaplan et al. (2011) calibration data set. Ages presented assume a 0 mm/kyr erosion rate to obtain a minimum exposure age, use the time dependent LSDn scaling method (Lifton et al., 2014) and are calculated as uncertainty weighted means (UWM) of multiple samples taken over single moraine ridges/contemporaneous sets, rounded to the nearest 0.1 ka.

4.3. Results

4.3.1. Landform inventory of the northern MSL sector

Combining remote sensing and field mapping, including within forested areas, has allowed this study to map in greater detail the landforms of the study area. Subsequently this study has identified previously unmapped landforms and increased the extent and detail of those mapped in previous studies in this region that have relied on satellite imagery (Glasser and Jansson, 2005, 2008; Turner et al., 2005; Glasser et al., 2009a, 2012; Bendle et al., 2017; Davies et al., 2018). The landform inventory for the northern MSL sector contains 19 primary landform types (Figure 4.2) which includes 1,083 individual moraine ridges mapped alongside rivers, lakes, outcropping bedrock and bedrock gorges. Mapping of sections of the Upper Tranquilo valley and eastern Tranquilo valley is in part after Araya et al. (2014). Mapping in the north of the Salto valley is after Davies et al. (2018).

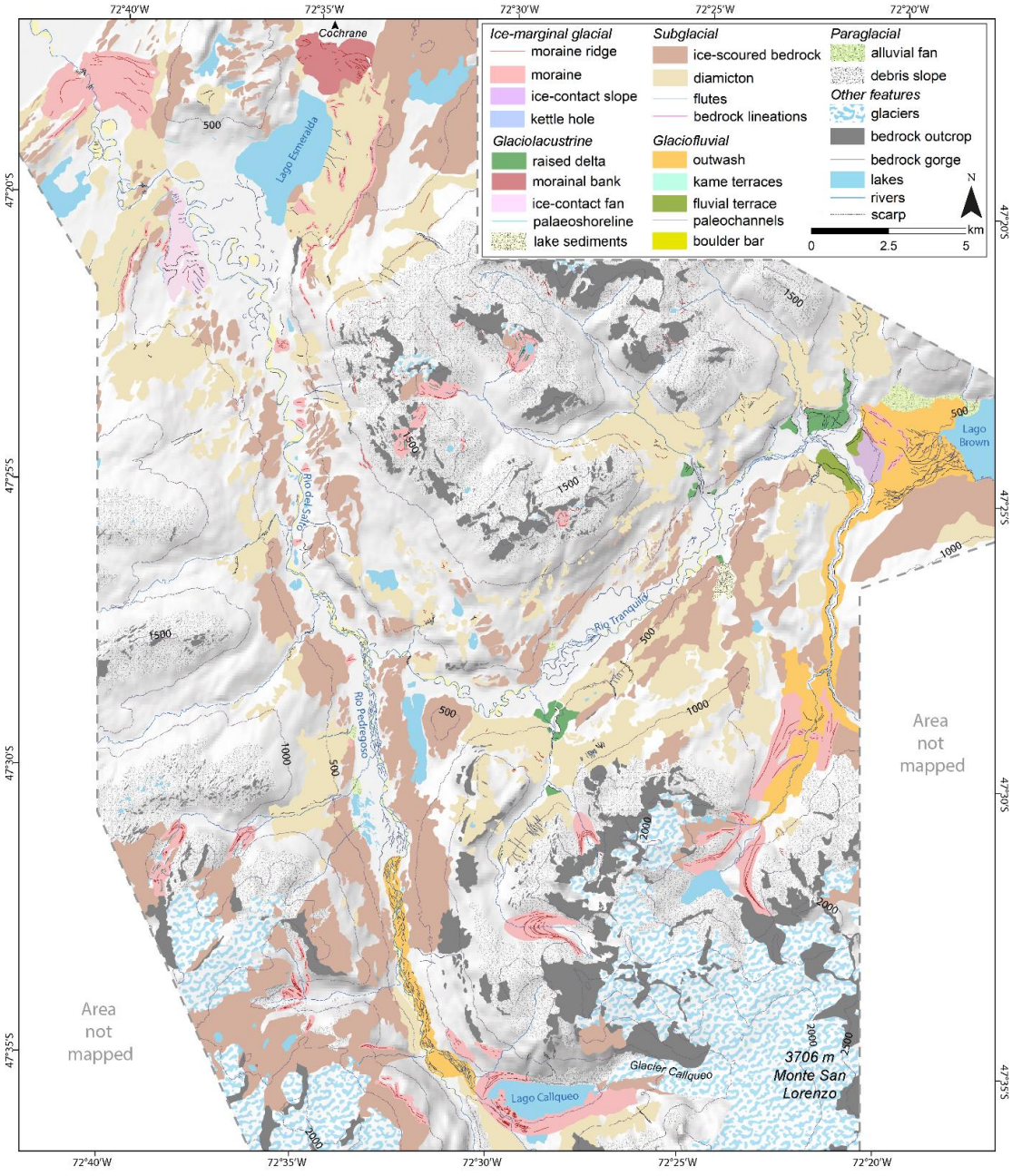

Figure 4.2. Geomorphological map of the study region to the north of MSL, including the Pedregoso, Salto and Río Tranquilo valleys. 500 m interval contour produced from ASTER DEM, showing the range of ice marginal glacial, glaciolacustrine, subglacial, glaciofluvial and paraglacial landforms alongside other features.

Critically, using field mapping to assist mapping from satellite imagery, we have identified 14 primary moraine sets (labelled M1a, M1b and M2 to M13) including 7 newly identified ice margin positions (M5 to 8 and M10 to 12) (Figure 4.3). Previously identified sets have been ground-truthed and extended in their mapped extent. The Esmeralda and Brown moraines are labelled M1a and M1b respectively, as the furthest advanced moraine sets in their respective

Salto and Tranquilo valleys. Moraines of the same colour are interpreted as forming coevally as part of the same moraine system.

4.3.2. Ice-marginal sediment-landform associations

4.3.2.1. Frontal moraines

The Esmeralda (M1a, cf. Davies et al., 2018) and Brown (M1b) moraines situated at the northern and eastern ends of the Salto and Río Tranquilo valleys respectively are the most substantial frontal moraines, up to 80 m and 100 m above the valley floor respectively. The M1a frontal moraine formed coevally with the 7.5 km long, valley-parallel lateral moraine component (Davies et al., 2018) (Figure 4.3). We speculate that the M1b moraine also formed at this time, due to their similar relative size and position in the Tranquilo valley (Figure 4.3). Inset of M1a in the Salto valley are a series of cross-valley, sharp-crested, steep-sided, both arcuate and more straight frontal moraines (M4 to M9) formed sequentially, positioned incrementally along the eastern valley side stretching south until the confluence with the Río Tranquilo valley. They are up to 40 m in height above the valley floor and up to 300 m long (Figure 4.3). M4 (also known as the "Moraine Mounds", *ca* 12.7 ± 0.4 ka cf. Glasser et al., 2012; Davies et al., 2018) and M6 are associated with semi-isolated masses of moraine producing an uneven surface of material on the ridges' ice-proximal side (Figure 4.2 and Figure 4.3). M6, 7, 8, and 9 notably extend perpendicular from terraces on the eastern valley side, only part way across the valley floor, east of the Río Salto (Figure 4.2 and Figure 4.3). The moraine ridges are composed of stratified massive and laminated sands, coarse sub-rounded to sub-angular gravels, and diamictons (e.g., M5: Figure 4.3E and Figure 4.5, M8: Figure 4.3I and Figure 4.6). Multiple sub-rounded to sub-angular, faceted granitic to dioritic boulders, up to 1 m in size, can be found along the ridge crests, strewn over larger areas of associated morainic material and within exposed sections. Across the study area, clast-shape data taken from moraine sites shows predominantly blocky clasts, with C_{40} percentages below 50% (Figure 4.3). The moraines in the Salto valley are dominated by sub-angular to sub-rounded clasts, whilst those in the Tranquilo valley have a

largely sub-angular to very-angular form. The M1b moraines consist of a series of discontinuous, sinuous ridges between 60 and 700 m long, arranged in an arcuate form, spanning 2 km across the valley. They occur on a topographic high, *ca* 120 m about the valley floor to the east, with a steep ice-contact slope on the western, ice-proximal side, and a more gently-sloping outwash plain on the eastern, ice-distal side.

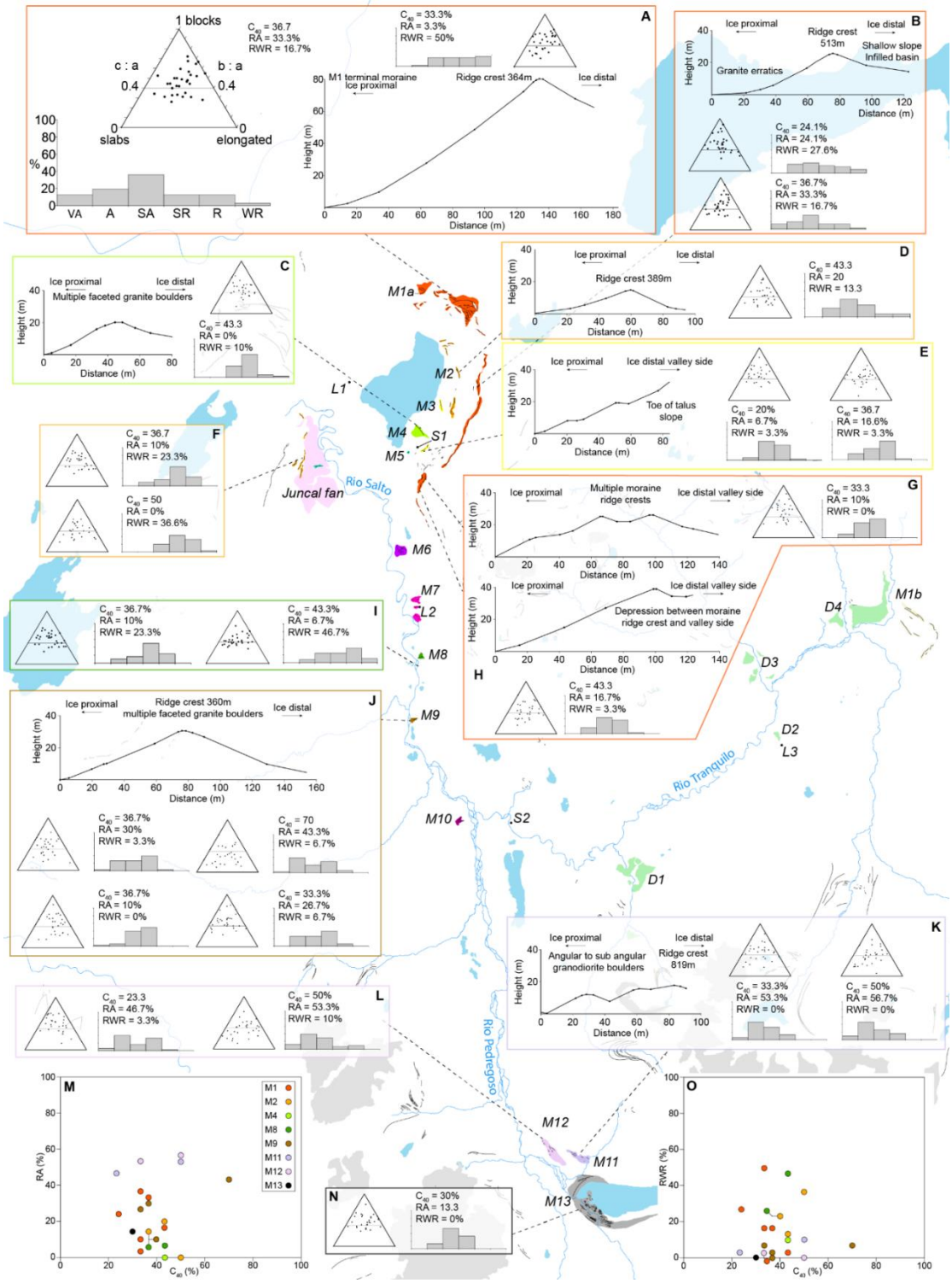

Figure 4.3. Above. (A) to (N) Moraine profiles and clast-shape data from sites along the Salto and Pedregoso valleys. (M) and (O) show RA-C_{40}% and RWR-C_{40}% plots respectively. Moraine sets, delta, lake sediment and diamicton section sites are labelled M1 to M13, D1 to D4, L1 to L3 and S1 to S2 respectively. Map shows 7 newly identified ice margin positions (M5 to 8 and M10 to 12), including sharp crested profiles of frontal moraines M1a and M9. Clast-shape data taken from moraine sites shows predominantly blocky clasts, with C40 percentages below 50%. The degree of clast roundness increases from south to north, reflecting increased sediment transport and reworking from the source by glaciofluvial processes.

Figure 4.4. Photo of cross-valley terminal moraines in the Esmeralda, Salto and Brown valleys. (A) Arcuate M4 moraine ridge in front of the Esmeralda 'Moraine Mounds'. (B) View south up the Salto valley and inset C. (C) M6 moraine and inset mounds. (D) Section through the M8 moraine ridge with associated kame terrace in the Salto valley. (E) M9 moraine ridge and associated kame terrace in the Salto valley. (F) Western end of the Brown valley, showing raised deltas and the inner M1b Brown moraine ridge.

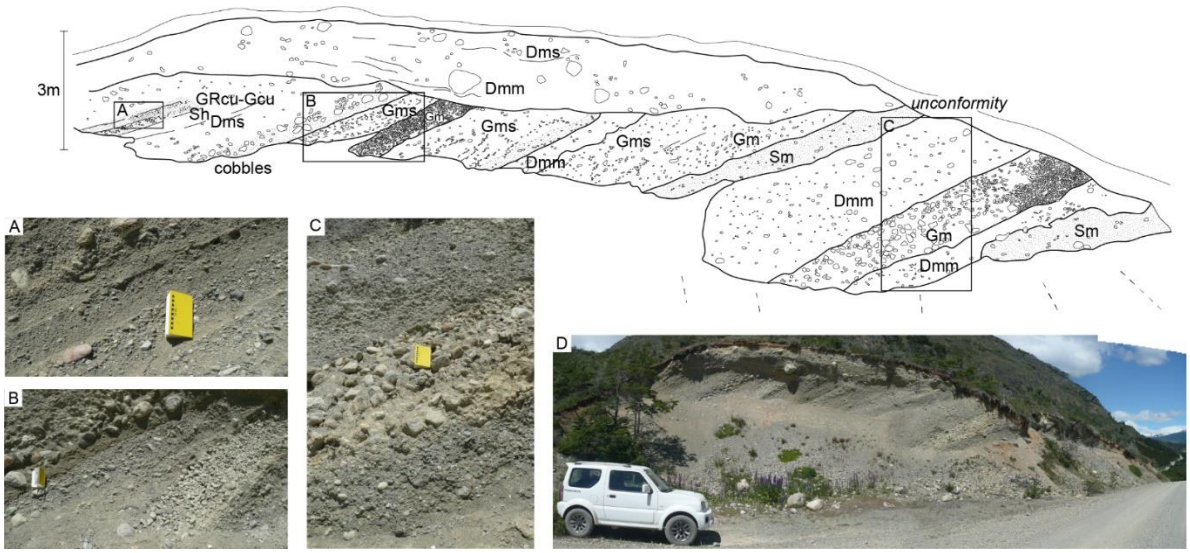

Figure 4.5. Section and photos at the M5 moraine. (A) to (C) show zoomed in photos of section, their locations labelled on the sketch. (D) Photo of exposed section through the M5 moraine. Shows example of frontal moraine ridge composition of stratified massive and laminated sands, coarse sub-rounded to sub-angular gravels, and diamictons.

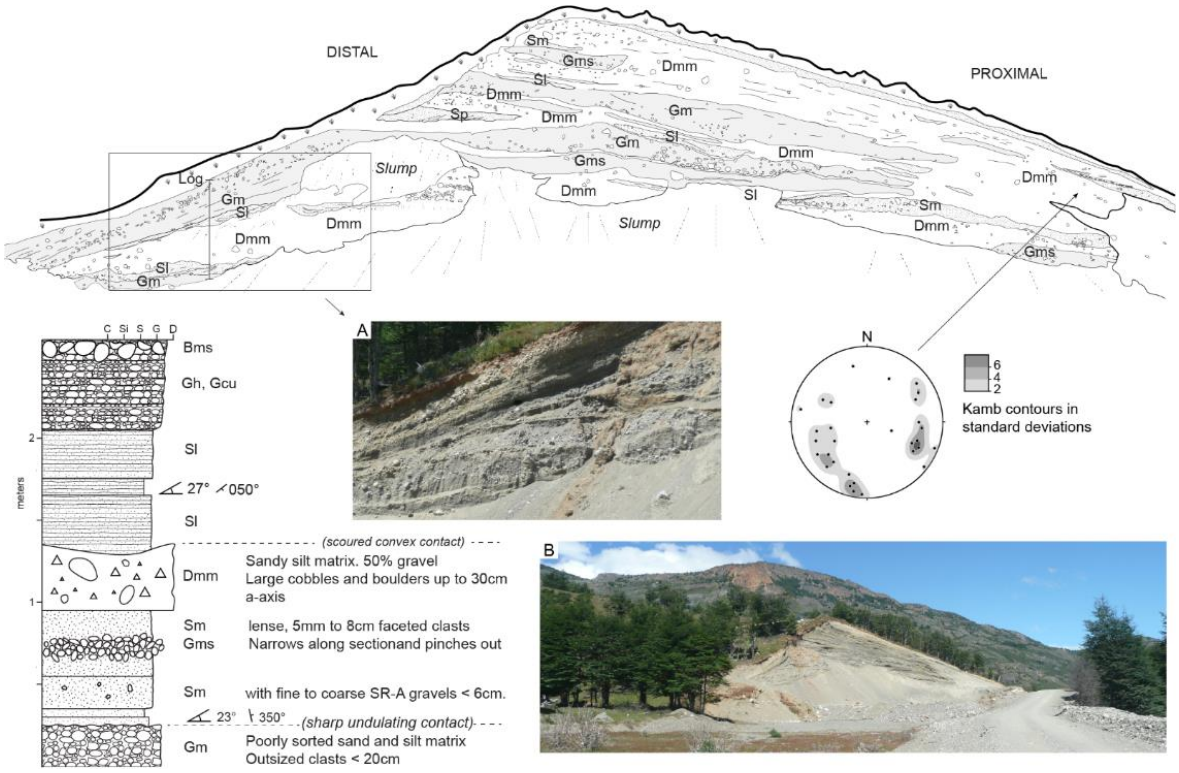

Figure 4.6. Sedimentary section, log and stone data from a quarry section at M8. (A) Zoomed in photo of a section of the exposure on the ridge's distal side through which the sedimentary log was taken. (B) Exposed face in full. Shows example of frontal moraine ridge composition with stratified gravels, diamictons and sands.

4.3.2.2. Lateral moraines

Valley-parallel, lateral moraine ridges in the study region have three primary morphologies. The first are large, laterally-extensive ridges with narrow crests and broadly symmetrical sides (Figure 4.3 M1 to M3, Figure 4.7A, C to F). The second group are smaller, closely-spaced pairs or

groups of laterally-discontinuous ridges with broadly equally-dipping sides, dissected by meltwater channels. They are found on topographically-flat bedrock plateaus on the northern flank of Cordon Esmeralda below M1 and at the southern end of the Salto valley (M11 and M12) (Figure 4.3). The third are small, discontinuous, ridges up to a meter high and 100 m long, found on the sloping valley side southeast of Lago Esmeralda, between M1 and M4, forming the lateral component of M3 (Figure 4.3).

The M1a (cf. Davies et al., 2018), M1b and M2 ridges are characterised by massive, silty and sandy diamictons and gravels, with numerous faceted granitic and dioritic cobbles and boulders up to 2 m along the a-axis (Figure 4.7A, Figure 4.8). M2 is overtopped by poorly defined units of clast-supported, sandy coarse gravel, and clast-supported silty fine gravel, edge rounded and faceted pebbles. Stones are primarily sub-angular to sub-rounded, blocky and elongated (Figure 4.3D).

Figure 4.7. Photographs of lateral moraines in the Esmeralda and Salto valleys. (A) M2 lateral moraine, with context of Esmeralda terminal moraines (M1a) and Esmeralda 'Moraine Mounds' (M4). (B) Moraine ridge on the lower northern side of Cordon Esmeralda. (C) M2 lateral moraine ridge pair. (D) View north along the ridge crest of M1a lateral moraine. (E) View of a glacially-transported boulder on the ridge crest of M1a lateral moraine. (F) View of the M1a lateral moraine ridge on the north western flank or Cordon Esmeralda, looking down over the Esmeralda valley. (G) Boulder on a ridge crest within the M12 moraine complex. (H) Boulder strewn ridge crests in the M11 moraine complex.

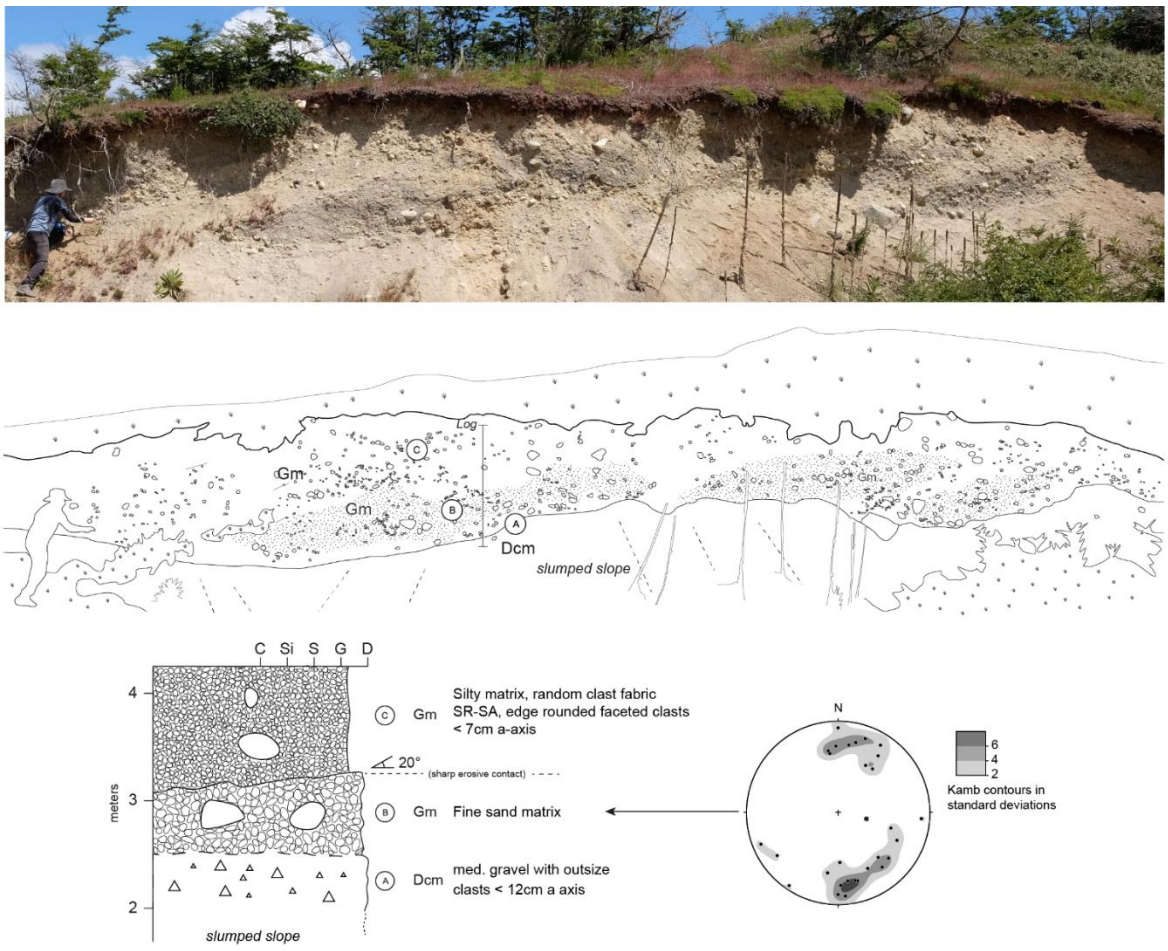

Figure 4.8. Sedimentary log, section and clast fabric data of the M2 lateral moraine, illustrating the massive, silty and sandy diamicton and gravels composition of the moraine, with numerous faceted granitic and dioritic cobbles and boulders up to 2 m along the a-axis.

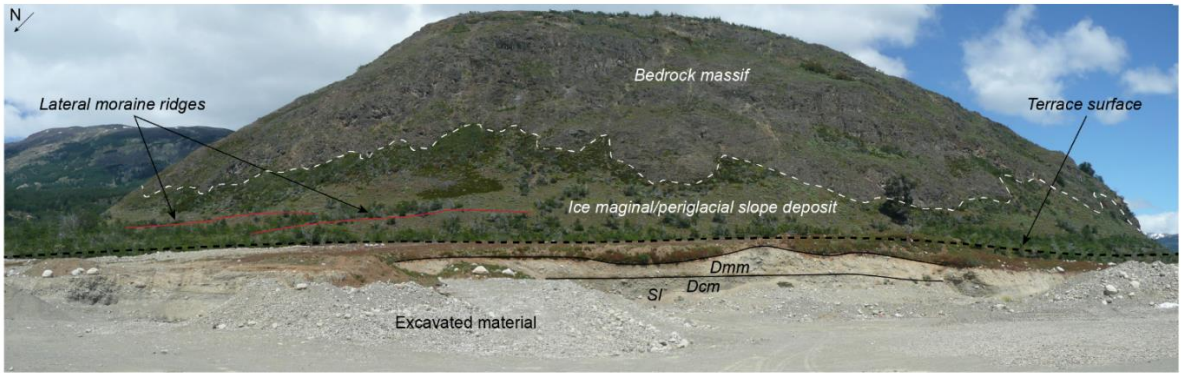

Figure 4.9. Section through diamicton at site S1 to the southeast of Lago Esmeralda, with lateral moraine ridges in Figure 4.7B visible on the side of the slope.

4.3.2.3. High-altitude valley moraines

Alongside the moraines in the lower valleys, well-preserved late Holocene lateral and frontal moraines are found close to the present-day Calluqueo glacier margin (Figure 4.2), in part damming Calluqueo proglacial lake, and in high altitude cirques in the upper Tranquilo valley and on Cordon Esmeralda. The largest Calluqueo moraine (M13) manifests as a sharp-crested,

steep-sided arcuate frontal terminal moraine ridge, *ca* 100 m above the valley floor and a broader-crested lateral moraine on the southern side of Lago Calluqueo. Numerous smaller, closely-spaced sinuous elongated parallel ridges are found along the broad lateral moraine ridge at the southwestern end of the lake. They are up to 3 m high with surfaces scattered with numerous loose, angular to subangular granodiorite cobbles and boulders. The small valleys on Cordon Esmeralda also contain numerous well-preserved, densely-spaced terminal ridges close to cirques, between 5 and 20 m apart superimposed over valley-parallel flutings (Figure 4.10). In front of these are larger moraine ridges with a classic saw-tooth morphology (cf. Evans et al., 2017).

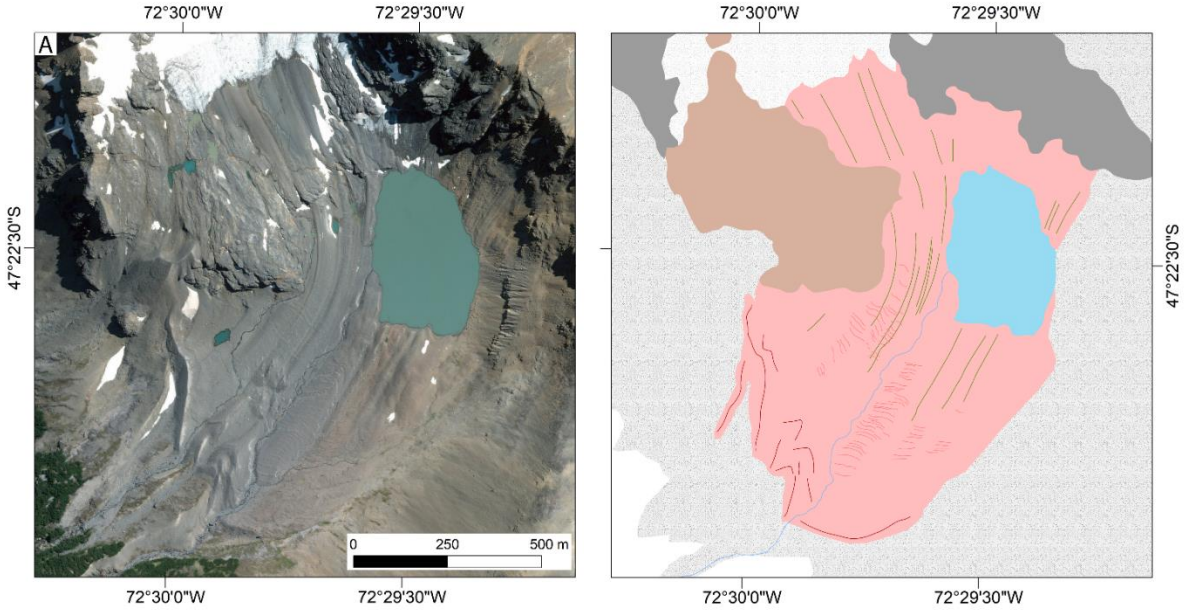

Figure 4.10.(A) Satellite image (Digital Globe EsriTM) of cirque on Cordon Esmeralda. (B) Mapped landforms from satellite image in (A). Colours correspond to key in Figure 4.2. Figure illustrates the saw-tooth moraines found in the high altitude valleys, as well as subglacially formed elongated parallel flutings.

4.3.2.4. Meltwater channels

Meltwater channels are found in association with the groups of laterally-discontinuous ridges on the bedrock plateaus on the northern flank of Cordon Esmeralda below M1. The largest is a gently-sloping, approximately-straight channel running the 200 m along the length of the complex, parallel to contemporary contours and the axis of moraine ridges. We interpret this

channel as ice-marginal (Greenwood, 2007). There is a notable lack of meltwater channels observed elsewhere.

4.3.3. Subglacial associations

4.3.3.1. Ice scoured bedrock

Isolated areas of ice-scoured bedrock occur along the lower sides of the Esmeralda, Salto and Río Tranquilo valleys, obscured in places by vegetation cover and separated by areas of diamicton plastered on to the valley sides and floor (Figure 4.2). It is not found at higher elevations or topographic crests between valleys, where instead bedrock crops out as blocky or sharp-sided exposures. Ice-scoured bedrock is also reported in neighbouring valleys east of the NPI (Glasser et al., 2009b; Bendle et al., 2017; Davies et al., 2018). Bedrock lineations can be identified orientated broadly NE-SW at the confluence of the Salto and Río Tranquilo valleys on a bedrock high set away from the valley side (Figure 4.11).

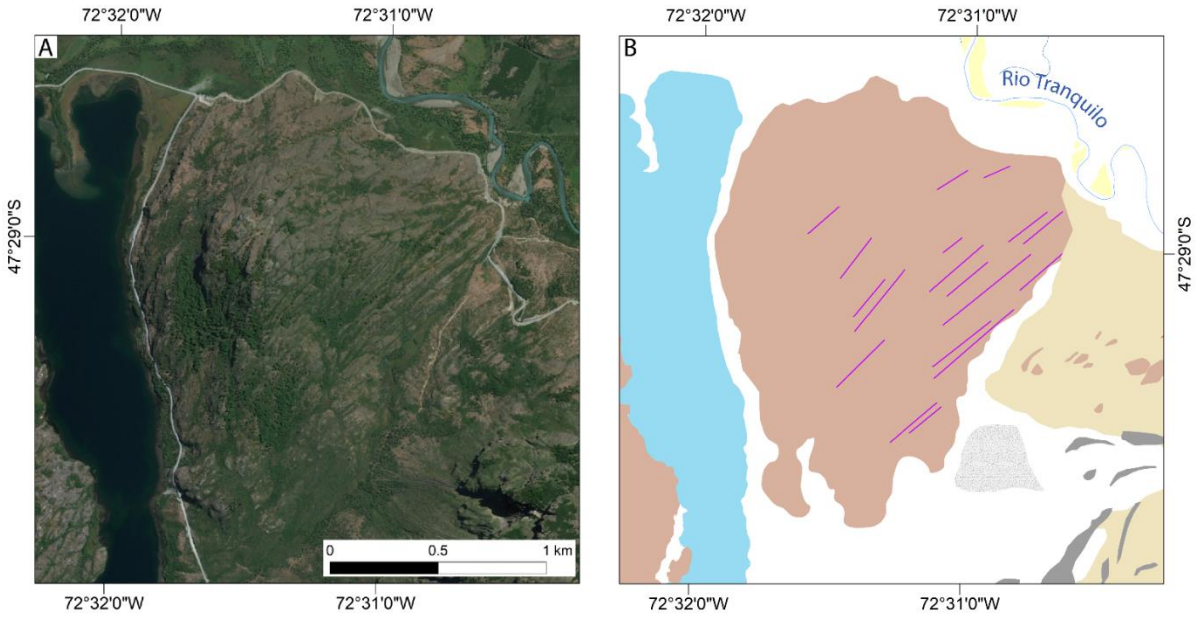

Figure 4.11. (A) Satellite image (Digital Globe EsriTM) of the confluence of the Salto and Río Tranquilo valleys. (B) Mapped landforms in area (A) showing ice-scoured bedrock and glacial lineations. Colours of landforms reflect those in Fig. 4.2.

4.3.3.2. Glacial diamicton

Areas of diamicton can be found plastered along the valley sides and at elevations both above and below ice-scoured bedrock. A flat-topped surface of diamicton is found on the eastern side of the Esmeralda valley on the western flank of Cordon Esmeralda (Figure 4.3 S1, Figure 4.9) showing a stone-rich, silty diamicton, stratified into a clast-supported layer below a matrix supported layer. Both layers contain boulders up to 30 cm in size. A small section of laminated sands is found at the base of the lower unit. Near the confluence of the Esmeralda and Río Tranquilo valleys (Figure 4.3 S2), a road cutting reveals a section of sediment plastered onto the side of bedrock. This comprises a silty diamicton, stratified in places, containing faceted boulders and rich in striated, faceted stones and interbedded with a layer of stratified, planer-bedded gravels. These are disrupted by inverted triangular structures of massive gravels. The lower diamicton is dissected by a sub-vertical unit of matrix-supported massive gravel and contains a discontinuous unit of partly-laminated medium sand at its base.

4.3.3.3. Flutes

In the high-altitude cirque on Cordon Esmeralda elongated parallel flutings 3 m to 7 m wide run along the valley length, found in association with closely-spaced moraine ridges, inset of large saw-tooth moraines (Figure 4.10). They are predominantly straight but curve with the profile of the valley. They are not found in the less recently deglaciated lowland Salto, Pedregoso and Tranquilo valleys.

4.3.4. Glaciolacustrine associations

4.3.4.1. Raised deltas

Large flat-topped, steep-fronted bodies of sediment are found along the length of the Río Tranquilo valley at three main sites: the western end (D1), centre (D2 and D3) and eastern end (D4) of the valley (Figure 4.2 and Figure 4.3). They are found in stepped sequence, incised by active and abandoned river channels at the opening of a ravine. Three primary terrace levels are defined: 600 m asl (at D1), 520 m asl (at D3 and D4) and 425 m asl (at D1, D2 and D3). D1 (Figure

4.12) reveals alternating well-defined beds of clast and coarse sand matrix-supported gravels, coarse gravely sands and hyper-concentrated clast-supported cobble beds up to 50 cm in thickness. Clasts are sub-rounded to rounded. These beds dip at 25° west-northwest towards the valley floor and are overtopped and truncated by a coarse, clast-supported, cobble-rich gravel bed. At the northern end of the section, the dipping beds give way to a clast-supported unit of cobbles up to 30 cm in size (Figure 4.12B). A section in the D4 delta (Figure 4.4) reveals a structure of dipping foresets.

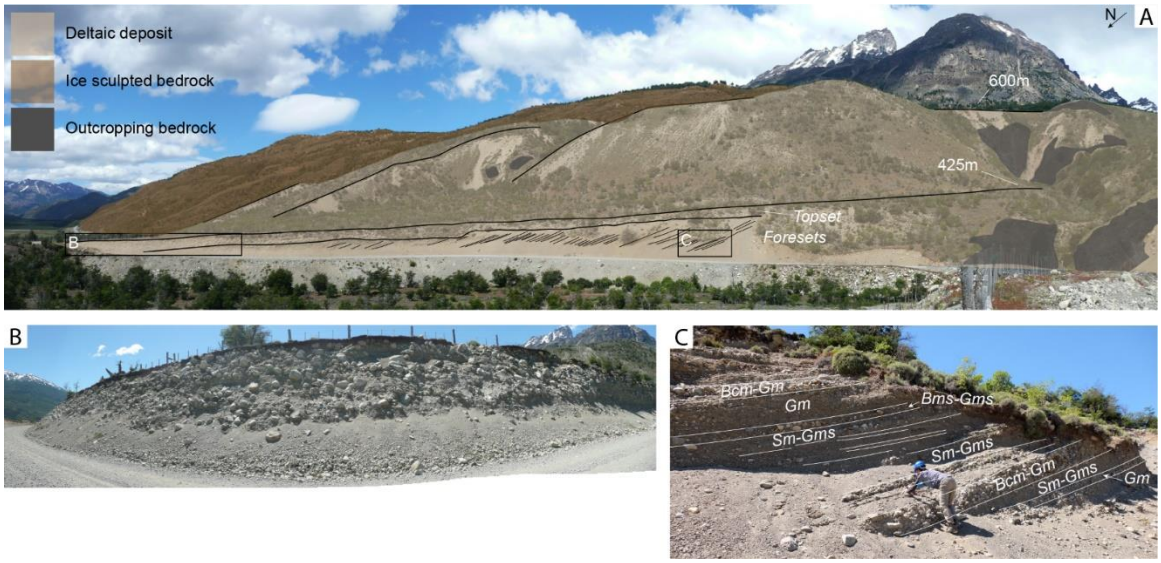

Figure 4.12. (A) 600 m and 425 m stepped terrace on the southern side of the Tranquilo valley with an incised gorge on the right of the image. (B) The northern section of road cutting, composed of clast-supported cobbles. (C) The southern section showing dipping sand and gravel foresets. This is an example of a classic Gilbert form delta.

4.3.4.2. Morainal banks

Next to the steep-sided Esmeralda moraines (M1b) is a distinctly-different moraine landform interpreted as a subaqueous morainal bank (Davies et al., 2018). It is wedge-shaped and dips gently west towards Lago Esmeralda while the eastern flank is much steeper. Exposures show a silty, stone-rich diamictic composition interbedded with sands and gravels (Davies et al., 2018).

4.3.4.3. Glaciolacustrine sediment

Roadside exposures north of Lago Esmeralda show diamicton overtopped by 2 mm thick silt and clay rythmites with isolated stones (Figure 4.3 L1, Figure 4.13A). Similar facies are found on the eastern side of the Salto valley within the broader M7 moraine complex (Figure 4.3 L2, Figure

4.13B). A 3 m high section through the top of a small ridge reveals upward-fining sands overtopped with rhythmites, interbedded with sands at their top, and a stone-rich silty diamicton. The rhythmites contain numerous dropstones with associated deformed and draped laminations. Up a small tributary valley from D2, between two bedrock highs are large roadside exposures of bedded sands and gravels (Figure 4.3 L3). On the western side is 4 m of well-sorted, bedded, fine sand with occasional gravel dropstones and ripple-cross laminations in places (Figure 4.13C). This is separated by a sharp erosional contact from overlying trough cross-bedded, and then massive gravelly sands. These contain inclusions of planar laminated fine sands. On the eastern side of the tributary valley, and *ca* 70 m below the western site, is a 6 m high exposure of well sorted sands with draped ripple cross-laminations and massive sand beds (Figure 4.13D).

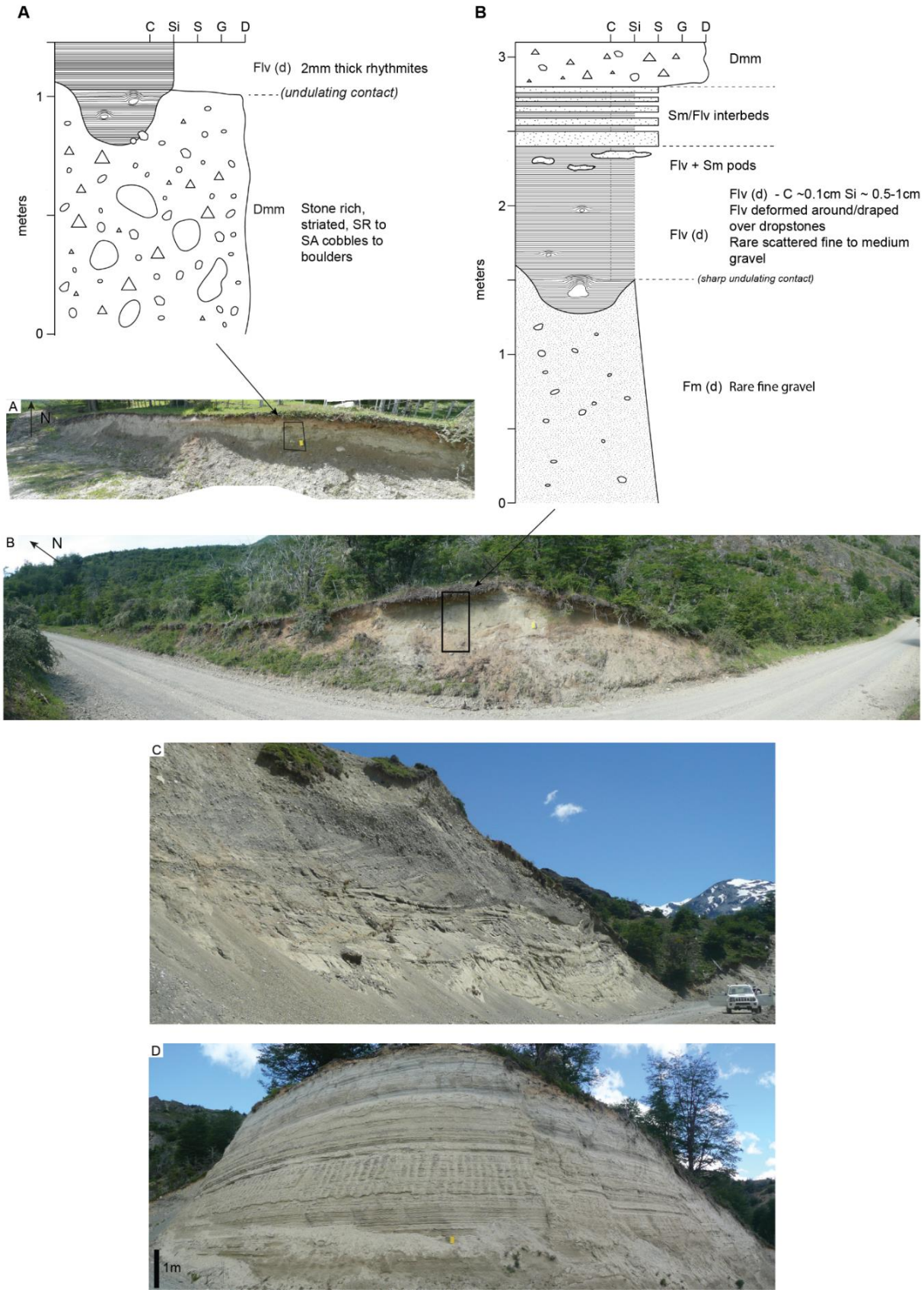

Figure 4.13. (A) L1 section logged through roadside exposure north of Lago Esmeralda. (B) L2 section logged through roadside exposure in Salto valley through part of the M7 moraine complex. (C) L3 western section through roadside exposure of massive sands and gravelly sands. (D) L3 eastern section through roadside exposure through well sorted bedded sands. Sections show examples of variety of glaciolacustrine deposits found across the study region, from rhythmites to massive sands.

4.3.4.4. Palaeoshorelines

Inside the Esmeralda moraines, palaeoshorelines are carved into valley-side diamicton in the northern Salto valley on the eastern side of the Juncal Massif, on the southern side of Cerro Ataud and southeast of Lago Esmeralda (Davies et al., 2018). The palaeoshorelines form of gently-dipping platforms with scarp slopes on the valley floor side, running flat or shallowly-dipping in long profile.

4.3.5. Glaciofluvial associations

4.3.5.1. Outwash plains

A palaeo-outwash plain of glaciofluvial sands and gravels is located east of the M1b moraines sloping gently down towards and terminating at Lago Brown (Figure 4.2). The surface is covered by cross-cutting sinuous palaeochannels. Narrow valley constrained outwash, or 'valley trains', cover the entire floor of the southern section of the Pedregoso valley and contain active braided river channels.

4.3.5.2. Fluvial terraces

Stepped, fluvial terraces are found at the eastern end of the Tranquilo valley, either side of Rio Tranquilo (Figure 4.2). The western terraces run for 1.6 km along the valley side on two levels, separated by a small scarp slope. The upper terrace slopes from 470 m to 415 m asl and the lower terraces slope from 450 m to 405 m asl, grading down to the valley floor level at their northern-most point. The two eastern terraces are adjacent to the ice-contact slope and grade south to the valley floor, with large scarp slopes on the northern sides.

4.3.5.3. Kame terraces

Along the eastern side of the Salto valley, masses of sediment with flat tops at *ca* 370 m asl run discontinuously south to the confluence with the Río Tranquilo valley (Figure 4.2). The top surface slopes gently away from the valley side before a steep break in slope forms a scarp down to the valley floor. The terrace surfaces are 40 m above the valley floor, gently undulating and

dissected by channels from the valley side. They contain hollows in places, some manifesting as lakes, producing kame and kettle topography (cf. Livingstone et al., 2010). The largest terrace is 3.9 km long and up to 550 m wide, located just north of the confluence with the Tranquilo valley, and found in association with moraine ridge M9 (Figure 4.4E). At the opening on the Salto valley, an exposure at the terrace base shows cross-bedded alternating coarse sands and gravels, dipping 20° southwest towards the valley floor, fining upwards in places (Figure 4.14). Pebbles are faceted and edge-rounded and can be found in lags at the base of beds. These alternating sand and gravel beds are topped by gravel lenses and broad, shallow scours of trough cross-bedded gravels and sands.

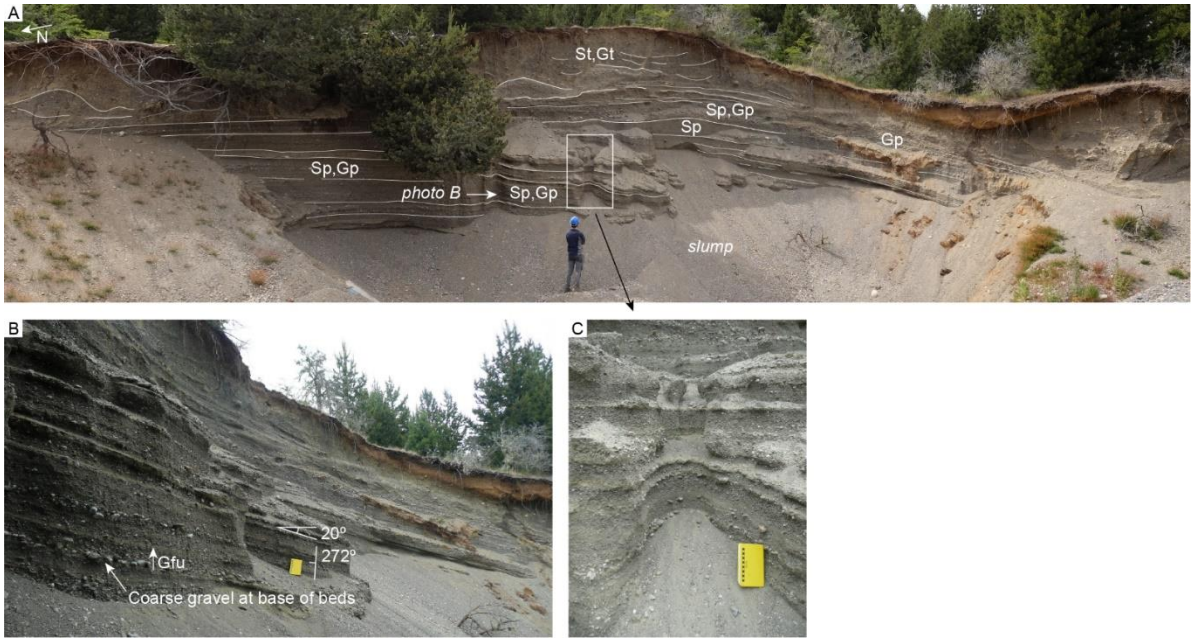

Figure 4.14. Section exposing the sedimentary composition and structure at the base of a kame terrace on the eastern side of the opening of the Salto valley, south of Lago Esmeralda. (A) Overview of the section. (B) Photo taken looking left to right illustrating the dipping sand and gravel beds. (C) Close-up photo of dipping interbedded sands and gravels.

4.3.5.4. Boulder bar

Inset of the terminal Salto moraine complex is an elongated, 360 m long by 160 m wide bar of morainic material (Figure 4.2, Figure 4.15C), topped by sporadic boulders on its surface. Its elongated, tapered form is analogous to boulder bars observed in valleys to the north, formed by large outburst floods of Lago GCBA likely reworking valley floor morainic material (Thorndycraft et al., 2019).

4.3.5.5. Fluvial bars and palaeochannels

Both mid-channel, bank-attached and point bars are found as part of the active Rio Tranquilo, Pedregoso and Salto glaciofluvial systems (cf. Collinson, 1996). Palaeobars are found on the floodplain bordering these rivers and in conjunction with glaciofluvial palaeochannels (Figure 4.15).

4.3.6. Paraglacial associations

4.3.6.1. Floodplain

The floors of the Salto and Tranquilo valleys are covered by floodplain associated with sand and gravel bar deposits. This differs from the morphology of the outwash plain east of the M1b Brown moraines, which is built up above the level of the valley floor. Numerous abandoned river-channels are found across the valley floor throughout the Salto and Tranquilo valleys and within the floodplain are a number of small lakes infilling pits (Figure 4.15) (cf. Benn and Evans, 2010; Brynjólfsson, 2015; Giles et al., 2017).

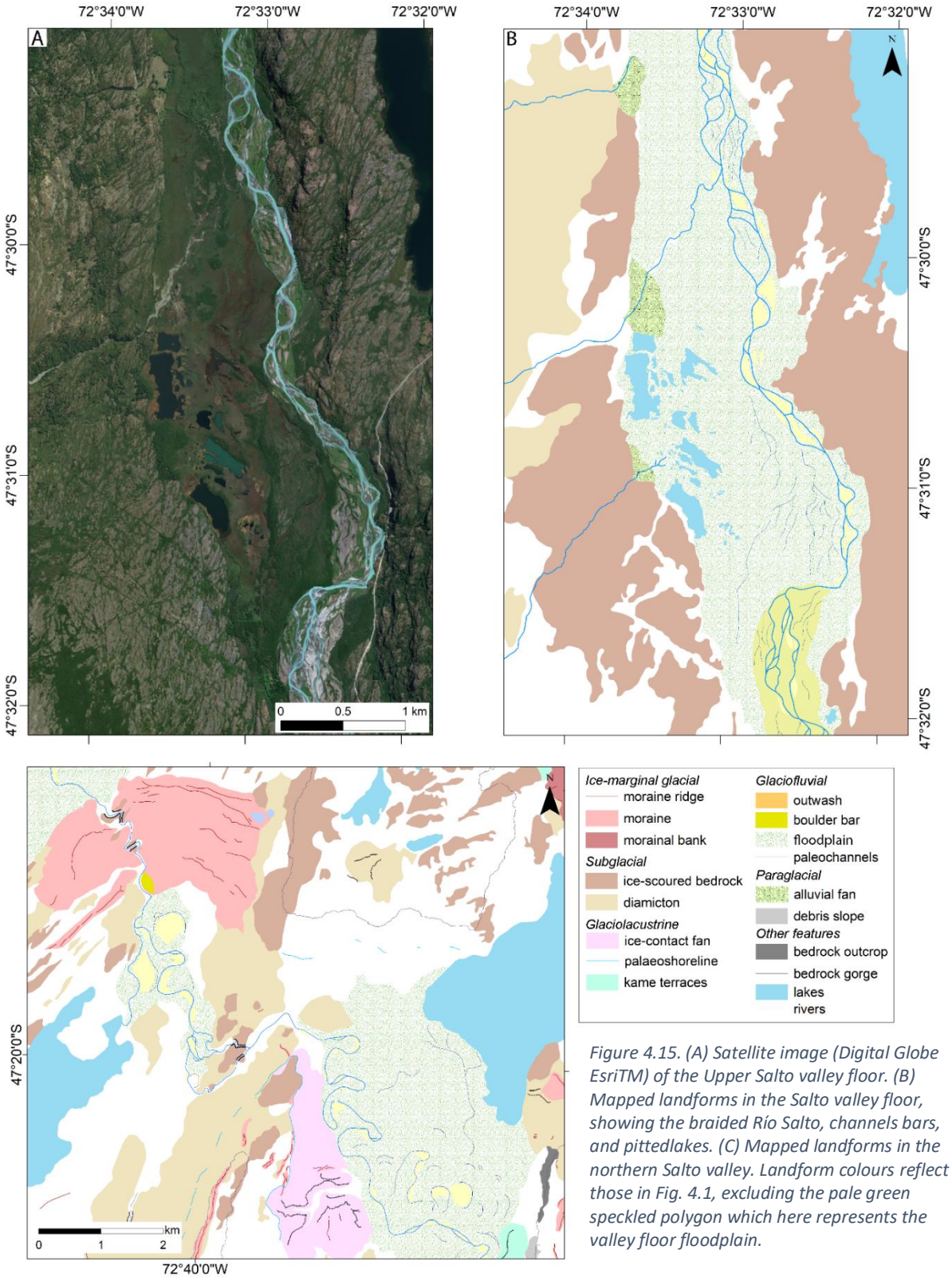

Figure 4.15. (A) Satellite image (Digital Globe EsriTM) of the Upper Salto valley floor. (B) Mapped landforms in the Salto valley floor, showing the braided Río Salto, channels bars, and pittedlakes. (C) Mapped landforms in the northern Salto valley. Landform colours reflect those in Fig. 4.1, excluding the pale green speckled polygon which here represents the valley floor floodplain.

4.3.6.2. Slope deposits

Unvegetated, modified drift-mantled slopes are found at the sides of the most recently deglaciated (post-LIA) valleys. They comprise upper sections of gullies cut into glaciogenic deposits (including lateral-moraine ridges), above coalescing debris cones and fans of reworked sediment (cf. Curry, 1999; Ballantyne, 2002; Curry et al., 2006). The clearest example is on the northern and southern valley sides above Lago Calluqueo. We also find examples of paraglacial rock-slope failure. These are primarily talus accumulations high on the valley sides comprising angular boulders up to 15 m in size.

4.3.6.3. Alluvial fans

Alluvial fans are found at the opening of gullies at the sides of the Pedregoso and Tranquilo valleys, where the valley side meets the valley floor floodplain. They slope gently between 2° and 10°, are well vegetated, and often associated with active river systems and fluvial downcutting.

4.4. Discussion

The observed geomorphology and sedimentology of the Salto, Pedregoso, Tranquilo and surrounding high-altitude valleys allows us to produce landsystem models which operated during and following a period of late Quaternary warming. The region can be divided into distinctive areas whose core sediment-landforms associations are characterised by either glaciolacustrine, land-terminating glacial or mountain-valley landsystems. These are then overprinted by both glaciofluvial and paraglacial landsystems, with varying degrees of modification of the glaciated landscape. These palimpsest environments can be thought of as existing within an overarching glaciated valley landsystem acting as a ‘family of landsystems’, documenting significant variability (Benn et al., 2003).

4.4.1. Landsystems north of Monte San Loreno

4.4.1.1. Glaciolacustrine landsystem

The glaciolacustrine sediment-landform associations of the Tranquilo valley consist of raised stepped deltas and glaciolacustrine sand and sandy gravel deposits. Deltas have the classic Gilbert form (Gilbert, 1885), deposited into a former ice-dammed lake (Ashley, 2002; Longhitano, 2008; Benn and Evans, 2010), and are analogous to those found around the margins of Lago GCBA (Bell, 2008, 2009; Glasser et al., 2009a; Bendle et al., 2017) and in the Torres del Paine region of Patagonia (García et al., 2014). Similar Gilbert form deltas are also found outside Patagonia, in the Thompson valley in British Columbia (Johnsen and Brennand, 2004, 2006) and at Glen Roy (Peacock, 1986; Palmer and Lowe, 2017; Sissons, 2017), the northern Cairngorms (Brazier et al., 1998) and Achnasheen, Scotland (Benn, 1989, 1992). Alongside the glaciolacustrine sediments, they provide evidence for the palaeolake Tranquilo occupying the Tranquilo valley at 520 m asl and then 425 m asl following punctuated lake drainage (Figure 8.1; Chapter 8).

The D1 delta terrace (Figure 4.3, Figure 4.12A) at 600 m asl likely reflects a higher elevation ice-marginal lake formed when ice occupied the Tranquilo valley, damming valley side tributaries. Further, such higher elevation terrace surfaces are found in neighbouring small tributary valleys. Deltas at D3 and D4 and bedded sands south of D2 indicate that when the lake level was at 520 m asl the frontal ice-margin sat between D2 and D3 and the confluence with the Salto valley for a period of relative stability or slow recession to allow for such masses of sediment to accumulate (Figure 8.1C; Chapter 8). The bedded sands at L3 likely formed through relatively low-energy deposition of well-sorted sediment into the lake. The draped ripple-cross laminations indicates a high rate of sediment aggradation relative to horizontal transport and flow (Evans and Benn, 2004). The formation of these deltas is reliant on both the presence of the large water body and local topography channelling rivers and fluvially-transported sediment from the mountain valley catchments through tributary valleys and gullies into the main valley. A topographic control is also evident through the absence of deltas in the northern Salto valley glaciolacustrine landsystem which lacks sediment input from tributary valleys.

The Brown moraines in the east sit on a topographic high with ridges up to *ca* 535 m asl and a glacial outflow channel at *ca* 520 m asl dissecting these ridges. An outwash plain east of the Brown moraines is incised by the large primary glacial outflow channel and multiple glaciofluvial braided palaeochannels. This provides evidence for a 520 m asl col at the Brown moraines for the upper, 520 m asl palaeolake Tranquilo lake level and drainage to the east into Lago Brown and on into Lago CP (Figure 8.1C; Chapter 8). With the Tranquilo valley floor dropping in elevation to the west, the lake was dammed by ice flowing north from the Pedregoso valley into the Tranquilo valley, having receded from its frontal position at the Brown moraines (Figure 8.1B and C; Chapter 8). Both topography and the location of the ice mass therefore controls the extent and depth of the lake.

There is a notable absence of cross-valley ridges in the Tranquilo valley which could be due to a number of factors. Benn (1989) elucidates a requirement of grounding line stability for the formation of ridges at Achnasheen in Scotland. Subaerial cross-valley ridges formed in the neighbouring Salto valley during this same period suggest that periodic local ice stability did occur. Therefore the calving of ice into palaeolake Tranquilo may have caused the instability of the ice front and its steady continuous retreat (cf. Carrivick and Tweed, 2013).

Following ice recession a lower elevation drainage pathway, and potentially subglacial drainage indicated by a bedrock incised channel, opened into the Salto valley at the Tranquilo-Salto confluence and the lake stabilised at 425 m asl (Figure 8.1D; Chapter 8). This punctuated drainage and later final drainage of palaeolake Tranquilo may have resulted in outburst floods down the Salto valley. Evidence for large flood events may be provided by the aforementioned inset boulder bar of the Salto moraine complex, and bedrock incision in the lowermost reach of the Rio Tranquilo and in the middle of the Salto moraines, downstream of the Lago Esmeralda reach (Figure 4.15C). The boulder bar and bedrock incision are consistent with flood evidence in the Baker valley (Thorndycraft et al., 2019).

Davies et al. (2018) present a glaciolacustrine landsystem model for the northern Salto valley to document the formation of the asymmetric Esmeralda moraine ridge and bank, and Juncal fan as part of a landform assemblage formed as ice terminated into Lago Chelenko palaeolake and subsequently receded to the more steeply topographically constrained section of the Salto valley south of the present-day Lago Esmeralda. Subaerial and subaqueous moraines, subaqueous fans and constant-altitude palaeoshorelines are all found in conjunction.

Silt and clay rhythmites north of Lago Esmeralda (Figure 4.3 L1, Figure 4.13A) are typical of ice-distal glaciolacustrine sediments deposited in proglacial lakes, sourced from underflows from the ice front, accompanied by the periodic deposition of ice rafted debris (Church and Gilbert, 1975; Smith and Ashley, 1985; Palmer et al., 2008; Sugiyama et al., 2016). We interpret those exposed at L1 to have formed in this way, in Palaeolake Chelenko following ice recession. Those at L2 likely formed in a short-lived ice-contact proglacial lake following ice recession up the Salto valley, dammed by the large M7 moraine ridge. Coarsening to the top of the section into interbedded sands and a diamicton cap is suggestive of a minor readvance, however could also be the product of increased meltwater input and sediment capacity during the onset of further ice recession.

4.4.1.2. Land-terminating glacial landsystem

The main landform components of the Salto valley are the cross-valley terminal moraine ridges (M6-M9). (Figure 4.4C-E). Due to their substantial size, sharp-crested form and absence of internal deformation structures, we interpret these as dump moraines, formed at the glacier's terminus by the remobilisation of supraglacial debris by roll, fall or glaciofluvial transport during periods of glacier stillstand (Boulton and Eyles, 1979; Benn and Owen, 2002; Benn and Evans, 2010) as ice receded up the Salto valley. Their association with kame terraces and stratified gravel and sand and diamictic composition (e.g., M8, Figure 4.6) indicate significant sediment transport and deposition by meltwater at the glacier margins. RA-C_{40} and RWR-C_{40} covariance clast data at moraine sites throughout the Salto valley (Figure 4.3) suggest glaciofluvial input and

reworking within the subglacial transport system (Lukas et al., 2013). This evidence for significant meltwater is characteristic of a temperate glacial setting. The shallow bed gradient of the Salto valley provides a setting in which an extensive, gently-sloping glacier would be sensitive to small changes in climate and ELA, leading to the formation of multiple cross valley moraine ridges due to numerous small ice margin fluctuations during overall recession. The lack of cross valley moraines in the Pedregoso valley could be the product of an ice mass less responsive to minor climate fluctuations having now receded into a more steeply-sloping valley (Barr and Lovell, 2014). We interpret M11 and M12 as having formed at minor glacier stillstands during glacier recession. Their location, confined to bedrock plateaus on the valley side, suggest that their formation had an element of topographic control.

Significant meltwater input from the glacier terminus proximal to the moraine ridges and from the surrounding catchment, likely contributed to the partial erosion of the M6-M9 moraine ridges. Increased river flow and migration during ice recession up valley would have been significant and, alongside any glacier lake outburst floods, exploited and widened any opening between the ridge and western valley-side. The valley floor is covered by a floodplain, containing a series of kettle-hole lakes, indicating breakoff of ice from the glacier tongue and subsequent burial by glacial outwash.

The exposure of diamicton at S2 is interpreted as subglacial till (Benn and Evans, 2010) with a combination of homogenised material and stratified sediments deposited by water. The presence of water deposited sands and gravels and lack of widespread deformation suggests water flow at the ice-bed interface and ice-bed decoupling (Eyles et al., 1983; Piotrowski and Tulaczyk, 1999; Phillips et al., 2013, 2018). We interpret the two massive gravel features as burst out and simple clastic dyke fluid escape structures, indicating high levels of subglacial water pressure.

4.4.1.3. Mountain-valley landsystem

The upland valley landsystem in the study area is characterised by a landform assemblage of cirques, saw-tooth moraines, closely-spaced cross-valley moraines, flutes on the valley floor and talus slopes on the surrounding steep valley-sides; the product of recent deglaciation. The closely-spaced moraine ridges are interpreted as push moraines formed during frequent minor readvances or stillstands (cf. Evans et al., 1999, 2018). The larger saw-tooth terminal moraines formed as a result of a more sustained readvance. As ice opens into a less well constrained valley section, radial crevasses form in the glacier tongue resulting in a saw-toothed shaped ice front and moraine ridges with distinctive tooth and notch pairings upon the push up of glacially-reworked material (Matthews et al., 1979; Burki et al., 2009).

Cirques and headwalls with over-deepenings formed by erosion at the base of the glacier through freeze-thaw weathering and plucking (Hooke, 1991) indicating warm-based ice as well as abundant meltwater (Glasser and Bennett, 2004). Flutes are a product of subglacial sediment deformation, forming ridges running parallel to the direction of ice flow under temperate conditions (Boulton, 1976; Gordon et al., 1992; Benn and Evans, 2010). It is to be expected that flutes and small valley-bottom recessional moraine ridges are most commonly found in areas proximal to present-day ice fronts (Benn, 1995; Evans and Twigg, 2002) due to their poor preservation potential (Benn and Evans, 2010). Closely-spaced moraines superimposed on these subglacial bedforms indicate both numerous oscillations of the frontal ice margin and an exposed valley bed not subsequently covered by debris, both indicative of a 'clean' valley glacier (Eyles, 1979; Benn and Evans, 2010).

Unlike in the lower valleys, the glaciofluvial component to the landsystem has a minor impact, manifesting as only narrow single channels, dissecting the cross-valley and saw-tooth moraines in places. The sediment transport pathway is short, with subglacial material sourced from the headwall and cirque bed, and paraglacial processes creating talus slopes bringing material into the valley bottom from the valley sides. At what was once the glacier's terminus, clast roundness data collected from the M13 moraine showed 0 % rounded or well-rounded clasts, reflecting the

short transport pathway. A low percentage of angular and very angular clasts however does indicate sediment reworking from glacial meltwater, further illustrating the glacier's temperate thermal regime. Similar cirque architectures are seen on the Isle of Skye at the Coire Lagan formed during the Younger Dryas (Benn and Evans, 2010), as well as in front of present-day, actively-receding glaciers such as at Maradalsbreen, Norway (Benn et al., 2003) and Charquini Sur, Bolivia (Malecki et al., 2018).

4.4.1.4. Paraglacial landsystem

The paraglacial landsystem is the product of fluvial, flood and slope based processes reshaping the glaciated landscape and can be broken down into a combination of sediment sources, stores, sinks and transport pathways (Ballantyne, 2002). Recently deglaciated and exposed bedrock and drift-mantled slopes in high-altitude valleys and on the slopes above the present-day Calluqueo glacier terminus provide the sediment source for talus slopes and debris cones on the valley sides following rockfall and slope failure. The former are a product of initially large, and later smaller scale rockfalls as part of progressive bedrock adjustment following deglaciation and debutressing (Wyrwoll, 1977; Ballantyne, 2002). Material is glaciofluvially transported and reworked down into the lowland valleys either directly through the main Pedregoso, Salto and Tranquilo river systems or via valley side gullies. At such gullies material manifests as alluvial fans (Figure 4.2, Figure 4.15) forming a secondary sediment store. Material within the primary river systems, and that subsequently reworked from alluvial fans, is redistributed as floodplain valley-fill deposits. The product of this is a floodplain with a braided river system and associated point bar deposits. Meltwater fed rivers with variable annual and seasonal discharge lead to a dynamic migratory river system, producing braiding and abandoned palaeochannels. A lack of subsequently formed river terraces along the Salto valley suggest a maintained sediment supply and balance between sediment input, transport through and redistribution across the valley. There may be slight positive balance in favour of sediment input to counter incision expected as a product of isostatic uplift.

4.4.1.5. Glaciofluvial landsystem

Glaciofluvial process operate at the lateral and frontal ice-margins forming kame terraces and outwash plains in the Salto and Tranquilo valleys respectively in conjunction with the land-terminating glacial landsystem, and as part of the paraglacial landsystem following deglaciation as in section 4.4.1.4. Glaciofluvial processes dominate the proglacial environment forming braided valley trains in sparsely vegetated, non-cohesive material; a product of high bedloads and fluctuations in glacially fed discharge (Miall, 1992; Marren, 2005). Such a feature is found in the southern reach of the Pedregoso valley at the outflow of Lago Calluqueo a steep gradient of 6 to 7 m km^{-1}, typical of braided systems (Benn and Evans, 2010). In the more gently sloping Salto and Tranquilo valleys (1.5 to 2 m km^{-1}), through to the northern reach of the Salto valley adjacent to Lago Esmeralda, the river transitions from a braided system to an increasingly sinuous main river channel with channel bars, islands and occasional subsidiary channels. Finally the Rio Salto establishes a meandering fluvial landsystem with point bars, palaeochannels and palaeobars in a wider floodplain (Figure 4.15C) (Miall, 1985).

4.4.2. Temperate Patagonian glacier systems during Late Quaternary deglaciation

Most landsystem studies of contemporary glaciers come from terrestrial-terminating, and topographically-unconstrained, piedmont glacier and ice-lobe settings (Bentley, 1996; Andersen et al., 1999; Schlüchter et al., 1999; Glasser et al., 2009b) so are not appropriate analogues for the type of mountain icefield landsystems encountered in Patagonia. Furthermore, many formerly glaciated valleys in Patagonia are forested and inaccessible. Therefore, the detailed Late Quaternary landsystem of MSL afforded by good availability of sections, provides an important new geomorphological dataset to help understand the dynamics of temperate Patagonian glacier response to warming climate. In particular our geomorphological and sedimentological data will be relevant for understanding the smaller ice caps located in the cordillera (72-73°W) to the east of the Patagonian Icefields (e.g., Araos et al., 2018; Sagredo et al., 2018). These smaller ice-caps have important implications for understanding palaeoclimate

(Sagredo et al., 2018) given their position in the Andean rain-shadow. Furthermore, they potentially play a role in controlling regional drainage as demonstrated in the Baker valley through the separation of MSL and NPI ice (Thorndycraft et al., 2019).

Our sediment-landform data from MSL demonstrate that the regional glacial geomorphology conforms to the concept of a mountain icefield landsystem (Benn and Evans, 2010). The diverse topography and climatic settings of MSL result in a broad landsystem encompassing elements of multiple smaller-scale landsystems. Benn et al. (2003) discuss the spatial and temporal changes in glacial landsystems at the Ben Ohau Range in New Zealand, citing long term climate change as the key driver of spatial and temporal landsystem evolution. Similarly, in central Patagonia, atmospheric warming at the end of the ACR caused regional ice recession, and the subsequent drainage of Lago Chelenko to the Pacific (Thorndycraft et al., 2019) and Lago Tranquilo into the Salto valley, changing the terminal ice environment from lacustrine to terrestrial. The glaciolacustrine dynamics of Lago Tranquilo, and in particular the drainage reversal, highlight the important role of topography in local to regional scale landscape change. Across Patagonia, Thorndycraft et al. (2019) hypothesise that although the broad pattern of ice recession may be similar, driven by Southern Hemisphere palaeoclimate, the timing of palaeolake drainage events is diachronous due to regional topographic settings.

Understanding the spatial and temporal glaciolacustrine dynamics of Patagonian glaciers provides insights for the interpretation of the Late Quaternary landform record. As an illustrative example from this study, the only fluvial terraces in the study area are at the upstream end of the former 425 m asl Lago Tranquilo lake level. Repeat satellite-derived valley floor DEMs from the Cachet II ice-dammed lake (Colonia valley, NPI) provide a modern analogue that demonstrates valley floor incision and upstream enlargement of the lake during successive lake drainage-refill events (Jacquet et al., 2017). Using this analogue for palaeolake Tranquilo, we interpret that the formation of the Tranquilo terraces were caused by base-level fall from palaeolake drainage rather than regional tectonic (Guillaume et al., 2013) or isostatic uplift

(Thorndycraft et al., 2019). Our study therefore demonstrates the need for a detailed, holistic approach to the elucidation of glacier, lakes and topographic interactions.

4.5. Conclusions

We have used detailed geomorphological mapping and sedimentology to describe the landforms and sediments found in valleys directly north of MSL in Chilean Patagonia.

- The primary landforms identified in the study area are lateral and terminal moraine ridges, ice-scoured bedrock, cirques and headwalls, flutes, deltas, ice-contact fans, glaciolacustrine deposits, palaeoshorelines, kame terraces and outwash and floodplains. These form ice-marginal, subglacial, glaciolacustrine, glaciofluvial and paraglacial sediment-landform associations, from which we infer a range of glacial and paraglacial processes which led to their formation through the Late Pleistocene and Holocene.
- We have identified 7 new moraine sets and ground-truthed and extended the spatial extent of a further 7 through extensive field mapping. This highlights the limitations of identifying and mapping ice margins from satellite imagery alone and in the absence of high-resolution LiDAR DEMs. It is clear that when possible geomorphological field mapping is required to comprehensively identify ice-marginal glacial landforms.
- Our study reveals glaciolacustrine, land-terminating glacial, mountain valley and paraglacial landsystems within the same valley systems, evolving and transitioning during deglaciation. We identify and constrain for the first time an ice-dammed palaeolake Tranquilo which occupied the Tranquilo valley following recession of ice from the Brown moraines.
- For the period of warming after the ACR we have identified three key controls on sediment-landform associations and landsystem development. Firstly this study region illustrates how climate provides a broad-scale control by both dictating the temperate thermal regime of the glacier and the subglacial bedforms created and by causing overall ice recession. As ice recedes, ice-dammed lake drainage pathways open and frontal

margins move to higher elevations, transitioning through landsystems as they do so. Secondly, ice-dammed lakes provide a control on glacier frontal stability and in turn ice-marginal landform formation. Finally, topography operates as a control on both a local scale determining the location of sediment supply, and regionally in combination with ice masses to control the extent and level of ice dammed lakes. Landsystem development in this instance is not dependent on tectonics or isostatic adjustment.

5. Glacier chronology and post-ACR recession

5.1. Introduction

5.1.1. Rationale

Patagonia has experienced complex changes in climate, glacier dynamics and landsystems following the LGM (Chapter 2.1.3). A stepwise reconstruction of the deglaciation of the Patagonian icefields since the LGM (Davies et al. submitted) has been made possible through the widespread collection of chronological and geomorphological data from around the icefields, however a lack of detailed sequences of dated moraines from single valleys has meant data on rates of glacier recession, for example in response to past rapid climate change, is limited. In the Salto valley draining the MSL ice cap, two newly dated moraines (M9 and M12, Chapter 4) combined with the M4 moraine dated by Glasser et al., (2012) and M1a moraine dated by Davies et al., (2018) (Figure 5.1) provides the opportunity to better constrain the spatial and temporal reconstruction of the deglaciation, and landsystem evolution, of the northern MSL ice cap and the opportunity for understanding the rate of ice recession at Calluqueo glacier during a period of climate warming following the ACR. This provides the geomorphic framework to constrain the output of numerical glacier models (Mackintosh et al., 2017), which can then be used to better understand the mass balance sensitivities to the variable palaeoclimate conditions that drove past Calluqueo glacier advance and recession (Chapters 6 and 7).

5.1.2. Research questions, aims and objectives

To help address current gaps in understanding, this chapter aims to answer the following two key research questions within **RQ 2** of this thesis: **1) At what time were moraine ridges within the Salto and Pedregoso valleys deposited? 2) What was the style and rate of retreat at Calluqueo glacier during warming following the ACR?** The aim of the work presented in this chapter, addressing **Aim 1** of this thesis, is to quantify the timing and rate of recession of ice discharging north from MSL following the ACR. This is done through **Obj. 2** of this thesis, dating the formation of glacier margins using cosmogenic nuclide surface exposure dating of glacially transported boulders. This chapter builds on the geomorphological evidence presented in *Chapter 4*. Seven ice margins were identified in the Salto and Pedregoso valleys, comprising single or multiple distinct moraine ridges, complimenting the seven previously identified ice limits (Glasser et al., 2005, 2009, 2012; Turner et al., 2005; Araya et al., 2014; Bendle et al., 2017; Davies et al., 2018). Two of these newly identified limits (M9 and M12) were found to have boulders that met the necessary position, size and compositional requirements for surface

exposure dating (section 3.4.2). This chapter presents these new dates to compliment previously published chronological data from the Esmeralda moraines and Moraine Mounds in the northern Salto valley (Glasser et al., 2012; Davies et al., 2018). In Section 5.3, sample details and locations are presented, before an analysis of ages using kernel plots and a reduced chi-squared test in section 5.5.2. In Section 5.5.3 these new and previously published dates are combined with geomorphological information and applied to a Bayesian model. In section 5.5.4 the output of this Bayesian model is used to robustly constrain a chronology of glacier recession following the ACR.

5.2. Review of existing work

Existing chronological data from sites north of MSL are shown on Figure 5.1 and selected regional surface exposure data in Table 5.2. The sequence of primary moraine ridge complexes of interest to this study are labelled M1 to M13. In existing literature, M1a is referred to as the Esmeralda moraines (Davies et al., 2018), M1b as the Brown moraines, M1c as the Salto moraines (Davies et al., 2018) and M4 as the Moraine Mounds (Glasser et al., 2012). 'M' notation is used to maintain consistent notation with the other moraines of interest. The chronological data in Figure 5.1 have been obtained through cosmogenic nuclide surface exposure dating of glacial transported boulders, dated tephra deposits and radiocarbon ages of organics. Ages are recalibrated as per protocols outlined in section 5.4. Glacially transported boulders on the ridges of M1a in the northern Salto valley have been dated to the ACR, marking the largest readvance in central Patagonia since the LGM (Davies et al., 2018). Five boulders on M1a moraine give a UWM age of 13.4 ± 0.2 ka, providing an approximate age for moraine formation. Three boulders on the M1c moraine have been dated, two situated below the 350 m asl palaeolake shoreline at 349 m asl and 338 m asl and one above at 359 m asl. Those below the shoreline have been dated to 12.6 ± 0.4 ka and 12.5 ± 0.5 ka giving an approximate age for lake drainage (Thorndycraft et al., 2019). The boulder located above the shoreline, dated to 12.9 ± 0.5 ka, provides an approximate age for moraine formation. Two further boulders on M4 at the opening of the Salto valley give an UWM age of 12.7 ± 0.4 ka (Glasser et al., 2012) marking a frontal ice margin following ice recession from the ACR position. Prominent moraine complexes RT1 to RT4 in the Upper Tranquilo valley have also been dated to the ACR period (Sagredo et al., 2018). RT1 (UWM 13.8 ± 0.5 ka) marks the maximum ACR readvance of Tranquilo glacier. RT4 (UWM 13.6 ± 0.3 ka), although statistically indistinguishable from RT1 by age, morphostratigraphically marks the end of the ACR moraine sequence in the Upper Tranquilo valley (Sagredo et al., 2018). Overall recession of Tranquilo glacier following the ACR was punctuated by minor stability and readvance in the early Holocene (RT5 UWM 12.1 ± 0.5 ka) and mid Holocene (RT6 UWM 5.6 ± 0.1 ka).

Organic deposits taken from a road cutting and bog cores in the Upper Tranquilo, Tranquilo and Pedregoso valleys have been radiocarbon dated with the oldest ages at these sites dating from 8.5 to 5.8 ka (Gardeweg and Sellés, 2013; Stern et al., 2016) (Figure 5.1). The early to mid-Holocene H1 and MEN1 tephra are also found at these sites, however their eruption dates are poorly refined, with statistically significant discrepancies between those derived from lake cores and those derived from surface deposits (Stern et al., 2016). These radiocarbon ages and tephra deposits provide a minimum date by which ice had receded past the respective sites, including back into the Pedregoso valley by at least 8.5 ka. The present study adds to the existing chronological dataset, through cosmogenic dating of moraine limits M9 and M12 (Figure 5.1) specifically to refine the timing and rate of recession of ice from Calluqueo glacier up the upper Salto and Pedregoso valleys during post-ACR warming.

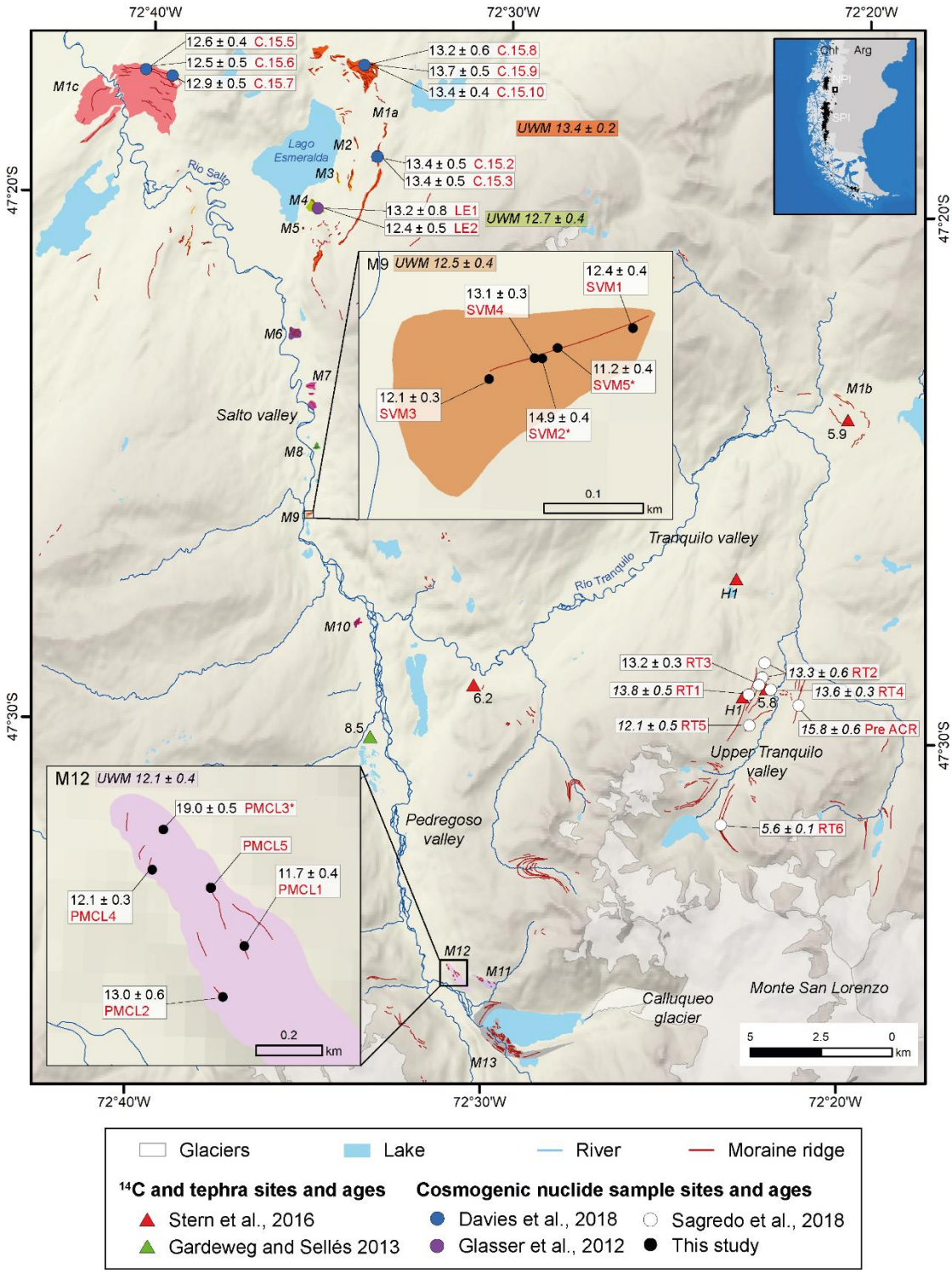

Figure 5.1. Map of the study area north of the MSL icecap including chronological data sites from this study and the published literature. Moraines are coloured differently to aid distinction between the different 'M' moraine sets.

5.3. Site selection criteria, location and description

The Salto and Pedregoso valleys contain regularly spaced frontal and lateral moraines (*Chapter 4*; Martin et al., 2019), which when dated, can provide a valuable opportunity to study glacial retreat. Moraines to be dated were selected to fill in chronological gaps in the sequence of ice recession in the Salto and Pedregoso valleys. To compliment previously dated sites in the lower

Salto valley, this study identifies boulders on moraine ridges suitable for surface exposure dating at two further sites (M9 and M12, Figure 5.1), to quantify the rate of recession during post-ACR climate warming. M9 was selected as it marks a frontal ice-margin position between M4 and the opening to the Tranquilo valley. Direct ice-margin dating is absent in this part of the upper Salto valley, so constraining the age of formation of M9 fills in a valuable chronological reference point in this part of the ice's overall recession. M9 is a 380m long, 30m high steep-crested, frontal moraine ridge extending from a kame terrace at the eastern side of the Salto valley *ca* 24 km down-valley of the current Calluqueo frontal ice margin (Figure 5.1). The moraine ridge from 365m to 375 m asl is the southernmost of a series of 4 similar cross valley ridges located over a distance of 6.5 km in a reach between the confluence with the Tranquilo valley in the south, and the opening of the valley to Lago Esmeralda in the north. Like the other 3 ridges, this moraine only extends part way across the valley floor, with a 250 m gap through which runs the Rio Salto between the western end of the ridge and the western side of the valley. Five boulders were sampled, given sample IDs SVM1 to SVM5 (Table 5.1, Figure 5.1 and Figure 5.2).

Figure 5.2. Representative photos of boulders sampled at M9. They are faceted and securely placed on the moraine ridge, indicating likely subglacial transport and ample surface erosion, as well as being less likely to have undergone post-depositional movement.

The second sample site at M12 is a lateral moraine complex located at the upper end of the Pedregoso valley, with ridges running *ca* south east along the eastern valley side, 200 m above the Rio Pedregoso and immediately down-valley of the Calluqueo glacier proglacial lake (Figure 5.1). This moraine complex was selected for surface exposure dating as it marks the lateral ice margin position of Calluqueo glacier in the Pedregoso valley, giving a terminal position south of the Salto-Tranquilo river confluence. Dating this margin therefore further constrains a terminal ice position where data is currently absent, as well as dating a reduction in ice thickness to this point on the valley side. It consists of eight parallel, laterally-discontinuous ridges 50 to 150 m in length with broadly equally-dipping sides located on a topographically-flat bedrock plateau at *ca* 580 m asl. Five boulders were sampled, named PMCL1 to PMCL5 (Table 5.1, Figure 5.1 and Figure 5.3). Analysis of sample PMCL5 failed due to insufficient quartz content and therefore is not reported.

Figure 5.3. Representative photos of boulders sampled at M12.

Table 5.1. Properties and description of boulders sampled for cosmogenic nuclide surface exposure dating at the Salto valley moraine and Pedregoso moraine complex.

Location	Sample ID	Lithology	Boulder description	Dimensions (length x width x height m)	Significance	Date sampled
M9	SVM1	Granite	Faceted (6 faces) pitted up to 3mm, well embedded, no rolling or rotation. Minor exfoliation. No jointing or cracks.	1.65 x 2.39 x 0.7	Dates terminal position of Calluqueo glacier during overall period of ice recession	09/12/2016
	SVM2	Granite	Faceted (5 faces), pitting up to 2mm, well embedded, no rolling or rotation. Small fracture on underside.	1.11 x 1.09 x 0.41	Replicate sample	09/12/2016
	SVM3	Granite	Faceted (6 faces), pitting 1-2mm, isolated pits up to 1cm. 2cm exfoliated layer running across top surface. Otherwise smooth surface, no exfoliation or flakes. No rolling or rotation.	1.23 x 0.95 x 0.7	Replicate sample	09/12/2016
	SVM4	Granite	Faceted (6 faces), pitted up to 3mm. No exfoliation. Well embedded, approximately 50% exposed.	1.97 x 1.44 x 0.87	Replicate sample	09/12/2016
	SVM5	Granite	Faceted (5 faces), pitting 1-2mm. Minor exfoliation	1.33 x 1.22 x 0.58	Replicate sample	09/12/2016
M12	PMCL1	Granodiorite	Faceted (5 visible faces), pitting 1-2mm, fractures 2cm deep, exfoliation on upper side, 0.5cm protruding quartz vein	1.11 x 1.09 x 0.41	Dates lateral position of Calluqueo glacier during overall period of ice recession	11/12/2016
	PMCL2	Granodiorite	Facetted, (6 visible faces), 'bullet' shape. Pitting up to 1cm, little exfoliation, no flakes	1.24 x 0.97 x 1.05	Replicate sample	11/12/2016
	PMCL3	Granite	Faceted (6 visible faces), 1.5cm pit, 0.5-1cm ridge resistant to erosion, fractures and bowl-like depression preferentially weathered, no flakes. Secure position.	1.88 x 1.54 x 0.78	Replicate sample	11/12/2016
	PMCL4	Granite	Faceted (8 visible faces), up to 2cm pits, protruding quartz ridge 0.5cm. Some exfoliation and jointing. On flat surface, stable, no rotation.	2.30 x 1.75 x 1.39	Replicate sample	11/12/2016
	PMCL5	Granodiorite	Faceted (6 visible faces), sub-rounded, up to 1-2 mm pits, secure position, some exfoliation	1.20 x 0.60 x 0.43	Replicate sample	11/12/2016

5.4. Results

Analytical data and surface exposure ages are presented in Table 5.2. Ages were calculated using the CRONUS-Earth online calculator version 3. Ages referred to in the text were calculated using the regional Patagonian spallation production rate of 3.88 ± 0.15 atoms g^{-1} yr^{-1} from the Kaplan et al., (2011) calibration data set, assumed a 0 mm kyr^{-1} erosion rate and used the LSDn scaling method (Lifton et al., 2014), unless otherwise stated and a rock density of 2.7 g/cm^3. Comparisons of ages calculated using a different criterion are discussed in section 5.5.1.

*Table 5.2. Sample data used to calculate cosmogenic nuclide surface exposure ages and ages calculated using the LSDn scaling method and presented at a 0 mm kyr^{-1} and 1 mm kyr^{-1} erosion rate. *Samples SVM2, SM5 and PMCL3 are excluded from uncertainty weighted mean (UWM) ages based on outlier analysis. See text for details.*

Location	Sample ID	Lat (dd)	Lon (dd)	Elevation (m asl)	Sample thickness (cm)	Shielding	^{10}Be (atoms/g)	Erosion rate (0 mm/kyr)					Erosion rate (1 mm/kyr)				
								^{10}Be LSDn age (yrs)	Internal uncert. (yrs)	External uncert. (yrs)	UWM	± 1σ	^{10}Be LSDn age (yrs)	Internal uncert. (yrs)	External uncert. (yrs)	UWM	± 1σ
M9	SVM1	-47.4329	-72.5868	376	3	0.996948	67290 ± 2112	12449	392	1090			12575	400	1112		
	SVM2*	-47.4332	-72.588	366	4.5	0.996443	80173 ± 2091	14941	391	1282			15120	401	1314		
	SVM3	-47.4334	-72.5887	368	4.5	0.996431	63794 ± 1667	12059	316	1034			12180	323	1055		
	SVM4	-47.4332	-72.5881	366	3	0.996621	70516 ± 1845	13106	344	1124			13240	351	1149		
	SVM5*	-47.4331	-72.5878	362	3	0.996479	59264 ± 1940	11193	367	985	**12.5**	**0.4**	11291	374	1003	**12.7**	**0.4**
M12	PMCL1	-47.5779	-72.5123	600	4	0.98959	76646 ± 2663	11739	409	1042			11852	417	1063		
	PMCL2	-47.5793	-72.5131	575	4.5	0.992224	83048 ± 3945	12950	617	1225			13079	630	1251		
	PMCL3*	-47.5759	-72.5161	528	4.5	0.990063	119019 ± 2936	18963	470	1621			19261	485	1673		
	PMCL4	-47.5748	-72.5157	517	4	0.981709	72580 ± 1744	12059	291	1027	**12.1**	**0.4**	12181	297	1048	**12.3**	**0.4**
Esmeralda latero-terminal moraine (M1a)	C.15.2	-47.3195	-72.5615	512	5	0.9986	81093 ± 2780	13403	461	1188			13548	471	1215		
	C.15.3	-47.3197	-72.5615	508	4	0.9986	81195 ± 2828	13361	467	1187			13505	477	1214		
	C.15.8	-47.2917	-72.5651	365	5	0.9985	69717 ± 3253	13199	618	1243			13337	631	1270		
	C.15.9	-47.2917	-72.5651	365	5	0.9985	72633 ± 2531	13709	479	1218			13854	490	1246		
	C.15.10	-47.2917	-72.5653	368	4	0.9985	71402 ± 2384	13357	447	1179	**13.4**	**0.2**	13501	457	1206	**13.6**	**0.2**
Moraine mounds (M4)	LE1	-47.3370	-72.5880	365	5	1	69800 ± 4400	13181	834	1362			13320	852	1392		
	LE2	-47.3370	-72.5880	365	5	1	65100 ± 2700	12368	515	1133	**12.7**	**0.4**	12492	525	1157	**12.8**	**0.4**

5.4.1. Production rates and scaling factors

To compare ages produced using different calculation criteria, ages were calculated using both a regional Patagonian production rate (Kaplan et al., 2011) as well as a global production rate (Borchers et al., 2016). Calculations assumed both 0 mm kyr^{-1} and 1 mm kyr^{-1} erosion rates, as well as with the St (Lal, 1991; Stone, 2000), Lm (Nishiizumi et al., 1989; Lal, 1991; Stone, 2000) and LSDn (Lifton et al., 2014) scaling methods for further comparison. Figure 5.4 shows that samples calculated with different criteria overlap in age within their internal uncertainties. Within this using a regional Patagonian production rate gives samples ages on average 2.5 % older than those calculated using a global production rate. It is evident that sample elevation impacts the degree to which calculated ages vary between scaling schemes (Figure 5.5A), with the greatest difference in age where the sample elevation differs furthest from *ca* 700 to 800 m asl. Such a variation with elevation is to be expected, given that each scaling scheme uses elevation to produce a local production rate, where changes in atmospheric pressure must be taken into account. Each scaling scheme predicts a characteristic scaling gradient as a function of altitude and latitude (Lifton et al., 2014) leading to these age discrepancies. It can also be seen that the difference in ages when using different scaling schemes, erosion rates and production rates increases with sample age (Figure 5.5B and C) as systematic age differences are exacerbated.

Using a 1 mm yr^{-1} erosion rate gives an older sample age than when no erosion is taken into account. This is because the 1 mm yr^{-1} erosion is compensated for as such erosion of the rock surface would remove the top layer in which cosmogenic nuclides are produced, as well as leaving a contemporary sampled surface which may have been exposed later than date of boulder exposure from the ice (Gosse and Phillips, 2001). Within the sample ages' internal errors, it is evident that when using different calculation criteria, the ages are indistinguishable, and the choice of production rate dataset, erosion rate or scaling methods has negligible influence of the final age calculation (Figure 5.4). For the purpose of comparison with published and future work, ages presented in this study assume a 0 mm kyr^{-1} and use the most recently developed and advanced scaling method, LSDn. Reference samples for a regional Patagonia production rate (Kaplan et al., 2011) are used under the rationale that they will provide a production rate more representative of the locations of samples collected in this study, than if reference samples located globally were used.

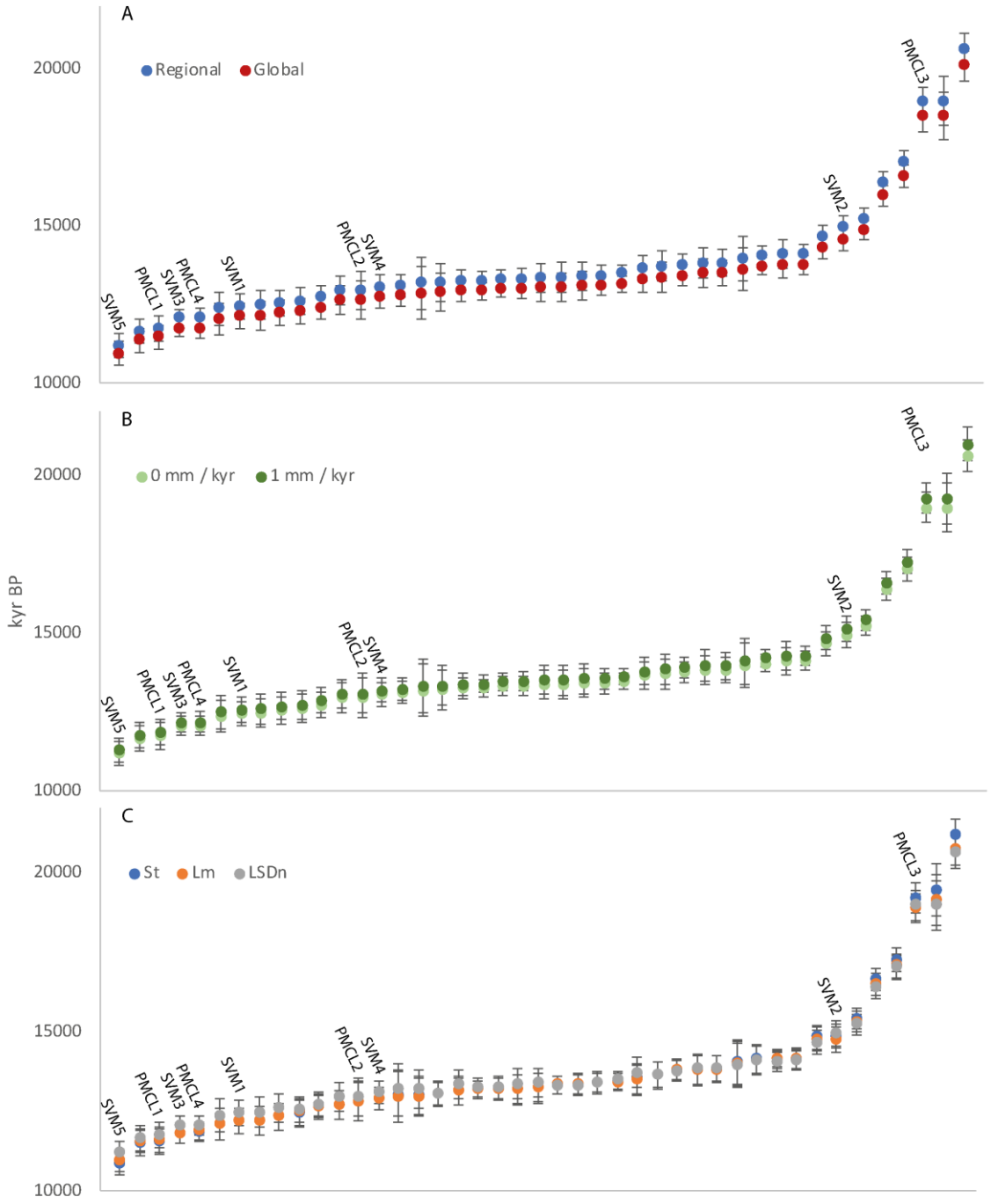

Figure 5.4. Graphs showing surface exposure ages from boulder samples taken from the region north of MSL (Golledge et al., 2012; Davies et al., 2018; Sagredo et al. 2018) including from this study (labelled), for the purpose of comparing: A) regional (Kaplan et al., 2011) and global (Borchers et al., 2016) production rates, B) 0 mm kyr^{-1} and 1 mm kyr^{-1} erosion rates and C) St (Lal, 1991; Stone, 2000), Lm (Nishiizumi et al., 1989; Lal, 1991; Stone, 2000) and LSDn (Lifton et al., 2014) scaling methods. Ages are arranged in chronological order and presented with error bars of the ages' internal uncertainty. Graphs show that samples calculated with different reference production rates, erosion rates and using different scaling schemes overlap in age within internal uncertainties.

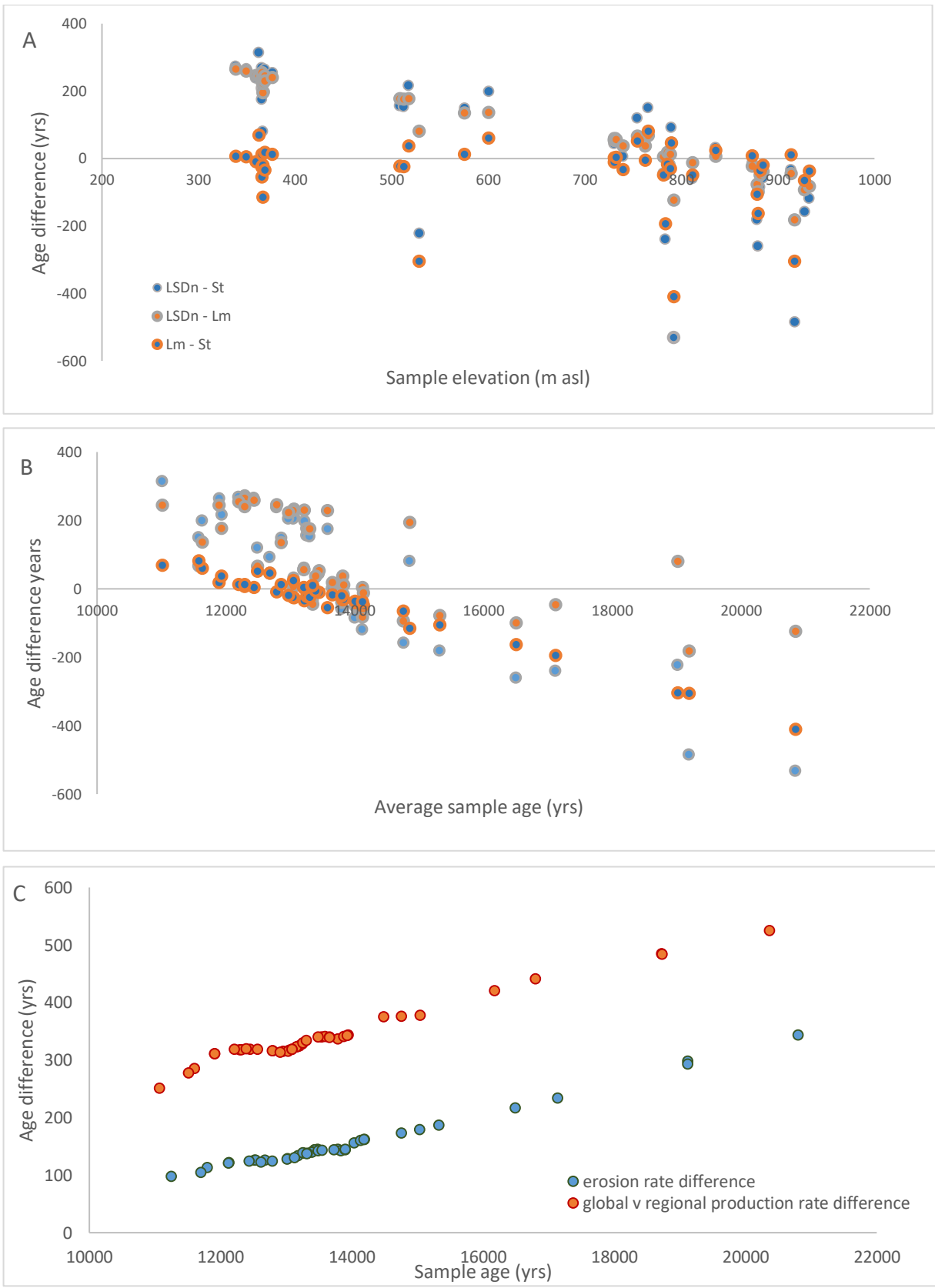

Figure 5.5. Graphas to illustrate calculate age differences between A) LSDn, St and Lm scaling schemes relative to samples elevation, B) LSDn, St and Lm scaling schemes relative to average sample age across the three schemes, and C) 1 mm yr^{-1} and 0 mm yr^{-1} erosion rates and using the global v regional production rates, plotted against sample age. Graphs show the impact of sample elevation on calculated ages when compared between scaling schemes. The greatest difference is where elevation differs from 700 to 800 m asl.

5.4.2. ^{10}Be cosmogenic nuclide surface exposure ages

M9 ages range from 14.9 ± 0.4 ka to 11.2 ± 0.4 ka. Normal kernal density estimate plots (Figure 5.6A) plotted with internal uncertainties show a significant spread in ages from the M9 moraine. Removing ages SVM2 and SVM5 dated to 14.9 ka and 11.2 ka respectively and applying the reduced chi-squared test to the remaining ages is required to give a statistical result indicative of a consistent age population for this feature (Table 5.3). A reduced chi-squared test value $\mathrm{x}_{\mathrm{R}}^{2}$ less than the 2σ envelope criterion k indicates a > 95% probability that the data could be drawn from a single population (Spencer et al., 2017). SVM2 and SVM5 could therefore be considered as outliers. The UWM of the remaining ages provides an age estimate for the moraine of 12.5 ± 0.4.

M12 ages range from 19.0 ± 0.5 ka to 11.7 ± 0.4 ka. The M12 complex samples have a distinct Gaussian curve peak at 19.0 ka (sample PMCL3). We can discount this sample as being unrepresentative of the individual feature based upon its younger stratigraphic position inside and up-valley of M1a, M1c, M4 and M9, all of which have samples dated to be *ca* 5.5 to 6.5 ka younger (Glasser et al., 2012; Davies et al., 2018). Applying the reduced chi-squared test to the remaining ages indicates the remaining samples are likely representative of a single population, and subsequently a UWM of 12.1 ± 0.4 is calculated.

The UWM ages of M9 (12.5 ± 0.4) and M12 (12.1 ± 0.4) are younger than those UWM ages at sites progressively down valley, at the M4 (12.7 ± 0.4 ka), M1a (13.4 ± 0.2 ka) and the single age at M1c (12.9 ± 0.5 ka) (Table 5.2, Figure 5.1), showing glacier recession from the ACR limit of ice-readvance at M1a and M1c. There is overlap of the UWM ages within one standard deviation, however the geomorphologic evidence for the known sequence of recessional moraines constrains the ages to a set order. The known sequence of moraine formation, independent of dating, allows the application of a Bayesian age model (Section 5.3.3) to narrow the range of uncertainty around the dates of formation of the individual features.

*Table 5.3. Reduced chi-squared test (x_R^2) and 2σ criterion (κ) values for ages from selected moraine sites. Those sites not tested contained two or less samples and such a test is deemed inappropriate. *Sample PMCL3 is removed from the test on the Pedregoso moraine complex samples as it is previously identified as an outlier.*

Location	x_R^2	κ	$x_R^2 < κ$
Salto valley moraine	14.04	2.41	no
SVM2 removed	5.02	2.63	no
SVM2 and SVM5 removed	2.75	3	yes
Pedregoso moraine complex	67	2.63	no
PMCL3 removed	2.25	3	yes
Esmeralda latero-terminal moraine	0.14	2.41	yes

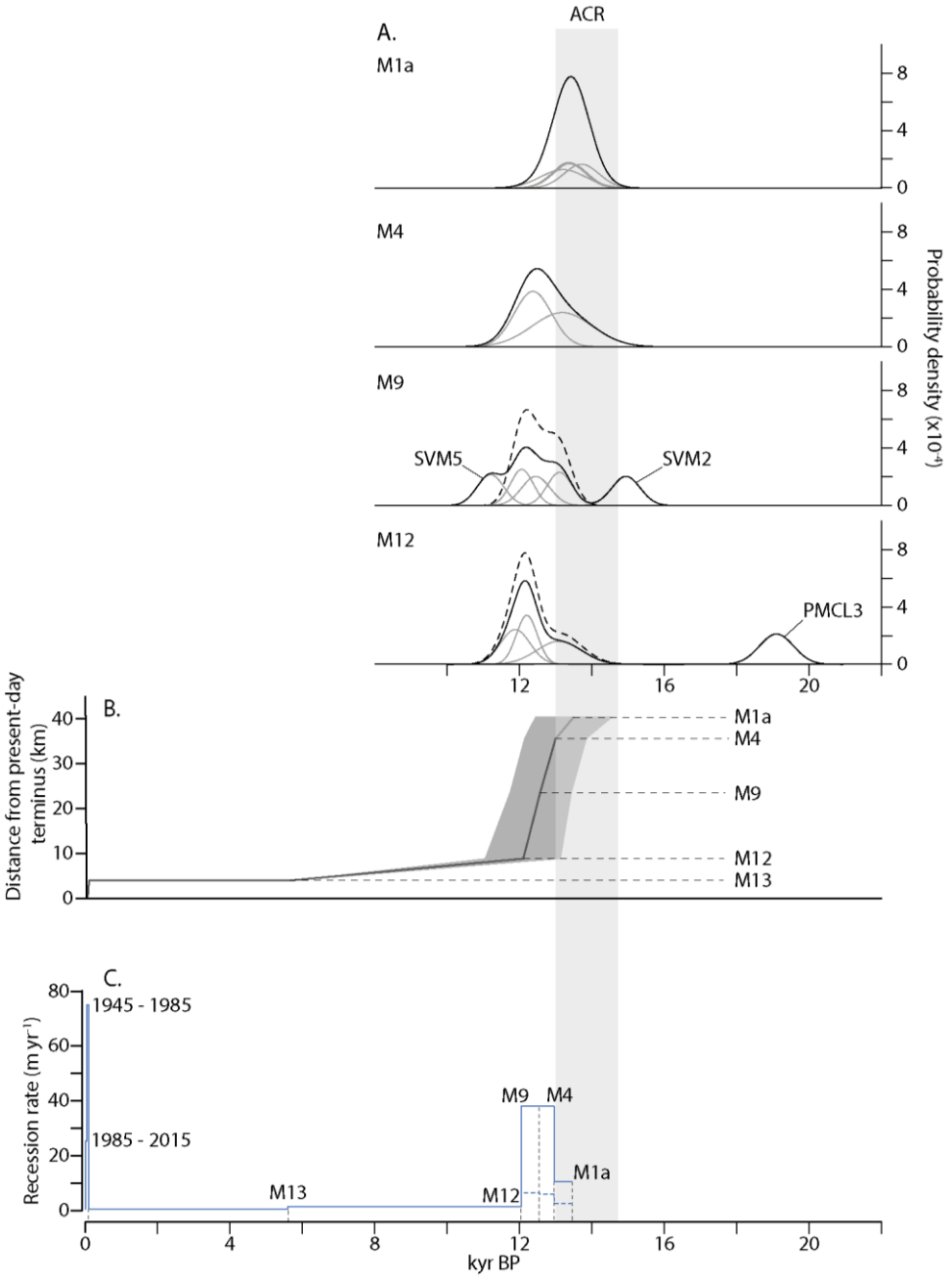

Figure 5.6. A) Normal kernel density estimates of published and new (this study) cosmogenic nuclide surface exposure ages from the Pedregoso and Salto valleys. Light grey Gaussian kernels represent a single sample age with the width equal to the 1 σ error in the age internal uncertainty. The black curve represents the sum of the kernals. The dashed curves of M9 and M12 represent the sum of the kernals after outliers SVM2, SVM5 and PMCL3 have been removed. B) Reconstructed glacier terminus distance from the present day Calluqueo terminus based upon the location and Bayesian modelled (model 2) ages of M1a, M4, M9, M12 (inferred terminus from lateral ice margin) and M13 mid-Holocene, LIA and 1945 moraine discussed in section 5.5.4. The grey envelope represents the range within the maximum to minimum age for the modelled phase. C) Ice recession rate between dated ice margins in the Salto and Predregoso valleys, based upon the median Bayesian modelled (model 2) ages for M1a, M4, M9, M12, and ages for M13 and a 1985 limit as discussed in section 5.5.4. The dotted line represents the minimum recession rate.

5.4.3. Bayesian age modelling

Bayesian age modelling was used to constrain the timing of moraine formation and evaluate the sample ages and calculated UWM ages within the geomorphological framework of a known sequence of events. Sequence algorithms (Bonk Ramsey, 2008) were used in conjunction with the General Outlier Model (Bronk Ramsey, 2009), enabling outliers to be identified and retained in the model, but their influence scaled down. Two model instances were run. Model 1 used the General Outlier Model. PMCL3 was not included in the model (but is presented in Figure. 5.7 and Figure. 5.8 for context) as it has been clearly identified as anomalous and unrepresentative of the Pedregoso moraine complex. SVM2 and SVM5 were retained in the model given their closer association with the other ages from the Salto valley moraine but were confirmed as outliers within the General Outlier Model. Agreement values between samples SVM2 and SVM5 and the model of 27.6% and 57.6% respectively were below the recommended acceptable 60% threshold (Bronk Ramsey, 2009). Their influence was hence proportionally scaled down. Model 2 was run with SVM2 and SVM5 excluded. Table 5.4 shows the 2σ age range produced for each moraine phase, alongside the UWM moraines ages obtained from surface exposure dating. Figure. 5.7 and Figure. 5.8 show the output of both Bayesian models. The posterior density estimate (2σ age range) generated by the model is shown in dark grey and the relative probability of each sample age within the range of the external uncertainty is in light grey. The age model provides additional support for the UWM.

Table 5.4. 2σ age range of modelled ages for moraine formation in the Salto and Pedregoso valleys during the recession of Calluqueo glacier rounded to one decimal place.

		Model 1					Model 2				
Event		Range (ka)			μ/± (ka)	$\overline{\mu}$	Range (BP)			μ/± (ka)	$\overline{\mu}$
M1a	(start)	14.5	-	12.5	13.4 ± 0.5	13.3 ± 0.3	14.5	-	12.4	13.4 ± 0.5	13.3 ± 0.3
	(end)	14.1	-	12.4	13.2 ± 0.4		14.1	-	12.4	13.2 ± 0.4	
M4	(start)	13.8	-	12.3	13.0 ± 0.4	12.9 ± 0.3	13.8	-	12.3	13.0 ± 0.4	12.9 ± 0.3

	(end)	13.5	-	12.1	12.8 ± 0.3		13.6	-	12.1	12.8 ± 0.4		
M9	(start)	13.3	-	12.0	12.7 ± 0.3	12.5 ± 0.3	13.4	-	11.9	12.6 ± 0.4	12.6 ± 0.3	
	(end)	13.2	-	11.7	12.5 ± 0.4		13.2	-	11.7	12.4 ± 0.4		
M12	(start)	13.1	-	11.4	12.3 ± 0.4	12.2 ± 0.4	13.1	-	11.4	12.2 ± 0.5	12.2 ± 0.3	
	(end)	13.1	-	11.0	12.1 ± 0.5		13.1	-	11.0	12.0 ± 0.6		

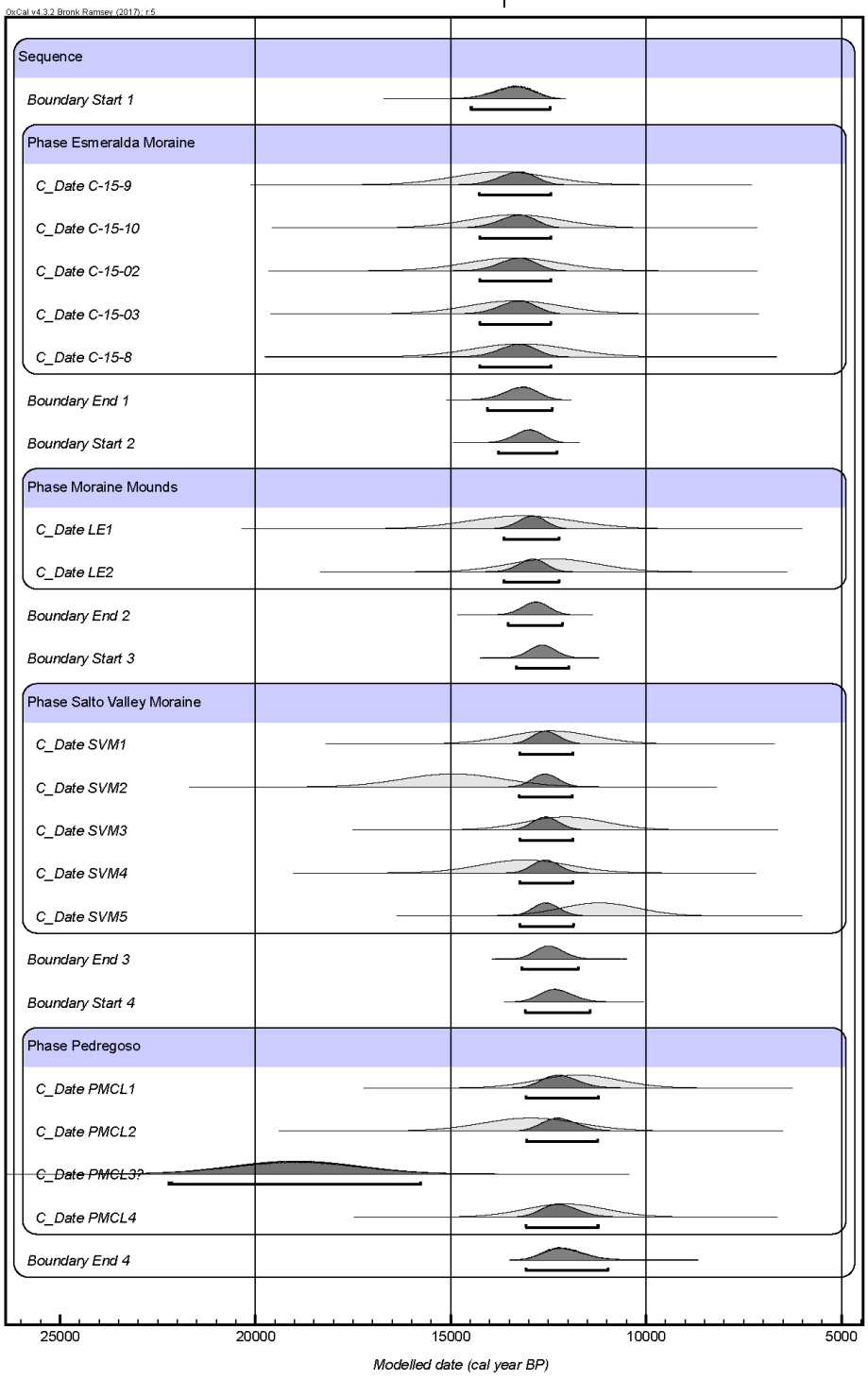

Figure. 5.7. Model 1. Bayesian age model for the timing of moraine formation in the Salto and Pedregoso valleys. PMCL3 is not included in the model but plotted here for context. Light grey shows relative probability of each age estimate and with the posterior density estimate (2σ age range) generated by the model in dark grey.

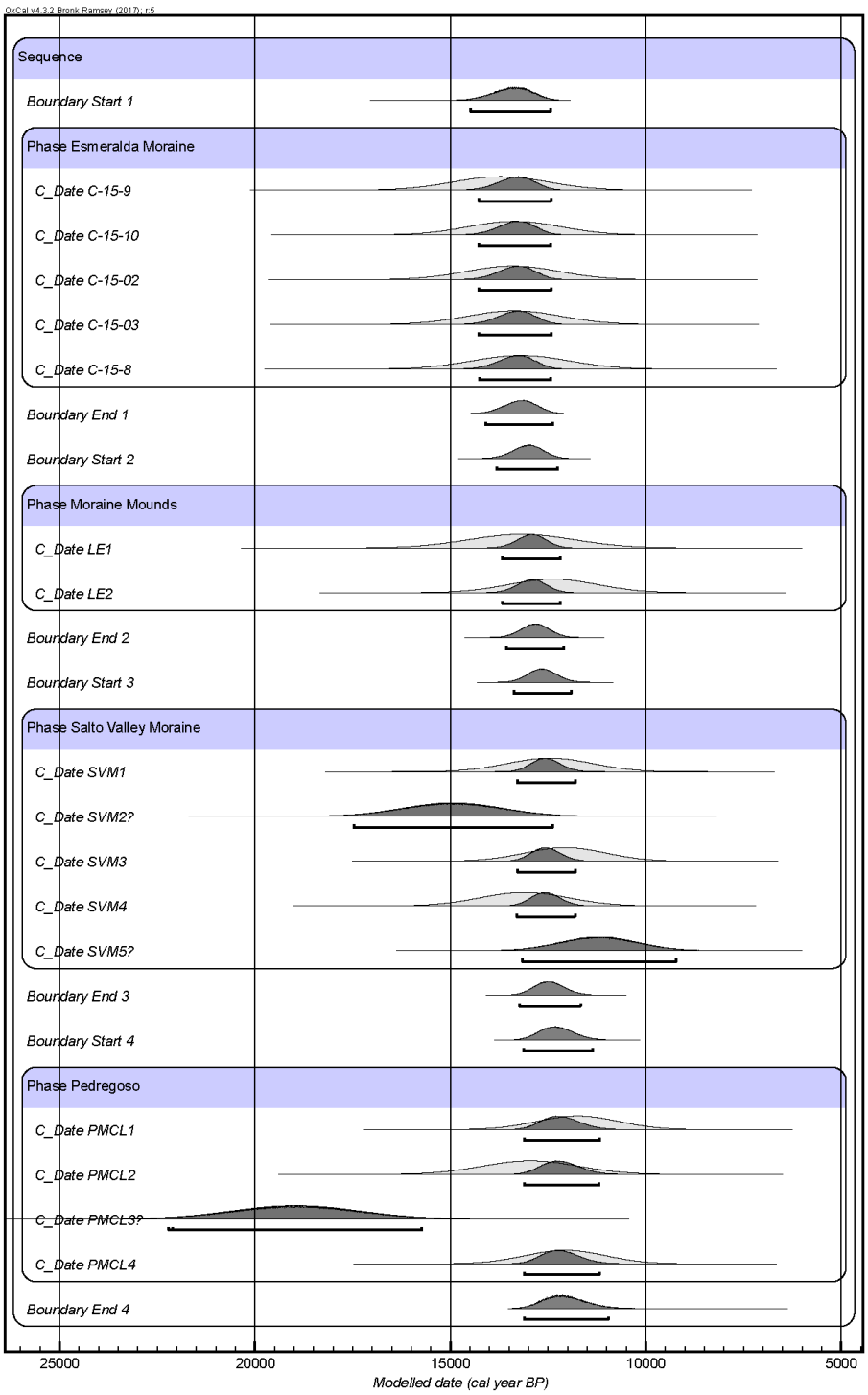

Figure. 5.8. Model 2. Bayesian age model for the timing of moraine formation in the Salto and Pedregoso valleys. SVM2, SVM5 and PMCL3 are not included in the model but plotted here for context. Light grey shows relative probability of each age estimate and with the posterior density estimate (2σ age range) generated by the model in dark grey.

5.4.4. Rates of ice recession

The new surface exposure ages and Bayesian age model produced by this study creates an unprecedented dataset of 4 dated ice margins in a single valley to document ice recession during a phase of rapid warming following the ACR. The ages reveal rapid recession of Calluqueo glacier during post-ACR warming with ice receding a total of 31.5 km over 1.3 ka from its ACR position to M12. Glacier rates of recession were calculated using both the UWM surface exposure ages and mean ages of each Bayesian modelled phase, where each phase corresponds to the formation of a moraine in the sequence (Table 5.4).

The frontal ice margin position was used to calculate distance of recession between dated ice limits. At position M12, where a lateral moraine was dated, the frontal ice margin was inferred by extrapolating the M12 moraine along the valley side at a constant gradient (Figure 5.9). The M13 moraine has not been dated so to extend our analysis of recession rates through the Holocene, geomorphological and chronological evidence from other glaciation valleys is used. It is hypothesised that ice was present at the M13 limit in the mid-Holocene, and the LIA through to the mid-20th century. This hypothesis is supported, firstly by the regional evidence for a mid-Holocene neoglaciation. Moraines dated to this time are found east of the NPI in the Colonia valley with a UWM 5.4 ± 0.2 ka (Nimick et al., 2016), and on the northern flank of MSL in the Upper Tranquilo valley (UWM of 5.6 ± 0.1 ka) (Sagredo et al., 2018) (Figure 5.1), to the southeast of MSL at Río Lacteo (radiocarbon age of 5.2 ± 0.7 cal. ka) (Mercer, 1968) as well as in southern Patagonia in the Lago Argentino basin (Strelin et al., 2014). The lack of moraines between M12 and M13 suggest that the M13 limit, 4.7 km inset of the inferred M12 frontal margin, marks the frontal ice position during a mid-Holocene neoglaciation and likely formed at this time. For the purpose of estimating retreat rates, this study takes a mid-Holocene age for M13 of 5.6 ± 0.1 ka, the UWM value of the dated mid-Holocene moraine from Tranquilo valley on the northern flank of MSL (Sagredo et al., 2018).

Secondly, late-Holocene and LIA Neoglacial moraines have been dated in the region based upon dendrochronology, lichenometry and historical records (Aravena, 2007; Glasser et al., 2011; Aniya, 2013; Morano-Büchner and Aravena, 2013; Strelin et al., 2014; Nimick et al., 2016; Garibotti and Villalba, 2017). In particular on the northern flank of MSL at Arroya San Lorenzo, Aravena (2007) and Morano-Büchner and Aravena (2013) date two latero-terminal moraines to 1536 A.D. and 1802 A.D. respectively. Like at M13, they present as large moraines with clear trimlines and unvegetated morainic material or exposed bedrock inset of the moraine ridge, and can be observed across the region (Davies and Glasser, 2012). This morphological similarity alongside the absence of a large moraine limit between M13 and present day, suggests an ice advance to the M13 limit at the LIA. Evidence from a historical map (1907) (Argentine Oficina de

Límites Internacionales) and aerial photographs (1945), used to produce a 1956 Chilean Geographic Military Institute (IGM) 1: 50000 map, demonstrate that 20th century recession from M13 onward occurred from the 1950s (see Morano-Büchner and Aravena, (2013)). Smaller, closely-spaced moraine ridges on the shore of Lago Calluqueo inset of the larger M13 moraine ridge (Chapter 4) likely formed immediately following ice recession from the primary M13 ridge by minor annual to decadal glacier fluctuations. Landsat imagery from 1985 shows the glacier's frontal margin a further 3 km up valley of M13, at the eastern end of Lago Calluqueo, 750 m in front of the present-day glacier.

Using the mean for moraine formation from 'Model 2' (Table 5.5, Figure 5.6), ice receded from the ACR M1a position to M4 at a minimum rate of 13 m yr $^{-1}$, given the time taken for intermediary moraine formation which is not taken into account in the calculation. Once ice receded into the steep sided southern section of the Salto valley (ice position M4 to M9) ice receded more rapidly for up the Salto and Pedregoso valleys for 50 km at a minimum rate of 38 m yr $^{-1}$ to the inferred frontal margin of the M12 ice position. The absence of spatial and temporal constraint of the frontal ice margin between M12 (*ca* 12.1 ka) and M13 (mid-Holocene and LIA), makes assigning a value to the rate of recession very speculative. The frontal ice margin may have receded rapidly up valley past the M13 moraine, before a mid-Holocene and later LIA readvance. Equally, the glacier could have undergone multiple phases of rapid recession, stillstand and readvance over approximately 12 kyr. The 0.8 m yr^{-1} recession rate between M12 and M13 is therefore an absolute minimum rate of ice recession.

Ice remained relatively stable at M13 until the mid-20th century, after which it receded rapidly at *ca* 75 m yr^{-1} for approximately 3km during the 1945 to 1985 period, and a further 750 m at 25 m yr^{-1} from 1985 to present. The calculated rates of recession should be taken as minimum rates, given that the time at which the glacier is at stillstand for the formation of the dated moraines, as well as the intermediate moraines, is not taken into account. Although it is possible to use the Bayesian modelled age ranges for each moraine phase to obtain a minimum recession rate, based on the maximum age of the down-valley moraine and minimum age of the up-valley moraine (Figure 5.6), it is not plausible to obtain a maximum rate as the youngest age for the down-valley moraine overlaps with the oldest age of the up-valley moraine.

*Table 5.5. Rates of recession of Calluqueo glacier between the M1a and M13 moraines based on UWM ages of dated ice limits and Bayesian modelled mid-point ages. *For the purpose of calculating estimated retreat rates, the age of the M13 moraine is taken to be 5.6 ± 0.1 ka, the UWM value of the dated mid-Holocene moraine from Tranquilo valley on the northern flank of MSL (Sagredo et al., 2018), based on geomorphological interpretations.*

			UWM ages		Model 1		Model 2	
Valley section	Distance (m)	Valley floor gradient (%)	Period (ka)	Recession rate (m yr^{-1})	Period (ka)	Recession rate (m yr^{-1})	Period (ka)	Recession rate (m yr^{-1})
M1a to M4	5000	0.1	13.4 to 12.7	7	13.3 to 12.9	12.5	13.3 to 12.9	12.5
M4 to M9	11500	0.2	12.7 to 12.5	58	12.9 to 12.5	28.8	12.9 to 12.6	38.3
M9 to M12	15000	0.4	12.5 to 12.1	38	12.5 to 12.5	50	12.6 to 12.2	37.5
M12 to M13 (mid-Holocene)	4700	1.3	12.1 to 5.6*	0.8	12.2 to 5.6*	0.7	12.2 to 5.6*	0.7

Table 5.6 Rates of recession of Calluqueo glacier between the M13 moraine and present based on geomorphic interpretations and historical mapping evidence. For the purpose of calculating estimated retreat rates, the age of the M13 moraine is taken to be 5.6 ± 0.1 ka, the UWM value of the dated mid-Holocene moraine from Tranquilo valley on the northern flank of MSL (Sagredo et al., 2018), based on geomorphological interpretations. The 1945 A.D. age for the M13 moraine comes from a 1956 Chilean Geographic Military Institute (IGM) 1: 50000 map based on aerial photograph of 1945 A.D. (see Morano-Büchner and Aravena, (2013)). The frontal ice position at 1985 is taken from Landsat imagery.

Valley section	Distance (m)	Valley floor gradient (%)	Period (ka)	Recession rate (m yr-1)
M13 (mid-Holocene) to present	3750	4	5.6 to present	0.7
M13 (1945 A.D.) to 1985 A.D.	3000	4	0.07# to 0.03	75
1985 A.D. to present	750	4	0.03 to present	25

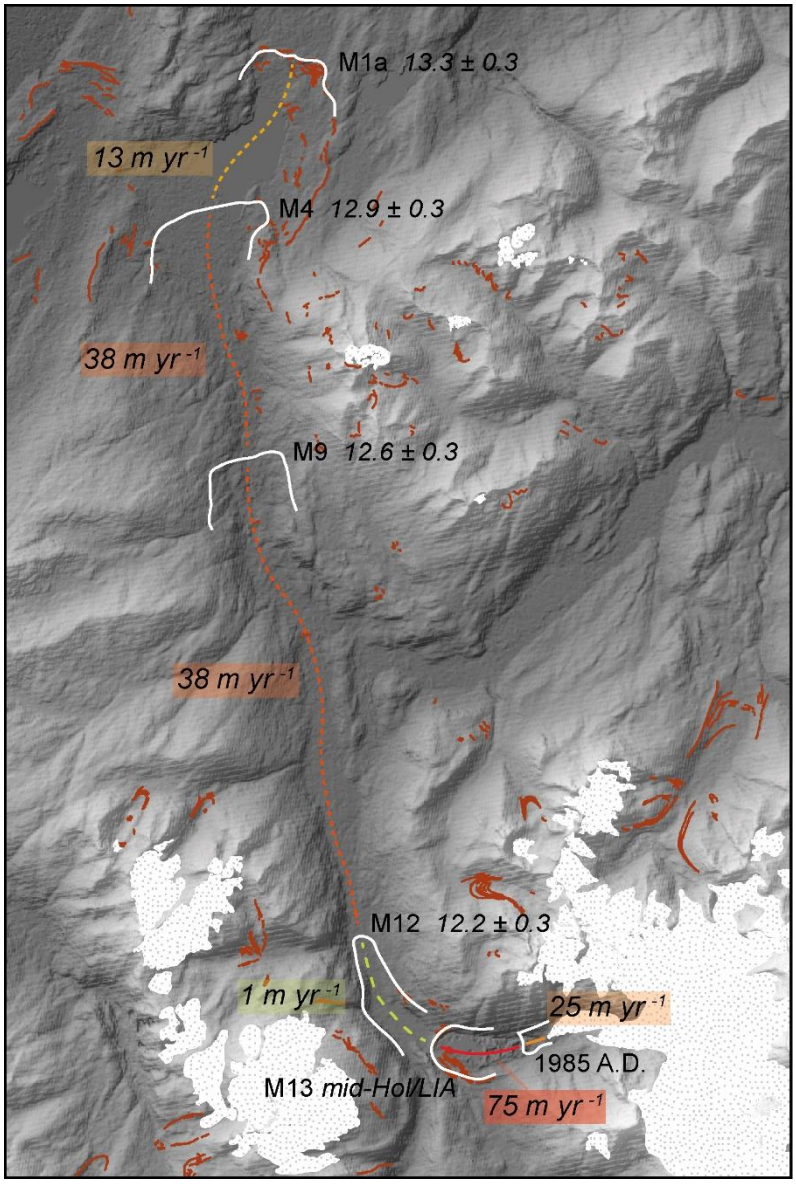

Figure 5.9. Rates of recession of Calluqueo glacier from the M1a frontal limit to the present day. Ages in italics are taken from Bayesian Model 2. Dashed lines show the glacier flowline. Rates of recession are minimum average rates, calculated from the modelled ages. The larger dashed green line between M12 and M13 indicates greater uncertainty in the rate of recession, given the large time period during which any chronological or spatial constraint is missing. Initial gradual recession between M1a and M4 becomes more rapid upon entering the confined Salto valley between M4 and M12. M12 to M13 is an area of uncertain ice behaviour reconstruction through the Holocene, during which time ice may have receded, readvances and been at stillstand multiple times. Recent recession in the C. 21st is the most rapid in the record.

5.5. Discussion

The new ages from this study show that the vast majority of ice recession following the ACR to present day occurred in the first *ca* 1.3 ka, receding *ca* 36 km over this period to the M12 ice position (12.1 ± 0.4 ka). In the subsequent ~6.5 ka of the early to mid-Holocene, the geomorphological evidence indicates that the Calluqueo ice margin only receded a further 4.7 km to the M13 moraine, prior to recession and readvance at the LIA and final rapid recession for a further 3.75 km from 1945 to its present-day position. This pattern of recession is likely due to a combination of the rapid *ca* 2.5 ^{o}C warming which occurred over a period of one thousand years after the ACR, starting *ca* 12.7 ka (Cuffey et al., 2016) and the shallowly sloping nature of the Salto and Pedregoso valleys (Table 5.5). Ice receded more slowly between M1a and M4 than between M4 and M9 which could be because rapid warming did not occur until 12.7 ka (Chapter 8). Recession from M1a to M4 prior to the onset of rapid warming could have been aided by the glacier calving into palaeolake Chelenko during this time. (Chapter 4). Following 12.7 ka, warming temperatures would lead to an increase in glacier ELA and significant ablation over the extensive length of ice occupying the Salto and Pedregoso valleys. The slight decrease in recession rate between M9 and M12 in comparison to between M4 and M9 may be due to the slightly steeper valley floor in the Pedregoso valley (0.4% compared to 0.02% in the Salto valley between M4 and M9). Given the late of data and likely multiple stages of ice recession and readvance, it is not possible to obtain a rate of recession between M12 and M13 with great certainty (section 5.4.4). The 0.7 m yr^{-1} rate of recession calculated does not account for phases of recession and readvance and is therefore an absolute minimum.

The rapid recession of Calluqueo glacier from 1945 to 1985 was likely caused both by rapid warming but also instability of the frontal ice margin calving into Lago Calluqueo. Once the glacier became land terminating following 1985, the recession rate decreased. This is the opposite scenario to what is observed between M1a and M4 and M4 and M9. Initial recession between M1a and M4 while the glacier is lake terminating is slower than between M4 and M9 following lake drainage. In this later scenario, the faster recession in the second phase is caused by the onset of rapid warming, which is the primary driver of glacier recession. During the second half of the 20th century the rate of warming was broadly constant, if not slightly increasing (Stocker et al., 2013). Increased stability of the glacier's frontal margin after moving from lake to land-terminating therefore likely caused recession rate change.

The rapid post-ACR recession seen in the Salto and Pedregoso valleys is an order of magnitude greater than that which can be estimated to have occurred in the Colonia valley during a similar period. In the Colonia valley, ice receded approximately 11 km from its inferred ACR limit (Davies

et al. in prep) to an early Holocene limit at 11.3 ± 0.3 ka. Taking the ACR dated Colonia lateral moraine UWM age of 13.6 ± 0.7 ka gives a retreat rate of 4.8 m yr^{-1}. This comparatively low rate of recession is likely due to the Colonia glacier being fed by the larger NPI, therefore having a longer and less dramatic response to rapid warming.

5.6. Conclusions

- Dating of two previously undated moraine complexes in the Salto and Pedregoso valleys by ^{10}Be cosmogenic nuclide surface exposure dating of glacially transported boulders provides new with UWM ages of 12.5 ± 0.4 ka and 12.1 ± 0.4 ka for M9 and M12 respectively.
- By combining these new ages with existing work and through the application of a Bayesian sequential phase model, this study obtains approximate ages of 12.6 ± 0.3 ka and 12.2 ± 0.3 ka for M9 and M12 respectively.
- Both using UWM ages from cosmogenic nuclide dating of moraine boulders and from ages obtained by the application of a Bayesian model to sample ages yield valid results. Applying a Bayesian approach gives the advantage of identifying and suppressing the impact of outliers and producing a probabilistic framework, taking into account data holistically, incorporating all chronological data and an independent known sequence of events.
- This new record shows ice in the Salto and Pedregoso valleys receded rapidly for 27 km over a period of *ca* 1.3 kyrs until *ca* 12.1 ka, at a minimum average recession rate of 20 m yr^{-1}. Ice likely underwent multiple phases of recession and readvance and/or stabilization during the Holocene. Ice receded rapidly from 1945 to the present-day at an average rate of 54 m yr^{-1}. This presents one of the few detailed, well temporal constrained LGIT and Holocene records of ice recession in a single valley in Patagonia.
- Although ice-frontal stability whilst lake terminating may have contributed to initial recession of Callqueuo glacier, an abrupt increase in temperature following the ACR caused a faster rate of glacier recession. In the second half of the 20th century while the rate of temperature increase was largely constant, the transition from a lake to land-terminating frontal margin had greater effect on ice dynamics, leading to a reduction in glacier recession rate.

6. Palaeoglacier and ELA reconstruction

6.1. Introduction

6.1.1. Rationale

The patterns of ice recession and landsystem change north of MSL have been reconstructed from a detailed process-based sediment-landform study, based upon geomorphological mapping and sedimentological investigation (Chapter 4). The new chronological data obtained from surface exposure dating of glacially transported boulders found on moraine ridge crests in the Salto and Pedregoso valleys anchors Calluqueo glacier and landsystem evolution (Chapter 5). In this chapter the glacier and landsystem reconstruction (Chapter 4) is combined with the new and existing chronological data (Chapter 5) to reconstruct the timing of glacier evolution. Furthermore, from the temporally constrained reconstruction of ice extent it is possible to investigate changes in Equilibrium-Line Altitude (ELA) through a period of warming following the ACR and through the Holocene. These ELA reconstructions are then combined with existing temperature records to calculate estimations of precipitation at Calluqueo glacier over this period. The output of this chapter provides the empirical data (temporally constrained ice and landsystem reconstruction) with which to constrain and test a glacier model of the north section of the MSL ice cap (Chapter 7). ELA based, quantitative precipitation reconstructions provide a hypothesis for precipitation levels and changes during a period of rapid warming following the ACR and then more gradual warming through the Holocene which can be tested with a glacier model.

6.1.2. Research questions, aims and objectives

This chapter aims to answer three key research questions within **RQ 2 and RQ 4** of this thesis: **1) What was the temporal context of deglaciation and of the valleys to the north of MSL? 2) How did the ELA of Calluqueo glacier change following the ACR and through the Holocene? 3) What were the levels of precipitation at MSL following the ACR and through the Holocene and how did precipitation change through this period?** The aim of the work presented in this chapter, addressing **Aim 1** of this thesis, is to synthesise the deglaciation and landsystem reconstruction from Chapter 4, with the new and existing chronological data presented in Chapter 5. This synthesis is then used as the basis to reconstruct palaeo-glacier ELAs when Calluqueo glacier was at the M12 and M13 ice margins. This is done through **Obj. 3** and **Obj. 4** of this thesis, by reconstructing the palaeo-ice surface using the GlaRe GIS tool for ArcGIS (Pellitero et al., 2016), from which an AABR derived ELAs is calculated. From this, first order estimates of palaeoprecipitation following the ACR are made. This is calculated following

Ohmura et al., (1992) by combining the reconstructed ELAs with palaeotemperature data (Chapter 3.6).

6.2. Palaeoglaciological reconstruction

The reconstruction of the MSL ice cap based on the geomorphological mapping (Chapter 4) and chronological data (Chapter 5) is shown in Figure 6.1. The reconstruction shows the deglaciation of the northern section of the MSL ice cap in eight stages following the ACR and though the Holocene to its present day position. The eight stages are described below.

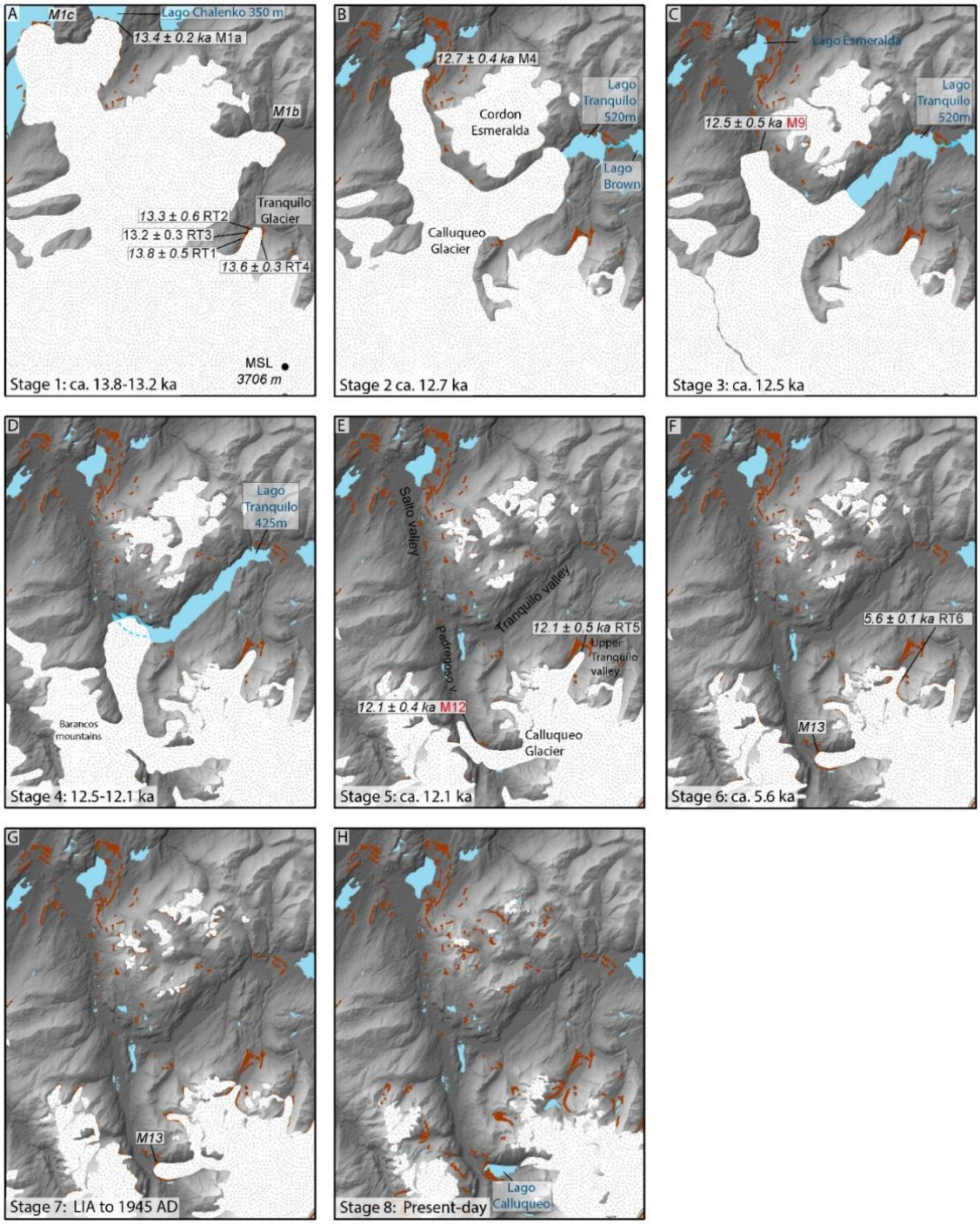

Figure 6.1. Reconstruction of the deglaciations of the northern section of the MSL ice cap. Ages presented are uncertainty weighted mean values of surface exposure ages of glacially transported boulders found on moraine ridges calculated with internal uncertainty and presented with ± 1σ error. Ages in red (from moraines M9 and 12) are from this study. Ages in black from moraines M1a, M4 and RT1 to RT6 are recalculated from Davies et al., (2018), Glasser et al., (2012) and Sagredo et al., (2018) respectively.

A) Ice is advanced to its ACR limit, merged with glaciers from the Barancos mountains, dated with UWM ages between 13.8 and 13.2 ka at the subaerially formed M1a latero-terminal moraine in the northern Salto valley (Davies et al., 2018) and at the RT1 to RT4 latero-terminal moraines at Tranquilo glacier (Sagredo et al., 2018). At this point ice in the Salto valley is terminating in the 350m Palaeolake Chelenko and M1c was deposited subaqueous below this 350 m lake level (Davies et al., 2018; Thorndycraft et al., 2019). I speculate that ice was also advanced to the M1b limit at the ACR given the moraine's position as the furthest advanced moraine set in the Tranquilo valley (Chapter 4).

B) Following the ACR, ice in the northern Salto valley receded, dated at its M4 margin to an UWM age of 12.7 ± 0.4 ka (Glasser et al., 2012). It was approximately at this time, when ice was located at the M4 margin that the regionally extensive Palaeolake Chelenko (occupying Valley Grande and the Cochrane basin), drained following recession of Pared Norte Glacier and the opening of the Rio Baker drainage route to the Pacific (Figure 1.2) (Davies et al., 2018; Thorndycraft et al., 2019). Ice also receded west from the M1b moraines, resulting in the formation of the 520 m ice-dammed palaeolake Tranquilo, which drained east into Lago Brown (Chapter 4).

C) By *ca* 12.5 ka ice has receded further up the Salto valley forming a series of well-defined cross-valley moraine ridges (Chapter 4), the southern most of which is M9 with a UWM age of 12.5 ± 0.5 ka. At this time ice in the Tranquilo valley also receded further, increasing the extent of Palaeolake Tranquilo.

D) Between *ca* 12.5 and 12.1 ka, ice in the Salto and Tranquilo valleys receded back to the valleys' confluence, facilitating partial drainage of palaeolake Tranquilo to 425 m asl, possibly by GLOF drainage (Chapter 4).

E) Subsequent ice recession up the Pedregoso valley caused Palaeolake Tranquilo to drain completely. Ice stabilised forming the M12 lateral moraine on the eastern side of the Pedregoso valley and RT5 moraine in the Upper Tranquilo valley (Sagredo et al., 2018).

F) Ice receded further during the early-Holocene and I hypothesise that Calluqueo glacier stabilised/readvanced in the mid-Holocene (*ca* 5.6 ka) at the M13 limit in the Pedregoso valley, based on the evidence of the RT6 moraine in the Tranquilo valley (Sagredo et al., 2018).

G) Calluqueo glacier remained stable at M13 during the late Holocene, or may have undergone recession during this time, and then readvance during the LIA as evidenced by multiple moraines crests at this locality (Chapter 4). Glaciers at MSL, Cordon Esmeralda and the Barancos mountains stabilised at the LIA, forming well defined timelines in their respective valleys.

H) Calluqueo glacier began receding to its present-day margin after 1945 AD,leading to the formation of Lago Calluqueo, dammed by M13.

6.3. Ice surface and ELA reconstruction

To obtain a quantitative estimate of precipitation for periods during the retreat of Calluqueo glacier, this study calculates the ELA of Calluqueo glacier when positioned at the M12 lateral moraine limit (UWM 12.1 ± 0.4 ka) and M13 latero-terminal moraine limit. The M12 and younger moraine limits were chosen because ice had separated from other glaciers by the time it receded to the M12 limit. The undated M13 limit is hypothesised to mark the advanced position of Calluqueo glacier at both the LIA and during a regional mid-Holocene neoglaciation (section 5.6). The Accumulation Area Balance Ratio method (Osmaston, 2005; Pellitero et al., 2015) is used in combination with the GlaRe GIS based ice surface reconstruction tool (Pellitero et al., 2016) (section 3.6) to obtain an ELA of the reconstructed glacier. The method of Ohmura et al., (1992) is then used with surface air temperature data to obtain quantitative precipitation values for phases of glacier stillstand at M12 and M13.

There are few quantitative LGIT and Holocene surface air temperature records for Patagonia. Massaferro et al. (2014) present a chironomid transfer function derived temperature record from Huelmo mire (41 °S) in the Chilean Lake District, 650 km north of MSL. This record indicates stable temperatures between 15 ka and 13.2 ka, before a drop of approximately 1 °C, sustained until 11.5 ka. There is contrast with the chironomid-derived quantitative temperature reconstruction at Lake Potrok Aike (52 °S), 500 km south of MSL (Massaferro and Larocque-Tobler, 2013) .This shows stable temperatures during the ACR until 13 ka, before 0.8 °C rise in temperature to the period between 12.5 ka and 11.7 ka. Variation within and across these records could be introduced by insufficient sample size and local variability. In order to gain a broader indication of palaeotemperature, this study uses relative temperature offsets from the West Antarctic Ice Sheet (WAIS) Divide surface air temperature reconstruction (Cuffey et al., 2016). Changes in West Antarctic temperatures have been shown to be synchronous with cryospheric changes in Patagonia's mid-latitudes (Bendle et al., 2019), with upwelling of warm deep water in the Southern Ocean a potential driver of warming across the mid and high-latitudes (Pedro et al., 2016). Although the quantitative transmission of this temperature change is unclear, the degree of temperature change across the ACR and the early Holocene as recorded

in the chironomid records provides an indication that fluctuations in temperature are similar in the Patagonian mid-latitudes observed in the WAIS Divide surface air temperature record (Cuffey et al., 2016). In light of an absence of coherent quantitative surface air temperature data from Patagonia across the LGIT and through the Holocene, this study uses relative temperature offsets from present day from the WAIS Divide surface air temperature record (Cuffey et al., 2016) to obtain mean annual surface air temperature values at MSL for this period.

The same methods were used to reconstruct the present-day Calluqueo glacier ELA based upon present-day ice extent as a form of method evaluation and comparison. Balance ratios from 1.5 to 2.5 were used to provide a range of possible ELAs, with a representative 'global' value of 1.75 selected for comparison to present day empirical data (Rea, 2009).

*Table 6.1. AABR ELAs calculated for Callqueuo glacier at three phases of ice extent: present-day and reconstructions of ice matching the M13 and M12 limits. ELAs are presented with corresponding calculations of precipitation following the method of Ohmura et al., (1992) under given temperature offsets from present. *Modern day precipitation values are derived at the ELAs calculated using a 1.75 balance ratio using data from the Cochrane Aerodromo meteorological station and a 0.00252 mm/m precipitation lapse rate (Bravo et al. 2015) for the purpose of comparison. Uncertainty in precipitation is that introduced by the range in mean summer temperature (± 0.5 °C) used to calculate precipitation, obtained from present day temperature records at Cochrane Aerodromo meteorological station.*

							Precipitation (mm w.e.)			
Balance ratio	1.5	1.75	2	2.25	2.5	Temperature offset from present (°C)	Modelled at ELA (using 1.75 BR)	uncertainty	Modern day at ELA*	% difference
Modern ELA	1614	1614	1589	1589	1564	0	2465	204	2353	-4 to 12
Precipitation at ELA	*2465*	*2465*	*2539*	*2539*	*2614*					
M13 ELA	1341	1291	1266	1241	1216	-0.7 (LIA)	3112	217	2353	19 to 29
Precipitation at ELA	*2824*	*2978*	*3056*	*3134*	*3213*	-0.3 (mid-Holocene)	3318	208	2353	24 to 33
M12 ELA	1158	1108	1083	1058	1033	-1.1	3511	209	2352	33 to 37
Precipitation at ELA	*2915*	*3071*	*3149*	*3228*	*3308*					

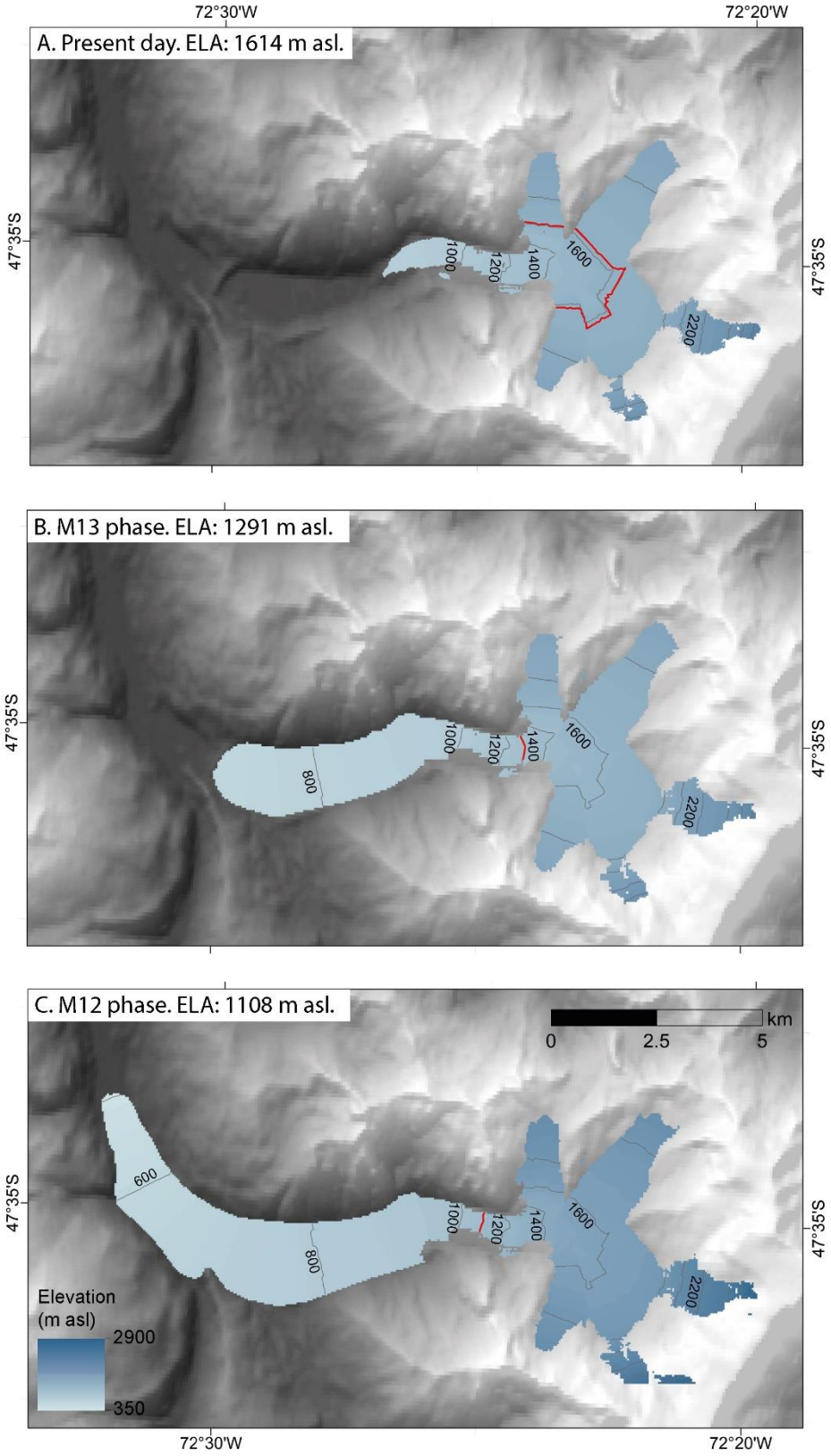

Figure 6.2. Reconstructed ice surfaces of Calluqueo glacier using the GlaRe GIS based ice surface reconstruction tool (Pellitero et al., 2016) at A) present day, B) M13 and C) M12. Ice surface contours are at 50m intervals. The red contour highlights the position of the ELA calculated using the Accumulation Area Balance Ratio method (Osmaston, 2005; Pellitero et al., 2015), based on a balance ratio of 1.75.

The reconstructed ice surfaces and ELA positions are presented in Figure 6.2. Using a 1.75 balance ratio the ELA of Calluqueo glacier increases from 1108 m asl at the M12 phase, to 1291 m asl at the M13 phase, to 1614 m asl at present-day ice extent (Figure 6.2). The ELA for ice at the M12 phase with a relative temperature difference of -1.1 °C from present day gives a calculated precipitation value of 3511 ± 209 mm w.e., 33% to 37% higher than present-day levels. This decreases to 3318 ± 208 mm w.e., 24% to 33% higher than present at the M13 mid-Holocene phase and 3112 ± 217 mm w.e., 19% to 29% higher than present at the M13 LIA phase. Reconstructing present-day precipitation based upon a present-day ELA gives a precipitation value of 2465 ± 204 mm w.e., between 4% lower and 12% higher than the value derived from measured precipitation at the Cochrane Aerodromo meteorological station (180 m asl, 40 km northeast), 2353 mm w.e.. This present-day precipitation value is within the uncertainty of the reconstructed present-day precipitation value.

6.4. Discussion

Ice extent reconstructions at the chronologically constrained M12 and M13 limits, alongside mapped present-day ice extent, provides the opportunity to investigate ELA change at Calluqueo glacier following the ACR, through the Holocene to the present day. During this period from *ca* 12.1 ka through the mid Holocene, the ELA increases from 1108 m asl to 1291 m asl. The Late Glacial and Holocene moraine record from Tranquilo glacier on the northern flank of MSL provides reconstructed ELAs of 1210 m asl at the ACR, and 1320 m asl in the mid-Holocene (González et al., 2013). The slightly higher ELAs at Tranquilo glacier are to be expected given the glacier's northeast facing accumulation area, while Calluqueo glacier faces to the west. MSL acts a barrier to the precipitation bearing westerlies, causing a negative west-east precipitation gradient.

The present-day ELA at Calluqueo glacier is calculated to be 1614 m asl, slightly lower than has been reported for the western side of MSL elsewhere (1700 to 1750 m asl (Wenzens, 2002)). This may be due to the underestimation of ice in the accumulation area made by the GlaRe GIS based ice surface reconstruction tool (Pellitero et al., 2016) (Figure 6.2A). This present-day Calluqueo glacier ELA is also lower than reported present-day ELAs from glaciers on the eastern and northern sides of the massive (1800 to 1850 m asl (Wenzens, 2002; Falaschi et al., 2013; Sagredo et al., 2017). Again this is to be expected given the precipitation gradient across the massif. Based upon the ELA calculations of the Calluqueo glacier reconstructions at M12 and M13, and temperature reconstructions inferred from the WAIS ice core record, this study is able to produce quantitative estimates of precipitation on the western flank of MSL at ca 12.1 ka and

at the time of a mid-Holocene neoglaciation. Precipitation at both 12.1 ka and the mid-Holocene are calculated to be higher than present-day, by 18% to 28% and 15% to 26% respectively.

6.5. Conclusions

- This study presents a new temporally constrained palaeoglaciological reconstruction of Calluqueo Glacier and the northern flank of the MSL ice cap.
- Quantitative precipitation estimates east of the NPI following the ACR and at a mid-Holocene neoglaciation show that precipitation at MSL was 24% to 37% higher than present day.
- Such quantitative estimates add vital detail to previously qualitative reconstructions of precipitation and provide a hypothesis with which to test a glacier numerical model (Chapter 7).

7. Numerical modelling of the Monte San Lorenzo ice cap

7.1. Introduction

7.1.1. Rationale

The majority of ice masses in Patagonia have retreated and thinned in recent decades (Rignot et al., 2003; Moller et al., 2007; Lopez et al., 2010; Davies and Glasser, 2012; Falaschi et al., 2016); however, sparse measured glacier mass balance and physical glaciological data limits our understanding of the dynamics of current ice mass change and climate interaction. This lack of data impedes our ability to relate past glacier fluctuations explicitly to changes in palaeoclimate, as mass balance sensitivities are poorly understood. Geomorphological and chronological evidence collected from the valleys north of MSL (Chapters 4 and 5), shows that glaciers receded rapidly through the Last Glacial-Interglacial Transition (LGIT) and the Holocene. During this period Patagonia experienced changes in temperature and precipitation (Moreno et al., 2009, 2018; Tonello et al., 2009; Waldmann et al., 2010; Kilian and Lamy, 2012; Oehlerich et al., 2015; Moreno and Videla, 2016; Quade and Kaplan, 2017) but which of these forcings were the primary control on glacier change is unclear. An improved understanding of present-day glacier dynamics and sensitivities can inform our understanding of both past and future glacier response to climate change.

Glacier numerical modelling can be applied to reconstruct glacier mass balance distribution, physical behaviour and properties in the absence of measured empirical data. The model can then be used to assess the sensitivity of an ice mass to both external climatic forcings and physical parameters which impact ice flow and glacier mass balance (e.g. Golledge et al., 2012; Putnam et al., 2013; Ziemen et al., 2016; Nielsen et al., 2018; Yan et al., 2018).

This chapter presents the set up of the Parallel Ice Sheet Model (PISM) (see Chapter 3.7.2) for the MSL ice cap, calibrated to match present-day ice extent and dynamics. The results of model sensitivity experiments are also shown, assessing the impact of surface air temperature, precipitation, snow and ice melt factors, bed strength and ice rheology on the simulated ice cap. These new data improves our understanding of the key controls on the behaviour of the present-day MSL ice cap. Obtaining a tuned simulation of the present-day ice cap also provides the basis for response time experiments, modelling historical ice mass extents to obtain envelopes of palaeoclimate conditions, and investigating potential future ice cap change under different climate evolution scenarios.

7.1.2. Existing work

There is limited understanding of current glacier mass balance distribution, climate sensitivity and active glacier behaviour in Patagonia due to a scarcity of empirical data and only a small number of modelling studies. Existing studies commonly use degree-day models forced by down-scaled modelled climate or local sparse weather station data. Schaefer et al. (2013) used NCAR/NCEP Reanalysis and ECHAM5 climate model data, downscaled using the Weather Research and Forecasting regional climate model, to run a 450 m resolution mass balance model over the NPI. Annual accumulation values up to 24 m w.e. were found at the highest altitudes over the NPI, decreasing to 5 to 10 m w.e. between 1500 and 2000 m asl. Between 1000 and 1500 m asl on the plateaus of San Rafael and San Quintin Glaciers, accumulation and ablation rates are similar, between 2 to 5 m w.e.. Ablation is greatest in the lower section of the eastern outlet glaciers, up to 18 m w.e. at Colonia glacier and 14 m w.e. on the western glaciers. Koppes et al. (2011) also used NCAR/NCEP Reanalysis data alongside sparse local observation data as input to a degree-day model to model the surface mass balance of San Rafael Glacier (western NPI). They were able to estimate annual accumulation, ablation, thinning and calving fluxes, finding an overall annual surface mass balance for the period from 1960 to 2005 to be +0.71 km^3 w.e..

Schaefer et al. (2015) also used a downscaled, reanalysis data forced mass-balance model to model the SPI. Annual surface mass balance was found to be up to 20 m w.e. at the highest altitudes, dropping to 0 to 5 m w.e. on glacier plateaus, and up to -15 m w.e. at the outlet glacier tongues. Calving fluxes could also be inferred, showing agreement with velocity-field derived data from satellite imagery. On the eastern side of the SPI, Rivera (2004) focused on Chico Glacier, using a degree-day model forced by climate station data from around the icefield in combination with accumulation field data to investigate glacier mass balance. Average modelled annual accumulation and ablation from 1975 to 2001 were 3.6 ± 0.3 m and 4.4 ± 0.3 m respectively, giving an average annual mass balance of -0.8 ± 0.3 m. Glaciar Perito Moreno has also been investigated (Stuefer et al., 2007), with a degree-day model forced by local climate data used to reconstruct a 50 year span of glacier mass balance and assessment of mass balance sensitivity. Degree-day factors for ice were found to be between 2.7 to 4.3 mm w.e. $°C^{-1}$ d^{-1}, with mean annual surface mass balance between -7688 and -9640 kg m^{-2} in the ablation area, and an equal sensitivity to both temperature and precipitation.

The MSL ice cap and alpine glaciers at Cordon Gorra de Nieve, Gran Nevado and Sierra de Sangra, east of the NPI ice cap, have been studied through SRTM and SPOT5 DEM differencing to reveal

glacier-surface elevation changes between 2000 and 2012 (Falaschi et al., 2016). Although this has provided an insight into the distribution of surface elevation and overall mass change, a full reconstruction of surface mass balance and glacier flow dynamics, such as the role of ice deformation versus sliding and bed strength, is yet to be undertaken.

7.1.3. Research questions, aims and objectives

To address the current gap in understanding surrounding the behaviour of the MSL ice cap, this chapter aims to answer the following research questions as part of **RQ3** and **RQ4** of this thesis: **1. What is the magnitude and spatial distribution of glacier surface mass balance, accumulation and ablation processes? 2. What is the distribution of temperate and cold based ice? 3. What is the nature of ice flow velocity and shear? 4. To what degree is the present-day MSL ice cap sensitive to changes in climate, physical ice flow and mass balance parameters?** The parameters investigated are: temperature, precipitation, ice softness through a flow enhancement factor, bed shear strength, and positive degree-day snow and ice melt factors.

In line with **Aim 2** and **Aim 3** of this thesis, this chapter details a numerical simulation of the present-day MSL ice cap, from which information detailing the ice cap's surface mass balance distribution, physical ice properties and flow dynamics can be extracted. This will be achieved using a numerical model (PISM), tuned to match present day ice extent, thickness and velocity empirical data in line with **Obj. 5** of this thesis. A series of sensitivity experiments in which the model will be initialised under different precipitation and temperature conditions, physical parameters of ice softness and bed shear strength, and mass balance parameters of positive degree day snow and ice melt factors.

7.2. Methods

7.2.1. Modelling strategy

The following modelling strategy (Figure 7.1) was used to set up, calibrate and test a numerical model of the present-day MSL ice cap. Firstly, the climate data used for model initialisation was evaluated. Two modelled climate gridded datasets, RACMO2.3 and WorldClim2 (section 7.3.3), were compared to measured meteorological station surface air temperature and precipitation data to evaluate the ability of the respective models to replicate measured climate in the study area (section 7.3.4). It was important to initially evaluate the modelled climate data being used to force the ice sheet model to ensure that they were applicable to ice-cap scale modelling in Patagonia. Given the inherent differences between the data the models draw upon and their output resolutions (sections 7.3.3), it was key to evaluate and compare both the RACMO2.3 and

WorldClim2 datasets. By comparing two different climate models, it is possible to more thoroughly identify their relative applicability.

Neither climate model was found to provide precipitation datasets which realistically reflect the likely precipitation magnitude and distribution across the study area. A lapse rate derived precipitation dataset from precipitation measured at the Cochrane Aerodromo meteorological station was therefore used alongside the WorldClim2 surface air temperature dataset.

Secondly, the model was tuned to produce a steady state model simulation of the present-day ice cap with empirical ice extent and thickness, velocity and surface elevation change data as a target (section 7.4.2). Tuned parameters included a precipitation lapse rate, ice rheology, bed strength and the degree day melt factors (DDF) for snow and ice.

Thirdly, sensitivity experiments were run to quantify the impact of the tuned parameters on model output. Model sensitivity to temperature and precipitation, were then assessed. When one or more variables were tested, the remaining variables were fixed to default values (Table 7.4).

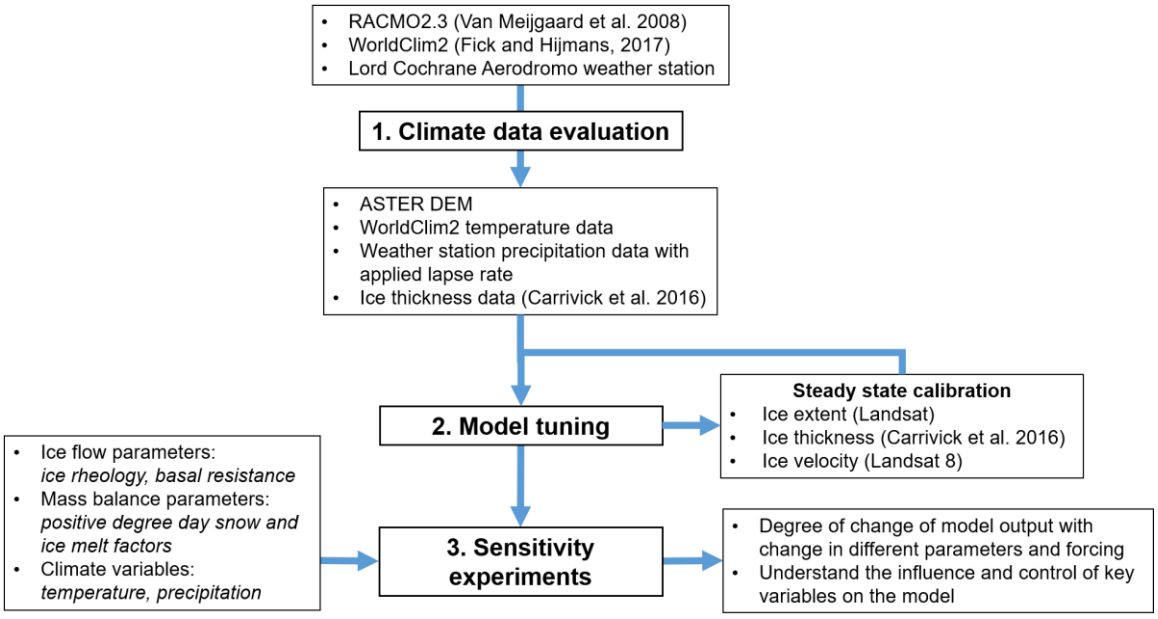

Figure 7.1. Modelling strategy for this study outlining the inputs and outputs of each phase of the investigation through climate data evaluation, model tuning and sensitivity experiments.

PISM is written within the Python programming language, operated within a Unix based environment. Processes were distributed across 12 computational cores. A modelled estimate of present-day ice thickness (section 7.3.4.1, Figure 7.5j) (Carrivick et al., 2016) was used as a starting point for the model. The model was run on a 250 m (x, y) by 20 m (z) resolution gridded domain over an area of 80 km by 108 km (x, y) by 5 km (z), reflecting 138,993 horizontal grid cells, 200 vertical ice layers and 50 bedrock layers. For precipitation and temperature sensitivity

experiments, where simulations produce a significantly greater volume of ice, a 500 m (x, y) resolution grid was used to enable feasible wall-clock run times of less than 24 hours. A multi-phase spinup was used to mitigate against false mass changes at the start of the simulations due to coupling shocks and was run under constant-climate conditions. A short smoothing run was first performed with simplified physics, followed by two longer runs with increasingly evolved ice physics. The final phase used the full hybrid ice physics model and was run to allow the modelled ice to reach an approximate equilibrium state of constant ice area and volume. This occurred after 100 to 500 model run years. 193 model runs were undertaken during model setup and testing and when writing and testing run scripts. Two data evaluation, 11 tuning and 38 sensitivity targeted experiments were then run, the setup and results of which are documented in sections 7.4 (Table 7.5).

7.3. Data for numerical model initialisation

This section outlines, evaluates and selects the data required for PISM initialisation and set up. PISM is initialised using spatially variable precipitation and temperature datasets, a bedrock DEM, 'present-day' ice thickness and a constant geothermal basal heat flux. Each of these forcing factors are described in detail below.

7.3.1. Ice thickness and bedrock digital elevation model (DEM)

In the absence of ice-thickness surveys of MSL outlet glaciers (section 7.3.3), 'present-day' ice thickness data is taken from a dataset derived from the output of a perfect-plasticity model (Carrivick et al., 2016) where ice thickness h is estimated based upon τ_b the basal shear stress, f the shape factor needed to account for valley sides supporting the glacier's weight, p the ice density, and α the ice surface slope.

$$h = \frac{\tau_b}{fpg\tan\alpha} \qquad (7.1)$$

For this dataset, glacier centre lines were mapped manually by Carrivick et al., (2016). Glacier outlines and drainage basins used for the model were mapped from Landsat Enhanced Thematic Mapping Plus (ETM+) images from 2010-2011 (Davies and Glasser, 2012). An ice thickness error of ± 11% is reported, introduced to the model through the assumption that the ice behaves under perfect-plasticity and through the spatial interpolation from the ice thickness modelled at the centreline to the ice thickness across the entire glacier width (Carrivick et al., 2016). This degree of error is in line with that observed globally when modelled ice thickness is compared to radar measurements (Li et al., 2012; James and Carrivick, 2016). However, with these potential sources of uncertainties understood and acknowledged, it is advantageous to use a modelled ice thickness derived bedrock DEM rather than a surface DEM for PISM initialisation.

A bedrock DEM was therefore produced by subtracting the modelled ice thickness from an ASTER GDEM in ArcMap v10.3.

7.3.2. Geothermal heat flux

Due to the absence of geothermal empirical data in Patagonia, a modelled value for the basal heat flux across the domain is used (0.07842 Wm^{-2}) based upon the relationship between basal heat flux and geology over a 2° by 2° equal area grid (Davies, 2013). Although this relationship is found to be limited, it presents a value more accurate than that of assuming a global average. The granitic lithology of the MSL massif may lead to a locally higher geothermal heat flux due to higher concentration of radioactive elements (Haenel et al. 1988), however there are no empirical data constraining this.

7.3.3. Precipitation and temperature climate data

PISM must be forced using two-dimensional gridded mean annual precipitation and surface air temperature datasets, either in the form of modelled climate data or meteorological station point data extrapolated over the domain by applying temperature and precipitation lapse rates. Seasonal variations are accounted for by applying a cosine yearly cycle function to the mean annual surface air temperature dataset (section 7.3.4.1.).

7.3.3.1. Meteorological station data

The nearest meteorological station to the MSL ice cap is located on the western lateral moraine of San Lorenzo Sur Glacier (47°42'S, 72°19'W, 1140 m asl) (Figure 7.2), from which Falaschi et al. (2015) report a mean annual air temperature of 3.8°C measured over the period from 2002 to 2013 using a HOBO temperature logger. The nearest station recording both temperature and precipitation is at Lord Cochrane Aerodromo (47°15'S, 72°35'W, 182 m asl) 40 km to the north of MSL and 3624 m below its summit. Data recorded after 2000 is largely absent, however a full record from 1970 to 2000 documents a mean annual temperature of 9.4°C (ranging from 8.4°C to 10.8°C) and mean annual precipitation of 726 mm a^{-1} (ranging from 522 mm a^{-1} to 1187 mm a^{-1}) The two mean annual temperature records from San Lorenzo Sur and Lord Cochrane Aerodromo at 1140 m asl and 182 m asl respectively give a temperature lapse rate estimate of 0.0058 °C m^{-1}. This is within the range of observed across Patagonia (0.0048 °C m^{-1} to 0.0072 °C m^{-1} (Table 7.2)).

The low station density in the region, and in particularly across the MSL ice cap in the case of this study, means that measured climate data must be extrapolated, or modelled climate data used to obtain a spatially variable record of temperature and precipitation across the entire study region. Two modelled climate gridded datasets, the Regional Atmospheric Climate Model

(RACMO), version 2.3 for Patagonia (Lenaerts et al., 2014) and WorldClim 2 (Fick and Hijmans, 2017), were therefore investigated for their applicability to the study area and potential use to drive PISM spinup to 'present-day' conditions.

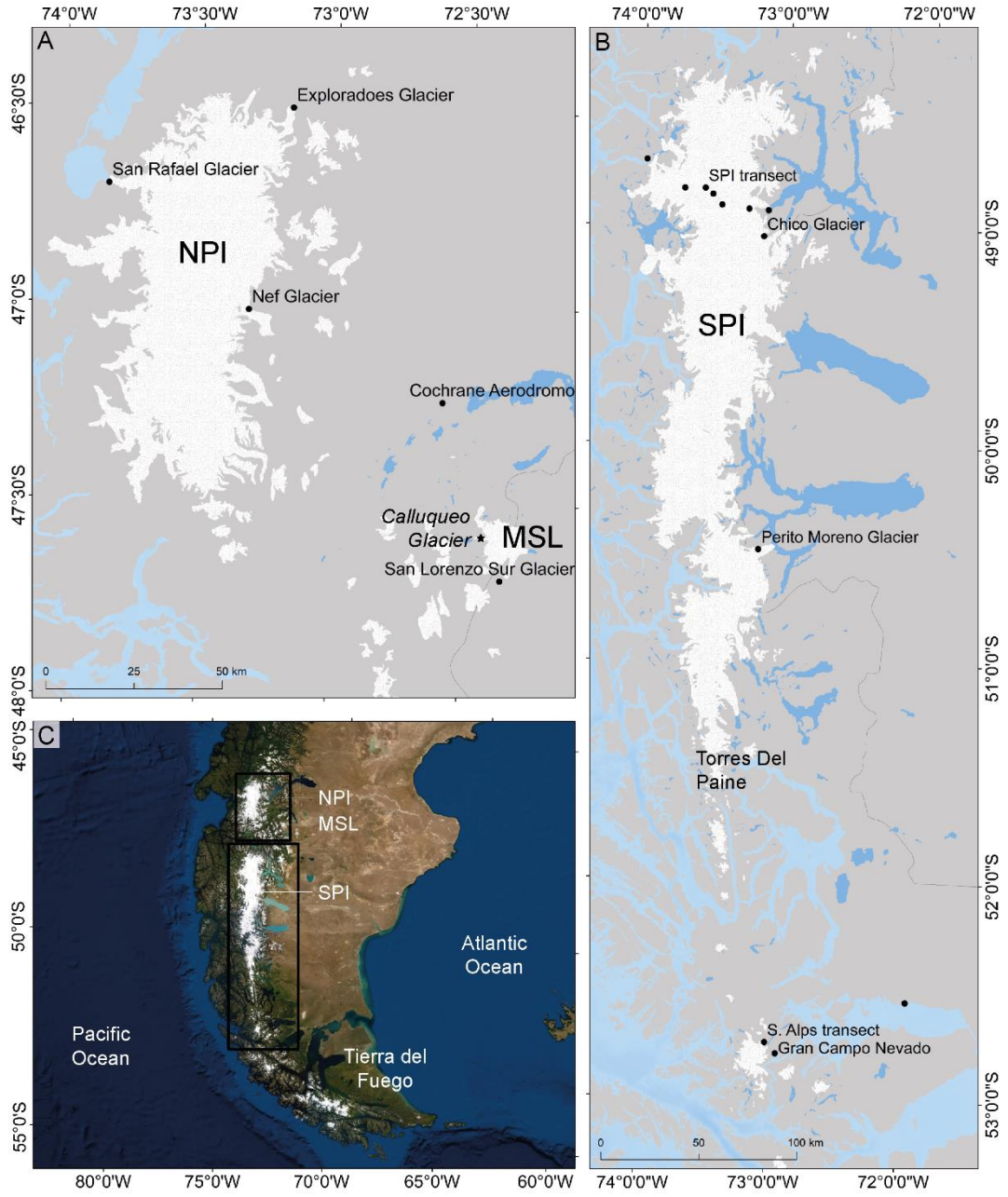

Figure 7.2. Maps highlighting sites of meteorological stations (black circles) from the NPI (A) and SPI (B) as well as MSL.

7.3.3.2. RACMO2.3

RACMO2.3 is the latest version of the regional atmospheric climate model developed by the Royal Netherlands Meteorological Institute (KNMI) (Van Meijgaard et al., 2008). RACMO2.3 employs the dynamical core of the High-Resolution Limited Area Model (HIRLAM) (Undén et al., 2002) with the atmospheric physics module from the European Centre for Medium-Range Weather Forecasts Integrated Forecast System cycle CY33r1 (ECMWF-ISF) (Noël et al., 2015).

RACMO2.3 has been applied to Antarctica (e.g. Lenaerts et al., 2013; Van Wessem et al., 2014), Greenland (e.g. Noël et al., 2015; Steger et al., 2017) and Patagonia (PAT5.5, Lenaerts et al., 2014)). PAT5.5 consists of a 330 by 254 point grid at 0.05° (5.5 km) resolution of monthly temperature and precipitation data for the period 1979 to 2012. The dataset covers southern South America, from northern Patagonia (41°S) to the Drake Passage south of Chile (57°S).

7.3.3.3. WorldClim2

The WorldClim2 dataset (Fick and Hijmans, 2017) consists of gridded 30 arc-second (*ca* 1 km) spatial resolution monthly climate data (temperature, precipitation, solar radiation, vapour pressure and wind speed) for global land areas between 1970 and 2000 (Figure 7.3). The dataset is derived from monthly average climate data sourced from weather station records globally which are interpolated using a thin-plate smoothing spline (Hutchinson and Xu, 2013). Records from between 1960 and 2010 were considered providing they contained at least 10 years of data, although the greatest frequency of observations came from the period 1970 to 2000. This assumption was under the premise that for remote locations, larger error would be introduced from low station data density than from taking data from a wider temporal range. For the mean temperature element, following implementation of selection criteria, data is taken from 20268 stations globally (2833 in South America). Maximum and minimum land surface temperature and cloud cover from the Moderate Resolution image Spectroradiometer (MODIS) satellite and covariates of elevation and distance to the coast were also included in the interpolation. The final climate surface output was derived from a combination of model formulations, chosen specifically for each variable and region depending on their performance in a 3° by 3° "checkerboard' cross-validation test.

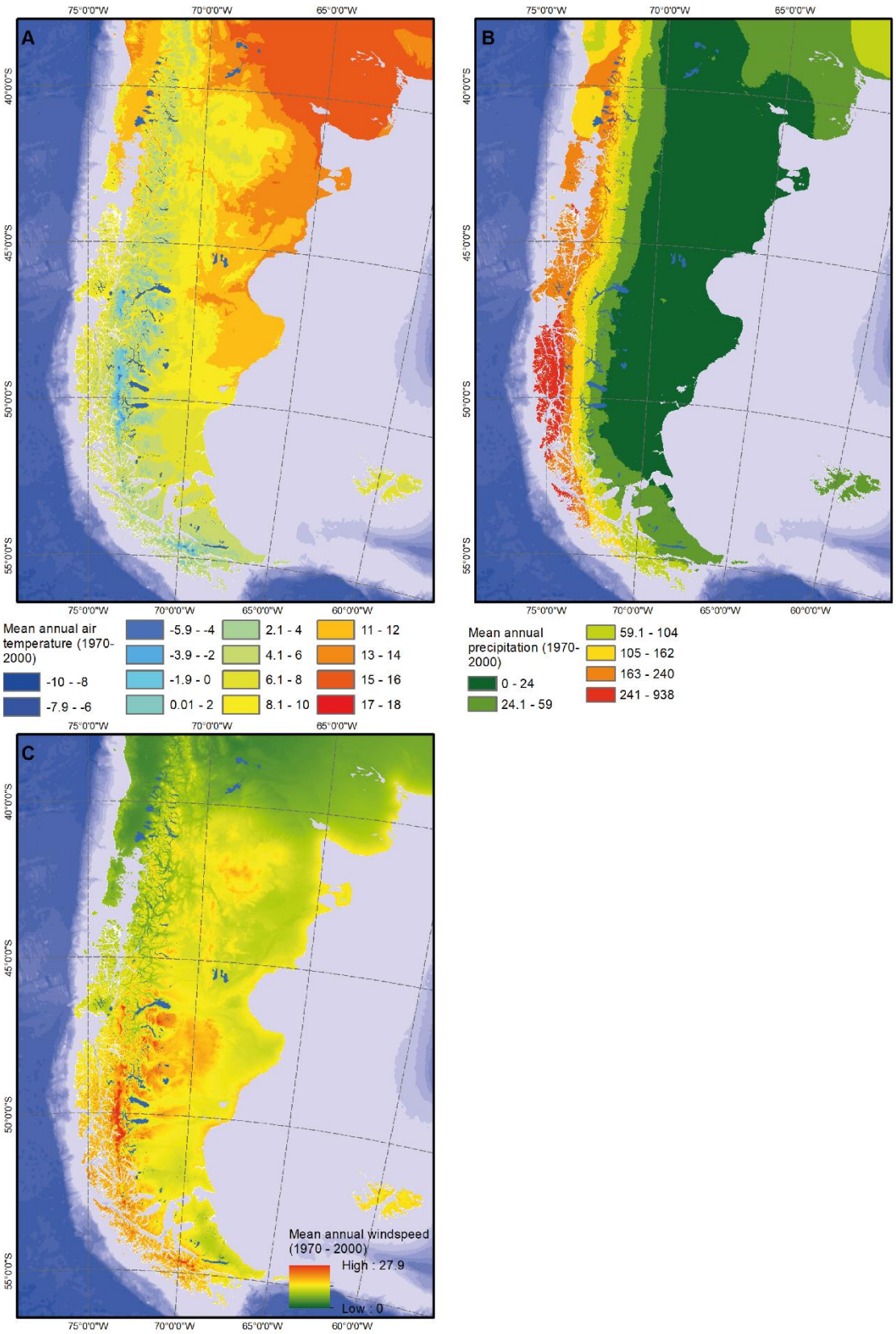

Figure 7.3. A) Mean annual air temperature (°C), B) mean annual precipitation (mm) and C) mean annual air windspeed (m s^{-1}) for the period 1970-2000 at 30 arc seconds resolution, from the WorldClim2 dataset (Fick and Hijmans, 2017). From Davies et al. (accepted).

7.3.4. Modelled climate data comparison to Lago Cochrane Aerodromo meteorological data

7.3.4.1. Surface air temperature

Average annual and monthly measured temperature and precipitation climate records from Lord Cochrane Aerodromo for the period 1970-2000 were compared to the respective modelled data from RACMO2.3 PAT5.5 and WorldClim2, alongside examinations of the datasets' modelled climate values for precipitation and temperature at Calluqueo Glacier, MSL (Table 7.1), to establish which dataset is most appropriate to use to force PISM under 'present-day' climate conditions. For surface air temperature, mean annual temperature point values, effective lapse rates, cosine yearly temperature cycles and dataset resolution are all assessed.

Table 7.1. Point climate data and calculated lapse rates from instrumental records, RACMO2.3 and WorldClim2. Lapse rates are calculated relative to Cochrane Aerodromo. Instrumental data from Cochrane Aerodromo meteorological station and WorldClim2 modelled climate data covers the period 1970 to 2000. Modelled climate data from RACMO2.3 covers the period 1979 to 2000.

Location	Coordinates	m asl	Mean annual surface air temperature (°C)			Lapse rate (°C/m)		Mean annual precipitation (mm)			Lapse rate (mm/m)	
			Instrumental data	RACMO	WorldClim	RACMO	WorldClim	Instrumental data	RACMO	WorldClim	RACMO	WorldClim
Cochrane Aerodromo	47°14’37"S, 72°35’06"W	182	9.4	9.1	8.6			726	741	740		
Calluqueo tongue	47°35’05"S, 72°27’25"W	600		1.4	6.3	-0.0184	-0.0056		3042	555	5.5048	-0.4426
San Lorenzo Sur	47°41’46"S, 72°21’04"W	1140	3.8	-1.0	3.8	-0.0105	-0.0058		2175	547	1.4812	-0.2182
Calluqueo mid	47°35’32"S, 72°23’20"W	1500		-2.4	1.9	-0.0087	-0.0051		6640	619	4.4755	-0.0918
Calluqueo upper	47°36’07"S, 72°21’40"W	2000		-4	-1.1	-0.0072	-0.0054		7225	645	3.5669	-0.0523

At Cochrane Aerodromo, both RACMO2.3 and WorldClim2 have temperature point values within 1 °C of the instrumental data (Table 7.1), although of this WorldClim2 is notably colder. However, with increased elevation at Calluqueo Glacier, RACMO2.3 modelled temperature is unrealistically cold compared with the meteorological data (Table 7.1; Falaschi et al., 2013). The calculated lapse rates based upon RACMO2.3 point values (0.0072 °C m^{-1} to 0.018 °C m^{-1}) also suggest that the modelled air temperature values from RACMO2.3 are unrealistically cold within the context of those observed across Patagonia (Table 7.2). WorldClim2 produces lapse rates (0.0051 °C m^{-1} to 0.0056 °C m^{-1}) more akin to the observed regional values, including the lapse rate between San Lorenzo Sur and Lord Cochrane Aerodromo (0.0058 °C m^{-1}).

Table 7.2. Observed temperature lapse rates from across Patagonia. Locations are shown on Figure 7.2.

Location	Grid reference	Temperature lapse rate (°C m^{-1})	Source	Reference
Frias Glacier	41°09' S, 71°50' W	0.0048	Reanalysis data	Leclercq et al. (2012)
Exploradores Glacier	46°30' S, 73°10' W	0.0053	Met. station	Inoue et al. (1987)
San Rafael Glacier	46°40' S, 73°50' W	0.0055	Reanalysis data	Koppes et al. (2011)
Cochrane – San Lorenzo Sur Glacier	47°15' S, 72°34' W-47°41' S, 72°17' W	0.0058	Met. station	Falaschi et al. (2013)
SPI transect	48°45’ S	0.0072 (east), 0.0055 (west)	Met. station	Bravo et al. (2019)
SPI	50°38' S, 73°15' W	0.0053	Assumed	Aristarain and Delmas 1993
Gran Campo Nevado	52°48’S, 72°56’W	0.0062	Met. station	Schneider et al. (2003)

In order to create seasonality within the mean annual temperature dataset, PISM has the facility to use a cosine yearly cycle temperature model, with the option of amplitude scaling (*A*). The annual temperature cycle is based upon mean annual and mean July temperatures and the year fraction since the previous July (*t*) (equation 7.1).

$$T(\text{time}) = T_{\text{mean annual}} + A(\text{time}) \cdot \left(T_{\text{mean July}} - T_{\text{mean annual}}\right) \cdot \cos(2\pi t) \qquad (7.2)$$

The fit was therefore examined between average monthly measured climate data at Cochrane Aerodromo and the cosine yearly cycle climate model produced by PISM for this location based upon RACMO2.3 and WorldClim2 mean annual and mean July temperatures (Figure 7.4). From this we determine which dataset, when an amplitude scaling is applied, best fits the instrumentally measured seasonality.

It is evident that cosine yearly temperature cycles based upon data from RACMO2.3 and WorldClim2, without an amplitude scaling factor applied, do not produce the required amplitude of the measured annual temperature cycle (Figure 7.4A). The amplitude scaling factors which produce the best-fit annual temperature cycles to the measured cycle and are 1.55 and 1.25 for RACMO2.3 and WorldClim2 respectively (Figure 7.4A and B). Of these, WorldClim2 produces the closest fit to the measured instrumental climate cycle at Cochrane Aerodromo (Figure 7.4D), producing a temperature cycle ranging from 1.5°C to 15.8°C (measured temperature cycle ranges from 1.8°C to 15.6°C, RACMO range from 1.5°C to 16.7°C).

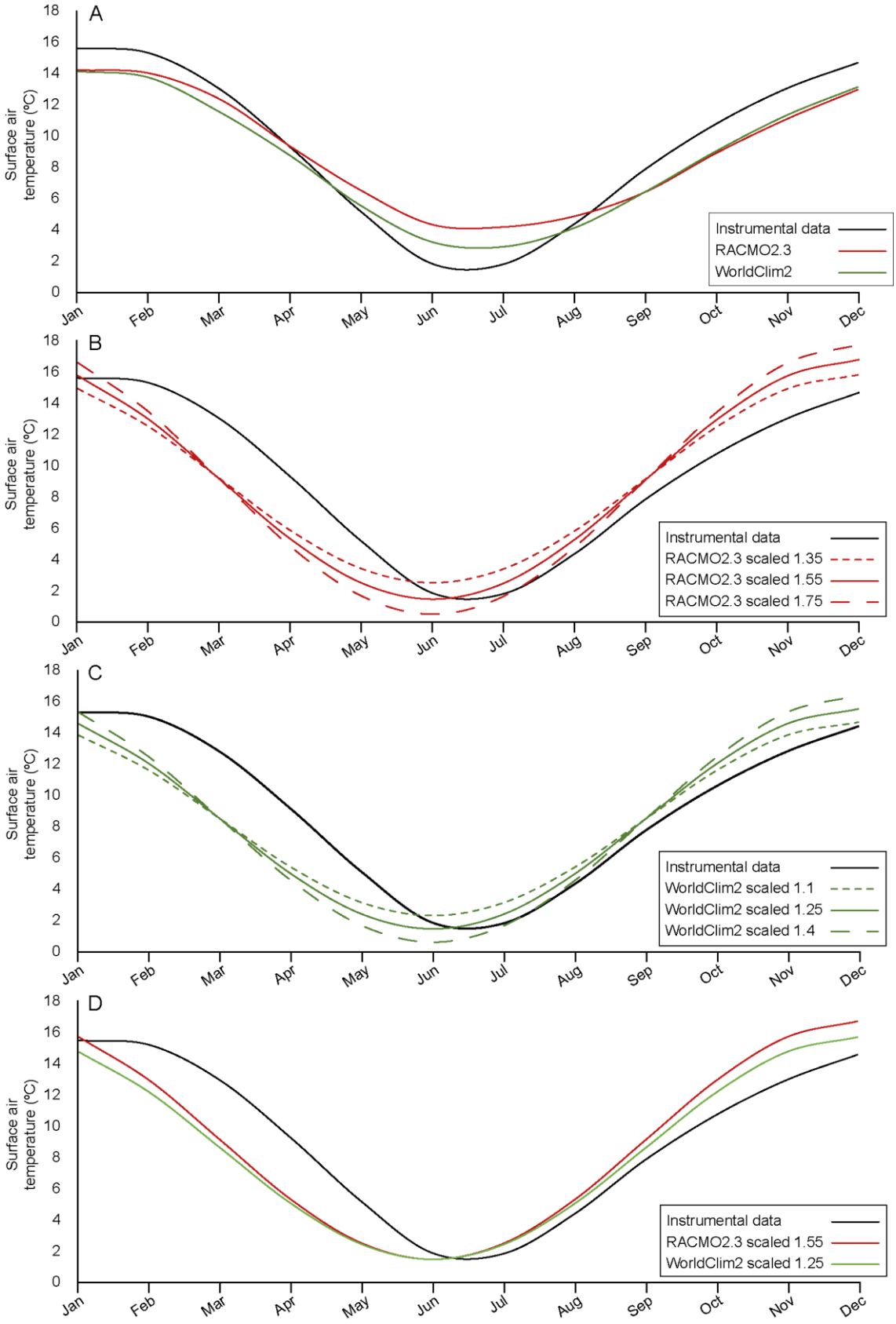

Figure 7.4. Comparisons of annual temperature cycles from instrumental data from the Cochrane Aerodromo meteorological station and cosine curves for modelled climate data: A) with no amplitude scaling factors applied, B) RACMO2.3 data with amplitude scaling factors applied, C) WorldClim2 data with amplitude scaling factors applied and D) RACMO2.3 and WorldClim2 data with 1.55 and 1.25 amplitude scaling respectively, representing the best fit scaled cosine curves with the meteorological station data.

7.3.4.2. Data grid resolution

When modelling glaciers with steep long profiles (e.g. Calluqueo with a surface profile *ca* 20° gradient over a 7.75 km distance), it is important to take into account the resolution of climate dataset being used to initialise the model. This is important because elevation and in turn surface air temperature and precipitation change over a small horizontal distance. A climate dataset with an insufficient resolution will be unable to resolve these climatic changes. The higher resolution WorldClim2 dataset is better able to pick out temperature variations across and within the narrow valleys and highly varied mountain topography (Figure 7.5b,i). The lower resolution RACMO dataset is unable to affectively pick out such changes. Notably the cold region over the summit of MSL extends further west than WorldClim2, into the lower elevations of Calluqueo valley, resulting in an unrealistically cold valley at low elevations (Figure 7.5e).

Due to appropriate lapse rates and realistic temperatures, amplitude scaled cosine yearly temperature cycles and a higher resolution dataset, the WorldClim2 temperature dataset was used to force PISM under 'present-day' climate conditions, using mean annual and mean July surface air temperature from 1970 to 2000, with an applied 1.25 amplitude scaling factor.

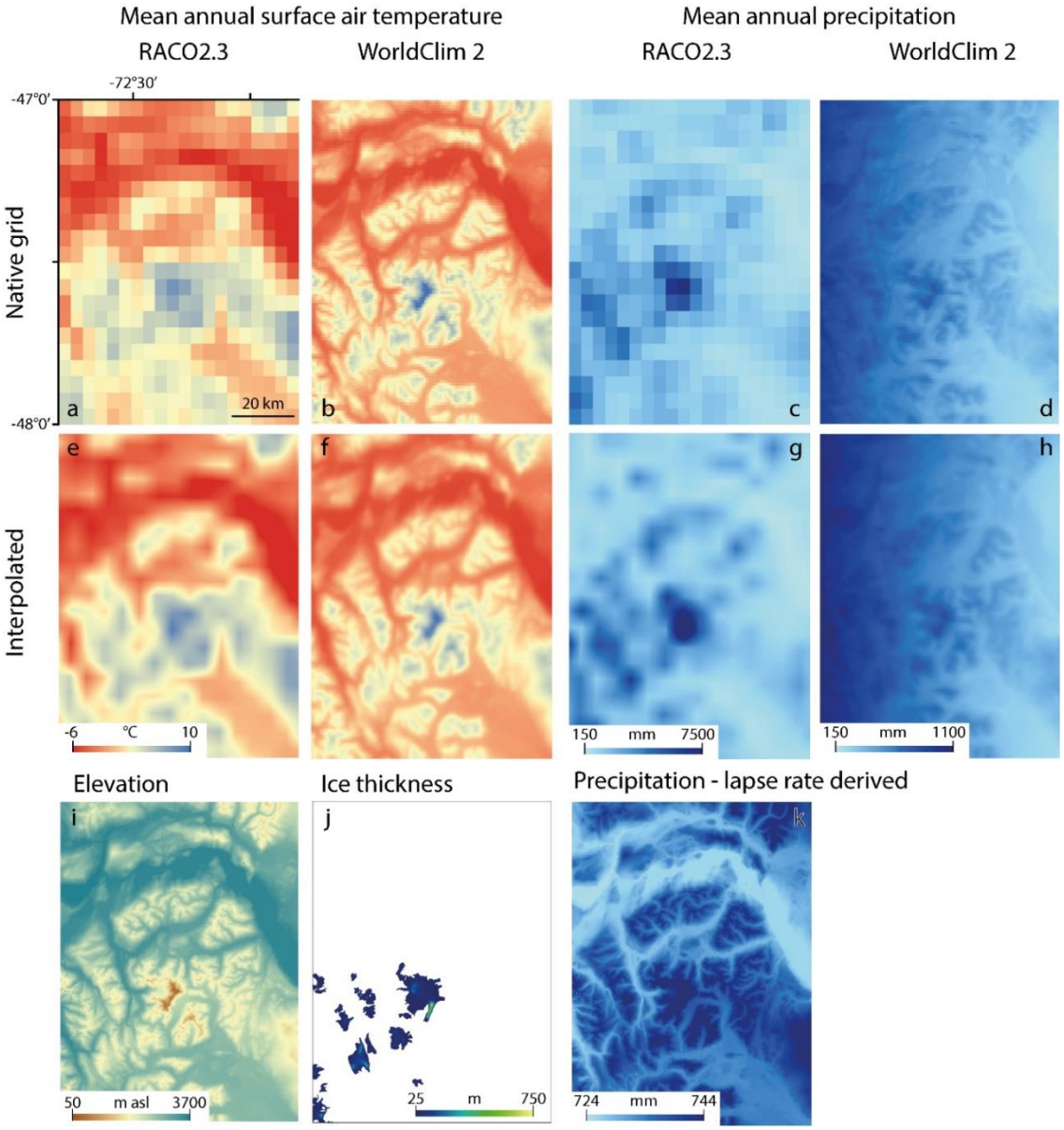

Figure 7.5. a to h) Gridded climate model data evaluated for use in PISM at both native resolution (RACMO2.3: 5.5 km, WorldClim2: 1 km) and bilinearly interpolated for input into PISM. i) ASTER GDEM j) modelled ice thickness data (section 7.3.1 (Carrivick et al. 2016) and k) gridded precipitation dataset derived from Cochrane Aerodromo meteorological station precipitation data, an applied 1.35 mm/m precipitation lapse rate and ASTER GDEM (i) (section 7.3.4.3 and 7.4.2).

7.3.4.3. Precipitation

The RACMO2.3 and WorldClim2 datasets both model mean annual precipitation at Cochrane Aerodromo to be slightly higher than the measured value (Table 7.1). At Calluqueo Glacier, RACMO2.3 models mean annual precipitation up to 7725 mm. This is considered to be an unrealistically high value given measured and modelled precipitation levels across Patagonia (Table 7.3), and MSL's position inland of the Andes. Precipitation lapse rates calculated from RACMO2.3 point data on Calluqueo Glacier also give values higher than the few records from Patagonia (Table 7.3). Annual accumulation on the windward, western side of the NPI at San Rafael Glacier has been measured to between 4800 and 10000 mm (Fujiyoshi et al., 1987;

Escobar et al., 1992; Carrasco et al., 2002), with similar annual precipitation recorded in west of the Southern Andes (Schneider et al., 2003), and reflected in climate modelling (Garreaud et al., 2013). Over the NPI, annual precipitation levels above 15000 mm have been modelled, decreasing to ranges between 10000, 5000 mm and 2000 mm at progressively lower elevations on the ice field (Schaefer et al., 2013b). Such levels of precipitation are also reflected in river discharge models (Escobar et al., 1992). On the eastern, lee side of the SPI, annual precipitation of 4070 mm was measured at Chico Glacier (Rivera 2004), and modelled to be 7600 at 2500 m asl on Perito Moreno Glacier (Stuefer et al., 2007).

Table 7.3. Modelled and measured precipitation and accumulation data across Patagonia.

Location	Latitude and Longitude	Precipitation (m w.e.) (accumulation*)	Precipitation lapse rate (mm m^{-1})	Source	Reference
Lago Aculeo	33°S to 34°S	0.69	0.25	Multiple met. stations	Jenny et al. (2003)
Frias Glacier	41°09' S, 71°50' W	8.2 (2000 m).	1.5	Mass balance model	Leclercq et al. (2012)
Chico Glacier	49°03' S, 73°10' W	4.07 (1440 m)	3 < 1440 m asl. 3.7 > 1400 m asl.	Mass balance model/Met. station	Rivera (2004)
Regional	40°S to 55°S		0.00252	Regional met. station data	Bravo et al. 205
San Rafael Glacier (icefield plateau)	46°40' S, 73°50' W	4.8* to 10*		Met. station	Fujiyoshi et al. (1987) Escobar et al. (1992) Carrasco et al. (2002)
Nef Glacier	47°01' S, 73°19' W	2.2 (1500 m)		Met. station	
NPI		15 to 24 (highest alt.) 5 to 10 (1500-2000 m) 2 to 5 (1000-1500 m)		Mass balance model/reanalysis data	Schaefer et al. 2013
NPI SPI		6.7 7		River discharge model	Escobar et al. (1992)
Patagonia region		5 to 10 (western) 0.5 to 0.7 (east of cont. divide)		Modelled climate	Garreaud et al. (2013)
Perito Moreno Glacier	50°30' S, 73°30' W	7.6 (2500 m) 0.84 (670 m)		Modelled climate	Stuefer et al. (2007)
Southern Andes transect	53°S	4.4 (75°W, 0 m) 10.9 (73°W, 383 m) 0.9 (71°58' W, 8 m) 0.5 (70°53' W, 6 m)		Met. station	Schneider et al. (2003)

MSL's location 90 km inland of the Andes, at the edge of the rain shadow and sharp contrast between vegetated and arid landscapes, would suggest a lower annual precipitation than that observed and modelled to its west. Such a decrease in precipitation on the eastern side of the

Andes is reflected in the mean annual measured precipitation at Cochrane (726 mm), north-northwest of MSL, as well as in modelled and measured precipitation at other low elevation sites east of the Andes range (Schneider et al., 2003; Stuefer et al., 2007; Garreaud et al., 2013). MSL sits at the northern edge of a break in the Andean range and therefore will experience less of a 'rain shadow' effect than those regions latitudinally level with the SPI and NPI. However its location 160 km inland of the coast, east of mountains at the southern tip of the NPI, will be factors contributing to lower levels of precipitation than at the NPI and SPI which sit closer to the coast without orographic barrier to the precipitation bearing SWW. There is significant absence of precipitation measurements at higher elevations in the mountains to the east of the Patagonian icefields. Precipitation at MSL would be expected to be higher than these values obtained in the low valleys, due to the ice cap's significant elevation, and in particular at Calluqueo Glacier due to the west-facing accumulation catchment and the addition of wind-blown snow. WorldClim2 provides mean annual precipitation values at Calluqueo ranging from 555 mm to 645 mm, lower than instrumentally measured values at Cochrane Aerodromo.

Initialising the ice cap model with WorldClim2 and RACMO2.3 precipitation data (experiment B, section 7.4.1), alongside WorldClim2 temperature data and 'default' physical parameter values (Table 7.4) produced model simulations with too little and too much ice respectively in comparison to present-day ice extent (Figure 7.6). Both RACMO2.3 and WorldClim2 precipitation datasets were therefore considered unrepresentative of precipitation at Calluqueo Glacier, with precipitation being too high and too low respectively. Although the spatial distribution of RACMO2.3 precipitation data across the catchment appears reasonable (Figure 7.2g), scaling down precipitation across the catchment to create a more realistic value at MSL would in turn create unrealistically arid lower-altitude valleys.

A new dataset was therefore created to model precipitation across the domain, based upon the 30 year mean annual measured precipitation value at Cochrane Aerodromo, a given lapse rate and an ASTER GDEM (fig 2i and k). A range of lapse rate values were tested, and a final value selected through the process of model tuning (described further in section 7.4.2) with present-day ice extent, thickness and velocity as a target. This method allows precipitation values at MSL to be tuned while still maintaining a realistic spatial distribution of precipitation across the domain. However, we acknowledge that it does not account for east-west gradients in the complex mountain topography of the study region.

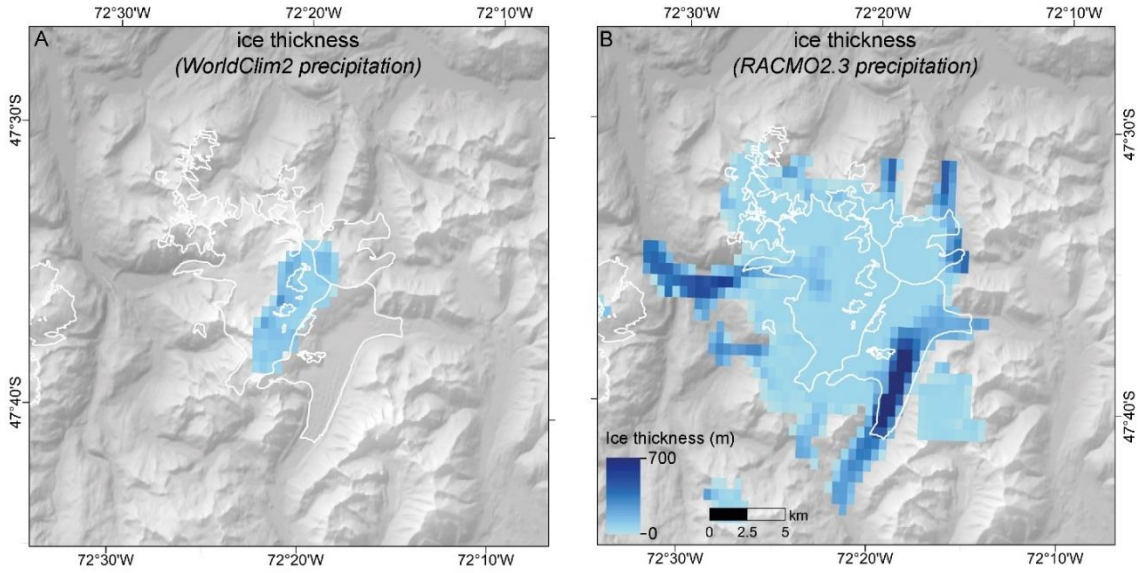

Figure 7.6. Modelled ice thickness when initialised with precipitation from the WorldClim2 (A) and RACMO2.3 (B) modelled climate datasets.

7.4. Model experiments

7.4.1. Model parameter values

Establishing realistic and suitable parameter values within PISM forms the basis of simulating the MSL ice cap. Incorrect model parameter values will lead to unrealistic simulations of the ice cap, skewing interpretations. The model is therefore aligned to match present-day glacier extent, thickness and velocity by tuning the initialising precipitation dataset (through adjusting the precipitation lapse rate) in combination with default established physical constant values from the literature (Table 7.4). Four sensitivity experiments with a total of 38 model runs were then undertaken using parameter value ranges from the literature to explore the impact of variation in ice rheology, bed strength and snow and ice positive degree-day melt factors on the modelled ice cap (Table 7.5). The suitability of the choice of literature-based parameter values and tuned precipitation dataset and is discussed in sections 7.4.3 and 7.5.

Table 7.4. Physical constants and parameter values used within the PISM model of the MSL ice cap.

Name	Default	Units	Description	Source for default value and ranges in Table 7.3
Physical constants				
A	3.8 x 10^{-24}	$Pa^{-3}\ s^{-1}$	Glenn's flow law ice softness coefficient	Gudmundsson (1994) and Paterson (1994)
g	9.81	$m\ s^{-1}$	Acceleration due to gravity	
ρ_i	910	$kg\ m^{-3}$	Ice density	Greve and Blatter (2009)
ρ_w	1000	$kg\ m^{-3}$	Fresh water density	Greve and Blatter (2009)
Fixed default parameters				
e_{ssa}	0.6		SSA enhancement factor	
n_{sia}	3		SIA exponent	
n_{ssa}	3		SSA exponent	
Mz	200		Number of vertical ice layers	
Mbz	50		Number of vertical bedrock layers	
Bed smoothing	50	m	Half-width of bedrock smoothing	
Tuned parameters				
Precipitation lapse rate	1.35*	$mm\ m^{-1}$	Change in precipitation with change in elevation	
Sensitivity tests				
(e_{sia})	3		SIA enhancement factor	Golledge et al., (2012); Putnam et al., (2013); Ziemen et al., (2016); Yan et al., (2018)
(τ_c)	35	kPa	Basal yield stress	Boulton and Jones (1979); Brown et al., (1987); Iverson et al., (1994); Porter et al., (1997); Golledge et al., (2012)
(F_{snow})	3	mm w.e.	Positive degree day melt factor for snow	

(F_{ice})	8	mm w.e.	Positive degree day melt factor for ice	Lang (1986); Takeuchi et al., (1996); Arendt and Sharp (1999); Hock (2003); Anderson and Mackintosh (2006); Schneider et al., (2007); Golledge et al., (2012); Jouvet et al., (2017); Yan et al., (2018)

*Table 7.5. Model tuning and sensitivity experiments included in this study, documenting the number of model runs, variable(s) tested, range of parameters explored, the model resolution and model run lengths for each experiment. *references for selected parameters ranges are given under the respective variable in Table 7.2.*

Experiment	Aim	Number of model runs	Variable(s) tested	Parameter range*	Resolution (m)	Run length (model years)
(A) Data evaluation	Test the suitability of modelled precipitation datasets for initialisation	2	Precipitation dataset	RACMO2.3, WorldClim2	500	250
(B) Tuning	Tune precipitation to match model to present day ice cap	11	Precipitation lapse rate	0.01 – 1.5 mm/m	250	250
(C) Sensitivity	Determine sensitivity of the ice cap to changes in SIA enhancement factor in combination with basal yield stress	9	SIA enhancement factor Basal yield stress	1 – 5 25 – 50 kPa	250	250
(D) Sensitivity	Determine sensitivity of the ice cap to changes in positive degree day melt factors for snow and ice in combination	9	Degree day factor for snow Degree day factor for ice	1.5 – 8 mm w.e. 3 – 16 mm w.e.	250	250
(E) Sensitivity	Determine sensitivity of the ice cap to changes in surface air temperature, offset from present-day	5	Surface air temperature	-1 – -5	500	750
(F) Sensitivity	Determine sensitivity of the ice cap to changes in mean annual precipitation, scaled from present-day	6	Precipitation	75% – 200%	500	500
(G) Sensitivity	Determine sensitivity of ice cap to changes in temperature and precipitation combinations	9	Surface air temperature Precipitation	-1 – -3 125 – 200%	500	500

7.4.2. Model tuning (*Experiment B*)

Due to the absence of an appropriate precipitation dataset (section 7.3.4.3), experiments were run to tune precipitation to simulate the present-day ice cap by changing the lapse rate of the initialising precipitation dataset. A range of precipitation lapse rates from 0.1 mm m^{-1} to 1.5 mm m^{-1} were applied to the 30 year mean annual measured precipitation value at the Cochrane Aerodromo weather station. Default flow enhancement factor (3), basal yield strength (35 kPa) and DDF values (3 mm w.e. snow and 8 mm w.e. ice) were used (Table 7.4) alongside a constant

'present-day' WorldClim2 temperature dataset (section 7.3.3.3). Figure 7.7A shows significant differences in simulated ice extent when the model is forced with precipitation datasets derived from different precipitation lapse rates. Although there are discrepancies between simulated ice extent and present-day ice extent, a simulation forced by a precipitation dataset derived using a lapse rate of 1.35 mm m^{-1} matches closest to the present-day ice extent. Due to the discrepancies around the ice cap (over estimations in the north and south of the ice cap and underestimations of San Lorenzo and Rio Lacteo Glaciers) and with this wider study focusing on Calluqueo Glacier, we aim to obtain a best model fit with Calluqueo Glacier on the western side of the ice cap (Figure 7.7B). The suitability of a lapse rate value of 1.35 mm m^{-1} within a regional context and an assessment of the best fit model scenario is discussed in section 7.5.

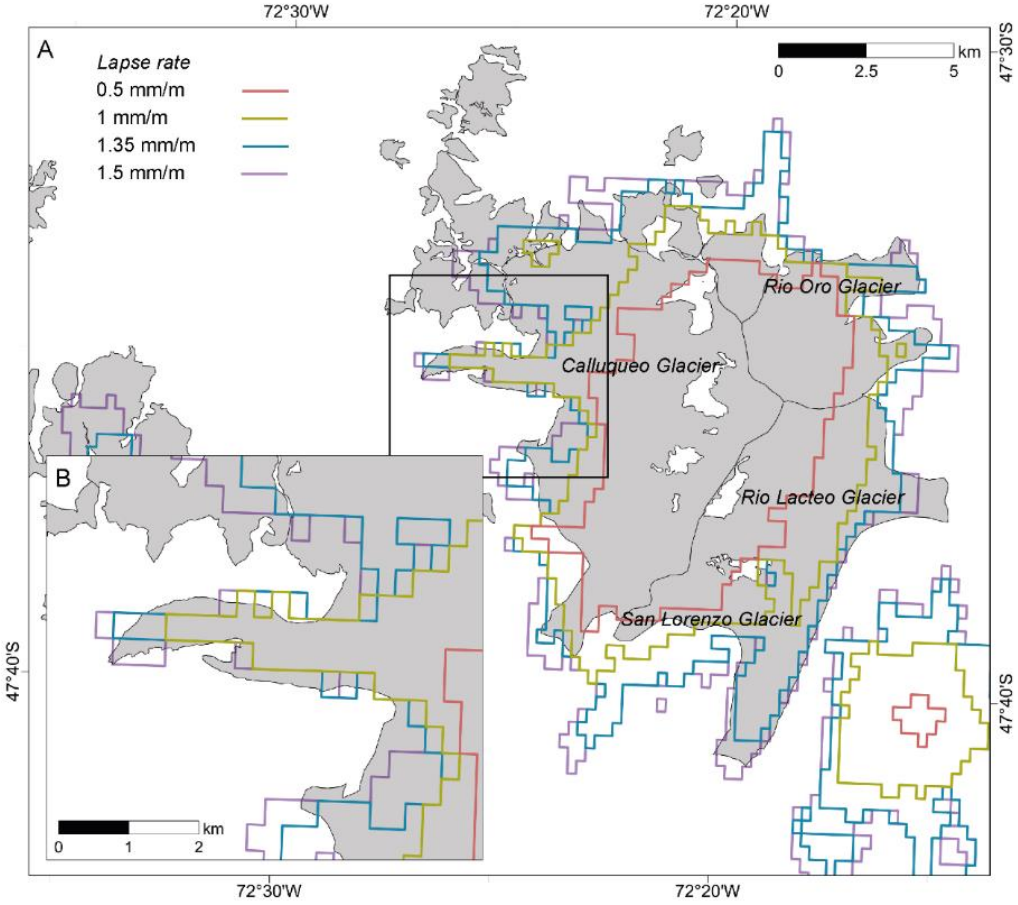

Figure 7.7. A) Simulated ice extent produced by PISM forced using spatially variable precipitation datasets derived from different precipitation lapse rate values. The grey polygon indicates present day ice area. B) inset map of an enlarged section of Calluqueo Glacier.

7.4.3. Model sensitivity experiments

7.4.3.1. Ice rheology and bed strength (*Experiment C*)

The rheology of modelled ice can be adjusted using an enhancement factor to account for variables which may cause increased softening within the ice, such as anisotropy or the inclusion of sediment (Ritz et al., 1996; Parizek and Alley, 2004; Golledge et al., 2012). The shallow ice

approximation enhancement factor is applied to the relationship of the strain rate tensor of the ice with the ice temperature and liquid fraction:

$$D_{ij} = eF(\sigma, T, \omega, P, d)\sigma'_{ij} \quad (7.3)$$

D_{ij}	strain rate tensor	σ	stress
d	grain size	σ'_{ij}	stress deviator tensor
e	enhancement factor	T	ice temperature
P	pressure	ω	liquid factor

This relationship is incorporated within the Glenn-Patterson-Budd-Lliboutry-Duval flow law (Paterson and Budd, 1982; Lliboutry and Duval, 1985; Aschwanden et al., 2012). Values of 1, 3 and 5 were chosen (Table 7.5) to reflect the range of values used and found to fit empirical data in other ice modelling studies in mountain environments (Golledge et al., 2012; Putnam et al., 2013; Ziemen et al., 2016; Yan et al., 2018). A uniform fixed basal yield strength is applied to represent the strength of aggregate material at the ice-bed interface (the PISM authors, 2017). Values of 25 kPa, 35 kPa and 50 kPa were tested (Table 7.5), reflecting a range of measured values (Boulton and Jones, 1979; Brown et al., 1987; Iverson et al., 1994; Murray, 1997; Porter et al., 1997) and those tested in modelled mountain valley glaciers (Golledge et al., 2012). Previous sensitivity analysis of ice rheology and basal yield strength reveals a co-dependency between variables (Golledge et al., 2012) and hence they are tested in combination.

Changing the basal shear strength parameter within PISM acts as a control on ice thickness and extent (Figure 7.8). Although it would be expected that a lower basal shear strength simulating a weaker substrate would lead to a longer and thinner glacier profile (Golledge et al., 2012), the simulations show that the lowest strength value tested (25 kPa) produces the shortest simulation of Calluqueo Glacier. As the model simulations evolve, they show initial rapid glacier advance beyond the final equilibrium position, before recession and stabilisation (Figure 7.8). Calluqueo Glacier advances rapidly at the start of the simulation due to an initial net positive mass balance. The simulation with a basal shear strength of 25 kPa advanced furthest to a maximum distance *ca* 6.25 km down valley of the present-day glacier terminus, whereas the 50 kPa simulation advanced only *ca* 5.25 km ahead of the present-day terminus, but produced a thicker glacier. This difference in glacier extent and thickness is a product of the basal shear strength where low bed strength initially leads to a longer and thinner glacier, with the ice able to flow down valley more readily. Excess ablation then leads to retreat of the terminus back to its equilibrium position (Cuffey and Paterson, 2010). Having established a greater thickness of

ice, the simulation with the stronger bed maintains its length and thickness during the ablation phase better than the thinner glacier formed over the weaker bed.

It is thought that in scenarios of sudden decreases in basal shear strength, e.g. due to the input of meltwater and increase in basal water pressure, the accumulation zone thins as a result of increased mass flux down the glacier, with this thinning propagating down the glacier, increasing its length and reducing its thickness (Fountain et al., 2004; Cuffey and Paterson, 2010).

The simulations show that implementing a flow enhancement factor of 3 produces a longer glacier profile, as would be expected for simulating 'softer' ice which deforms more easily by internal shear (Ritz et al., 1996; Parizek and Alley, 2004). Although not shown on Figure 7.8, implementing an enhancement factor of 5 does not change the glacier's long profile when modelled at a 250 m horizontal resolution. It may be the case that running simulations at a higher resolution would enable the model to pick out these smaller variations in glacier profile.

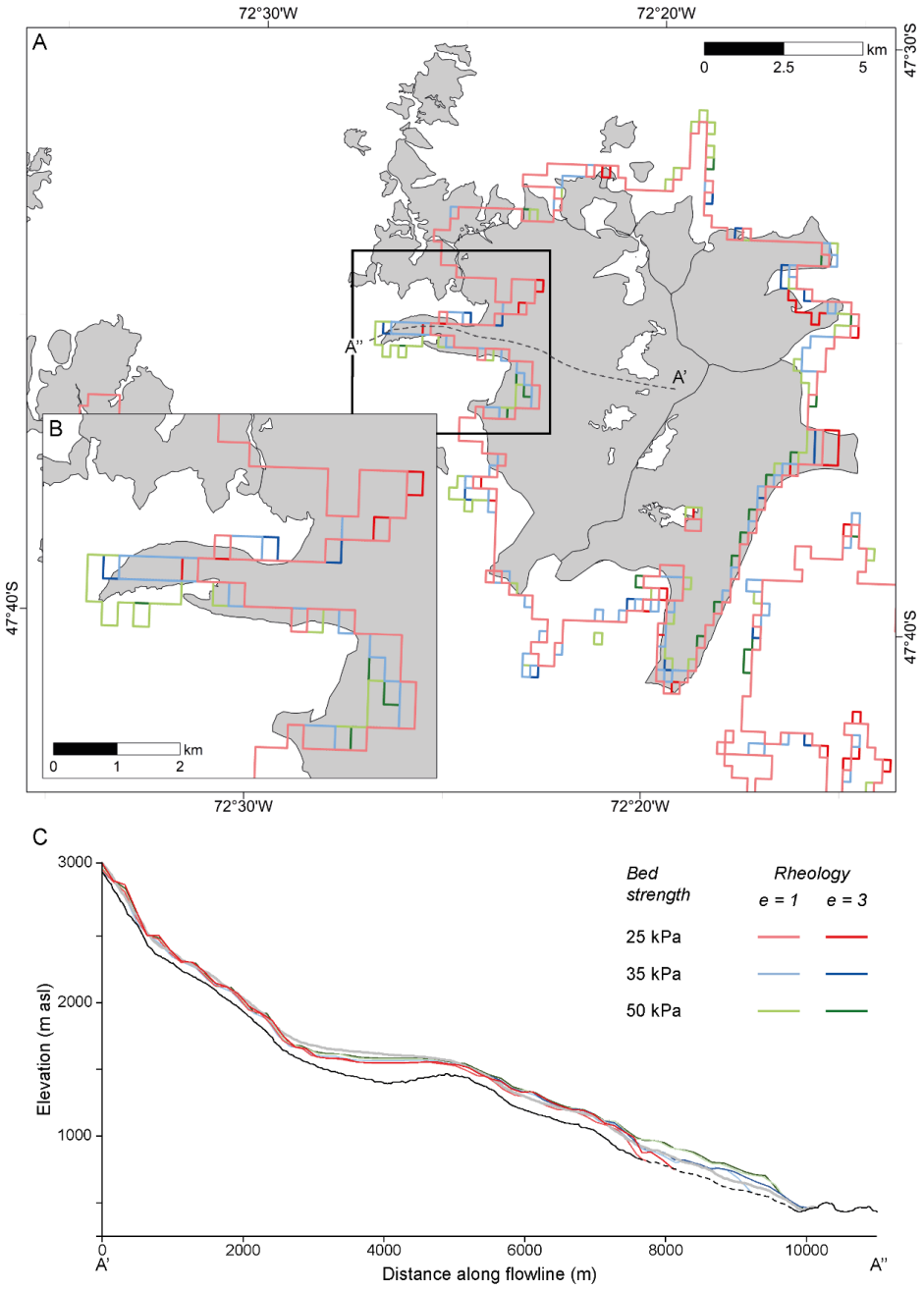

Figure 7.8. A) Simulated ice cap extents at MSL under different basal shear strengths and flow enhancement factors. Coloured lines correspond to legend in Figure 7.8C. B) Inset map focusing on Calluqueo Glacier. C) Long profile of Calluqueo Glacier, corresponding to the profile A' A" in Figure 7.7A. Note the modelled bedrock (section 7.3.1) is unable to resolve a realistic bed at the lower section of the glacier, indicating an ice thickness of zero. The bed geometry is therefore estimated and shown by a dotted black line.

7.4.3.2. Positive degree day melt factors (*Experiment D*)

For sensitivity experiments D, E and F of other model parameters (Table 7.5), a shallow ice approximation enhancement factor and basal yield strength of 3 and 35 kPa respectively were set as mid-range values, in line with those found to best fit a similar mountain valley glacier setting in New Zealand's Southern Alps (Golledge et al., 2012) and within the range observed globally (Table 7.4).

Glacier mass balance is determined in PISM by the implementation of a positive degree-day (PDD) model (section 3.7.2). Such a model is based upon the principle that snow and ice melt is strongly correlated to surface air temperature (Braithwaite and Olesen, 1989), due to its correlation with melt-driving energy balance components, in particular longwave atmospheric radiation and sensible heat flux (Sato et al., 1984; Braithwaite and Olesen, 1990; Lang and Braun, 1990; Hock, 2003). Degree-day factors for snow and ice are key parameters for surface melting, determining the thickness of snow and ice melted per degree per PDD. These are constants within PISM's degree-day model and can be tuned. Degree-day factor values vary spatially and temporally (Table 7.6), dictated by the relative weighting of individual components providing energy for melt (Hock, 2003). Where sublimation dominates in dry, high radiation areas, low degree-day factors are found, with less energy available for melt (Lang and Braun, 1990). Maritime environments in comparison to continental climates experience lower degree-day factors due to a larger degree of turbulent fluxes such as condensation. Elements such as higher air temperature and wind speed also dictate degree-day factors, resulting in a higher contribution of sensible heat flux relative to melting and in turn smaller degree-day factors, seen at lower elevation at the Greenland ice sheet (Ambach, 1988).

Table 7.6. Measured degree day factors in mm w.e. d-1 °C in part after Hock et al. (2003).

Location	Degree day factor (snow)	Degree day factor (ice)	Reference
Chico Glacier	4	6.5	Rivera (2004)
Perito Moreno Glacier		2.7 to 4.3	Stuefer et al. (2007)
		7.1	Takeuchi et al. (1996)
Franz Josef Glacier (NZ)	3	6	Bravo et al. (2015) after Woo and Fitzharris (1992)
	4.6	7.2	Anderson et al. (2006)
Campo Nevado Ice Cap		7.6	Schneider et al. (2007)
Aletschgletscher (Switzerland)	5.3		
John Evans Glacier (Canada)	2.7 to 5.5	5.5 to 7.6	Arendt and Sharp 1999

To assess the sensitivity of modelled glaciers at MSL to changes in degree-day factor values, a range in mm water equivalent (mm w.e.) of 1.5, 3 and 8 for snow and 3, 8 and 16 for ice were chosen to reflect the range observed in Patagonia mountain glacier settings globally (Table 7.6) (Lang, 1986; Takeuchi et al., 1996; Arendt and Sharp, 1999; Hock, 2003; Anderson B. et al., 2006; Moller et al., 2007; Schneider et al., 2007) and in line with previous mountain glacier modelling sensitivity studies (e.g. Golledge et al., 2012; Jouvet et al., 2017; Yan et al., 2018). For testing the

sensitivity of other model parameters, degree-day factor values of 3 mm w.e. and 8 mm w.e. are used for snow and ice respectively in line with aforementioned previous modelling studies and similar to those measured in southern Patagonia (3.5 mm w.e. snow and 7 to 7.6 mm w.e. ice at Gran Campo Nevado (Moller et al., 2007; Schneider et al., 2007) and 2.7 to 7.6 at Perito Moreno Glacier (Stuefer et al., 2007)). Local variations in albedo, slope, aspect, wind, shading and surface roughness dictated by topography can cause local variation in melt rates and degree-day factor values (Hock, 2003; Wake and Marshall, 2015). Hence the implementation of a positive degree-day model may not fully account for processes which could lead to spatial variability in mass balance. By targeting a single ice cap and focus on an individual glacier, the scope of this variation is reduced.

Model simulations show that setting low degree-day factors within PISM's positive degree-day model produce a greater ice extent, while high degree-day factors lead to a smaller ice extent (Figure 7.9). When using low degree-day factors (e.g. values of 3 and 1.5 for ice and snow respectively), outlet glaciers flowing into low altitude valleys experience less melt for the same surface air temperature as when higher degree day factors are used. This results in ice maintained in the low altitude valleys. More specifically, simulations show that for the same increase in degree-day factor for snow and ice, an increase in ice melt causes a greater reduction in ice extent and volume than the same increase in snow melt (Figure 7.9: $F_{snow} = 3$ $F_{ice} = 3$ verses F_{snow} = 8, $F_{ice} = 3$ and $F_{snow} = 3$, $F_{ice} = 8$). This indicates a greater sensitivity of the ice cap to melting of ice in the ablation area than a reduction in mass input in the accumulation area.

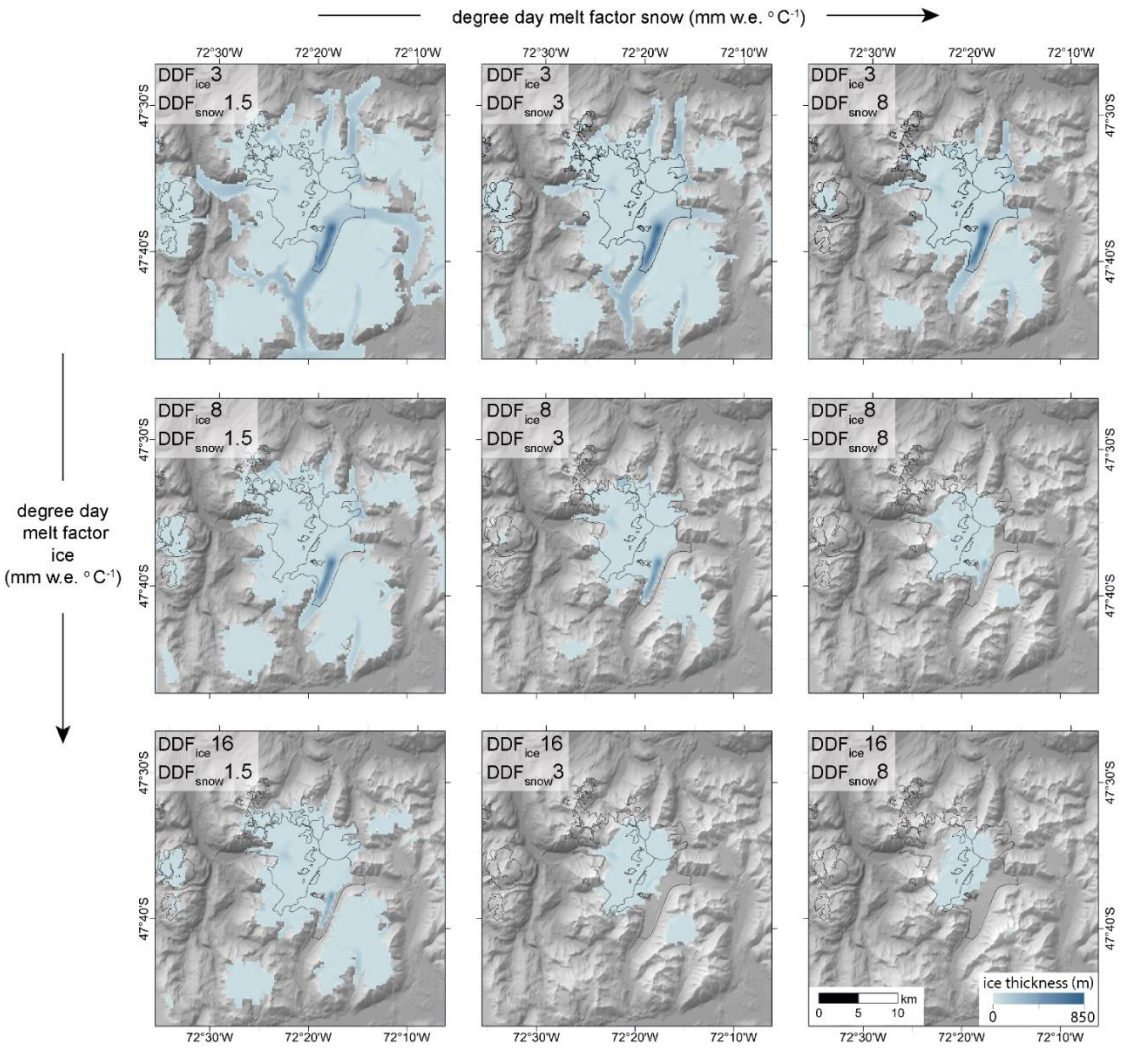

Figure 7.9. Model simulations of the MSL ice cap under the implementation of different degree-day factors within PISM's positive degree-day model.

7.4.3.3. Precipitation and temperature (*Experiments E, F and G*)

In order to then further establish the control changes in climate have on the modelled ice cap, model simulations are run at stepped changes in mean annual air temperature and precipitation. For mean annual air temperature, offsets at one-degree intervals are applied from -1 to -5 uniformly across the domain from the "present-day" WorldClim2 dataset. For precipitation a percentage scaling of 75%, 100%, 125%, 150%, 175% and 200% are applied across the domain from the "present-day" tuned precipitation dataset (section 7.4.2). For initial sensitivity experiments E and F precipitation scaling and temperature offsets are applied independently and systematically, with one variable changed for each simulation. Precipitation and temperature are then varied in combination in experiment G.

Running constant-climate model simulations with step cooling from -1°C to -5°C illustrates how ice area and volume expands at an increasing rate with progressively colder simulations (Figure 7.10 and Figure 7.11). Ice area increases with colder simulations as the ELA lowers, enabling

widespread ice growth. A thin layer of ice cover extends over areas of highest topography, alongside the growth of outlet glaciers into lower altitude valleys. Figure 7.11 shows how from -4°C to -5°C cooling from present-day, the rate of ice area growth begins to stabilise, while the rate of ice volume growth continues to increase. This is due to the distribution of ice growth at this stage of cooling. At -5°C the large areas of high topography are ice-covered and stable in their thickness. Ice growth is then primarily focused in the low altitude, steep sided valleys where ice is topographically confined and grows to large thicknesses for relatively small increases in ice area.

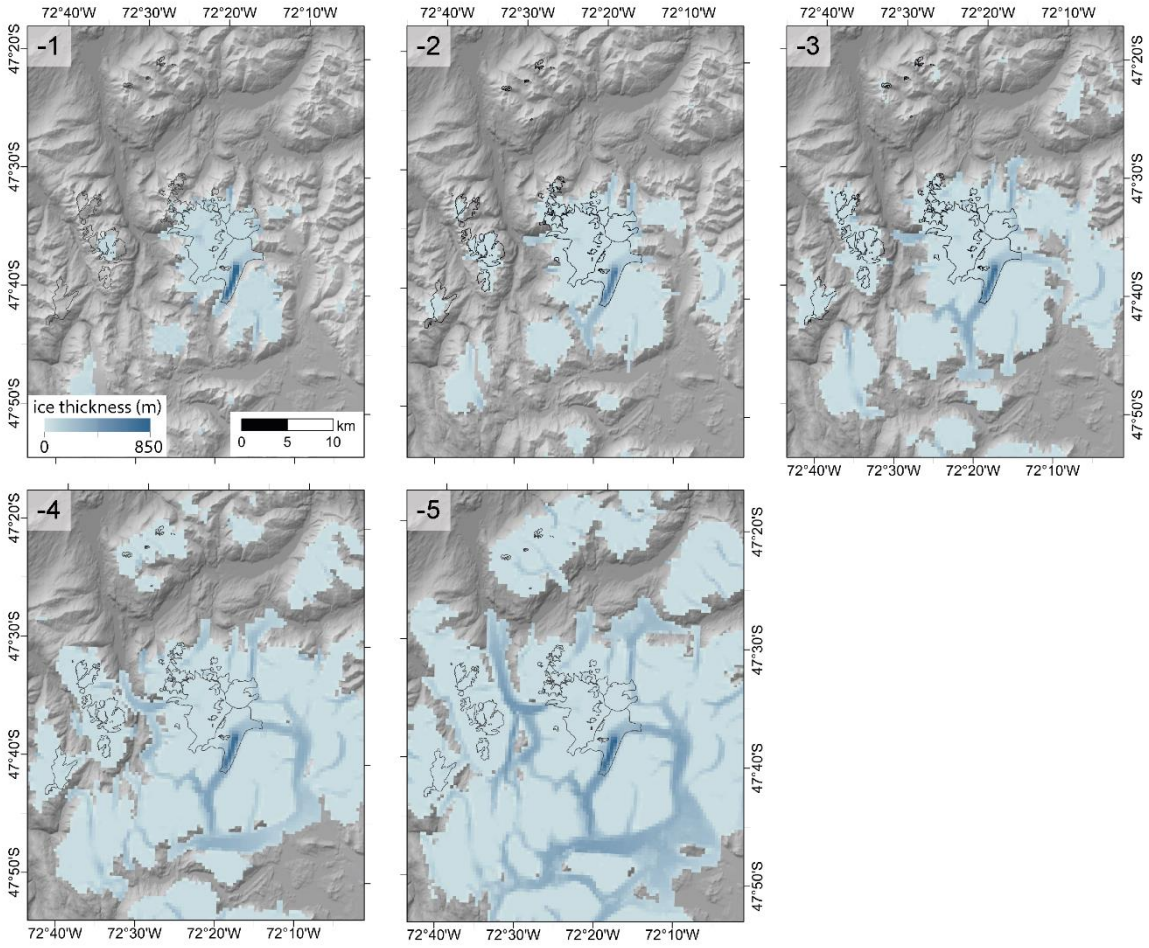

Figure 7.10. Model simulations of the MSL ice cap under surface air temperature step cooling of 1 to 5 °C and present-day constant precipitation. Present-day ice extent shown as black outline.

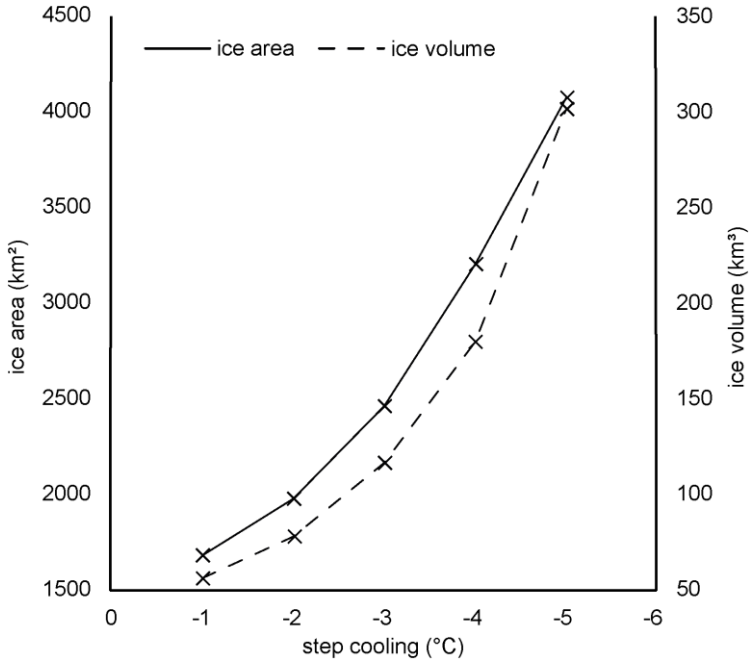

Figure 7.11. Modelled ice area and volume at equilibrium through five simulations under step cooling of -1 to -5 °C, corresponding to those shown in Figure 7.10.

Model simulations forced by increasing levels of precipitation demonstrate an increase in ice area and volume across the model domain (Figure 7.12). Unlike with progressively colder model simulations, ice area does not grow at an increasing rate as precipitation increases (Figure. 7.13). This indicates that an increase in precipitation is not as effective at glaciating unglaciated topography as decreasing surface air temperature. As with step cooling, ice volume increases at an ever-faster rate under greater precipitation forcing, as outlet glaciers begin to occupy lower altitude valleys which provide the topographic space for increasing ice volume growth with proportionally little increase in ice area.

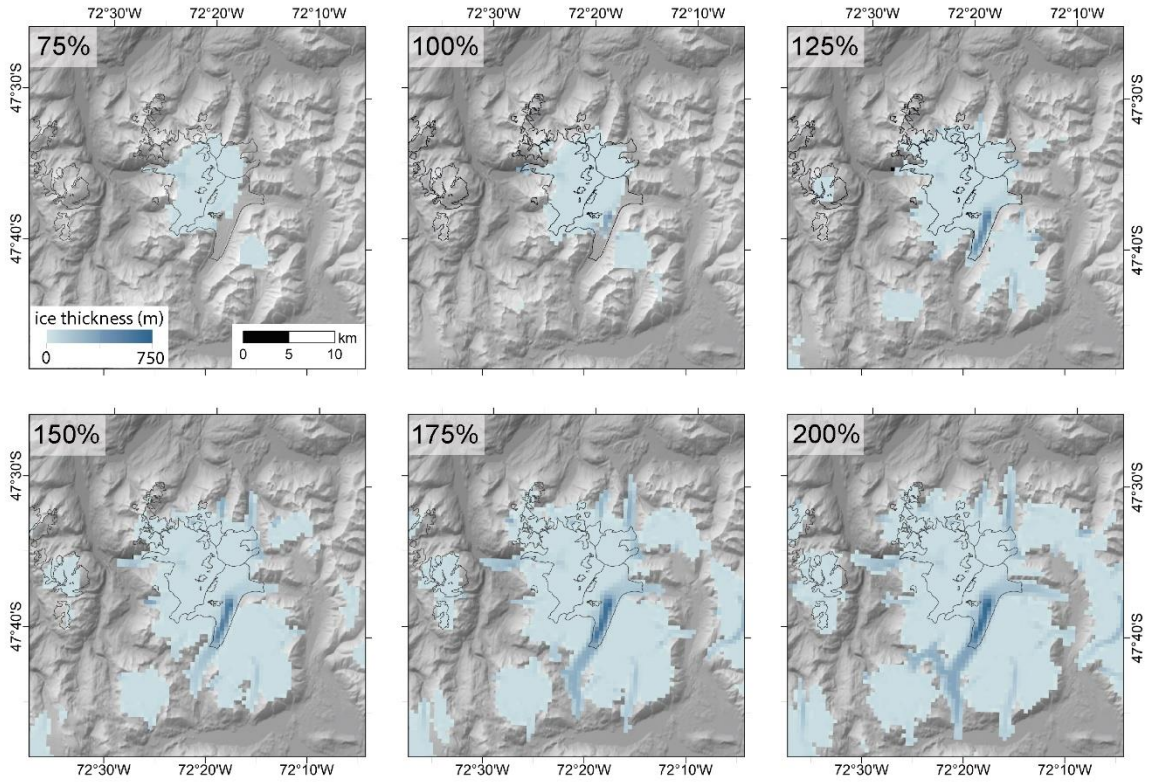

Figure 7.12. Model simulations of the MSL ice cap under increasingly scaled precipitation forcing from present-day. Surface air temperature is set constant to present-day. Present-day ice extent shown as black outline.

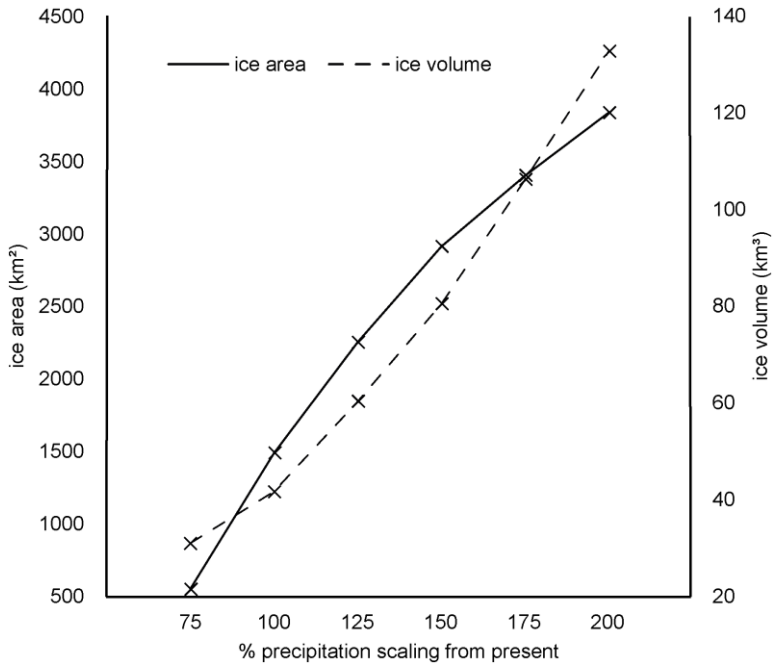

Figure. 7.13. Modelled ice area and volume at equilibrium through five simulations under increasingly scaled precipitation forcing, corresponding to those shown in Figure 7.12.

Model simulations initialised with combinations of decreasing temperature and increasing precipitation lead to significant ice growth. While independently decreasing temperature by 3°C and scaling precipitation by 200% only lead to a relatively small increase in the length of Calluqueo Glacier (*ca* 6 km from the present-day ice front) (experiments E and F, Figure 7.10),

combining this decrease in temperature and increased precipitation lead to a much greater advance in glacier length of 28 km (Figure 7.14). Such a difference in ice growth shows the impact of increased precipitation falling as snow due to the decreased temperature, combined with less of this snow melting annually. The simulation of advanced Calluqueo Glacier growth also shows how the glacier bifurcates at the Salto-Tranquilo valley confluence, having sufficient mass to advance up a reverse bed gradient. In this advanced state there is also contribution of ice from accumulation areas on the Barrancos mountains to the west and topographic highs to the south.

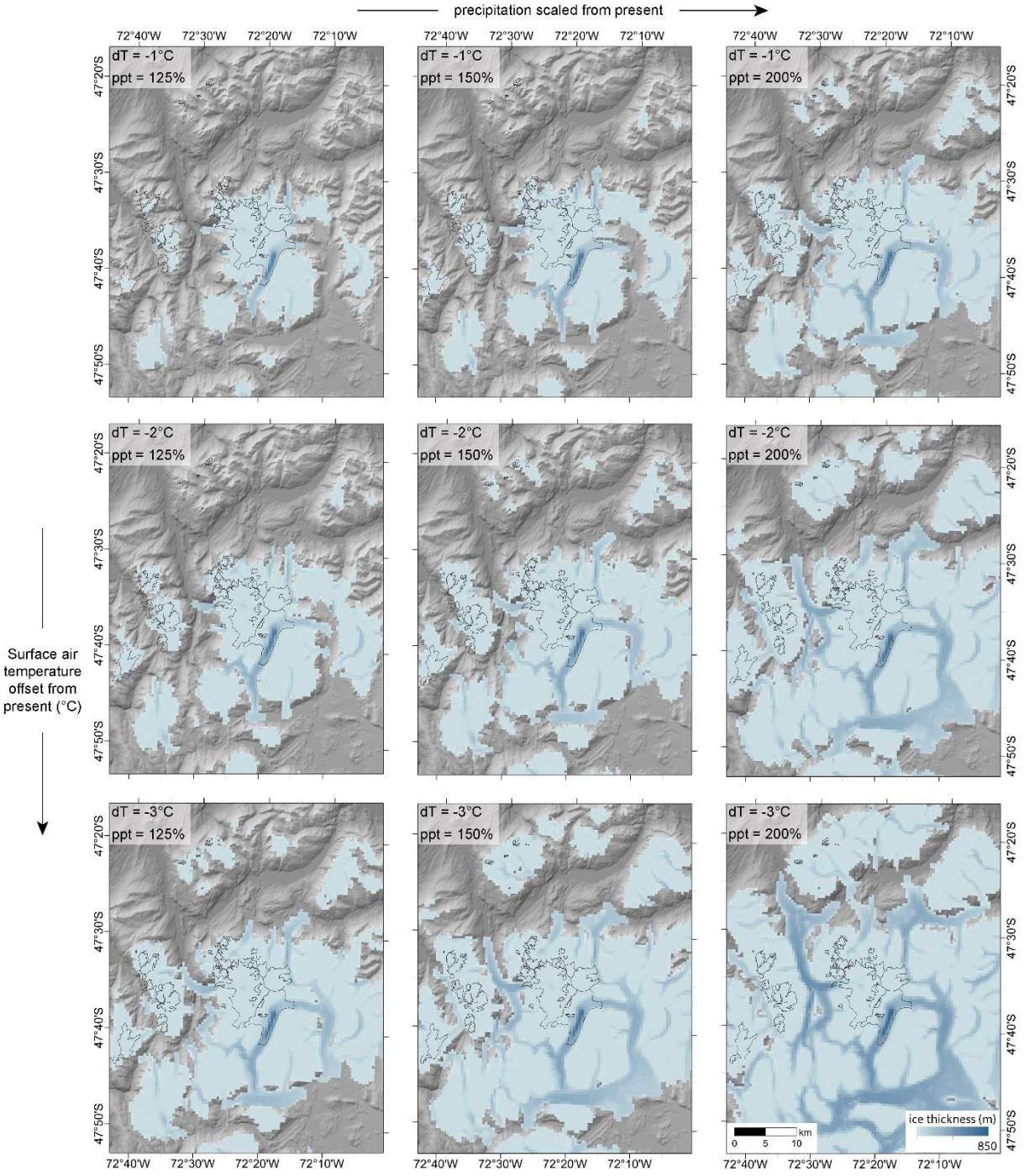

Figure 7.14. Model simulations of the MSL ice cap under combined surface air temperature step cooling of 1 to 3 °C and precipitation scaling of 125% to 200%.

7.5. Discussion

I have used the Parallel Ice Sheet Model (PISM) to produce a three-dimensional simulation of the MSL ice cap and outlet glaciers in a state approximate to that of the present-day, with a focus on Calluqueo Glacier. The simulation matches the present-day extent, thickness and ice-surface velocity of Calluqueo Glacier well, operating within a number of areas of uncertainty discussed here. The simulation was initialised using established 'default' parameter values from the literature (Table 7.4, sections 7.4.1 and 7.4.3) alongside an appropriate WorldClim2 modelled surface air temperature dataset and tuned precipitation dataset (section 7.4.2). The model was tuned for precipitation given the significant absence of and uncertainty surrounding measured and modelled precipitation data in the region (section 7.3.4).

7.5.1. Assessment of best fit scenario

Based upon a mean annual precipitation value of 726 mm $year^{-1}$ at 182 m asl, measured at Cochrane Aerodromo, an applied lapse rate of 1.35 mm m^{-1} produces a model output which best replicates the present-day ice cap (Figure 7.15A). Due to the scarcity of meteorological data from the Patagonian icefields and the surrounding region, in particular on ice masses at contrasting elevations, there is little measured precipitation lapse rate data (Table 7.3). This data is varied, ranging from 0.00252 mm m^{-1} to 3.7 mm m^{-1}, likely due to the complex topography creating strongly site-specific precipitation gradients. However, the best-fit lapse rate of 1.35 mm m^{-1} falls within this range. This gives precipitation values at Calluqueo Glacier of 1223 mm $year^{-1}$ at the glacier tongue (545 m asl) and 2659 mm $year^{-1}$ at the ELA (1614 m asl). Precipitation increases to 5483 mm $year^{-1}$ at the summit of the massif (3706 m asl). On a west-east transect, mean annual precipitation and accumulation values over the wetter western and central Patagonian icefields ranges from 2000 mm to 15000 mm (Fujiyoshi et al., 1987; Escobar et al., 1992; Carrasco et al., 2002; Garreaud et al., 2013; Schaefer et al. 2013), reducing to between 7600 mm and 2500 mm on the eastern outlet glaciers (Rivera 2004; Steufer et al., 2007) (section 7.3.4.3, Table 7.3). Precipitation between *ca* 1200 mm $year^{-1}$ and 5500 mm $year^{-1}$ at MSL, 70 km to the east of the NPI is therefore reasonable. The ELA-based precipitation reconstruction at Calluqueo Glacier from this study (chapter 6) gave a present-day precipitation estimate of 2465 ± 204 mm $year^{-1}$ at the ELA (1614 m asl), *ca* 7% drier than the model derived value, but within error. The use of established positive degree-day melt factor values when achieving the present-day simulation further suggests the precipitation estimate is realistic. Any variation in precipitation could be balanced by changing the degree-day melt factors.

Precipitation sensitivity experiments show that initialising the model with 25% less precipitation produces a small reduction in ice extent (Figure 7.12). Such a reduction could be counteracted

by a reduction in positive degree-day melt factors. Degree-day melt factor sensitivity experiments indicate that adjusting these values across a broad literature range causes a significantly larger change in ice extent than for a 25% change in precipitation. Hence, a 25% reduction in precipitation could likely be counteracted by a small change in melt factor values, relative to the range of values tested.

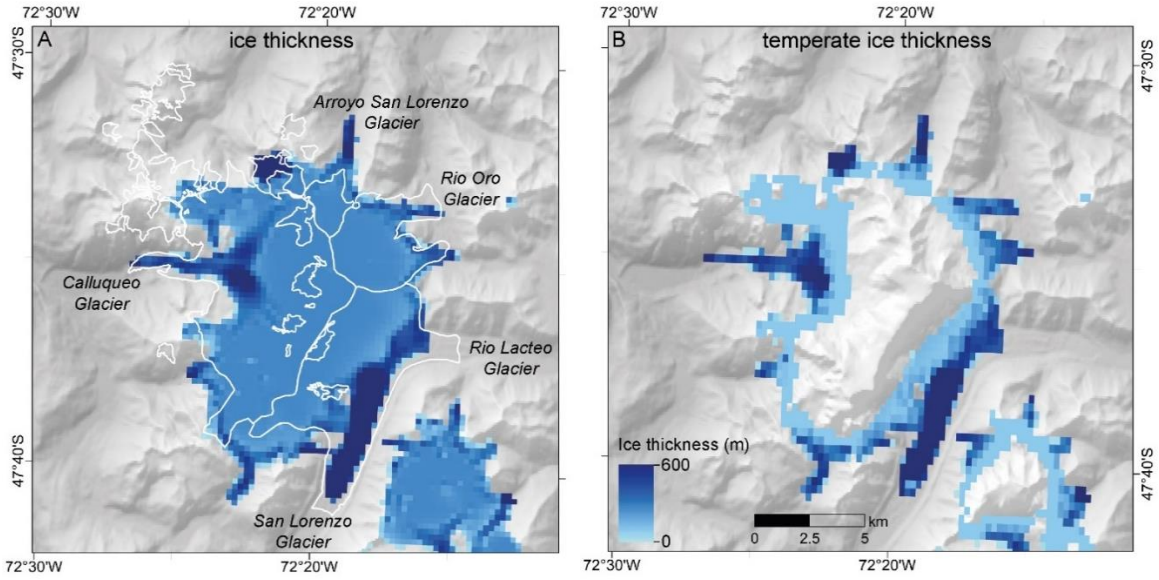

Figure 7.15 Total ice thickness (A) and temperate ice thickness (B) for the best-fit scenario of the modelled MSL ice cap. The white line in (A) denotes the present-day ice extent and glacier catchment divides.

While the model has been tuned primarily to match with Calluqueo Glacier, it is unable to replicate the extent of the ice cap as a whole (Figure 7.15A). The present-day model simulation overestimates ice to the north and south of the ice cap, forming glaciers in currently deglaciated valleys. This is likely because the spatial variation in precipitation across the ice cap is not well replicated by the precipitation lapse rate model dataset, making these high elevation valleys too wet. With the dominant precipitation source from the westerly winds, the north-east and south-east aspects of the valleys catchments are likely drier than the lapse rate derived precipitation dataset suggests. Reconstructing topographically controlled precipitation is especially difficult, especially in mountain environments where topography is complex and changes dramatically over a small area.

The model also underestimates the extent of San Lorenzo Glacier and Rio Lacteo Glacier. Satellite imagery shows that these glaciers are covered by a thick layer of debris, as illustrated by supraglacial ponding, which insulates the ice reducing melting. PISM simulations do not account for this reduction in melt, and hence may for this reason simulate debris covered glaciers to be greater in extent than those observed.

7.5.2. Key insights from modelling

7.5.2.1. Surface mass balance

The present-day simulation of the MSL ice cap shows accumulation over the high peaks up to 5.5 m w.e. per year (Figure 7.16A). At an elevation of 3000 to 2000 m asl, the accumulation is between 4.5 and 2.5 m w.e., decreasing to 1 to 0.5 m w.e. at the tongues of Calluqueo and San Lorenzo Sur Glaciers (1250 to 500 m asl). Ablation is highest at the outlet glacier tongues, up to 18 m w.e. on the tongue of Calluqueo Glacier and 12.5 m w.e. on the flat plateau of San Lorenzo Sur Glacier (Figure 7.16B). Ablation decreases with elevation up the ice cap, with a minimum of 0.5 mm w.e. annual ablation at the highest elevations. The maximum annual surface mass balance of the MSL ice cap is 4.8 m w.e. at the massif's peak, decreasing to zero at the equilibrium line between 1750 m asl and 2000 m asl (Figure 7.16C). The lowest mass balance occurs at the glacier tongues, with values of -3 m w.e. to -6.5 m w.e. in the lower ablation area of Calluqueo Glacier. It should be acknowledged that in these simulations the ice cap is modelled to a state of equilibrium with climate. In reality outlet glaciers at MSL are receding (Falaschi et al., 2013), and therefore it would be expected that the distribution of mass balance is more negative. However, this study provides the first quantitative estimate of mass balance at MSL, which in the absence of empirical mass balance data, is of value. Modelling the ice cap under a transient state of present-day recession is a potential area of future investigation.

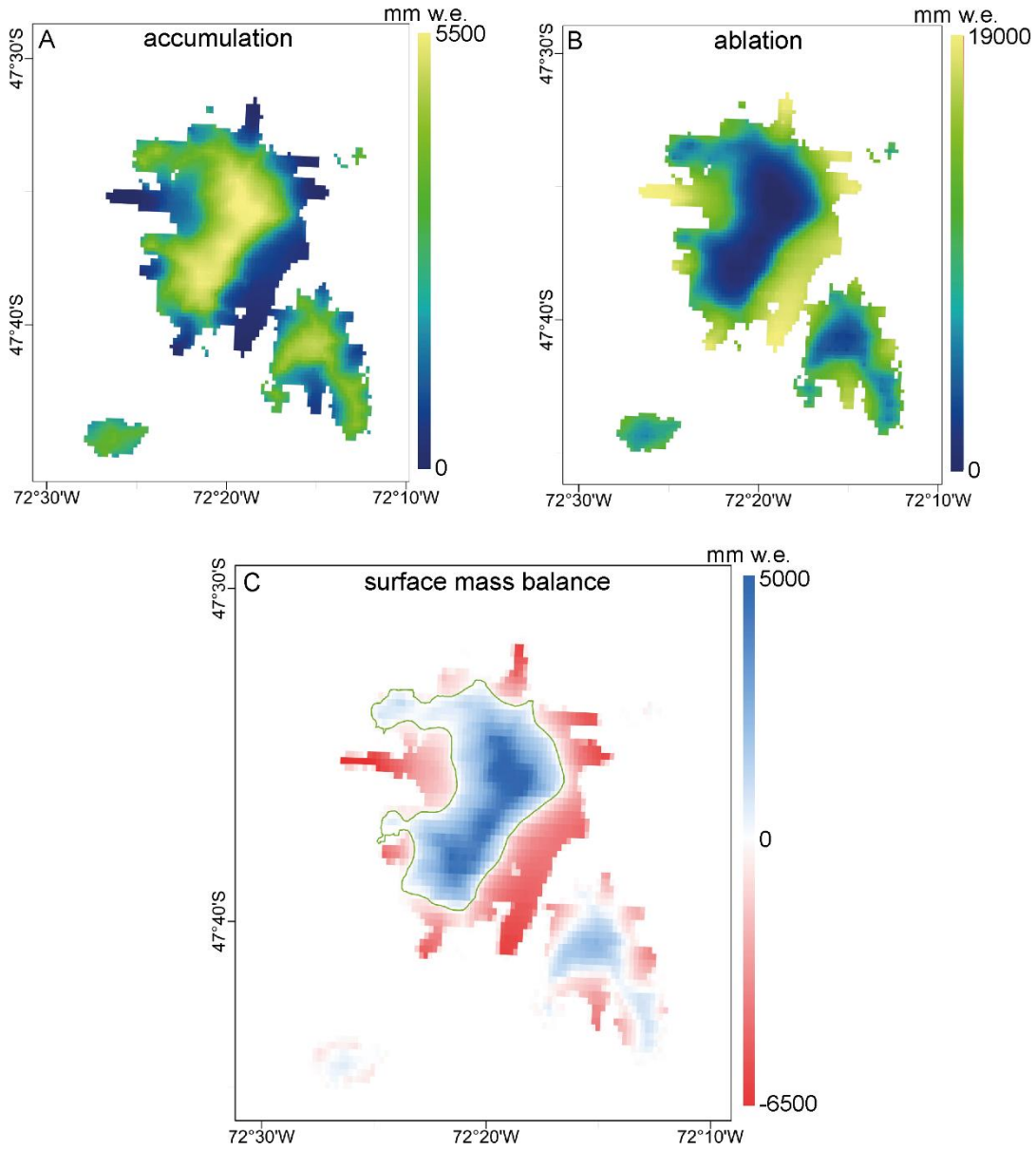

Figure 7.16 Spatial distribution of annual accumulation (A), ablation (B) and surface mass balance (C) across the MSL ice cap. The green line in (C) denotes the Equilibrium Line.

7.5.2.2. Ice velocity, basal sliding and temperate ice

Figure 7.17 shows a basal ice velocity up to *ca* 330 m a^{-1}, demonstrating basal sliding at the ice cap, in particular at locations of steepest bedrock slope, at Calluqueo Glacier in the west and in the catchment of San Lorenzo Glacier in the southeast. High basal driving stresses across the ice cap greater than the constant basal shear strength of 35 kPa (Figure 7.18) enable basal sliding, facilitated by temperate ice at the pressure melting point. At Calluqueo Glacier, driving stresses are between 50 kPa and 200 kPa. Temperate ice is found at MSL's outlet glaciers, where ice is thickest, the bed is insulated, and surface air temperature is warmer due to lower elevations (Figure 7.15). At highest elevations at the top of the massif, thinner ice and colder surface air temperatures results in cold-based ice, frozen to the bed and unable to slide.

The simulation shows good agreement with observed ice surface velocity from the Global Land Ice Velocity Extraction Landsat 8 (GoLIVE) Version 1 dataset (Fahnestock et al., 2016; Scambos et al., 2016) (Figure 7.17). The model replicates well the ice surface velocity at Calluqueo Glacier, particularly in the area of fast ice flow at the lower section of the glacier. This area has a GoLIVE measured velocity of 340 to 390 m a^{-1}, while the modelled ice has a surface velocity of 320 to 340 m a^{-1}. A similar magnitude in basal and ice surface velocity indicates that internal shear plays less of a role in ice flow and that the internal deformation velocity is negligible.

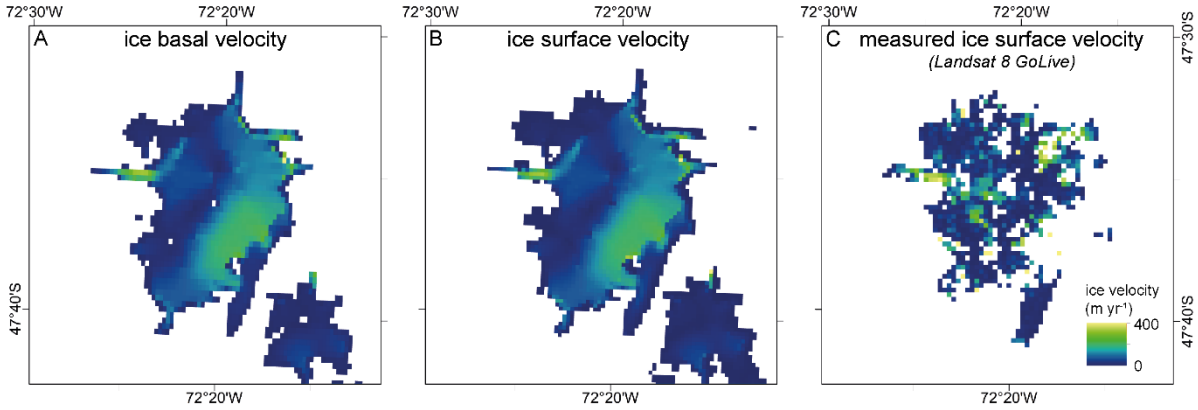

Figure 7.17. Basal ice (A) and surface ice (B) velocity of the modelled MSL ice cap. C) Ice surface velocity of the MSL ice cap taken from the Global Land Ice Velocity Extraction from Landsat 8 (GoLIVE), Version 1 (image L8_231_093_032_2017_307_2017_339_RTT1, 3/11/2017 to 5/12/2017) (Fahnestock et al., 2016; Scambos et al., 2016).

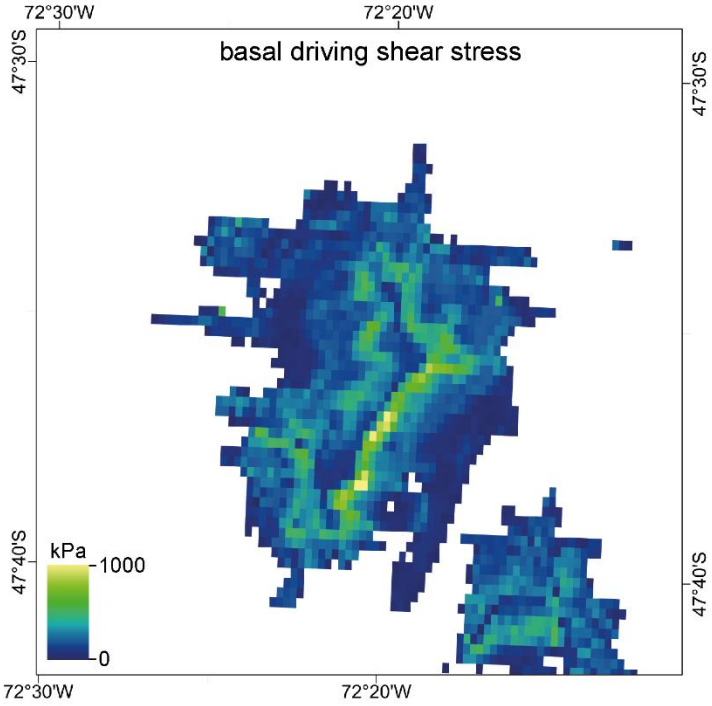

Figure 7.18 Driving stress at the base of the ice as a result of the driving force due to gravity.

The x,y horizontal grid resolution used in the model simulations has a significant impact on the model's ability to resolve glacier dynamics such as ice-flow distribution and ice velocity, but also

dictates the model wall clock time. An optimal resolution therefore had to be found considering experimental efficiency. At the lowest resolution run (1 km), the model is unable to simulate ice growth within the narrow outlet valleys, most notably Calluqueo Glacier draining to the west of the ice cap, and San Lorenzo Glacier draining to the south (Figure 7.19). This is to be expected given the present-day glacier width where confined to these valleys is *ca* 1 km to 1.5 km, and therefore glacier extent is underestimated. This is improved at higher resolution, with a 250 m horizontal grid sufficient to simulate present-day ice extent and thickness at Calluqueo Glacier, San Lorenzo Glacier and Rio Oro Glacier.

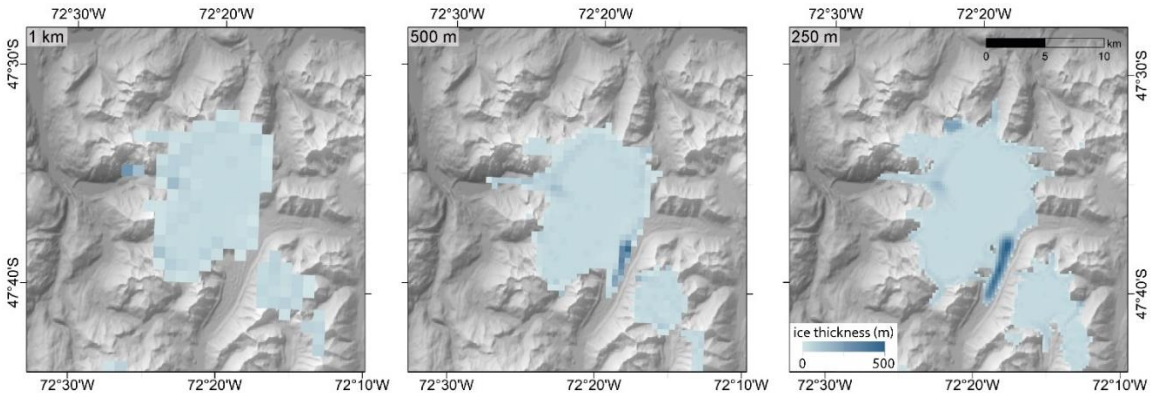

Figure 7.19. Modelled ice cap extent and thickness for three model simulations under the same model parameters and climate forcing, but at 1 km, 500 m and 250 m horizontal grid resolutions.

7.5.2.3. Sensitivity to past climate

Once a tuned simulation of the present-day ice cap has been obtained, the model can then be forced under palaeoclimate conditions to examine the agreement between simulations of the past ice cap and ice cap reconstructions obtained from empirical data (chapter 6). The West Antarctic Ice Sheet (WAIS) Divide surface air temperature reconstruction (Cuffey et al., 2016) provides estimates of past temperature offsets from present-day, while ELA reconstructions of Calluqueo Glacier allow estimates of past precipitation to be calculated for these given temperatures following the method of Ohmura et al., (1992) (chapter 6) (Table 7.7). The ELA and precipitation reconstructions are limited to periods where Calluqueo Glacier has a single flowline fed by a single isolated catchment, so it was not possible to obtain precipitation estimates for periods older than *ca* 12.1 ka when Calluqueo Glacier was advanced, bifurcated and fed by multiple catchments.

	WAIS Divide – ELA reconstruction		Model climate forcing	
Time period	Temperature offset from present (°C)	Precipitation at ELA from present (%)	Temperature offset from present (°C)	Model precipitation scaled from present (%)
LIA	-0.7	119 to 129	-1	125
Mid-Holocene (*ca* 5.6 ka)	-0.3	124 to 133	0	150
12.1 ka	-1.1	133 to 137	-2	150

Table 7.7 Calculations of precipitation based upon ELA reconstructions (chapter 6), following the method of Ohmura et al., (1992) under given temperature offsets from present (West Antarctic Ice Sheet (WAIS) Divide surface air temperature reconstruction (Cuffey et al., 2016)). Temperature and precipitation forcing combinations which initialise the ice cap model to best fit empirical ice extent reconstructions (Figure 7.20).

The WAIS Divide temperature and ELA-based precipitation reconstructions provide an indication of past climatic conditions with which to compare to climate conditions required by the model to simulate the respective reconstructed ice extents. Figure 7.20 shows the best fit model simulations to reconstruction of ice extent for the LIA and mid-Holocene (A, B and C), 12.1 ka (D) and 12.5 ka and the ACR (E). Three tested precipitation and temperature combinations provided an approximate fit of the simulated Calluqueo Glacier to the LIA and mid-Holocene reconstruction, constrained by the latero-terminal M13 moraine. The closest of these to the WAIS Divide and ELA-precipitation reconstructions for the LIA is a combination of -1°C and 125% precipitation (Figure 7.20B, Table 7.7). The closest of these to the WAIS Divide and ELA-precipitation reconstructions for the mid-Holocene is a combination of 0°C offset and 150% precipitation (Figure 7.20B, Table 7.7). A greater agreement could potentially be achieved through higher model resolution simulations, and smaller iterations of temperature and precipitation offset. This should be an area for further investigations to further constrain past climate conditions at the LIA and mid-Holocene. While Calluqueo Glacier extends to the LIA latero-terminal moraine under these climate conditions, Tranquilo Glacier on the north side of MSL does not reach the LIA limit. This is likely because Tranquilo Glacier has smaller, lower elevation cirque (*ca* 1000 m asl.) with a steep headwall, and hence when forced with a lapse-rate derived precipitation dataset, has a comparatively lower accumulation.

The best fit model simulation to ice at the 12.1 ka reconstruction of Calluqueo Glacier requires model initialisation of -2°C and 150% precipitation from present, 0.9°C colder and ca 15% wetter than from the WAIS Divide-ELA reconstruction (Figure 7.20D, Table 7.7). The WAIS-Divide record suggests that surface air temperature at the ACR was up to 3°C colder than present, while pollen and charcoal records indicate a cold and wet climate during this period (Moreno, 2004; Whitlock et al., 2007; Villa-Martínez et al., 2012). Initial model runs at -3°C from present and 200 % present-day precipitation are not able to simulate the full extent of Calluqueo Glacier at the ACR (Figure 7.20E), producing a glacier 16 km short of the ACR dated M1a frontal moraine (Davies et al., 2018) (chapter 5). This simulation barely reaches further than the reconstructed 12.5 ka ice

extent, at which time the WAIS-Divide record indicates -2°C surface air temperature from present. The simulation however greatly overestimates the size of Tranquilo Glacier, likely due to an overestimation of precipitation. The strong east-west precipitation gradient is not taken into account, and given the northeast orientation of Tranquilo Glacier's catchment, a lower level of precipitation would be expected than is found within the lapse rate derived precipitation dataset for the lee side of MSL.

The large discrepancies seen between the model simulations of Calluqueo Glacier and WAIS Divide-ELA climate reconstructions at 12.1 ka, 12.5 ka and the ACR are likely because at the ACR, ice was in a period of readvance during overall deglaciation from the LGM. The climate conditions at this point therefore reflect a readvance and stabilisation from an already large ice mass and are not cold enough to force the simulation to form such a significant mass of ice. It may therefore be the case that the model should be forced under significantly colder and potentially wetter LGM conditions to grow an ice mass far beyond the ACR limit. The model should then be run under transient climate conditions with the aim to simulate an ACR readvance.

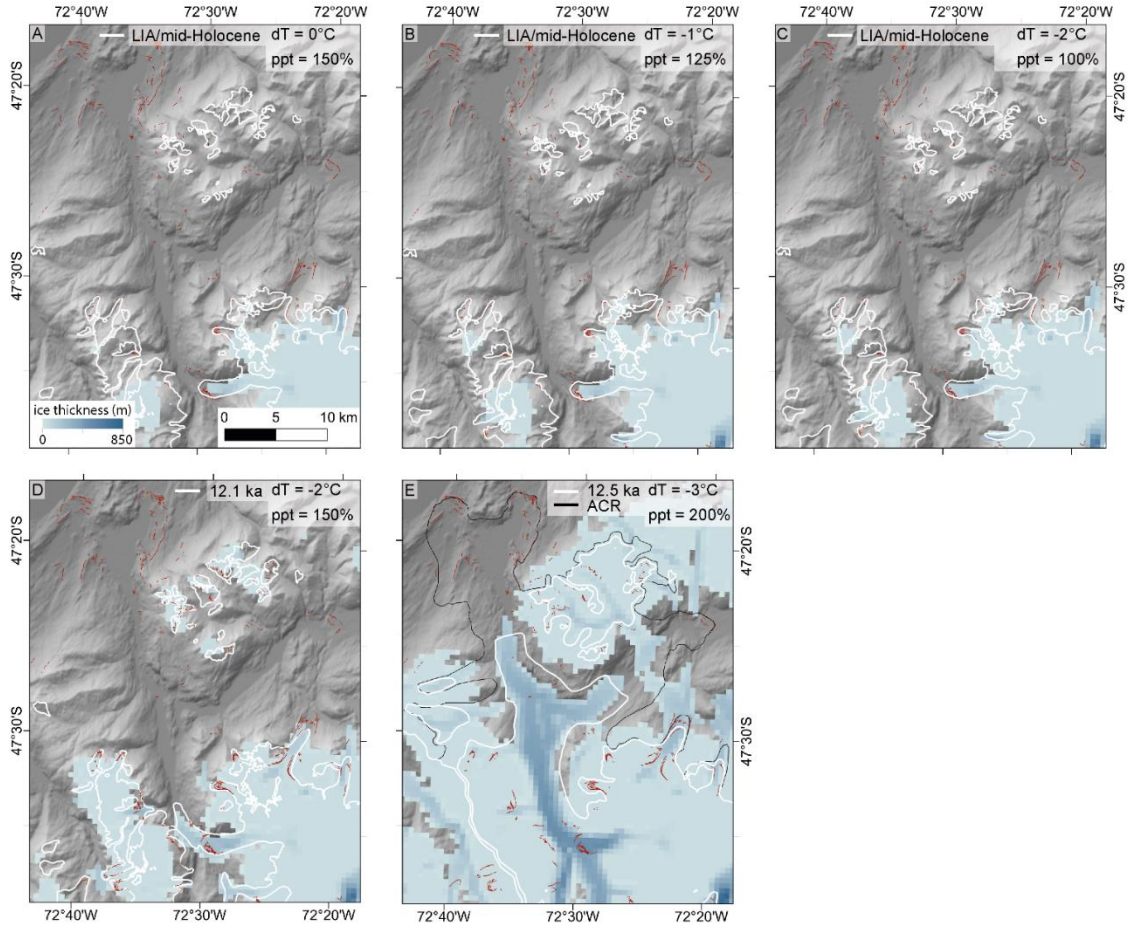

Figure 7.20 Model simulations of the MSL ice cap under combined surface air temperature step cooling of 1 to 3 °C and precipitation scaling of 125% to 200% to best fit palaeo ice mass reconstructions (chapter 6) from the Little Ice Age (LIA), mid-Holocene, ca 12.1 ka, 12.5 ka and the ACR.

7.5.3. Future research

This new simulation of the present-day MSL ice cap provides the basis for future work. Due to the variability in simulated ice extent, volume and dynamics under different model parameters, it would be of benefit to undertake further sensitivity experiments testing initialising parameters in combination. For example, it would be of benefit to explore combinations of precipitation lapse rates and degree-day factors which initialise the model to present-day ice extent, as there is little empirical data and significant natural variability. Geothermal basal heat flux is also difficult to constrain with no in-situ measurements, so running further sensitivity experiments to quantify its impact on model simulations would be of benefit. Higher resolution simulations of ice in the LIA and mid-Holocene at smaller climate increments would also be beneficial to better constrain climatic conditions during these periods. Alongside this, the bathymetry of Calluqueo lake should be incorporated into the model bedrock DEM to simulate these smaller ice extents as accurately as possible. Bathymetric data show that Calluqueo lake has a maximum depth of 220m (Piret and Bertrand, personal communication, 20 August 2019). Given current simulations give 175 m thick ice over the present-day lake, it is anticipated that incorporating

lake bathymetry could alter simulated Calluqueo Glacier ice thickness and extent at 250 m (x, y), by 50 m (z) or higher resolution.

Alongside response time experiments for abrupt changes in temperature and precipitation, simulating the ACR with transient model runs represents a priority for future work. These simulations would help to refine the envelope of past temperature and precipitation conditions at this time and allow investigations into to run investigating rates of ice change during deglaciation. A further key point of investigation is to examine the impact of calving on the simulated ice dynamics. This is particularly necessary given the evidence for large ice dammed palaeolakes north of MSL until *ca* 12.7 ka, into which Calluqueo Glacier terminated (Davies et al., 2018; Martin et al., 2019; Thorndycraft et al., 2019). Finally there is the potential to simulate the ice cap under IPCC scenarios of future climate to predict ice cap change though the 21st century.

7.6. Conclusions

- This study uses the Parallel Ice Sheet Model (PISM) to create a new simulation of the present-day MSL ice cap, initialised using WorldClim2 modelled surface air temperature and a tuned lapse-rate derived precipitation dataset. This is the first time PISM has been applied to model a Patagonian ice cap.
- A precipitation dataset based upon a lapse rate of 1.35 mm m^{-1} produces a simulation which matches well with present-day ice. It results in mean annual precipitation at Calluqueo Glacier, MSL, between 1200 mm and 5500 mm. These values are in line with sparse local measured records and regional modelled climate data.
- Sensitivity experiments show that higher basal shear strength leads to a thicker and longer profile of Calluqueo Glacier. This is due to the impact of ablation at low altitudes following rapid initial ice growth.
- Sensitivity experiments demonstrate a significant sensitivity of the model to changes in positive degree day snow and ice melt factors, with greater sensitivity being to melting of ice in the ablation area than a reduction in mass input through snow melt in the accumulation area.
- Precipitation and temperature sensitivity experiments demonstrate ice area and volume increase with cooling and precipitation increase. A decrease in temperature is shown to be more affective at glaciating unglaciated topography than an increase in precipitation.
- Cold-based ice, frozen to the bed, occupies higher elevations of the MSL ice cap (> *ca* 1800 to 2200 m asl), while temperature, warm-based ice of outlet glaciers is found at

lower elevations. Temperate ice flows at the bed at up to 330 m a^{-1}, with negligible internal ice flow velocity.

- The simulated ice cap shows high surface mass flux, with ablation at outlet glacier tongues up 18 m w.e. a^{-1}, and accumulation at highest elevations up to 5.5 m w.e. a^{-1}. Surface mass balance ranges from +4.8 m w.e. a^{-1} to -6.5 m w.e. a^{-1} with a simulated Equilibrium Line Altitude between 1750 m asl and 2000 m asl.
- Combined variable temperature and precipitation initialised simulations shows that the model matched WAIS Divide-ELA temperature and precipitation reconstructions at the LIA, however greater discrepancy is seen with simulations of greater ice extent, requiring further investigation through higher resolution and transient simulations.

8. Discussion

Herein, the results of this work and their implications are discussed within a broader regional and global context to address **RQ 5, Aim 3** and **Obj. 7** of this thesis. In section 8.1, the spatial and temporal evolution of landsystems north of the MSL ice cap, devised in chapter 4 from newly mapped sediment-landform assemblages, is firstly discussed. These landsystems are then compared to temperate and polythermal glacial landsystems observed globally, both through processes which operate and the landforms which result. In section 8.2, the newly established record of deglaciation at the MSL ice cap (chapter 6) is examined within the context of the record of post-ACR glacier recession on the eastern margin of the NPI and SPI. These records of Patagonian deglaciation are discussed to highlight the main periods of glacier readvance and still-stand immediately following the ACR and through the Holocene. The new post-ACR deglaciation record of Calluqueo glacier, alongside previously discussed Patagonian records, is then compared to late-glacial and Holocene southern hemisphere deglaciation records in New Zealand, the sub-Antarctic Islands and Antarctic Peninsula. In section 8.3 results of glacier model sensitivity and palaeo-glacier simulation experiment (chapter 7) are discussed within the context of highly climatically sensitive maritime and continental glaciers in Patagonia and New Zealand, to establish the relative key climate controls at the MSL ice cap. The post-ACR record of deglaciation of Calluqueo glacier (chapter 6) is then evaluated within the Patagonian and wider southern hemisphere palaeoclimate record. Key reference is made to evolution of the southern hemisphere ocean-atmosphere system during the period of rapid warming following the ACR, to help contextualise the drivers of deglaciation at the MSL ice cap.

8.1. Landsystems of the Monte San Lorenzo ice cap and northern region

8.1.1. Spatial and temporal evolution of landsystems

Chapter 4 details the landsystems found on the northern flanks of MSL and in the valleys directly to the north of the ice cap, revealed by sediment-landform assemblages. Evidence for valley-confined land-terminating glacier, high-altitude mountain valley glacier and glaciolacustrine landsystems are all found in this small region, juxtaposed in adjacent valleys. Of these only the high-altitude mountain valley landsystem is active today and it is evident the landsystems in these valleys have evolved through space and time following the ACR.

Davies et al. (2018) found that during an ACR readvance, ice sourced from MSL occupying the northern Salto valley discharged into the *ca* 350 m asl Lago Chelenko, and formed the Esmeralda moraines (M1a, chapter 4) at 13.4 ± 0.2 ka (Figure 8.1A). The glacier terminus remained in a glaciolacustrine environment likely during the first *ca* 1000 years of subsequent recession until

drainage of Lago Chelenko at *ca* 12.4-11.8 ka (Thorndycraft et al., 2019) (Figure 8.1B). At this time the glacier terminus was approximately at the margin of M5. Following lake drainage, the glacier became land-terminating and receded up the Salto valley with periodic stillstands or minor readvances (Figure 8.1C). A land-terminating glacial landsystem operated during the Holocene in the Salto valley and then continuing in the Pedregoso valley as ice receded further (Figure 8.1C to F). Following the LIA and the formation of M13 the present-day Calluqueo glacier terminated into Lago Calluqueo in a glaciolacustrine setting, before receding to its present-day, land-terminating position.

Ice occupying the Tranquilo valley, after initially existing in a land-terminating setting at the Brown moraines (Figure 8.1A), receded west to form the 520 m asl ice-dammed palaeolake Tranquilo, in turn transitioning into a glaciolacustrine landsystem (Figure 8.1B and C). Further recession and the resulting opening of the 425 m spillway at the Tranquilo-Salto confluence produced a drainage reversal of palaeolake Tranquilo (Figure 8.1C and D) with the Brown moraines outflow pathway abandoned at 520 m asl when lake level fell to 425 m asl. This drainage reversal would therefore have contributed increased meltwater flux as well as likely GLOF drainage events, a hypothesis supported by the Salto moraine boulder bar and incised bedrock reaches (chapter 4, Figure 4.15C).

Following final drainage of palaeolake Tranquilo as ice receded out of the Tranquilo valley, ice receded up the Predregoso valley (Figure 8.1D and E). The inferred frontal margin of the M12 lateral moraine, south of the Tranquilo-Pedregoso confluence and dated to a UWM age of 12.1 ± 0.4 ka, suggests that ice must have receded out of the Tranquilo valley by this time.

Once ice had receded up the Pedregoso valley a paraglacial landsystem operated with rock-slope failure forming talus slopes and cones, and the glaciofluvial remobilisation of glaciogenic sediment deposited as alluvial fans and valley floor floodplain (Figure 8.1E). It is evident that the well-vegetated and fluvially-entrenched alluvial fans are no longer depositionally active, but formed during the Holocene following ice recession, and as such resemble Holocene fans found elsewhere (Ryder, 1971; Ballantyne, 1991; Beaudoin and King, 1994). Alongside this, there is little evidence for significant active large-scale rock-slope failure, with only isolated minor rock falls on the high valley sides. An evident reduction in glacially conditioned sediment release through either exhaustion of sediment or sediment stability being attained, suggests that the paraglacial period in the Salto, Tranquilo and Pedregoso valleys has ended and moved towards a 'non-glacial' state (Ballantyne 2003). Active remobilisation of drift-mantled slopes in the most recently deglaciated sections of high-altitude mountain valleys, and near present-day ice margins, particularly at Calluqueo, suggests that paraglacial processes currently operate in these

areas. The high-sinuosity meanders of the lower Salto valley suggest a transitioning to a fluvial landsystem (Figure 8.1F).

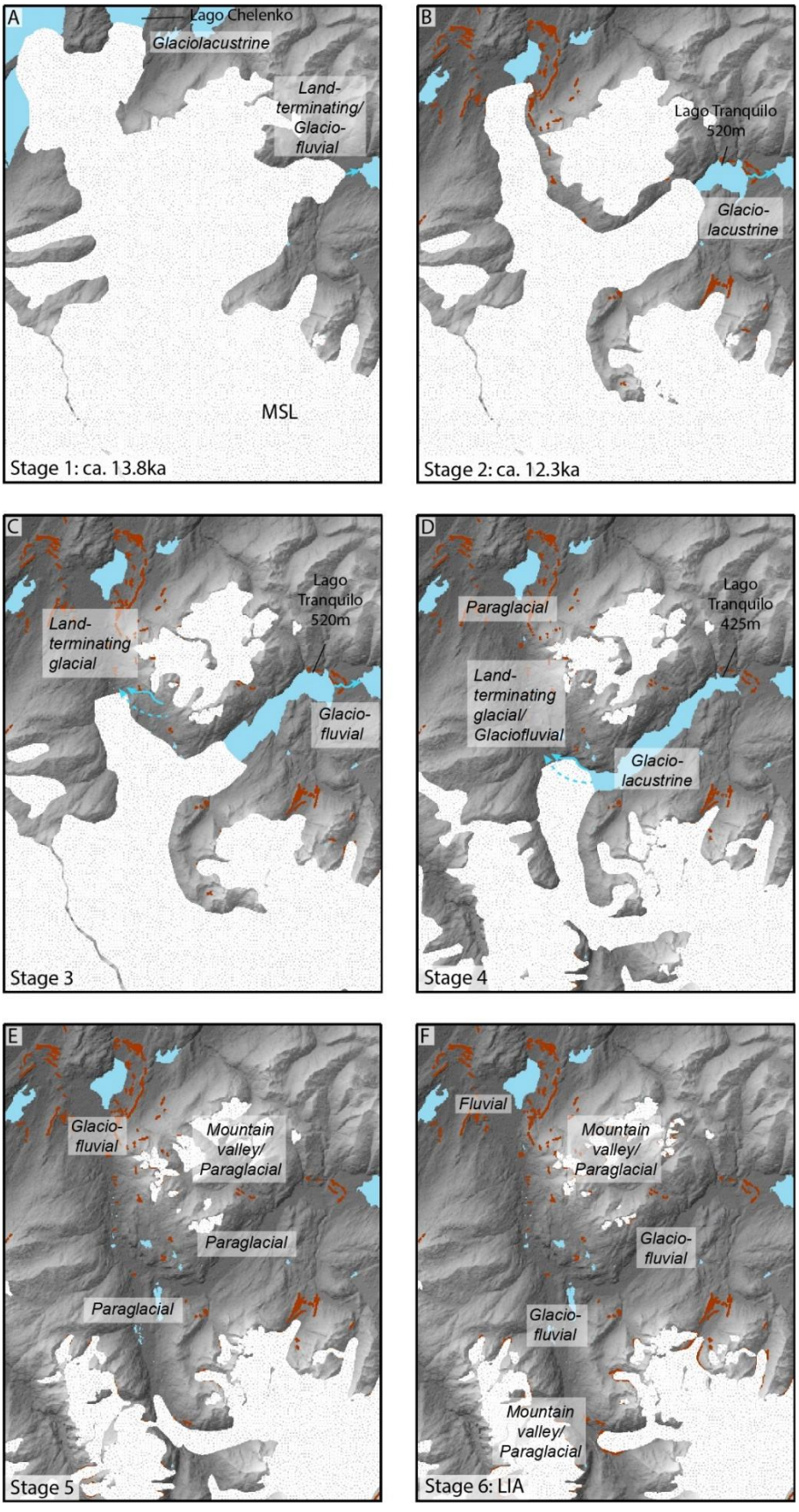

Figure 8.1. Glacier, palaeolake and landsystem evolution model of the deglaciation of the northern MSL ice cap highlighting the evolution in landsystems. Blue arrows show lake outflow pathways. Dashed blue arrow indicates potential subglacial drainage pathway. Red lines show moraine ridges.

8.1.2. Landsystems within a global context

The large range of landforms and sediments in temperate glacial settings globally reflects the variety of sediment source, transport, deposition and modification processes (Table 8.1, Table 8.2) (Eyles, 1983; Spedding and Evans, 2002; Benn et al., 2003; Golledge, 2007; Glasser et al., 2009; Hambrey and Glasser, 2012; Evans and Orton, 2015; Ingólfsson et al., 2016; Evans et al., 2018b; Malecki et al., 2018; Sutherland et al., 2019). The majority of temperate, land-terminating glacier landsystem studies focus on active glaciers, and as elucidated by Glasser et al. (2009), on the areas directly in front of the actively receding margin. A number of these studies come from Iceland (e.g. Evans et al. (1999); Evans and Twigg (2002); Bennett et al. (2010)) where the forelands of active piedmont glaciers are occupied by low amplitude, arcuate, linear and saw-tooth push moraines, closely associated with flutings and dissected by proglacial meltwater channels, leading to expansive, topographically unconstrained pitted outwash plains. These features are the typical product of active temperate glaciers. Basal ice at the pressure melting point and high volumes of sub-glacial meltwater facilitate basal sliding and bed deformation, leading to the formation of subglacial bedforms and annual to multi-decadal readvance push moraines (Boulton, 1976; Benn, 1994; Krüger, 1995; Evans and Hiemstra, 2005). Flutings overtopping moraines, crevasse-squeeze ridges and thrusted blocks of bedded outwash provide evidence for surge activity (Evans and Rea, 1999; Kjær et al., 2008; Evans et al., 2010, 2017).

These active systems have been used as modern analogues for reconstructing Quaternary glacial landsystems in the Southern Hemisphere, where similar landform assemblages are found. The outlet valleys of New Zealand's Southern Alps contain expansive outwash plains and drumlin fields associated with and often overprinted by eskers, flutes, and push-moraine ridges (Mager and Fitzsimons, 2007; Carrivick and Rushmer, 2009; Evans et al., 2013; Sutherland et al., 2019). Significant fluvial reworking occurs with proglacial meltwater channels dissecting and breaching larger end moraines. Unlike in Iceland, higher mountain topography facilitates valley-side debris input to the glacier surface from rockfall and scree, leading to supraglacial transport, deposition of angular boulders at the ice margins and irregular hummocky moraine (Boulton, 1972; Benn, 1992). The same assemblage of landforms is also found in the expansive topographic lowlands to the east of the Patagonian Icefields and in the Chilean Lake District (Table 8.1) (Bentley, 1996; Andersen et al., 1999; Schlüchter et al., 1999; Glasser et al., 2009; Bendle et al., 2017b; Darvill et al., 2017), although with notable abundance of glaciolacustrine landforms (raised deltas, palaeoshorelines, laminated lake sediments) in the Lago Buenos Aires and Lago Pueyrredón east

of the NPI (Glasser et al., 2005; Douglass et al., 2006; Hein et al., 2009, 2010; Smedley et al., 2016; Bendle et al., 2017b).

Again a similar array of temperate, subglacial landforms are found in the British Isles (Table 8.1), for example in the northern Pennines (Evans et al., 2018; Davies et al., submittedb) but with an abundance of lateral, subglacial and proglacial meltwater channels in the glaciated landscape. The formation of ice-marginal, lateral meltwater channels may be indicative of periodic polythermal or cold-based ice conditions at the margins of the icefield as a result of oscillating climatic conditions (Hooke, 2005; Evans et al., 2018). Lateral meltwater channels have been seen forming at active temperate glaciers in Alaska as a result of high subglacial hydraulic gradients towards the ice margin, therefore decreasing marginal permeability (Syverson and Mickelson, 2009). These features are less abundant in Patagonia and New Zealand providing further evidence for predominantly temperate conditions.

Numerical model simulations of the MSL ice cap give evidence for fast-flowing, temperate ice (chapter 7), however the landsystems of the high mountain valleys and lower altitude outlet valleys to the north of the ice cap are significantly different to the temperate piedmont, ice lobe and ice sheet systems. The high altitude mountain valleys of Cordon Esmeralda are more akin to the classic 'glaciated valley' landsystem (Boulton and Eyles, 1979; Eyles, 1979), with prominent arcuate terminal and established valley-side lateral moraines with smaller inset recessional dump and push moraines, dissected by proglacial meltwater channels. Similar assemblages are found in the Peruvian and Bolivian Andes and European Alps (Table 8.1). A primary component of these systems is traditionally supraglacial debris fed from the valley side and in turn debris covered glaciers. Those on Cordon Esmeralda however show a prevalence of annual moraines superimposed on well preserved flutes and subglacial sediments. This indicates both numerous oscillations of the frontal ice margin and an exposed valley bed not subsequently covered by debris, both indicative of a 'clean' valley glacier with less sediment supply from the valley side (Eyles, 1979; Benn and Evans, 2010). Similar cirque architectures are seen on the Isle of Skye at the Coire Lagan formed during the Younger Dryas (Benn and Evans, 2010), as well as in front of present day, actively receding glaciers such as at Maradalsbreen, Norway (Benn et al., 2003).

The temperate glacier landsystem in the lower-altitude, topographically constrained valleys differ further still. The main features are terminal dump moraines and kame terraces, formed at periodic stillstands during an overall period of steady ice recession, as opposed to minor readvances forming push moraines. As in the outlet valleys of the Younger Dryas plateau icefield system in the Monadhliath, Scotland, there is a general low abundance of valley floor moraines, and inter-valley variation. In Scotland, this has been attributed to low debris turnover and low moraine preservation due to the presence of buried ice, indicative of cold to polythermal glacier

conditions (Ó Cofaigh et al., 2003; Boston et al., 2015). In the temperate Patagonian setting however, the absence of valley floor moraines is likely due to the largely continuous ice retreat during deglaciation with little oscillation of the ice front, combined with high volumes of meltwater leading to dominant proglacial meltwater sediment transport and reworking processes (Table 8.2). Within the narrow, steep sided valleys, moraine features and subglacial bedforms seen in temperate settings elsewhere are absent, potentially removed or buried. The valley floor is filled with outwash and braided glaciofluvial valley systems.

Glaciolacustrine landsystems are found in central Patagonia in close association with the lowland, valley-confined glacier landsystems. North of the MSL ice cap, these two landsystems are juxtaposed in the adjacent Tranquilo and Salto valleys (chapter 4). The Tranquilo valley contains stepped deltas, analogous to those found around the margins of Lago General Carerra/Buenos Aires (Bell, 2008, 2009; Glasser et al., 2009; Bendle et al., 2017b) and in the Torres del Paine region (García et al., 2014). On a similar scale to Tranquilo, raised deltas as well as subaqueous fans are found along the margins of the Thompson valley in British Columbia, deposited in glacial palaeolake Thompson, dammed by ice during the decay of the Cordilleran Ice Sheet (Johnsen and Brennand, 2004, 2006). These deposits, as in the Tranquilo valley, are located at tributary valleys suggesting that tributaries were the primary source of sediment as opposed to the ice front. Mountain river catchments feeding into palaeolakes provide the sediment point source for the delta to form. In contrast, the Salto valley contains the large ice-contact subaqueous Juncal fan, with a clear ice-front sediment source and no valley-side tributaries and associated deltas. Ice-contact fans and deltas formed in ice-dammed lakes are also found in Scotland with examples at Glen Roy (Peacock, 1986; Palmer and Lowe, 2017; Sissons, 2017), the northern Cairngorns (Brazier et al., 1998) and Achnasheen (Benn, 1989; Benn, 1992). At the latter of these sites cross-valley morainic ridges are also found, deposited subaqueously, a scenario not seen in the Tranquilo valley.

Benn and Evans (2010) introduce the concept of a 'mountain ice field' landsystem, citing the Patagonian Ice Field and Younger Dryas ice fields in Scotland as examples (references therein). Due to their expansive nature, diverse topography and different climatic settings, these regions result in a broad landsystem encompassing elements of smaller-scale landsystems. It is evident that we see an element of this north of MSL through the diverse topography of the lowland Salto, Tranquilo and Pedregoso valleys in comparison to the high-altitude valleys on Cordon Esmeralda, the Barancos mountains and MSL. Due to the comparatively local scale of the study area, broad scale spatial changes in climate are less significant, and restricted to those controlled themselves by local topography. Benn et al. (2003) discuss the spatial and temporal changes in glacial landsystem at the Ben Ohau Range in New Zealand, citing long term climatic change as a

cause. We see that this is also the case north of MSL. Rising equilibrium line altitudes causes regional ice recession, opening drainage of Lago Chelenko to the Pacific, and Lago Tranquilo into the Salto valley, changing the terminal environment of ice in the Salto and Tranquilo/Pedregoso valleys from lacustrine to terrestrial. Accompanying this is the recession of ice from low altitude land terminating valleys to high altitude mountain valleys, moving ice from one distinct landsystem to another. Lastly ice recession exposes the glaciated valleys to glaciofluvial and paraglacial processes which now operate in the Salto, Tranquilo and Pedregoso valleys.

Ice marginal		Moraines						
Location	Glaciation style	latero-terminal	dump	push	saw-tooth	hummocky	lateral meltwater channels	kame terraces
Iceland[1]	*Ice lobe*	xxx	xxx	xxxxx	xxxx	xx	x	xx
British Isles[2]	*Ice sheet*	xxx	xxx	xxx	x	xxx	xxxx	xxx
European Alps[3]	*Mountain valley*	xxxxx	xxx	xxx	x	x	x	x
New Zealand[4]	*Ice lobe*	xxxx	xxx	xxxx	xx	xx	x	xx
	Mountain valley	xxxx	x	x	x	xx	x	x
Bolivian/Peruvian Andes[5]	*Mountain valley*	xxxxx	xx	xxx	xx	x	x	x
Patagonia[6]	*Mountain valley*	xxxxx	xx	xxxxx	xxxx	x	x	x
	Valley confined	xxxxx	xxxx	xx	x	x	x	xxxx
	Ice lobe/ ice sheet	xxxxx	xxx	xxxx	xxx	xx	xx	xx

Subglacial							
Location	Glaciation style	flutes	crevasse-squeeze ridges	drumlins	meltwater channels	eskers	ice scoured bedrock
Iceland[1]	*Ice lobe*	xxxx	xxxxx	xxx	x	xxx	x
British Isles[2]	*Ice sheet*	xxx	x	xxxx	xxxxx	xxxx	xxxx
European Alps[3]	*Mountain valley*	xxxx	x	x	x	x	xx
New Zealand[4]	*Ice lobe*	xxxx	xxxx	xxx	xx	xx	x
	Mountain valley	xx	x	x	x	x	xx
Bolivian/Peruvian Andes[5]	*Mountain valley*	xxxx	x	x	x	x	xxxx
Patagonia[6]	*Mountain valley*	xxxxx	x	x	x	x	xxxxx
	Valley confined	x	x	x	x	x	xxxxx
	Ice lobe/ ice sheet	xxxx	xxxx	xxx	xx	xxx	x

Proglacial					
Location	Glaciation style	Outwash plain	Ice-contact fan	meltwater channels	ice-dammed lake shorelines
Iceland[1]	*Ice lobe*	xxxxx	xxx	xxxxx	xx
British Isles[2]	*Ice sheet*	xxxx	x	xxxxx	x
European Alps[3]	*Mountain valley*	xxxxx	xxx	xxxxx	x
New Zealand[4]	*Ice lobe*	xx	xxx	xx	xxx
	Mountain valley	xxx	x	xxx	x
Bolivian/Peruvian Andes[5]	*Mountain valley*	xxxx	x	xxx	x
Patagonia[6]	*Mountain valley*	xxx	x	xxxxx	x
	Valley confined	xxxxx	xxxx	xxxxx	xxxxx
	Ice lobe/ ice sheet	xxxxx	xxx	xxxxx	xxxxx

Table 8.1. The relative abundance (from low (x) to high (xxxxx)) of a range of ice marginal, subglacial and proglacial landforms in different temperate and polythermal glacial environments globally. Superscript numbers correspond to references ***1)*** *Evans et al., (1999, 2010, 2016, 2017, 2018); Spedding and Evans (2002); Evans and Twigg (2002); Kjær and Korsgaard (2008); Bennett and Evans (2012); Evans and Orton (2015); Chandler et al. (2016a, 2016b)* ***2)*** *Benn and*

Lukas (2006); Golledge (2007); Graham and Hambrey (2007); Boston et al. (2015); Evans (2017); Evans et al. (2018); Davies (2019) ***3)*** *Eyles (1983); Kneisel and Kääb (2007); Dusik et al. (2015)* ***4)*** *Mager and Fitzsimons (2007); Carrivick and Rushmer (2009); Evans et al. (2013); Sutherland et al. (2019)* ***5)*** *Iturrizaga (2018); Malecki et al. (2018)* ***6)*** *Glasser et al. (2009); García (2012); Bendle et al. (2017); Darvill et al. (2017); Davies et al. (2018); Martin et al. (2019)***.**

Table 8.2. The relative importance (from low (x) to high (xxxxx)) of various processes operating in different temperate and polythermal glacial environments globally. Superscript numbers refer to reference in Table 8.1.

Processes									
Location	Glaciation style	deformation/ erosion	glacier surge	glacier velocity	basal sliding	subglacial meltwater	proglacial meltwater	supraglacial transport	valleyside debris input
Iceland[1]	*Ice lobe*	xxxxx	xxxxx	xxx	xxxx	xxx	xxxxx	x	x
British Isles[2]	*Ice sheet*	xxxx	x	xx	xxx	xxx	xx	xx	xx
European Alps[3]	*Mountain valley*	xxx	x	xxx	xxx	xx	xxxx	xxxxx	xxxxx
New Zealand[4]	*Ice lobe*	xxxxx	xxxx	xxx	xxxxx	xxxx	xxxx	xxxx	xx
	Mountain valley	xxx	x	xxx	xxxx	xxxxx	xxxxx	xxxxx	xxxxx
Bolivian/Peruvian Andes[5]	*Mountain valley*	xxxxx	x	xxx	xxxx	xxxx	xxxx	xxxxx	xxxxx
Patagonia[6]	*Mountain valley*	xxxxx	x	xxx	xxxxx	xxx	xxxxx	xxxxx	xxxxx
	Valley confined	xxx	x	xxx	xxxxx	xxxx	xxxxx	xx	xx
	Ice lobe/ ice sheet	xxxx	x	xxx	xxxx	xxxx	xxxxx	xx	xx

8.2. Deglaciation of the Monte San Lorenzo ice cap: a Southern Hemisphere context

8.2.1. Deglaciation in Patagonia

New geomorphological mapping (Chapter 4) alongside existing work reveals a sequence of 12 lateral and frontal moraines in the Salto and Pedregoso valleys, inset of the large ACR limits of the Esmeralda (M1a) and Salto (M1b) moraines in the north of the Salto valley. New dating of two of these limits (M9 and M12) reveals ages in the *ca* thousand years immediately following the ACR at 12.5 and 12.1 ka respectively. These ages sit within the context of the previously dated recessional M4 moraine (12.7 ka) (Glasser et al., 2012). Other ice margins east of the NPI inset of larger ACR limits have also been dated to the period immediately following the ACR and into the early Holocene, constraining ice recession during this period (Figure 8.2). Two samples taken from boulders atop of the Lago Plomo/Bertrand moraine, *ca* 16 km inset of the ACR dated Lago Bertrand moraine (Davies et al., 2018), date to 11.3 ± 1.0 ka and 11.1 ± 1.0 ka (UWM 11.2 ± 1.0 ka) (Glasser et al., 2012) mark the advanced frontal margin of Soler glacier. Surface exposure dating of boulder samples from a high lateral moraine in the Nef valley marks an advanced, vertically expanded lateral margin of Nef glacier at a UWM age of 11.1 ± 0.4 ka (Glasser et al., 2012), *ca* 9 km from the present-day ice margin. To the south in Colonia valley, boulders dated to between 10.9 ± 1.0 ka and 11.9 ± 1.0 ka atop of the Rio Claro lateral moraine mark the advanced margin of Colonia glacier, with a UWM age of 11.5 ± 0.3 ka (Nimick et al., 2016), 12.5 km down valley of the present-day glacier front.

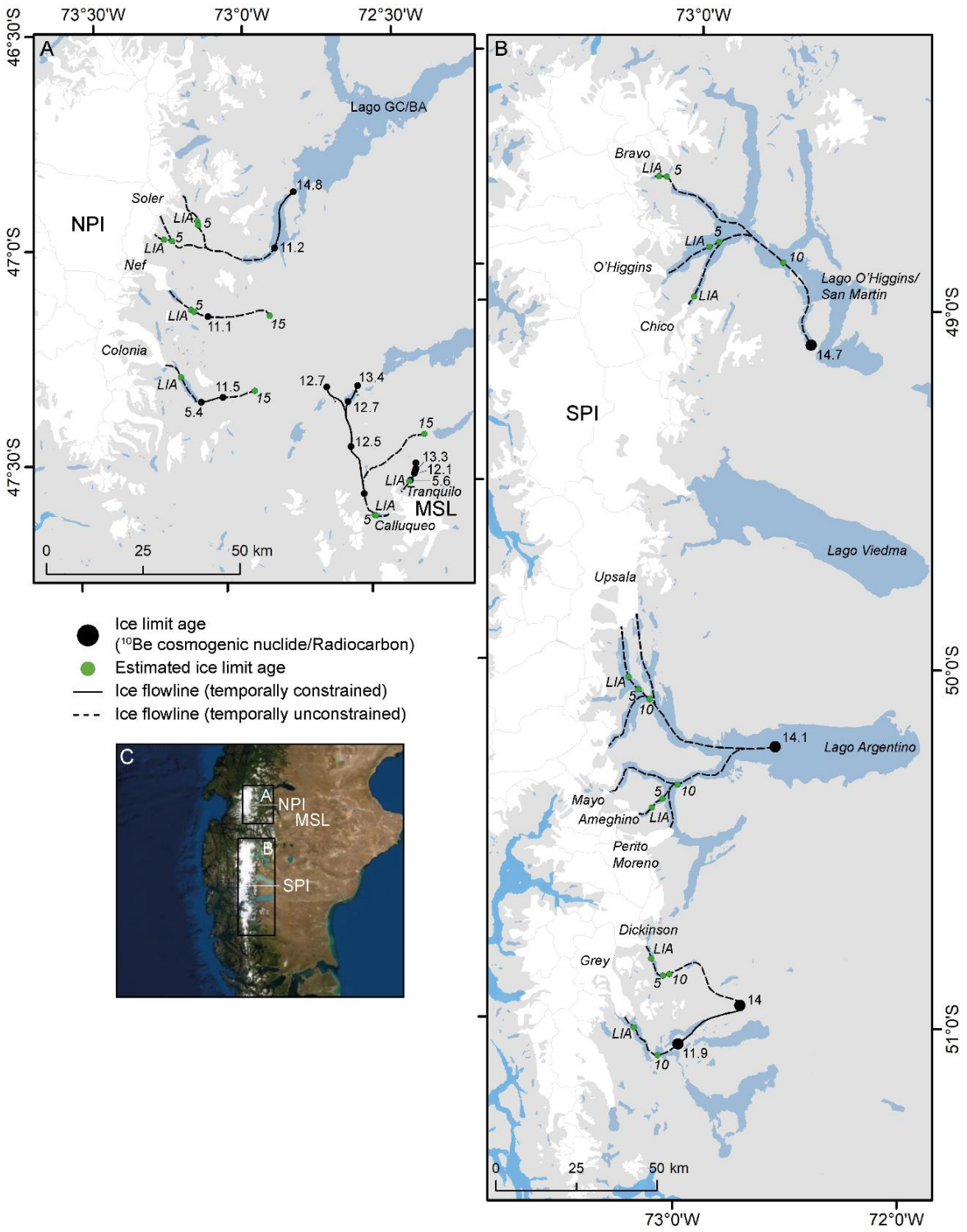

Figure 8.2. Recessional flowlines of outlet glaciers from (A) the eastern side of the NPI and MSL and (B) eastern side of the SPI following the ACR. Black circles and accompanying ages are uncertainty weighted mean ages in ka for ^{10}Be surface exposed dated boulders from moraines ridges denoting glacier margins. The 11.9 ka date from the recession of Grey glacier at the south of the SPI is a radiocarbon age denoting maximum date of ice at this position (Marden, 1997). Green circles represent estimated approximal frontal margin positions at approximately 15 ka, 10 ka, 5 ka and the LIA (Davies et al. 2019 submitted). It should be noted that the LIA positions have high confidence, reconstructed from clear trimlines. Solid black lines indicate periods of recession constrained between two dated frontal ice positions. Dashed black lines represent periods of recession between two undated, estimated frontal ice positions. C) Context of maps A and B within Patagonia.

To the east of these NPI outlet glaciers, post ACR moraines have been dated in the Rio Tranquilo valley, on the northern flank of MSL. The Rio Tranquilo valley contains large ACR dated latero-terminal moraines, inset of which is a smaller latero-terminal moraine (RT5), with a UWM age of 12.1 ± 0.5 ka (Sagredo et al., 2018) (Figure 5.1, Figure 8.2). At the opening of the Salto valley, the M4 moraine (Figure 5.1, Figure 8.2), 5 km inset of the ACR dated Esmeralda (M1a) moraine, has been dated to 12.7 ± 0.4 ka (Glasser et al., 2012). Surface exposure ages have also been acquired for boulders atop ridges of the Leones, Negro and Chacabuco moraines which date to between 10.8 ± 1.0 ka and 12.0 ± 1.2 ka (Glasser et al., 2012). These had previously been considered to have also dated the frontal margin of ice extending east from the NPI. However it is now thought, given their elevation below the 350 m asl palaeolake Chelenko, that they were deposited subaqueously, shielded by the lake, and instead date lake drainage (Davies et al., 2018; Thorndycraft et al., 2019).

Moraines dated to the millennia immediately following the ACR have also been identified in southern Patagonia. East of the SPI around the banks of Lago Argentino, radiocarbon ages of peat closely inset of frontal margins give minimum dates of ice from Upsala, Ameghino, Perito Morano and Mayo glaciers of 12.7 ± 0.07 ka east of Brazo Rico, 12.5 ± 0.08 ka in Peninsula Avellaneda and 12.3 ± 0.1 ka in Bahía Catalana (Strelin et al., 2011). Further south in Tierra del Fuego, northwest of Ushuaia, a recessional moraine of a mountain cirque glacier has been dated to 12.38 to 12.03 ka through radiocarbon dating of terrestrial moss directly above the till deposit (Menounos et al., 2013).

This study hypothesises that the M13 moraine at the western end of Lago Calluqueo marks the mid-Holocene ice limit of Calluqueo glacier (Chapter 5). This is in line with moraines dated to the mid-Holocene regionally, with a readvance across Patagonia between *ca* 6 to 4.5 ka suggested as a result (Mercer, 1976; Clapperton and Sugden, 1988; Aniya, 2013; Strelin et al., 2014; Davies et al., submitted). A terminal moraine in the Colonia valley on the southern bank of Lago Colonia has been dated with a UWM age of 5.4 ± 0.2 ka (Nimick et al., 2016) (Figure 8.2). On the northern flank of MSL, a latero-terminal moraine within the Upper Tranquilo valley moraine sequence dates to a UWM age of 5.6 ± 0.1 ka (Sagredo et al., 2018) (Figure 5.1), while on the eastern side of MSL a radiocarbon date of 5.2 ± 0.7 cal. ka gives a maximum age for a moraine *ca* 5km down valley of the present-day calving front of Rio Lacteo Glacier (Mercer, 1968). Lichenometric data at Rio Lacteo, as well as San Lorenzo Glacier to the south, gives evidence for stillstand at 5.8 ka to 4.5 ka (Garibotti and Villalba, 2017). South of MSL, further radiocarbon dates of organics within a moraine give a maximum age of 4.9 ± 0.8 cal. ka (Mercer, 1968; Wenzens, 2005). On the eastern side of the SPI, moraines in the upper reaches of the Lago Argentino basin, on the Herminita Peninsula and the southern end of Lago Pearson, *ca* 8 and 22 km from the present-

day ice margin of Upsala glacier respectively (Figure 8.2) have been dated to between 4.3 ± 0.2 ka to 5.6 ± 0.2 ka (Strelin et al., 2011; Kaplan et al., 2016). 80 km south in the southern end of the basin, latero-terminal moraines around the banks of Lago Frias are dated from 5.4 ± 0.3 ka to 6.6 ± 0.2 ka (Strelin et al., 2011; Kaplan et al., 2016), making advanced ice from Grande glacier.

Ice limits inset of mid-Holocene age moraines have been dated to the late Holocene, predominantly younger than 3.3 ka (Strelin et al., 2011; Hall et al., 2019. Davies et al., submitted) from which up to four late-Holocene neoglaciations have been hypothesised (Mercer, 1976; Clapperton and Sugden, 1988; Aniya and Sato, 1995; Aniya, 2013). Identifying isolated climate induced regional advances on this temporal scale however is difficult given that neighboring glaciers under the same climatic can show different length fluctuations, as is observed in the Lago Argentino basin (Strelin et al., 2011). The most recent and most clearly defined late-Holocene neoglaciation is marked across Patagonia by prominent sharp crested, lateral and terminal moraines, entirely or partly unvegetated, and associated with clear valley-side trimlines (Davies and Glasser, 2012). These limits have been dated to the LIA by dendrochronology, lichenometry and historical records (Aravena, 2007; Glasser et al., 2011; Aniya, 2013; Morano-Büchner and Aravena, 2013; Strelin et al., 2014; Nimick et al., 2016). Proposing Calluqueo glacier advanced to the M13 latero-terminal moraine during both the mid-Holocene and LIA (chapter 5) it is likely that Calluqueo glacier may have undergone multiple oscillations during the late-Holocene, with the record overprinted by subsequent readvances, the most recent being that at the LIA.. New cosmogenic nuclide surface exposure dating of boulders from ridge crests on, and inset of, the largest M13 ridge (Kaplan, personal communication, July 2019) may go some way to resolving these late-Holocene fluctuations in the ice front.

Although the record of glacier change in Patagonia is ever improving, Figure 8.2 and Figure 8.3 illustrate the absence of chronologically well-constrained sequences of ice recession in Patagonia from single valleys, covering deglaciation following the ACR. The well constrained sequence of recession newly mapped and dated by this study shows rapid recession of Calluqueo glacier following the ACR with 75% of ice length from present lost over a period of *ca* 1.3 kyr. A similar trend of higher rates of recession following the ACR and then more gradual recession during the Holocene is seen in other glacier records in Patagonia (Figure 8.3), however not to the extent seen at Calluqueo. The more rapid recession of Calluqueo Glacier could because it is sourced by an isolated small ice cap rather than the larger NPI or SPI, leading to shorter response times to climatic changes. It is also more sensitive to precipitation (discussed in section 8.3.1) so may experience greater and faster recession than other Patagonian glaciers during periods of precipitation change. Calluqueo Glacier's faster recession in comparison to Tranquilo Glacier, on the same ice cap, is likely due to Calluqueo Glacier much lower elevation

at the ACR (300 m asl compared to 700 m asl for Tranquilo Glacier). Its lower elevation, longer, more shallowly sloping profile mean that small increases in ELA in response to rising temperatures will result in significant ablation over the extensive length of the glacier.

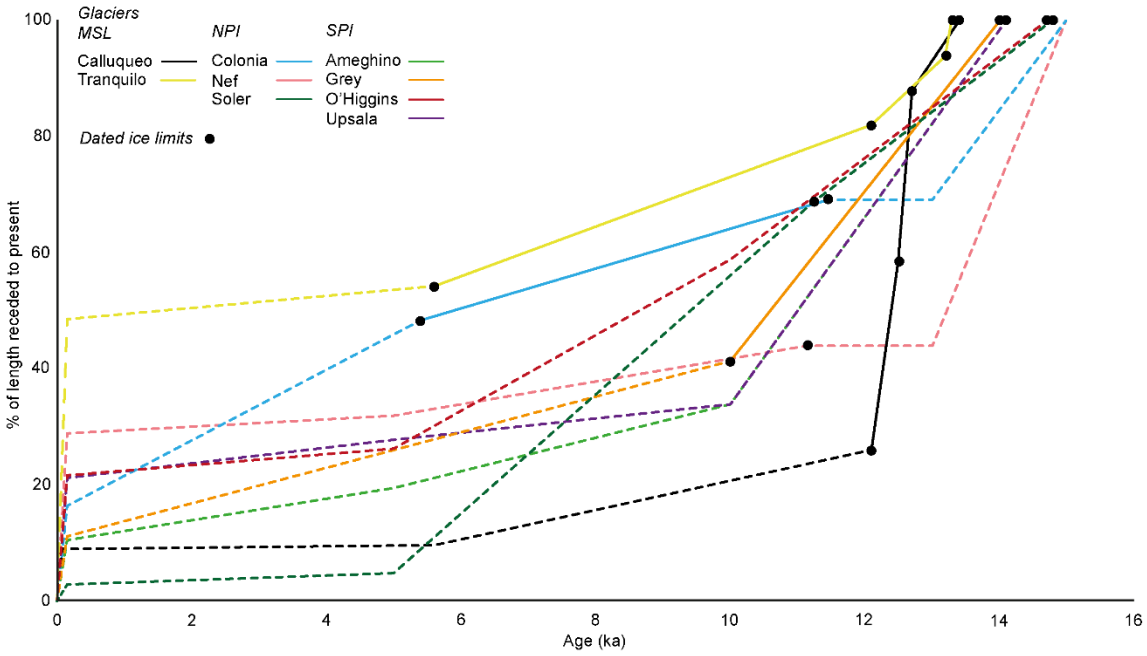

Figure 8.3. Graphs of recession of Patagonian glaciers following the ACR, corresponding to Figure 8.2. The Y axis presents the length of the glacier as a percentage of its length at ACR period, from present-day. Black circles represent empirically dated frontal ice positions corresponding to Figure 8.2. As in Figure 8.2, solid lines denote periods constrained between two dated frontal ice positions and dashed lines denote periods between estimated frontal ice positions.

8.2.2. Wider Southern Hemisphere deglaciation

As in Patagonia, records in New Zealand show glacier readvances in the ACR, followed by immediate recession over a *ca* 1.5 kyr period and on through the Holocene, punctuated by stillstands or minor readvances (Gellatly et al., 1988; Turney et al., 2007; Schaefer et al., 2009; Kaplan et al., 2010; Putnam et al., 2010, 2012; Doughty et al., 2013). As an example, a moraine sequence in the Irishman basin on the eastern side of New Zealand's Southern Alps has a prominent outer moraine with a mean ^{10}Be surface exposure age of 13.0 ± 0.5 ka, marking the distinct glacier terminal position at the end of the ACR (Kaplan et al., 2010). The glacier then receded by over half its *ca* 13 ka length until *ca* 12 ka, with only minor moraine formation statistically indistinguishable from the ACR limit forming during this time. A moraine 100 m further inset of the 12 ka limit has a mean age of 11.5 ± 0.4 ka, bracketing a significant reduction in glacier size over the ca 1.5 ka following the ACR. This well constrained record is in line with the rapid recession observed at Calluqueo glacier, where over 75% of the length of the glacier is lost over a period of *ca* 1.3 ka and follows the same pattern of recession over this period that can be approximated from the less well constrained Patagonian records (Figure 8.3). As in

Patagonia, the Holocene record of glacier stability/readvance during overall recession shows discrepancies between sites with broad patterns of alignment. Comparisons of records from Cameron Glacier (Putnam et al., 2012), Mueller, Hooker and Tasman Glaciers (Schaefer et al., 2009), the Ben Ohau Range (Kaplan et al., 2013), and radiocarbon records from across the Southern Alps (Gellatly et al., 1988) show an advance in the early Holocene (*ca* 10 to 11 ka) followed by small, isolated fluctuations until a more widespread stillstand at *ca* 6.5 ka to 7 ka. A large number of stillstands separated by and lasting multiple centuries are recorded in the moraine record following *ca* 4 ka. Early observations from the Southern Alps indicate glaciers an advanced LIA position until the mid-to-late 1800s (Lorrey et al., 2014).

In the sub-Antarctic Islands, cosmogenic nuclide, soil depth model and lichenometric dating on South Georgia marks an outermost ice advance forming a moraine at *ca* 12.2 ± 1.5 ka, with subsequent mid to late Holocene readvances at *ca* 3.6 ± 1.1 ka, 1.1 ka (Bentley et al., 2007) and 1870 A.D (Roberts et al., 2010). A similar pattern of post-ACR deglaciation followed by at least two mid to late Holocene readvances is seen on Iles Kerguelen (Frenot et al., 1997; Hodgson et al., 2014; Solomina et al., 2015). On the Antarctic Peninsula and neighboring islands records show deglaciation from the LGM extent continued from *ca* 18 ka through the Holocene, punctuated by minor Holocene still-stands and readvances (Yoon et al., 2004; Strelin et al., 2006; Hall, 2009; Carrivick et al., 2012; Simms et al., 2012; Davies et al., 2013; Cofaigh et al., 2014), however a low density of samples and poorly resolved chronologies means that a region wide pattern of Holocene readvances is yet to be developed (Solomina et al., 2015).

8.3. Climate controls at Monte San Lorenzo

8.3.1. Relative temperature and precipitation sensitivity

The sensitivity of a glaciers' mass balance to climate, and the proportion to which each climate variable impacts glacier mass change, varies globally (Mackintosh et al., 2017), owing to the range of factors which dictate mass balance sensitivity. Changes in air temperature can have a large impact on glacier mass balance due to the control temperature has on both accumulation and ablation. Accumulation has highest sensitivity to temperature at the snow/rain threshold (usually between 0°C and 3°C) (Anderson and MacKintosh, 2012). This relationship is therefore strongest where precipitation is highest and falls at temperatures close to the snow/rain threshold, a scenario found in maritime environments (e.g. Purdie et al., 2008; Cullen and Conway, 2015). Such settings are also temperate with low continentality (the difference in mean temperature between the warmest and coldest month), providing a greater proportion of the year in which temperatures are high enough for ablation through melt (Anderson and MacKintosh, 2012). These factors combined lead to a high mass turnover and result in maritime

glaciers having the highest sensitivity to changes in climate (Meier, 1984; Oerlemans and Fortuin, 1992; Braithwaite et al., 2002). The most climatically sensitive glaciers are found in the mid-latitudes of the Southern Hemisphere (Mackintosh et al., 2017) where high precipitation falls at maritime glaciers on the western flanks of the Andes and Southern Alps of New Zealand (Garreaud et al., 2013; Schaefer et al., 2013; Lenaerts et al., 2014). In Patagonia, due to the strong west-east precipitation gradient and increase in continentality further inland, it would be expected that glacier sensitivity to climate would decrease on the eastern, lee-side of the Andes compared to the west. However given the high levels of precipitation that still fall on the eastern flank (e.g. 7.6 m w.e. a^{-1} at Perito Moreno Glacier (Stuefer et al., 2007), and approximately 5.5 m w.e. a^{-1} at MSL from this study) and the temperate climatic setting, a high mass turnover and high degree of sensitivity to climate would still be expected. The effect of the Andean rain shadow may also be lower at MSL than other glaciers positioned east of the NPI and SPI, as it sits at the northern margin of a orographic break in the mountain chain.

Due to their high sensitivity to changes in climate, Patagonia glaciers can therefore provide a valuable insight into both past and present-day climatic change and glacier-climate relationships. However, with the control both precipitation and temperature have on glacier mass balance, it can be difficult to establish which variable a glacier is most sensitive to. Precipitation and continentality also commonly vary in tandem so it is not possible to separate their influence on mass balance sensitivity (Oerlemans, 2001; Braithwaite, 2005; Anderson and MacKintosh, 2012). Using a numerical model of the MSL ice cap (chapter 7), it is possible to ascertain the relative sensitivity of the ice cap to temperature and precipitation change. Sensitivity experiments independently simulating the ice cap under step changes in temperature and precipitation (section 7.4.3.3) show that a 1°C offset in surface air temperature is equivalent to a 21% change in precipitation in order to obtain the same change in ice volume. This can be considered within the context of other glaciers in Patagonia and New Zealand which range from 20% to 83% precipitation change, and a global average of 25% precipitation change (Figure 8.4). Glaciers which have a higher change in precipitation equivalent to a 1°C change in temperature are less sensitive to precipitation relative to temperature than those which have a lower change in precipitation equivalent to a 1°C change in temperature. For example, at Perito Moreno Glacier (20% precipitation change equivalent to 1°C temperature change) precipitation has a proportionally greater impact on glacier mass balance relative to temperature than at Gran Campo Nevado (50% precipitation change equivalent to 1°C temperature change), so a lower change in precipitation is required to have the same impact on glacier mass balance as a 1°C temperature change.

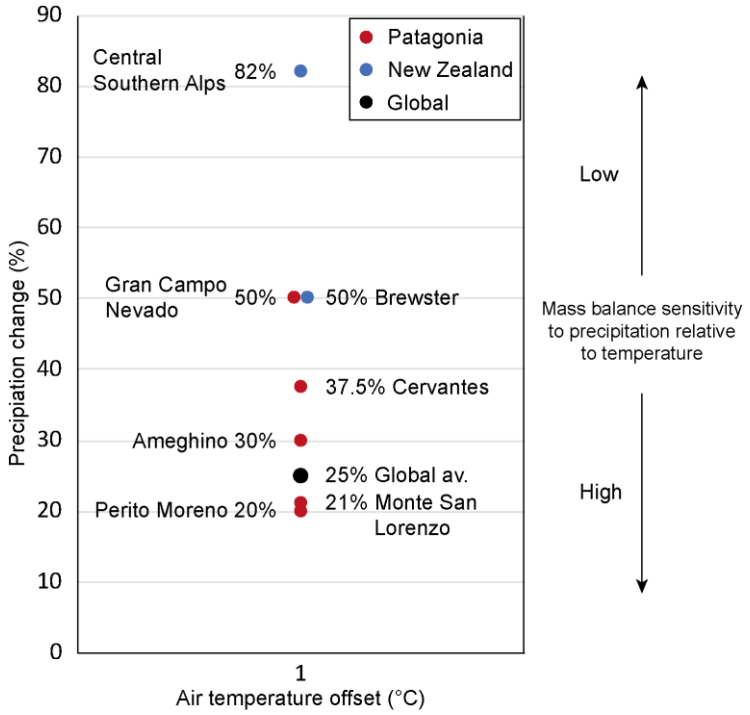

Figure 8.4. Precipitation change equivalent to 1°C change in air temperature at glaciers in Patagonia and New Zealand and a global average (black circle, (Oerlemans, 2005)). Red circles are glaciers in Patagonia at Perito Moreno, Ameghino and Cervantes Glaciers on the eastern side of the Southern Patagonian Andes (Bippus, 2007), the Gran Campo Nevado ice cap in southern Patagonia (53°S) (Moller et al., 2007) and the MSL ice cap (this study). Blue circles are glaciers in New Zealand's Southern Alps at Brewster Glacier (Anderson et al., 2007) and an average of a collection of glaciers from the central Southern Alps, including Franz Joseph, Fox and Tazman Glaciers (Anderson and MacKintosh, 2012).

Therefore, at MSL, compared to the other Patagonian and New Zealand glaciers studied, and the global average, precipitation plays a greater role in mass balance relative to temperature. In this region, the glaciers with a low sensitivity to precipitation relative to temperature are located in New Zealand's Southern Alps and the Gran Campo Nevado in southern Patagonia. At these strongly maritime glaciers where there is a higher level of precipitation falling close to the snow/rain threshold temperature, the impact of a small change in temperature has on mass balance, through changing the proportion of precipitation that falls as snow or rain, is exacerbated. Glaciers with comparatively higher mass balance sensitivity to precipitation relative to temperature are those in Patagonia on the eastern side of the Andes with greater continentality. Changes in temperature therefore have a lower impact on mass balance relative to precipitation, however there are variations between Cervantes, Ameghino, MSL and Perito Moreno glaciers. Perito Moreno Glacier, and Calluqueo glacier which dominates the accumulation area of glaciers at MSL, have much higher accumulation area ratios (0.68 at Calluqueo Glacier) and hence a smaller change in precipitation is needed for the equivalent mass balance change from a 1°C temperature variation. Although the dominant control on glacier mass balance is still temperature due to the strong empirical impact of temperature on accumulation (Anderson and MacKintosh, 2012), changes observed at MSL will have a

proportionally higher climatic signal than the majority of other glaciers in Patagonia. Glacier changes at MSL and Calluqueo glacier therefore provide an important indicator of precipitation change.

8.3.2. Palaeoclimate context

The new well-constrained chronology of glacier recession at Calluqueo glacier (chapter 5) provides the opportunity to examine deglaciation within the context of Patagonian palaeoclimate. Calluqueo Glacier receded rapidly after the ACR during the period of abrupt *ca* 2.5 °C warming that occurred from *ca* 12.7 ka to 11.7 ka, as recorded in the WAIS Divide ice core record (Cuffey et al., 2016) (Figure 8.5), alongside recession of glaciers across Patagonia (Figure 8.2). This Patagonian wide glacier recession has been interpreted in terms of the sharp increase in temperature recorded in Antarctica, as well as in sea surface temperature reconstructions (Kaiser et al., 2005; Quade and Kaplan, 2017).

The resumption of warming in the Southern Hemisphere following the ACR is currently considered to be a response to the onset of the Younger Dryas stadial in the Northern Hemisphere, through north-south climate coupling (Denton et al., 2010; Pedro et al., 2011). The manner to which this connection operates is still uncertain. The first mechanism is that of the 'biplor seesaw' where weakening and curtailment of the Atlantic Meridional Overturning Circulation (AMOC) caused by freshwater discharge into the North Atlantic at the Younger Dryas, causes heat to be retained in the southern ocean, promoting increased deep water formation and Southern Ocean and atmosphere warming (Broecker, 1998; Timmermann et al., 2007). Hemispheric warming results in a southward shift in the SWW (Fletcher and Moreno, 2011; Pedro et al., 2016). The second is by atmospheric teleconnection, where Younger Dryas cooling in the Northern Hemisphere causes a southward shift in the Intertropical Convergence Zone, in turn shifting the SWW further south (Toggweiler et al., 2006; Anderson et al., 2009; Toggweiler, 2009). This promotes Southern Hemisphere warming through the dispersion of sea ice via northward Ekman transport (Levermann et al., 2007) exposing the atmosphere to warmer upwelling ocean waters, increased heat transported southwards by eddies (Screen et al., 2009), and increased CO_2 degassing from the deep ocean (Denton et al., 2010).

Past latitudinal shifts and changes in intensity of the SWW have been inferred through reconstructions of precipitation from terrestrial pollen and charcoal proxies as well as lake-level stratigraphy (Moreno, 2004; Gilli et al., 2005; Markgraf et al., 2007; Whitlock et al., 2007; Lamy et al., 2010; Moreno et al., 2010; Fletcher and Moreno, 2011; Villa-Martínez et al., 2012; Van Daele et al., 2016; Quade and Kaplan, 2017) and the broad pattern and timing of latitudinal change in the wind belt has been estimated by Quade and Kaplan (2017) (Figure 8.5B). This

reconstruction shows a southward shift in the SWW over the period of warming following the ACR, in line with the two theoretical mechanisms of change in the southern hemispheric ocean-atmosphere system. This shift is reflected in latitudinally distributed proxy records showing SWW-derived moisture decreases in northwest Patagonia, accompanied by increased fire activity north of *ca* 50°S, and a moisture increase in southwestern Patagonia (Fletcher and Moreno, 2011).

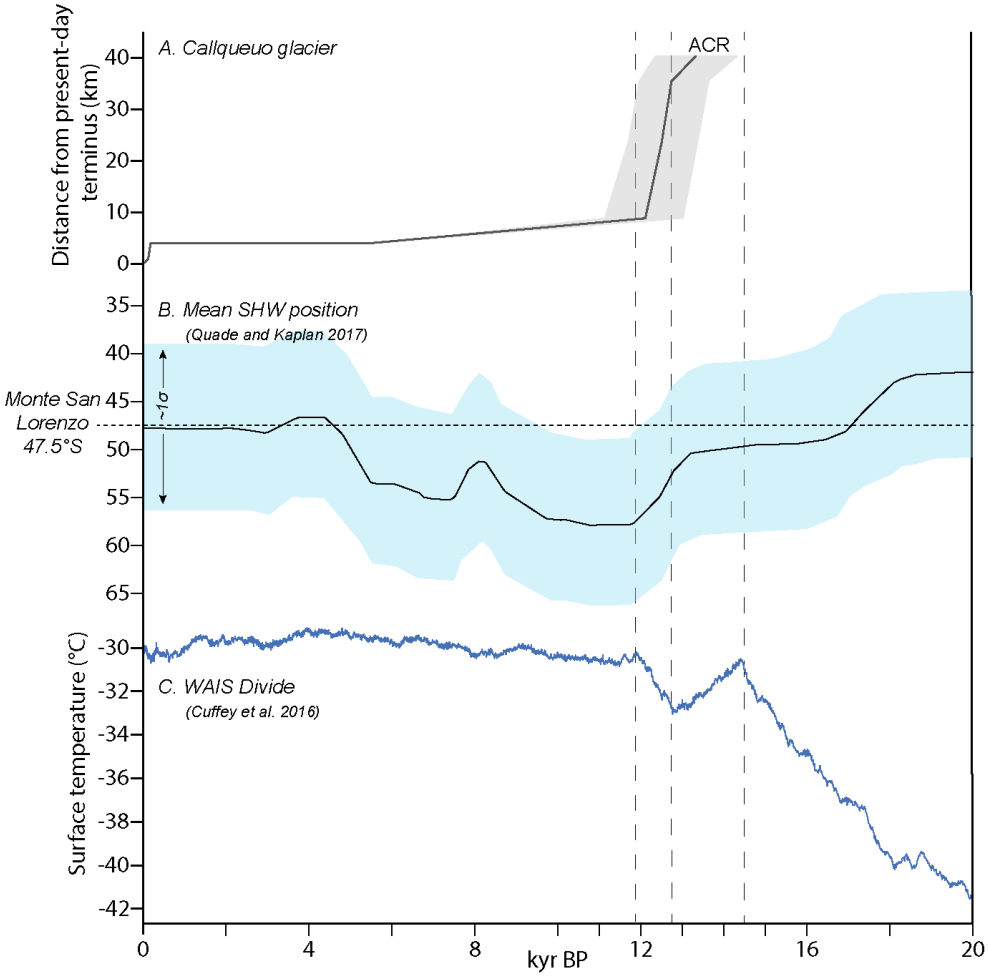

Figure 8.5. Comparison of A) the deglaciation of Calluqueo glacier, shown as distance of the ice front from the present-day terminus over the past 13.4 ka; B) the hypothesised latitudinal migration of the mean position of the Southern Westerly Winds (SWW). The blue shaded band shows the approximate 1σ latitudinal range, estimated from the near-normal distribution of westerly precipitation with latitude from western Chile (Quade and Kaplan, 2017). The dashed horizontal line shows the latitudinal location of the Monte San Lorenzo ice cap; C) surface air temperature reconstruction from the WAIS Divide ice core record (Cuffey et al., 2016).

Given the modelling findings of this study that the MSL ice cap is particularly sensitive to precipitation change alongside temperature change, it is likely this southward shift in the SWW belt to *ca* 55°S and resulting reduction in precipitation at MSL (47.5°S) contributed to the rapid recession of Calluqueo glacier over this warming period. Increased ocean upwelling during the post-ACR warming period is recorded in the increased opal flux in ocean sediment cores (Anderson et al., 2009), with increases in atmospheric CO_2 recorded in Antarctic ice cores (Augustin et al., 2004; Lemieux-Dudon et al., 2010). This increased ocean-atmosphere CO_2 flux

would have exacerbated warming (Denton et al., 2010). Kaplan et al. (2010) speculates that minor pauses in that rapid recession of ice in the Irishman basin in the Southern Alps, very similar the pattern of deglaciation at Calluqueo Glacier, could have been the result of fluctuations in CO_2.

Subsequent warming and decline in precipitation occurred in central Patagonia at the beginning of the Holocene (Moreno, 2004; Whitlock et al., 2007; Villa-Martínez et al., 2012), following by intensified wind strength and precipitation into the mid Holocene (Gilli et al., 2005; Markgraf et al., 2007; Van Daele et al., 2016). This is in line with the ELA studies of this work which estimate increased precipitation between 24% and 33% relative to present-day when Calluqueo glacier was at the M13 mid-Holocene limit (chapters 6 and 7) as well as regional neoglaciation.

8.4. Future work

8.4.1. Geomorphological and chronological constraints on deglaciations

New high-resolution geomorphological mapping by remote sensing and in the field has revealed seven new ice limits as part of the record of incremental ice recession north of the MSL ice cap (chapter 4). This has enabled the improved study of rapid deglaciation. Mapping of these limits was only possible through fieldwork, ground truthing remote sensing-based mapping, undertaking explorative geomorphological mapping in well-vegetated areas and studying the sedimentology of moraine deposits. The ability to identify ice limits and accurately identify and map landforms where their elevation is key to reconstructing landsystem evolution (e.g. raised deltas and palaeoshores) would also be improved through the acquisition of meter scale, high resolution digital elevation models such as LiDAR (Roering et al., 2013), which as well as affording a high resolution DEM provides the ability to map beneath the widespread forest in the region

Further fieldwork should therefore be undertaken in valleys across Patagonia to enable more widespread investigating into rapid deglaciation following the ACR and through the Holocene. Valleys should be targeted where such detailed mapping and exploratory work is currently limited, and the record of well-defined ice margins is limited to three or four covering post-ACR deglaciation (Figure 8.2 and Figure 8.3). Where late-glacial and mid-Holocene ice limits have been mapped and dated, further exploration could be undertaken to try to identify periodic stillstands immediately following the ACR, as observed at Calluqueo Glacier, as well as further Holocene neoglaciations (e.g. in the Nef and Colonia valleys). Following on from increased mapping of ice limits, dating of these limits will increase the number of temporally well constrained sequences of ice recession. Steep-sided moraines with glacially transported boulders atop sharp-crested ridges should be targeted for cosmogenic-nuclide surface exposure

dating. Kettle holes within moraine complexes (such as that at the M1c moraine at the eastern end of the Tranquilo valley (chapter 4) could be cored with organics carbon dated to provide a maximum are of moraine formation.

A particular area to target to reveal post-ACR recessional sequences is the valleys around small ice caps and isolated mountain glaciers. Mapping and dating valley sequences of ice limits at multiple sites along a latitudinal transect in Patagonia would provide the basis to investigate latitudinal variations in timings and rates of glacier recession within the context of latitudinal variability within the southern hemisphere climate system. Potential sites include Mount Tronador (41°S), the Queulat Ice Cap (44.5°S) and the Sierra de Sangra massif (48.5°S). Isolated smaller ice masses further south are more limited with outlets into fjords (e.g. Gran Campo Nevado (53°S)), and hence the record of ice recession is harder to constrain, so more detailed investigation is required to find potential isolated glaciers to study at these higher latitudes.

At MSL, further insight into deglaciation north of the ice cap could be obtained from a varve record, as effectively demonstrated by Bendle et al. (2017a). Exploratory coring in the Tranquilo valley, the site of ice-dammed palaeolake Tranquilo (chapter 4), would be beneficial. Such a varve record could reveal, on an annual to decadal scale, information regarding rates of ice recession in the period of rapid warming immediately following the ACR, resolving synchronicity or lag with high resolution atmosphere and ocean temperature records. This method has been proved to be valuable in defining the onset of deglaciation of the Buenos Aires ice lobe (46.5°S) (18,086 ± 214 cal a BP), where the record obtain by cosmogenic nuclide surface exposure dating is unable to resolve subcentennial response to rapid-warming (Bendle et al., 2017a). Anchoring any varve chronology in the Tranquilo valley is unlikely to be possible using tephra due to an absence of records in the *ca* 13 ka to 12 ka period during which palaeolake Tranquilo was present (Stern et al., 2016), and hence would rely on radiocarbon measurement of organic remains. However, even a floating varve chronology would have the potential to constrain the minimum duration of palaeolake Tranquilo.

8.4.2. Ice cap and ice sheet modelling

Through producing a numerical simulation of the MSL ice cap using the Parallel Ice Sheet (PISM) it has been possible to gain insights into mass balance variation, ice flow dynamics, climate sensitivity and palaeoclimate at the ice cap. The new simulation provides the basis for future work. Due to the variability in simulated ice extent, volume and dynamics under different model parameters, it would be of benefit to undertake further sensitivity experiments testing initialising parameters in combination. For example, it would be of benefit to explore combinations of precipitation lapse rates and degree-day factors which initialise the model to

present-day ice extent, as there is little empirical data and significant natural variability. Geothermal basal heat flux is also difficult to constrain with no in-situ measurements, so running further sensitivity experiments to quantify its impact on model simulations would be of benefit. Higher resolution simulations of ice in the LIA and mid-Holocene at smaller climate increments would also be beneficial to better constrain climatic conditions during these periods. Alongside this, the bathymetry of Calluqueo lake should be incorporated into the model bedrock DEM to simulate these smaller ice extents as accurately as possible. Bathymetric data show that Calluqueo lake has a maximum depth of 220m (Piret and Bertrand, personal communication, August 2019). Given current simulations give 175 m thick ice over the present-day lake, it is anticipated that incorporating lake bathymetry could alter simulated Calluqueo Glacier ice thickness and extent at 250 m (x, y), by 50 m (z) or higher resolution.

Alongside response time experiments for abrupt changes in temperature and precipitation, simulating the ACR with transient model runs represents a priority for future work. These simulations would help to refine the envelope of past temperature and precipitation conditions at this time and allow investigations into to run investigating rates of ice change during deglaciation. A further key point of investigation is to examine the impact of calving on the simulated ice dynamics. To fully integrate transient ice-lake coupling to simulate lake evolution, a non-trivial hydrological model would be required, which is currently not implemented into PISM. However given the constrained reconstructions of palaeolake evolution north of the MSL ice cap during (Davies et al., 2018; Martin et al., 2019; Thorndycraft et al., 2019) it may be possible to simulate lakes on a non-transient basis by applying PISM's calving model to pre-defined spatially variable sea-level forcing (Aschwanden, personal communication, July 2018). This is particularly necessary given the evidence for large ice dammed palaeolakes north of MSL until *ca* 12.7 ka, and in the Tranquilo valley, into which Calluqueo Glacier terminated (Davies et al., 2018; Martin et al., 2019; Thorndycraft et al., 2019). Finally, there is the potential to simulate the ice cap under IPCC scenarios of future climate to predict ice cap change though the 21st century.

This study has demonstrated for the first time the applicability of PISM to a small ice cap in Patagonia. The model could be applied to the ice caps and mountain glaciers identified for further study in section 8.4.1. Given its similar topographic and continental setting to that of MSL east of the NPI, glaciers at Sierra de Sangra are also likely to be particularly sensitive to precipitation change, providing a tool for further investigation into regional precipitation variation. Ultimately PISM could be used to simulate the NPI and SPI. PISM has been applied on an ice-field scale spanning *ca* 700 km to 800 km to model LGM ice extent in mountainous environments of New Zealand's Southern Alps (Golledge et al., 2012) and the European Alps

(Seguinot et al., 2018). In the latter of these a full transient glacial cycle was modelled. Modelling on this scale would require mode powerful computational resources. Golledge et al. (2012) used a super-computer, distributing horizontal components of the model domain across up to 4096 cores. A new review of deglaciation and 5 ka time-slice reconstruction of the Patagonian Icefield from 35 ka to 2011 AD (Davies et al., submitted) would provide the empirical data with which to calibrate the model simulation and investigate past climate conditions during the last glacial cycle. A model simulation of deglaciation would provide a valuable insight in the complex ice flow dynamics and interaction of multiple ice flowlines and the timing and pattern of separation of the NPI, SPI and surrounding massifs. It may be possible to simulate ice-dammed lakes formed around the Patagonian Ice Sheet during deglaciation (Davies et al., 2018; Thorndycraft et al., 2019; Davies et al., submitted) using the aforementioned application of PISM's calving model with spatially-variable sea-level forcing, however this remains an area which requires further investigation and development.

9. Conclusions

This thesis set out to improve our understanding of the timing, nature and drivers of deglaciation of the MSL ice cap as well as it's present-day characteristics and sensitivities, as outlined in the three primary research aims in Chapter 1.

The first aim, to elucidate the timing, nature and climate of deglaciation of outlet valleys north of the MSL ice cap through the Late Pleistocene and Holocene, was achieved through a new temporally constrained reconstruction of the deglaciation of Calluqueo Glacier and landsystem north of the ice cap, revealing in turn the primary controls on sediment-landform associations and landsystem development. ELA reconstructions provide quantitative estimates of palaeoprecipitation at glacier stillstands and readvances following the ACR and through the Holocene. In the absence of advanced ice spinup, high-resolution model experiments and small precipitation and temperature increments, the model simulation of the ice cap was unable to realistically reconstruct palaeoclimatic conditions at and following the ACR. This is a key target for future work in this area.

The second aim, to quantify present-day physical glacier properties, ice dynamics and sensitivities at the MSL ice cap, was achieved through a new model of the MSL ice cap turned to empirical data. The behaviour of the present-day ice cap, in active recession, was not fully replicated by the steady-state simulation used. Running transient simulations to replicate active recession is therefore a future priority. However, this study still provides a valuable insight into the properties, ice dynamics and sensitivities of the MSL ice cap, given the scarcity of empirical quantitative data.

The third aim, to determine the controls on deglaciation of the MSL ice cap, was achieved by evaluating the new reconstruction of Calluqueo glacier and our new understanding of climatic sensitivities at MSL within the broader context of the Southern Hemisphere climate system and abrupt climatic change following the ACR.

The main conclusions of this work are as follows:

- A detailed process-based sediment landform study of the Salto, Tranquilo and Pedregoso valley reveals lateral and terminal moraine ridges, ice-scoured bedrock, cirques and headwalls, flutes, deltas, ice-contact fans, glaciolacustrine deposits, palaeoshorelines, kame terraces and outwash and floodplains formed during deglaciation and subsequent paraglacial readjustment.
- During deglaciation the Salto, Tranquilo and Pedregoso valleys experienced transitions through glaciolacustrine, land-terminating glacial, mountain valley and paraglacial

landsystems, with these landsystems being juxtaposed and superimposed in the study region.

- The formation of sediment-landform assemblages is controlled by processes inherently linked to glacier's temperate setting, topography and ice-dammed lakes. High melt-water glacial processes, in particular sediment transport and reworking by proglacial meltwater, dominate the topographically constrained land-terminating glacial landsystem. Subglacial deformation, basal sliding and surpraglacial transport dominate the mountain valley landsystem.
- Seven newly mapped ice limits constrain the record of deglaciation at Calluqueo Glacier. ^{10}Be cosmogenic nuclide surface exposure dating of glacially transported boulders at two previously undated moraine complexes in the Salto and Pedregoso valleys provide new UWM ages of 12.5 ± 0.4 ka and 12.1 ± 0.4 ka respectively. When added to existing data this new record of deglaciation during a period of abrupt 2.5°C warming following the ACR shows rapid glacier recession averaging in excess of 44 m a^{-1}, just under twice the average rate of recession observed since 1985.
- A new model simulation of the present-day MSL ice cap reveals temperate, fast-flowing glaciers, with high mass turnover and surface mass balance ranging from +4.8 m w.e. a^{-1} to -6.5 m w.e. a^{-1} across the length of Calluqueo Glacier. Ablation at outlet glacier tongues reaches up 18 m w.e. a^{-1}.
- The MSL ice cap is sensitive to physical, mass balance and climate parameters, with decreases in temperature and increasing precipitation causing significant ice growth. Decreasing temperature is most effective at increasing the extent of glaciation due to decreases in the ELA.
- ELA reconstructions combined with the WAIS Divide temperature record give estimates of past climate at neoglacial advances following the ACR and through the Holocene of 1.1°C cooling and 33% to 37% higher precipitation at ca. 12.1 ka, 0.3°C cooling and 24% to 33% higher precipitation at ca. 5.6 ka and 0.7°C cooling and 19% to 29% higher precipitation at the LIA.
- Changes in mass balance of glaciers in Patagonia are primarily driven by temperature variations. However, the MSL ice cap, situated further inland with high continentality, is more sensitive to precipitation relative to temperature than those strongly maritime glaciers of the NPI and SPI, Gran Campo Nevado and glaciers of New Zealand's Southern Alps. 1°C offset in surface air temperature is equivalent to a 21% change in precipitation. Present-day and past glacier change at MSL therefore can provide an important insight into precipitation variations.

- Rapid recession of Calluqueo Glacier in the *ca* 1 ka following the ACR occurred during abrupt 2.5°C atmospheric warming recorded in Antarctica between 12.8 and 11.8 ka. In light of the sensitivity of MSL to precipitation change, rapid recession of Calluqueo glacier recorded between ca. 12.7 ka and 12.1 ka was likely driven by both atmospheric warming and precipitation reduction. Rapid deglaciation of Calluqueo glacier during this time, therefore, provides further evidence for a southward migration of the SWW following the ACR.

By revealing the temporal and spatial evolution of interconnected landsystems during deglaciation in a small number of valleys east of the NPI, this study highlights the importance of detailed, process based, wholistic landsystem studies to reveal the history of a once glaciated landscape. Incorporating both remote sensing and field-based mapping, alongside sedimentological studies and landform dating is needed to fully understand the changing environments and processes of deglaciation, their controls and relative and absolute temporal context. This study also shows the practicality and value of applying a fully three-dimensional ice sheet model to an ice cap/mountain valley environment at sub-km scale resolution. This further proof of concept has implications for applying such a model at higher resolutions to other ice caps and small ice sheets globally. By identifying MSL as an ice cap with particularly high sensitivity to precipitation relative to temperature, this study highlights the value of studying the deglaciation of such ice caps to elucidate past changes in atmospheric systems.

Future work should focus on dating multiple moraine sequences of other valleys along a latitudinal transect across Patagonia to improve regional models of deglaciation, in particular during periods of rapid climate change. Such studies should also aim to combine both cosmogenic dating of moraines with annually resolved varve records where possible to improve the temporal resolution of glacier dynamics during the Late Pleistocene and Holocene. Further glacier modelling should look to run high resolution, transient simulations of deglaciation and future glacier evolution, incorporating proglacial lakes. Glacier modelling is, to date, unable to fully resolve past climate estimates and requires further work at higher model resolution (< 500m) and smaller precipitation and temperature increments.

Appendices

The appendices for this thesis are include on a CD accompanying this document. These are three published papers and one submitted manuscript which I contributed work to. Martin et al. (2019) has been adapted to form Chapter 4 and contribute to Chapter 1.5 of this thesis.

- Martin, J.R.V., Davies, B.J., Thorndycraft, V.R., 2019. Glacier dynamics during a phase of Late Quaternary warming in Patagonia reconstructed from sediment-landform associations. Geomorphology 337, 111–133
  I wrote the manuscript and drew the figures. All authors assisted with fieldwork, contributed ideas and edited the manuscript.
- Thorndycraft, V.R., Bendle, J.M., Benito, G., Davies, B.J., Sancho, C., Palmer, A.P., Fabel, D., Armitage, S., Medealdea, A., Martin, J.R.V., 2019. Glacial lake evolution and Atlantic-Pacific drainage reversals during deglaciation of the Patagonian Ice Sheet. Quat. Sci. Rev. 203, 102–127
  I assisted with fieldwork and data collection in November/December 2016.
- Davies, B.J., Thorndycraft, V.R., Fabel, D., Martin, J.R.V., 2018. Asynchronous glacier dynamics during the Antarctic Cold Reversal in central Patagonia. Quat. Sci. Rev. 200, 287–312
  I assisted with fieldwork and data collection in November/December 2017.
- Davies, B.J., Darvill, C.M., Lovell, H., Bendle, J., Dowdeswell, A., Fabel, D., García, J., Geiger, A., Glasser, N.F., Gheorgiu, D.M., Harrison, S., Hein, A.S., Kaplan, M,R., Martin, J., Mendelova, M., Palmer, A., Pelto, M., Rodés, Á., Sagredo, E.A., Smedley, R., Smellie, J., Thorndycraft., V.R., Wolff., submitted. The evolution of the Patagonian Ice Sheet from 35 ka to the Present Day (PATICE)
  I contributed writing to topics of proxy records in Patagonia and the Monte San Lorenzo ice cap. Initial, unedited drafts of my contribution to this work are adapted in part for Chapter 2.1.3 and 2.1.4 of this thesis.

Abbreviations

- AABR Accumulation Area balance Ratio
- ACR Antarctic Cold Reversal
- cal. ka BP calibrated thousands of years ago
- ELA Equilibrium Line Altitude
- GIS Geographical Information System
- ka thousands of years ago
- CP Cochrane-Pueyrredón
- DEM Digital Elevation Model
- GCBA General Carrera-Buenos Aires
- LGIT Last Glacial-Interglacial Transition
- LGM Last Glacial Maximum
- LIA Little Ice Age
- m asl metres above sea level
- MSL Monte San Lorenzo
- NPI Northern Patagonian Icefield
- PDD Positive degree day
- PIS Patagonian Ice Sheet
- PISM Parallel Ice Sheet Model
- SAM Southern Annular Mode
- SIA Shallow Ice Approximation
- SPI Southern Patagonian Icefield
- SPOT Satellite Pour l'Observation de la Terre
- SRTM Shuttle Radar Topography Mission
- SSA Shallow Shelf Approximation
- SWW Southern Westerly Winds
- UWM Uncertainty weighted mean
- WAIS West Antarctic Ice Sheet

References

Ageta, Y., 1983. Characteristics of mass balance of the summer-accumulation type glacier in the Nepal Himalaya. Seppyo 45, 81–105.

Ageta, Y., Higuchi, K., 1984. Estimation of Mass Balance Components of a Summer-Accumulation Type Glacier in the Nepal Himalaya. Geogr. Ann. Ser. A, Phys. Geogr. 66, 249.

Alley, R.B., 1987. Firn Densification By Grain-Boundary Sliding : a First Model. Le J. Phys. Colloq. 48, C1-249-C1-256.

Alley, R.B., Lawson, D.E., Evenson, E.B., Strasser, J.C., Larson, G.J., 1998. Glaciohydraulic supercooling : a freeze-on nlechanisnl to create stratified , debris-rich basal ice : 11 . Theory 44, 563–569.

Alt, B.T., 1978. Synoptic Climate Controls of Mass-Balance Variations on Devon Island Ice Cap. Arct. Alp. Res. 10, 61.

Alvarez, D., Fagel, N., Araneda, a., Jana-Pinninghoff, P., Keppens, E., Urrutia, R., 2015. Late Holocene climate variability on the eastern flank of the Patagonian Andes (Chile): A 18O record from mollusks in Lago Cisnes (47 S). The Holocene.

Ambach, W., 1988. Heat balance characteristics and ice ablation, western EGIG-profile, Greenland.

Andersen, B.G., Denton, G.H., Lowell, T. V., 1999. Glacial geomorphologic maps of Llanquihue drift in the area of the southern Lake District, Chile. Geogr. Ann. Ser. A Phys. Geogr. 81, 155–166.

Anderson B., Lawson W., Owens I., Goodsell, B., 2006. Past and future mass balance of Ka Roimata o Hine Hukatere (Franz Josef Glacier). J. Glaciol. 52, 597–607.

Anderson, B., Mackintosh, A., 2006. Temperature change is the major driver of late-glacial and Holocene glacier fluctuations in New Zealand. Geology 34, 121–124.

Anderson, B., MacKintosh, A., 2012. Controls on mass balance sensitivity of maritime glaciers in the Southern Alps, New Zealand: The role of debris cover. J. Geophys. Res. Earth Surf. 117, 1–15.

Anderson, B., Mackintosh, A., Stumm, D., George, L., Kerr, T., Winter-Billington, A., Fitzimons, S., 2007. Climate sensitivity of a high-precipitation glacier in New-Zealand. J. Glaciol. 56, 114–128(15).

Anderson, B.E., Ali, S., Bradtmiller, L.I., Nielsen, S.H.H., Fleisher, M.Q., Anderson, B.E., Burckle, L.H., 2009. Wind-Driven Upwelling in the Southern Ocean and the Deglacial Rise in Atmospheric CO2. Science (80-.). 323, 1443–1448.

Anderson, R.S., Anderson, S.P., 2010. Geomorphology the mechanics and chemistry of landscapes. Cambridge University Press.

Andrews, J.T., 1975. Glacial systems. An approac to glaciers and their environments. Duxbury Press, North Scituate.

Aniya, M., 2013. Holocene glaciations of Hielo Patagonico (Patagonia Icefield), South America: A brief review. Geochem. J. 47, 97–105.

Aniya, M., Sato, H., 1995. Holocene glacial chronology of Upsala Glacier at Peninsula Herminita, Southern Patagonia Icefield. Bull. glacier Res. 13, 83–96.

Aniya, M., Sato, H., Naruse, R., Skvarca, P., Casassa, G., 1996. The Use of Satellite and Airborne Imagery to Inventory Outlet Glaciers of the Southern Patagonia Icefield , South America. Photogramm. Eng. Remote Sens. 62, 1361–1369.

Anonymous, 1969. Mass-balance terms. J. Glaciol. 8, 3–7.

Applegate, P.J., Urban, N.M., Keller, K., Lowell, T. V., Laabs, B.J.C., Kelly, M.A., Alley, R.B., 2012. Improved moraine age interpretations through explicit matching of geomorphic process models to cosmogenic nuclide measurements from single landforms. Quat. Res. 77, 293–304.

Applegate, P.J., Urban, N.M., Laabs, B.J.C., Keller, K., Alley, R.B., 2010. Modeling the statistical distributions of cosmogenic exposure dates from moraines. Geosci. Model Dev. 3, 293–307.

Araos, J.M., Le Roux, J.P., Kaplan, M.R., Spagnolo, M., 2018. Factors controlling alpine glaciations in the Sierra Baguales Mountain Range of southern Patagonia (50^{o} S), inferred from the morphometric analysis of glacial cirques. Andean Geol. 45, 357.

Aravena, J.C., 2007. Reconstructing climate variability using tree rings and glacier fl uctuations in the southern Chilean Andes. University of Western Ontario, London, Ontario, Canada.

Araya, P.S., Sagredo, E.A., Lowell, T. V, Aravena, J.C., 2014a. Glacial geomorphology at the Rio Tranquilo Valley (47° S): Reconstruction of the sequence of glacial events since the late-glacial through the Holocene, in: American Geophysical Union, Fall Meeting 2014.

Araya, P.S., Sagredo, E.A., Lowell, T. V, Aravena, J.C., 2014b. Glacial geomorphology at the Rio

Tranquilo Valley (47° S): Reconstruction of the sequence of glacial events since the late-glacial through the Holocene, in: American Geophysical Union, Fall Meeting 2014.

Arendt, A., Sharp, M., 1999. Energy balance measurements on a Canadian high Arctic glacier and their implications for mass balance modelling. IAHS Publ. 165–172.

Aristarain, A.J., Delmas, R.J., 1993. Firn-core study from the southern Patagonia ice cap, South America. J. Glaciol. 39, 249–254.

Aschwanden, A., Aøalgeirsdóttir, G., Khroulev, C., 2013. Hindcasting to measure ice sheet model sensitivity to initial states. Cryosphere 7, 1083–1093.

Aschwanden, A., Bueler, E., Khroulev, C., Blatter, H., 2012. An enthalpy formulation for glaciers and ice sheets. J. Glaciol. 58, 441–457.

Aschwanden, A., Fahnestock, M.A., Truffer, M., 2016. Complex Greenland outlet glacier flow captured. Nat. Commun. 7, 1–8.

Ashley, G.M., 2002. Glaciolacustrine Environments, in: Modern Glacial Environments: Processes, Dynamics, and Sediments. pp. 335–359.

ASTER GDEM Validation Team, 2011. ASTER global digital elevation model version 2 - summary of validation results, NASA Land Processes Distributed Active Archive Center and the Joint Japan-US ASTER Science Team Report.

Augustin, L., Barbante, C., Barnes, P.R.F., Barnola, J.M., Bigler, M., Castellano, E., Cattani, O., Chappellaz, J., Dahl-Jensen, D., Delmonte, B., others, 2004. Eight glacial cycles from an Antarctic ice core. Nature 429, 623–628.

Bahr, D.B., Pfeffer, W.T., Sassolas, C., Meier, M.F., 1998. Response time of glaciers as a function of size and mass balance: 1. Theory. J. Geophys. Res. Solid Earth 103, 9777–9782.

Bakke, J., Dahl, S.O., Nesje, A., 2005. Lateglacial and early Holocene palaeoclimatic reconstruction based on glacier fluctuations and equilibrium-line altitudes at northern Folgefonna, Hardanger, western Norway. J. Quat. Sci. J. Quat. Sci 20, 179–198.

Balco, G., 2011a. Contributions and unrealized potential contributions of cosmogenic-nuclide exposure dating to glacier chronology, 1990–2010. Quat. Sci. Rev. 30, 3–27.

Balco, G., 2011b. Contributions and unrealized potential contributions of cosmogenic-nuclide exposure dating to glacier chronology, 1990–2010. Quat. Sci. Rev. 30, 3–27.

Balco, G., Schaefer, J.M., 2006. Cosmogenic-nuclide and varve chronologies for the

deglaciation of southern New England. Quat. Geochronol. 1, 15–28.

Balco, G., Stone, J.O., Lifton, N.A., Dunai, T.J., 2008. A complete and easily accessible means of calculating surface exposure ages or erosion rates from 10Be and 26Al measurements. Quat. Geochronol.

Ballantyne, C.K., 2010. Extent and deglacial chronology of the last British-Irish Ice Sheet: Implications of exposure dating using cosmogenic isotopes. J. Quat. Sci. 25, 515–534.

Ballantyne, C.K., 2003. Paraglacial landsystems, in: Evans, D.J.A. (Ed.), Glacial Landsystems. Arnold, London, pp. 432–461.

Ballantyne, C.K., 2002. Paraglacial geomorphology. Quat. Sci. Rev. 21, 1935–2017.

Ballantyne, C.K., 1991. Holocene geomorphic activity in the Scottish Highlands. Scottish Geogr. J. 107, 84–98.

Ballantyne, C.K., 1989. The Loch Lomond Readvance on the Isle of Mull, Scotland: Glacier reconstruction and palaeoclimatic implications. J. Quat. Sci. 4, 95–108.

Bamber, J.L., Griggs, J.A., Hurkmans, R.T.W.L., Dowdeswell, J.A., Gogineni, S.P., Howat, I., Mouginot, J., Paden, J., Palmer, S., Rignot, E., Steinhage, D., 2013. A new bed elevation dataset for Greenland. Cryosph. 7, 499–510.

Barnes, P., Tabor, D., Walker, J.C.F., 1971. The Friction and Creep of Polycrystalline Ice. Proc. R. Soc. A Math. Phys. Eng. Sci. 324, 127–155.

Barr, I.D., Lovell, H., 2014. A review of topographic controls on moraine distribution. Geomorphology 226, 44–64.

Barrell, D.J.A., 2011. Quaternary Glaciers of New Zealand. Dev. Quat. Sci. 15, 1047–1064.

Beaudoin, A.B., King, R.H., 1994. Holocene palaeoenvironmental record preserved in a paraglacial alluvial fan, Sunwapta Pass, Jasper National Park, Alberta, Canada. Catena 22, 227–248.

Becker, P., Seguinot, J., Jouvet, G., Funk, M., 2016. Last glacial maximum precipitation pattern in the alps inferred from glacier Modelling. Geogr. Helv. 71, 173–187.

Bell, C.M., 2009. Quaternary lacustrine braid deltas on Lake General Carrera in southern Chile. Andean Geol. 36, 51–65.

Bell, C.M., 2008. Punctuated drainage of an ice-dammed Quaternary lake in southern South America. Geogr. Ann. Ser. A Phys. Geogr. 90, 1–17.

Bendle, J.M., Palmer, A.P., Thorndycraft, V.R., Matthews, I.P., 2017a. High-resolution chronology for deglaciation of the Patagonian Ice Sheet at Lago Buenos Aires (46.5°S) revealed through varve chronology and Bayesian age modelling. Quat. Sci. Rev. 177, 314–339.

Bendle, J.M., Thorndycraft, V.R., Palmer, A.P., 2017b. The glacial geomorphology of the Lago Buenos Aires and Lago Pueyrredón ice lobes of central Patagonia. J. Maps 13, 654–673.

Benn, D., 1994. Fluted moraine formation and till genesis below a temperate valley glacier: Slettmarkbreen, Jotunheimen, southern Norway. Sedimentology 41, 279–292.

Benn, D.I., 2014. Clast morphology, in: Evans, D.J.., Benn, D.I. (Eds.), A Practical Guide to the Study of Glacial Sediments. pp. 92–106.

Benn, D.I., 1995. Fabric signature of subglacial till deformation, Breidamerkurjökull, Iceland. Sedimentology 42, 735–747.

Benn, D.I., 1992. Scottish landform examples 5: The Achnasheen terraces. Scott. Geogr. Mag. 108, 128–131.

Benn, D.I., 1992. The genesis and significance of “hummocky moraine”: Evidence from the Isle of Skye, Scotland. Quat. Sci. Rev. 11, 781–799.

Benn, D.I., 1989. Controls on sedimentation in a late Devensian ice-dammed lake, Achnasheen, Scotland. Boreas 18, 31–42.

Benn, D.I., Andrews, S., 2007. Glacial Landforms , Sediments. Sediment. Geol. 904–909.

Benn, D.I., Ballantyne, C.K., 2005. Palaeoclimatic reconstruction from Loch Lomond Readvance glaciers in the West Drumochter Hills, Scotland. J. Quat. Sci. 20, 577–592.

Benn, D.I., Ballantyne, C.K., 1993. The description and representation of particle shape. Earth Surf. Process. Landforms 18, 665–672.

Benn, D.I., Evans, D.J.A., 2010. Glaciers and glaciation. Routledge.

Benn, D.I., Kirkbride, M.P., Owen, L.A., Brazier, V., 2003. Glaciated valley landsystems, in: Glacial Landsystems. pp. 372–406.

Benn, D.I., Lukas, S., 2006a. Younger Dryas glacial landsystems in North West Scotland: an assessment of modern analogues and palaeoclimatic implications. Quat. Sci. Rev. 25, 2390–2408.

Benn, D.I., Lukas, S., 2006b. Younger Dryas glacial landsystems in North West Scotland: an

assessment of modern analogues and palaeoclimatic implications. Quat. Sci. Rev. 25, 2390–2408.

Benn, D.I., Owen, L.A., 2002. Himalayan glacial sedimentary environments: A framework for reconstructing and dating the former extent of glaciers in high mountains. Quat. Int. 97–98, 3–25.

Benn, D.I., Owen, L.A., Osmaston, H.A., Seltzer, G.O., Porter, S.C., Mark, B., 2005. Reconstruction of equilibrium-line altitudes for tropical and sub-tropical glaciers. Quat. Int. 138–139, 8–21.

Benn, D.I., Warren, C.R., Mottram, R.H., 2007. Calving processes and the dynamics of calving glaciers. Earth-Science Rev. 82, 143–179.

Bennett, G.L., Evans, D.J.A., 2012. Glacier retreat and landform production on an overdeepened glacier foreland: The debris-charged glacial landsystem at Kvíárjökull, Iceland. Earth Surf. Process. Landforms 37, 1584–1602.

Bennett, G.L., Evans, D.J.A., Carbonneau, P., Twigg, D.R., 2010. Evolution of a debris-charged glacier landsystem, Kvíárjökull, Iceland. J. Maps 6, 40–67.

Bennett, M., Glasser, N., 2009. Glacial Geology, 2nd ed. ed, Journal of Chemical Information and Modeling. Wiley-Blackwell.

Bennett, M.R., Huddart, D., Thomas, G.S.P., 2002. Facies architecture within a regional glaciolacustrine basin: Copper River, Alaska. Quat. Sci. Rev. 21, 2237–2279.

Benson, C.S., 1961. Stratigraphic studies in the snow and firn of the Greenland Ice Sheet. Folia Geogr. Danica 70, 13–37.

Bentley, M., 1996. The role of lakes in moraine formation, Chilean Lake District. Earth Surf. Process. Landforms 21, 493–507.

Bentley, M.J., Evans, D.J.A., Fogwill, C.J., Hansom, J.D., Sugden, D.E., Kubik, P.W., 2007. Glacial geomorphology and chronology of deglaciation, South Georgia, sub-Antarctic. Quat. Sci. Rev. 26, 644–677.

Bertrand, S., Hughen, K.A., Lamy, F., Stuut, J.B.W., Torrej??n, F., Lange, C.B., 2012. Precipitation as the main driver of Neoglacial fluctuations of Gualas glacier, Northern Patagonian Icefield. Clim. Past 8, 519–534.

Bickerdike, H.L., Ó Cofaigh, C., Evans, D.J.A., Stokes, C.R., 2018. Glacial landsystems, retreat dynamics and controls on Loch Lomond Stadial (Younger Dryas) glaciation in Britain.

Boreas 47, 202–224.

Bippus, G., 2007. Modelling Mass Balance and Climate Sensitivity of Glaciers of the Southern Patagonia Icefield. Inst. Meterology Geophys. Masters of, 121.

Björck, S., Rundgren, M., Ljung, K., Unkel, I., Wallin, Å., 2012. Multi-proxy analyses of a peat bog on Isla de los Estados, easternmost Tierra del Fuego: A unique record of the variable Southern Hemisphere Westerlies since the last deglaciation. Quat. Sci. Rev. 42, 1–14.

Bjune, A.E., Bakke, J., Nesje, A., Birks, H.J.B., 2005. Holocene mean July temperature and winter precipitation in western Norway inferred from palynological and glaciological lake-sediment proxies. Holocene 15, 177–189.

Blunier, T., Schwander, J., Stauffer, B., Stocker, T., Dällenbach, A., Indermühle, A., Tschumi, J., Chappellaz, J., Raynaud, D., Barnola, J.-M., 1997. Timing of temperature variations during the last deglaciation in Antarctica and the atmospheric CO2 increase with respect to the Younger Dryas event. Geophys. Res. Let. 24, 2683–2686.

Boex, J., Fogwill, C., Harrison, S., Glasser, N.F., Hein, A., Schnabel, C., Xu, S., 2013. Rapid thinning of the late Pleistocene Patagonian Ice Sheet followed migration of the Southern Westerlies. Sci. Rep. 3, 1–6.

Borchers, B., Marrero, S., Balco, G., Caffee, M., Goehring, B., Lifton, N., Nishiizumi, K., Phillips, F., Schaefer, J., Stone, J., 2016a. Geological calibration of spallation production rates in the CRONUS-Earth project. Quat. Geochronol. 31, 188–198.

Borchers, B., Marrero, S., Balco, G., Caffee, M., Goehring, B., Lifton, N., Nishiizumi, K., Phillips, F., Schaefer, J., Stone, J., 2016b. Geological calibration of spallation production rates in the CRONUS-Earth project. Quat. Geochronol. 31, 188–198.

Boston, C.M., 2012. A glacial geomorphological map of the monadhliath mountains, central Scottish Highlands. J. Maps 8, 437–444.

Boston, C.M., Lukas, S., Carr, S.J., 2015. A Younger Dryas plateau icefield in the Monadhliath, Scotland, and implications for regional palaeoclimate. Quat. Sci. Rev. 108, 139–162.

Boulton, G.S., 1976. The origin of glacially fluted surfaces - observations and theory. J. Glaciol. 17, 287–309.

Boulton, G.S., 1972. The role of thermal regime in glacial sedimentation, in: Polar Geomorphology. IN, pp. 1–19.

Boulton, G.S., 1972. Modern Arctic glaciers as depositional models for former ice sheets. J.

Geol. Soc. London. 128, 361–393.

Boulton, G.S., Eyles, N., 1979. Sedimentation by valley glaciers: a model and genetic classification. Moraines and Varves 33, 11–23.

Boulton, G.S., Jones, A.S., 1979. Stability of temperate ice caps and ice sheets resting on beds of deformable sediment. J. Glaciol. 24, 29–43.

Bourgois, J., Cisternas, M.E., Braucher, R., Bourlès, D., Frutos, J., 2016. Geomorphic Records along the General Carrera (Chile)–Buenos Aires (Argentina) Glacial Lake (46°–48°S), Climate Inferences, and Glacial Rebound for the Past 7–9 ka. J. Geol. 124, 27–52.

Braithwaite, R.J., 2008. Temperature and precipitation climate at the equilibrium-line altitude of glaciers expressed by the degree-day factor for melting snow. J. Glaciol. 54, 437–444.

Braithwaite, R.J., 2005. Mass-balance characteristics of arctic glaciers. Ann. Glaciol. 42, 225–229.

Braithwaite, R.J., Olesen, O.B., 1990. Response of the Energy Balance on the Margin of the Greenland Ice Sheet to Temperature Changes. J. Glaciol. 36, 217–221.

Braithwaite, R.J., Olesen, O.B., 1989. Calculation of Glacier Ablation from Air Temperature, West Greenland. Springer, Dordrecht, pp. 219–233.

Braithwaite, R.J., Raper, S.C.B., Candela, R., 2013. Recent changes (1991-2010) in glacier mass balance and air temperature in the European Alps. Ann. Glaciol. 54, 139–146.

Braithwaite, R.J., Zhang, Y., Raper, S.C.B., 2002. Temperature sensitivity of the mass balance of mountain glaciers and ice caps as a climatological characteristic. Zeitschrift für Gletscherkd. und Glazialgeol. 38, 35–61.

Braun, M.H., Malz, P., Sommer, C., Farías-Barahona, D., Sauter, T., Casassa, G., Soruco, A., Skvarca, P., Seehaus, T.C., 2019. Constraining glacier elevation and mass changes in South America. Nat. Clim. Chang. 9, 130–136.

Bravo, C., Quincey, D.J., Ross, A.N., Rivera, A., Brock, B., Miles, E., Silva, A., 2019. Air Temperature Characteristics, Distribution, and Impact on Modeled Ablation for the South Patagonia Icefield. J. Geophys. Res. Atmos. 124, 907–925.

Brazier, V., Kirkbride, M.P., Gordon, J.E., 1998. Active ice-sheet deglaciation and ice-damned lakes in the northern Cairngorn Mountains, Scotland. Boreas 27, 297–310.

Broecker, W.S., 1998. Paleocean circulation during the Last Deglaciation: A bipolar seesaw? Paleoceanography 13, 119–121.

Bronk Ramsey, C., 2009a. Bayesian analysis of radiocarbon dates. Radiocarbon 51, 337–360.

Bronk Ramsey, C., 2009b. Dealing with Outliers and Offsets in Radiocarbon Dating. Radiocarbon 51, 1023–1045.

Bronk Ramsey, C., 2008. Deposition models for chronological records. Quat. Sci. Rev. 27, 42–60.

Brook, E.J., Nesje, A., Lehman, S.J., Raisbeck, G.M., Yiou, F., 1996. Cosmogenic nuclide exposure ages along a vertical transect in western Norway: Implications for the height of the Fennoscandian ice sheet. Geology 24, 207.

Brook, M.S., Lukas, S., 2012. A revised approach to discriminating sediment transport histories in glacigenic sediments in a temperate alpine environment: A case study from Fox Glacier, New Zealand. Earth Surf. Process. Landforms 37, 895–900.

Brown, L.E., Hannah, D.M., Milner, A.M., 2007. Vulnerability of alpine stream biodiversity to shrinking glaciers and snowpacks. Glob. Chang. Biol. 13, 958–966.

Brown, N.E., Hallet, B., Booth, D.B., 1987. Rapid soft bed sliding of the Puget glacial lobe. J. Geophys. Res. Solid Earth 92, 8985–8997.

Brynjólfsson, S., 2015. Dynamics and Glacial History of the Drangajökull Ice Cap, North- west Iceland.

Bueler, E., Brown, J., 2009. Shallow shelf approximation as a “sliding law” in a thermomechanically coupled ice sheet model. J. Geophys. Res. Solid Earth 114, 1–21.

Buizert, C., Cuffey, K.M., Severinghaus, J.P., Baggenstos, D., Fudge, T.J., Steig, E.J., Markle, B.R., Winstrup, M., Rhodes, R.H., Brook, E.J., Sowers, T.A., Clow, G.D., Cheng, H., Edwards, R.L., Sigl, M., McConnell, J.R., Taylor, K.C., 2015. The WAIS Divide deep ice core WD2014 chronology - Part 1: Methane synchronization (68-31 ka BP) and the gas age-ice age difference. Clim. Past 11, 153–173.

Burki, V., Larsen, E., Fredin, O., Margreth, A., 2009. The formation of sawtooth moraine ridges in Bødalen, western Norway. Geomorphology 105, 182–192.

Caldenius, C.C., 1932. Las glaciaciones cuaternarias en la Patagonia y Tierra del Fuego. Geogr. Ann. 14, 1–164.

Caldenius, C.R.C., 1932. Las glaciaciones cuaternarias en la Patagonia y Tierra del Fuego: una investigación regional, estratigráfica y geocronológica, una comparación con la escala geocronológica sueca. Dirección General de Minas y Geología.

Carrivick, J.L., Davies, B.J., Glasser, N.F., Nývlt, D., Hambrey, M.J., 2012. Late-Holocene changes in character and behaviour of land-terminating glaciers on James Ross Island, Antarctica. J. Glaciol. 58, 1176–1190.

Carrivick, J.L., Davies, B.J., James, W.H.M., Quincey, D.J., Glasser, N.F., 2016. Distributed ice thickness and glacier volume in southern South America. Glob. Planet. Change 146, 122–132.

Carrivick, J.L., Rushmer, E.L., 2009. Inter- and Intra-Catchment Variations in Proglacial Geomorphology: An Example From Franz Josef Glacier and Fox Glacier, New Zealand. Arctic, Antarct. Alp. Res. 41, 18–36.

Carrivick, J.L., Smith, M.W., Quincey, D.J., 2016. Structure from Motion in the Geosciences. John Wiley & Sons.

Carrivick, J.L., Tweed, F.S., 2013. Proglacial Lakes: Character, behaviour and geological importance. Quat. Sci. Rev. 78, 34–52.

Chandler, B.M.P., Evans, D.J.A., Roberts, D.H., 2016a. Characteristics of recessional moraines at a temperate glacier in SE Iceland: Insights into patterns, rates and drivers of glacier retreat. Quat. Sci. Rev. 135, 171–205.

Chandler, B.M.P., Evans, D.J.A., Roberts, D.H., 2016b. Characteristics of recessional moraines at a temperate glacier in SE Iceland: Insights into patterns, rates and drivers of glacier retreat. Quat. Sci. Rev. 135, 171–205.

Chandler, B.M.P., Evans, D.J.A., Roberts, D.H., Ewertowski, M., Clayton, A.I., 2016c. Glacial geomorphology of the Skálafellsjökull foreland, Iceland: A case study of 'annual' moraines. J. Maps 12, 904–916.

Chandler, B.M.P., Lovell, H., Boston, C.M., Lukas, S., Barr, I.D., Benediktsson, Í.Ö., Benn, D.I., Clark, C.D., Darvill, C.M., Evans, D.J.A., Ewertowski, M.W., Loibl, D., Margold, M., Otto, J.C., Roberts, D.H., Stokes, C.R., Storrar, R.D., Stroeven, A.P., 2018. Glacial geomorphological mapping: A review of approaches and frameworks for best practice. Earth-Science Rev. 185, 806–846.

Child, D., Elliott, G., Mifsud, C., Smith, A.M., Fink, D., 2000. Sample processing for earth science studies at ANTARES. Nucl. Instruments Methods Phys. Res. Sect. B Beam Interact. with Mater. Atoms 172, 856–860.

Chinn, T.J., 1996. New Zealand glacier responses to climate change of the past century. New Zeal. J. Geol. Geophys. 39, 415–428.

Chiverrell, R.C., Thrasher, I.A.N.M., Thomas, G.S.P., Lang, A., Scourse, J.D., Landeghem, K.J.J.V.A.N., Mccarroll, D., Clark, C.D., Evans, D.J.A., Ballantyne, C.K., 2013. Bayesian modelling the retreat of the Irish Sea Ice Stream 28, 200–209.

Church, M., Gilbert, R., 1975. Proglacial fluvial and lacustrine environments.

Clapperton, C.M., Sugden, D.E., 1988. Holocene glacier fluctuations in South America and Antarctica. Quat. Sci. Rev. 7.

Clark, C.D., Ely, J.C., Greenwood, S.L., Hughes, A.L.C., Meehan, R., Barr, I.D., Bateman, M.D., Bradwell, T., Doole, J., Evans, D.J.A., Jordan, C.J., Monteys, X., Pellicer, X.M., Sheehy, M., 2018. BRITICE Glacial Map, version 2: a map and GIS database of glacial landforms of the last British–Irish Ice Sheet. Boreas 47, 11-e8.

Clark, C.D., Hughes, A.L.C., Greenwood, S.L., Jordan, C., Sejrup, H.P., 2012. Pattern and timing of retreat of the last British-Irish Ice Sheet. Quat. Sci. Rev. 44, 112–146.

Clark, P.U., Dyke, A.S., Shakun, J.D., Carlson, A.E., Clark, J., Wohlfarth, B., Mitrovica, J.X., Hostetler, S.W., McCabe, A.M., 2009. The Last Glacial Maximum. Science 325, 710–4.

Clayton, L., Moran, S.R., 1982. A glacial process-form model, in: Glacial Geomorphology. Springer, pp. 89–119.

Cofaigh, C.Ó., Davies, B.J., Livingstone, S.J., Smith, J.A., Johnson, J.S., Hocking, E.P., Hodgson, D.A., Anderson, J.B., Bentley, M.J., Canals, M., Domack, E., Dowdeswell, J.A., Evans, J., Glasser, N.F., Hillenbrand, C.D., Larter, R.D., Roberts, S.J., Simms, A.R., 2014. Reconstruction of ice-sheet changes in the Antarctic Peninsula since the Last Glacial Maximum. Quat. Sci. Rev. 100, 87–110.

Cogley, J.G., 2010. Mass-balance terms revisited. J. Glaciol. 56, 997–1001.

Cogley, J.G., Hock, R., Rasmussen, L.., Arendt, A.., Bauder, A., Braithwaite, R.., Jansson, P., Kaser, G., Möller, M., Nicholson, L., Zemp, M., 2011. Glossary of Glacier Mass Balance and Related Terms. IHP-VII Tech. Doc. Hydrol. 86, 114.

Collins, M., Knutti, R., Arblaster, J., Dufresne, J.-L., Fichefet, T., Friedlingstein, P., Gao, X., Gutowski, W.J., Johns, T., Krinner, G., Shongwe, M., Tebaldi, C., Weaver, A.J., Wehner, M., 2013. Long-term climate change: Projections, commitments and irreversibility., in: Stocker, T.F., Qin, D., Plattner, G.K., Tignor, M., Allen, S.K., Boschung, J., Nauels, A., Xia, Y., Bex, V., P.M., M. (Eds.), Climate Change 2013: The Physical Science Basis. Contribution of Working Group I to the Fifth Assessment Report of the Intergovernmental Panel on Climate Change. Cambridge University Press, Cambridge, United Kingdom and New York,

NY, USA.

Collinson, J.D., 1996. Alluvial sediments, in: H.G., R. (Ed.), Sedimentary Environments. Oxford : Blackwell, pp. 37–82.

Corbett, L.B., Bierman, P.R., Rood, D.H., 2016. An approach for optimizing in situ cosmogenic 10Be sample preparation. Quat. Geochronol. 33, 24–34.

Cox, L.H., March, R.S., 2004. Comparison of geodetic and glaciological mass-balance techniques, Gulkana Glacier, Alaska, U.S.A. J. Glaciol. 50, 363–370.

Cuffey, K.M., Clow, G.D., Steig, E.J., Buizert, C., Fudge, T.J., Koutnik, M., Waddington, E.D., Alley, R.B., Severinghaus, J.P., 2016. The Deglacial Temperature History of West Antarctica 113, 1–6.

Cuffey, K.M., Paterson, W.S.B., 2010. The physics of glaciers. Academic Press.

Cullen, N.J., Conway, J.P., 2015. A 22 month record of surface meteorology and energy balance from the ablation zone of Brewster Glacier, New Zealand. J. Glaciol. 61, 931–946.

Curry, A.M., 1999. Paraglacial modification of slope form. Earth Surf. Process. Landforms 24, 1213–1228.

Curry, A.M., Cleasby, V., Zukowskyj, P., 2006. Paraglacial response of steep, sediment-mantled slopes to post-'Little Ice Age' glacier recession in the central Swiss Alps. J. Quat. Sci. 21, 211–225.

Dahl, S.O., Nesje, A., 1992. Paleoclimatic implications based on equilibrium-line altitude depressions of reconstructed Younger Dryas and Holocene cirque glaciers in inner Nordfjord, western Norway. Palaeogeogr. Palaeoclimatol. Palaeoecol. 94, 87–97.

Darvill, C.M., 2013. Cosmogenic nuclide analysis. Geomophological Tech. 10, 1–25.

Darvill, C.M., Bentley, M.J., Stokes, C.R., Shulmeister, J., 2016. The timing and cause of glacial advances in the southern mid-latitudes during the last glacial cycle based on a synthesis of exposure ages from Patagonia and New Zealand. Quat. Sci. Rev. 149, 200–214.

Darvill, C.M., Stokes, C.R., Bentley, M.J., Evans, D.J.A., Lovell, H., 2017. Dynamics of former ice lobes of the southernmost Patagonian Ice Sheet based on a glacial landsystems approach. J. Quat. Sci. 32, 857–876.

Darvill, C.M., Stokes, C.R., Bentley, M.J., Lovell, H., 2014. A glacial geomorphological map of the southernmost ice lobes of Patagonia: the Bahía Inútil - San Sebastián, Magellan, Otway, Skyring and Río Gallegos lobes. J. Maps 10, 500–520.

Davies, B.J., Darvill, C.M., Lovell, H., Bendle, J., Dowdeswell, A., Fabel, D., García, J., Geiger, A., Glasser, N.F., Gheorgiu, D.M., Harrison, S., Hein, A.S., Kaplan, M,R., Martin, J., Mendelova, M., Palmer, A., Pelto, M., Rodés, Á., Sagredo, E.A., Smedley, R., Smellie, J., Thorndycraft., V.R., Wolff., submitted. The evolution of the Patagonian Ice Sheet from 35 ka to the Present Day (PATICE)

Davies, B.J., Glasser, N.F., 2012. Accelerating shrinkage of Patagonian glaciers from the Little Ice Age (~AD 1870) to 2011. J. Glaciol. 58, 1063–1084.

Davies, B.J., Glasser, N.F., Carrivick, J.L., Hambrey, M.J., Smellie, J.L., Nývlt, D., 2013a. Landscape evolution and ice-sheet behaviour in a semi-arid polar environment: James Ross Island, NE Antarctic Peninsula. Geol. Soc. Spec. Publ. 381, 353–395.

Davies, B.J., Glasser, N.F., Carrivick, J.L., Hambrey, M.J., Smellie, J.L., Nývlt, D., 2013b. Landscape evolution and ice-sheet behaviour in a semi-arid polar environment: James Ross Island, NE Antarctic Peninsula. Geol. Soc. London, Spec. Publ. 381, 353–395.

Davies, B.J., Golledge, N.R., Glasser, N.F., Carrivick, J.L., Ligtenberg, S.R.M., Barrand, N.E., van den Broeke, M.R., Hambrey, M.J., Smellie, J.L., 2014. Modelled glacier response to centennial temperature and precipitation trends on the Antarctic Peninsula. Nat. Clim. Chang. 4, 993–998.

Davies, B.J., Thorndycraft, V.R., Fabel, D., Martin, J.R.V., 2018. Asynchronous glacier dynamics during the Antarctic Cold Reversal in central Patagonia. Quat. Sci. Rev. 200, 287–312.

Davies, J.H., 2013. Global map of solid Earth surface heat flow. Geochemistry, Geophys. Geosystems 14, 4608–4622.

Denton, G.H., Anderson, R.F., Toggweiler, J.R., Edwards, R.L., Schaefer, J.M., Putnam, A.E., 2010. The last glacial termination. Science 328, 1652–6.

Desilets, D., Zreda, M., Prabu, T., 2006. Extended scaling factors for in situ cosmogenic nuclides: New measurements at low latitude. Earth Planet. Sci. Lett. 246, 265–276.

Direccion Meteologica de Chile, 2001. Estadistica Climatologia Tomo III.

Doughty, A.M., Anderson, B.M., Mackintosh, A.N., Kaplan, M.R., Vandergoes, M.J., Barrell, D.J.A., Denton, G.H., Schaefer, J.M., Chinn, T.J.H., Putnam, A.E., 2013. Evaluation of Lateglacial temperatures in the Southern Alps of New Zealand based on glacier modelling at Irishman Stream, Ben Ohau Range. Quat. Sci. Rev. 74, 160–169.

Douglass, D.C., Singer, B.S., Kaplan, M.R., Ackert, R.P., Mickelson, D.M., Caffee, M.W., 2005.

Evidence of early Holocene glacial advances in southern South America from cosmogenic surface-exposure dating. Geology 33, 237–240.

Douglass, D.C., Singer, B.S., Kaplan, M.R., Mickelson, D.M., Caffee, M.W., 2006. Cosmogenic nuclide surface exposure dating of boulders on last-glacial and late-glacial moraines, Lago Buenos Aires, Argentina: Interpretive strategies and paleoclimate implications. Quat. Geochronol. 1, 43–58.

Dowdeswell, J.A., Hagen, J.O., Björnsson, H., Glazovsky, A.F., Harrison, W.D., Holmlund, P., Jania, J., Koerner, R.M., Lefauconnier, B., Ommanney, C.S.L., Thomas, R.H., 1997. The Mass Balance of Circum-Arctic Glaciers and Recent Climate Change. Quat. Res. 48, 1–14.

Dunai, T.J., 2010. Cosmogenic nuclides: principles, concepts and applications in the earth surface sciences. Cambridge University Press.

Dunai, T.J., 2001. Scaling factors for production rates of in situ produced cosmogenic nuclides: A critical reevaluation. Earth Planet. Sci. Lett. 176, 157–169.

Dusik, J.M., Leopold, M., Heckmann, T., Haas, F., Hilger, L., Morche, D., Neugirg, F., Becht, M., 2015. Influence of glacier advance on the development of the multipart Riffeltal rock glacier, Central Austrian Alps. Earth Surf. Process. Landforms 40, 965–980.

Dussaillant, A., Benito, G., Buytaert, W., Carling, P., Meier, C., Espinoza, F., 2010. Repeated glacial-lake outburst floods in Patagonia: an increasing hazard? Nat. Hazards 54, 469–481.

Dussaillant, I., Berthier, E., Brun, F., Masiokas, M., Hugonnet, R., 2019. Two decades of glacier mass loss along the Andes. Nat. Geosci. 21, 5143.

Egholm, D.L., Nielsen, S.B., Pedersen, V.K., Lesemann, J.-E., 2009. Glacial effects limiting mountain height. Nature 460, 884–887.

Elbert, J., Wartenburger, R., von Gunten, L., Urrutia, R., Fischer, D., Fujak, M., Hamann, Y., Greber, N.D., Grosjean, M., 2013a. Late Holocene air temperature variability reconstructed from the sediments of Laguna Escondida, Patagonia, Chile (45??30'S). Palaeogeogr. Palaeoclimatol. Palaeoecol. 369, 482–492.

Elbert, J., Wartenburger, R., von Gunten, L., Urrutia, R., Fischer, D., Fujak, M., Hamann, Y., Greber, N.D., Grosjean, M., 2013b. Late Holocene air temperature variability reconstructed from the sediments of Laguna Escondida, Patagonia, Chile (45°30'S). Palaeogeogr. Palaeoclimatol. Palaeoecol. 369, 482–492.

Elmore, D., Phillips, F.M., 1987. Accelerator mass spectrometry for measurement of long-lived

radioisotopes. Science (80-.). 236, 543–550.

Ely, J.C., Clark, C.D., Hindmarsh, R.C.A., Hughes, A.L.C., Greenwood, S.L., Bradley, S.L., Gasson, E., Gregoire, L., Gandy, N., Stokes, C.R., Small, D., 2019. Recent progress on combining geomorphological and geochronological data with ice sheet modelling, demonstrated using the last British–Irish Ice Sheet. J. Quat. Sci. jqs.3098.

Ely, J.C., Graham, C., Barr, I.D., Rea, B.R., Spagnolo, M., Evans, J., 2017. Using UAV acquired photography and structure from motion techniques for studying glacier landforms: application to the glacial flutes at Isfallsglaciären. Earth Surf. Process. Landforms 42, 877–888.

Escobar, F., Fernando, V., Garin, C., 1992. Water balance in the Patagonia Icefield, in: Naruse, R., Aniya, M. (Eds.), Glaciological Researches in Patagonia, 1990. Japanese Society of Snow and Ice, pp. 109–119.

Evans, D., Dinnage, M., Roberts, D.H., 2018. Glacial geomorphology of Teesdale, northern Pennines, England: Implications for upland styles of ice stream operation and deglaciation in the British-Irish Ice Sheet. Proc. Geol. Assoc. 129, 697–735.

Evans, D., Twigg, D., 2002. The active temperate glacial landsystem: a model based on Breioamerkurjokull and Fjallsjokull, Iceland 21, 2143–2177.

Evans, D.J.A., 2017. Chapter 4 Conceptual glacial ground models: British and Irish Case Studies. Eng. Geol. Geomorphol. Glaciat. Periglaciated Terrains. Eng. Gr. Work. Party Rep. 369–500.

Evans, D.J.A., 2014. Glacial landsystems. Routledge.

Evans, D.J.A., 2013. Glacial Landsystem. Encycl. Quat. Sci.

Evans, D.J.A., 2010. Controlled moraine development and debris transport pathways in polythermal plateau icefields: Examples from Tungnafellsj??kull, Iceland. Earth Surf. Process. Landforms 35, 1430–1444.

Evans, D.J.A., 2003a. Glacial Landsystems. Arnold, London.

Evans, D.J.A., 2003b. Ice-marginal terrestrial landsystems: active temperate glacier margins. Glacial Landsystems. Arnold, London 12–43.

Evans, D.J.A., Benn, D.I., 2004. A practical guide to the study of glacial sediments. Routledge.

Evans, D.J.A., Ewertowski, M., Orton, C., 2017. The glaciated valley landsystem of Morsárjökull, southeast Iceland. J. Maps 13, 909–920.

Evans, D.J.A., Ewertowski, M., Orton, C., 2016. Fláajökull (north lobe), Iceland: active temperate piedmont lobe glacial landsystem. J. Maps 12, 777–789.

Evans, D.J.A., Ewertowski, M., Orton, C., Graham, D., 2018. The Glacial Geomorphology of the Ice Cap Piedmont Lobe Landsystem of East Mýrdalsjökull, Iceland. Geosciences 8, 194.

Evans, D.J.A., Hiemstra, J.F., 2005. Till deposition by glacier submarginal, incremental thickening. Earth Surf. Process. Landforms 30, 1633–1662.

Evans, D.J.A., Lemmen, D.S., Rea, B.R., 1999. Glacial landsystems of the southwest Laurentide ice sheet: Modern Icelandic analogues. J. Quat. Sci. 14, 673–691.

Evans, D.J.A., Orton, C., 2015. Heinabergsjökull and Skalafellsjökull, Iceland: active temperate piedmont lobe and outwash head glacial landsystem. J. Maps 11, 415–431.

Evans, D.J.A., Rea, B.R., 1999. Geomorphology and sedimentology of surging glaciers. Ann. Glaciol. 28, 75–82.

Evans, D.J.A., Rother, H., Hyatt, O.M., Shulmeister, J., 2013. The glacial sedimentology and geomorphological evolution of an outwash head/moraine-dammed lake, South Island, New Zealand. Sediment. Geol. 284, 45–75.

Evans, D.J.A., Shulmeister, J., Hyatt, O., 2010a. Sedimentology of latero-frontal moraines and fans on the west coast of South Island, New Zealand. Quat. Sci. Rev. 29, 3790–3811.

Evans, D.J.A., Strzelecki, M., Milledge, D.G., Orton, C., 2012. Hørbyebreen polythermal glacial landsystem, Svalbard. J. Maps 8, 146–156.

Evans, D.J.A., Twigg, D.R., 2002. The active temperate glacial landsystem: a model based on Breiðamerkurjökull and Fjallsjökull, Iceland. Quat. Sci. Rev. 21, 2143–2177.

Evans, D.J.A., Twigg, D.R., Orton, C., 2010b. Satujökull glacial landsystem, Iceland. J. Maps 6, 639–650.

Evans, D.J.A., Twigg, D.R., Rea, B.R., Orton, C., 2009. Surging glacier landsystem of Tungnaárjökull, Iceland. J. Maps 5, 134–151.

Everest, J., Bradwell, T., Jones, L., Hughes, L., 2017. The geomorphology of Svínafellsjökull and Virkisjökull-Falljökull glacier forelands, southeast Iceland. J. Maps 13, 936–945.

Eyles, N., 1983. Glacial geology: a landsystems approach, in: Glacial Geology. Elsevier, pp. 1–18.

Eyles, N., 1979. Facies of supraglacial sedimentation on Icelandic and Alpine temperate

glaciers. Can. J. Earth Sci. 16, 1341–1361.

Eyles, N., Eyles, C., Miall, A.D., 1983. Lithofacies types and vertical profile models: an alternative approach to the description and environmental interpretation diamict sequences. Sedimentology 30, 393–410.

Fahnestock, M., Scambos, T., Moon, T., Gardner, A., Haran, T., Klinger, M., 2016. Rapid large-area mapping of ice flow using Landsat 8. Remote Sens. Environ. 185, 84–94.

Falaschi, D., Bolch, T., Rasterner, P., Lenzano, M.G., Lenzano, L., Lo Vecchio, A., Moragues, S., 2016. Mass changes of alpine glaciers at the eastern margin of the Northern and Southern Patagonian Icefields between 2000 and 2012. J. Glaciol. 1–15.

Falaschi, D., Bravo, C., Masiokas, M., Villalba, R., Rivera, A., 2013. First Glacier Inventory and Recent Changes in Glacier Area in the Monte San First Glacier Inventory and Recent Changes in Glacier Area in the Monte San Lorenzo Region 47º S, Southern Patagonian Andes, South America. Arctic, Antarct. Alp. Res. 45, 19–28.

Falaschi, D., Tadono, T., Masiokas, M., 2015. Rock Glaciers in the Patagonian Andes: an Inventory for the Monte San Lorenzo (Cerro Cochrane) Massif, 47° S. Geogr. Ann. Ser. A, Phys. Geogr. n/a-n/a.

Farrington, A., Mitchell, G.F., 1951. The End-Moraine north of Flamborough Head. Proc. Geol. Assoc. 62, 100–106.

Fick, S.E., Hijmans, R.J., 2017. WorldClim 2: new 1-km spatial resolution climate surfaces for global land areas. Int. J. Climatol. 37, 4302–4315.

Fletcher, M.S., Moreno, P.I., 2012. Have the Southern Westerlies changed in a zonally symmetric manner over the last 14,000 years? A hemisphere-wide take on a controversial problem. Quat. Int. 253, 32–46.

Fletcher, M.S., Moreno, P.I., 2011. Zonally symmetric changes in the strength and position of the Southern Westerlies drove atmospheric CO2 variations over the past 14 k.y. Geology 39, 419–422.

Fogwill, C.J., Golledge, N.R., Millman, H., Turney, C.S.M., 2016. The East Antarctic Ice Sheet as a source of sea-level rise : A major tipping element in the climate system ? 24, 2014–2015.

Fogwill, C.J., Turney, C.S.M., Hutchinson, D.K., Taschetto, A.S., England, M.H., Clark, P.U., Mix., A.C., Suggate, R.P., Vandergoes, M.J., Heusser, C.J., Heusser, L.E., Lowell, T. V., Rother, H., Timmermann, A., Sugden, D.E., Newnham, R., McCulloch, R.D., Collins, L.G., Kelley, S.E.,

Barrows, T.T., Reimer, P., Balco, G., Stone, J.O., Lifton, N.A., Dunai, T.J., Hein, A.S., Kaplan, M.R., Kaplan, M.R., Douglass, D.C., Kaplan, M.R., Boex, J., Putnam, A.E., Kaplan, M.R., Kidston, J., Taschetto, A.S., Thompson, D.W.J., England., M.H., Brayshaw, D.J., Hoskins, B., Blackburn, M., Otto-Bliesner, B., Collins, W.D., Rasch, P.J., Shemesh, A., Hodell, D., Crosta, X., Kanfoush, S., Charles, C., Guilderson, T., Putnam, A.E., McKinnon, K.A., Mackintosh, A.N., Anderson, B.M., Barrell, D.J.A., Doughty, A.M., Jakobsson, M., Long, A., Ingólfsson, Ó., Kjær, K.H., Spielhagen, R.F., Newnham, R.M., Lowe, D.J., Giles, T.M., Alloway, B. V., Wolff, E.W., Holling, J.T., Schilling, D.H., Denton, G.H., Hughes, T.J., Schaefer, J.M., Hallet, B., Putkonen, J., Putkonen, J., Swanson, T., Baillie, M.G.L., Denton, G.H., Indermühle, A., Monnin, E., Stauffer, B., Stocker, T.F., Wahlen, M., Lamy, F., Kaiser, J., Ninneman, U., Hebbeln, D., Arz, H.W., Stoner, J., 2015. Obliquity Control On Southern Hemisphere Climate During The Last Glacial. Sci. Rep. 5, 11673.

Fookes, P.G., Gordon, D.L., Higginbottom, I.E., 1975. Glacial landforms, their deposits and engineering characteristics. Eng. Behav. glacial Mater. 18–51.

Fountain, A.G., Neumann, T.A., Glenn, P.L., Chinn, T., 2004. Can climate warming induce glacier advance in Taylor Valley, Antarctica? J. Glaciol. 50, 556–564.

Fountain, A.G., Tangborn, W. V., 1985. The Effect of Glaciers on Streamflow Variations. Water Resour. Res. 21, 579–586.

Frenot, Y., Gloaguen, J.-C., Van De Vijver, B., Beyens, L., 1997. Datation de quelques sédiments tourbeux holocènes et oscillations glaciaires aux îles Kerguelen. Comptes Rendus l'Académie des Sci. - Ser. III - Sci. la Vie 320, 567–573.

Fujita, K., Ageta, Y., 2000. Effect of summer accumulation on glacier mass balance on the Tibetan Plateau revealed by mass-balance model. J. Glaciol. 46, 244–252.

Furbish, D.., Andrews, J.T., 1984. The Use of Hypsometry to Indicate Long-Term Stability and Response of Valley Glaciers to Changes in Mass Transfer. J. Glaciol. 30, 199–211.

García, J.L., 2012. Late pleistocene ice fluctuations and glacial geomorphology of the Archipiélago de Chiloé, southern Chile. Geogr. Ann. Ser. A Phys. Geogr. 94, 459–479.

García, J.L., Hall, B.L., Kaplan, M.R., Vega, R.M., Strelin, J.A., 2014. Glacial geomorphology of the Torres del Paine region (southern Patagonia): Implications for glaciation, deglaciation and paleolake history. Geomorphology 204, 599–616.

García, J.L., Hein, A.S., Binnie, S.A., Gómez, G.A., González, M.A., Dunai, T.J., 2018. The MIS 3 maximum of the Torres del Paine and Última Esperanza ice lobes in Patagonia and the

pacing of southern mountain glaciation. Quat. Sci. Rev. 185, 9–26.

García, J.L., Kaplan, M.R., Hall, B.L., Schaefer, J.M., Vega, R.M., Schwartz, R., Finkel, R., 2012. Glacier expansion in Southern Patagonia throughout the Antarctic Cold Reversal. Geology 40, 859–862.

Gardeweg, M., Sellés, D., 2013. Tephrochronology from Villa Castillo to Lago O'Higgens, Aysenm Chile: New insights on the 6,700 and 3,600 years BP eruptions of Hudson Volvano. Boll. di Geofis. Teor. ed Appl. 54, 155–157.

Gardner, A.S., Moholdt, G., Cogley, J.G., Wouters, B., Arendt, A.A., Wahr, J., Berthier, E., Hock, R., Pfeffer, W.T., Kaser, G., Ligtenberg, S.R.M., Bolch, T., Sharp, M.J., Hagen, J.O., van den Broeke, M.R., Paul, F., Meier, M.F., Cogley, J.G., Kaser, G., Cogley, J.G., Dyurgerov, M.B., Meier, M.F., Ohmura, A., Jacob, T., Wahr, J., Pfeffer, W.T., Swenson, S., Church, J.A., Zemp, M., Hoelzle, M., Haeberli, W., Moholdt, G., Nuth, C., Hagen, J.O., Kohler, J., Sasgen, I., Klemann, V., Martinec, Z., Luthcke, S.B., Arendt, A.A., Rowlands, D.D., McCarthy, J.J., Larsen, C.F., Wouters, B., Chambers, D., Schrama, E.J.O., Gardner, A.S., Moholdt, G., Wouters, B., Gardner, A.S., Bliss, A., Hock, R., Cogley, J.G., Rastner, P., Pritchard, H.D., Ligtenberg, S.R.M., Helsen, M.M., Broeke, M.R. van den, Hock, R., Woul, M. de, Radić, V., Dyurgerov, M., Rinne, E.J., Bolch, T., Bolch, T., Kääb, A., Berthier, E., Nuth, C., Gardelle, J., Arnaud, Y., Gardelle, J., Berthier, E., Arnaud, Y., Ivins, E.R., Willis, M.J., Melkonian, A.K., Pritchard, M.E., Ramage, J.M., Willis, M.J., Melkonian, A.K., Pritchard, M.E., Rivera, A., Melkonian, A.K., Schiefer, E., Menounos, B., Wheate, R., Berthier, E., Schiefer, E., Clarke, G.K.C., Menounos, B., Remy, F., Rignot, E., Rivera, A., Casassa, G., Gardner, A.S., Moholdt, G., Arendt, A., Wouters, B., Dyurgerov, M.B., Meier, M.F., Cogley, J.G., Adams, W.P., Shepherd, A., 2013. A reconciled estimate of glacier contributions to sea level rise: 2003 to 2009. Science 340, 852–7.

Garibotti, I.A., Villalba, R., 2017. Colonization of mid- and late-Holocene moraines by lichens and trees in the Magellanic sub-Antarctic province. Polar Biol. 40, 1739–1753.

Garreaud, R., Lopez, P., Minvielle, M., Rojas, M., 2013. Large-scale control on the Patagonian climate. J. Clim. 26, 215–230.

Garreaud, R., Lopez, P., Minvielle, M., Rojas, M., Garreaud, R., Lopez, P., Minvielle, M., Rojas, M., 2013. Large-Scale Control on the Patagonian Climate. J. Clim. 26, 215–230.

Garreaud, R.D., 2007. Precipitation and circulation covariability in the extratropics. J. Clim. 20, 4789–4797.

Garreaud, R.D., Vuille, M., Compagnucci, R., Marengo, J., 2009. Present-day South American

climate. Palaeogeogr. Palaeoclimatol. Palaeoecol. 281, 180–195.

Gellatly, A.F., Chinn, T.J.H., Röthlisberger, F., 1988. Holocene glacier variations in New Zealand: A review. Quat. Sci. Rev. 7, 227–242.

Geologische Bundesanstalt, W., 2013. Der Alpenraum zum Höhepunkt der letzten Eiszeit: Rekonstruktion der maximalen Gletscheraus- breitung während des Höhepunktes der letzten Eiszeit (Würm) von 26 000 bis 20 000 Jahren vor heute.

Gheorghiu, D.M., Fabel, D., Hansom, J.D., Xu, S., 2012. Lateglacial surface exposure dating in the Monadhliath Mountains, Central Highlands, Scotland. Quat. Sci. Rev. 41, 132–146.

Gilbert, G.K., 1885. The topographic features of lake shores. US Government Printing Office.

Giles, D.P., Griffiths, J.S., Evans, D.J.A., Murton, J.B., 2017. Chapter 3 Geomorphological framework: glacial and periglacial sediments, structures and landforms. Eng. Geol. Geomorphol. Glaciat. Periglaciated Terrains. Eng. Gr. Work. Party Rep. 28, 59–368.

Gilks, W.R., Richardson, S., Spiegelhalter, D., Richardson, S., Spiegelhalter, D., 1995. Markov Chain Monte Carlo in Practice. Chapman and Hall/CRC.

Gilli, A., Ariztegui, D., Anselmetti, F.S., McKenzie, J.A., Markgraf, V., Hajdas, I., McCulloch, R.D., 2005a. Mid-Holocene strengthening of the Southern Westerlies in South America - Sedimentological evidences from Lago Cardiel, Argentina (49??S). Glob. Planet. Change.

Gilli, A., Ariztegui, D., Anselmetti, F.S., McKenzie, J.A., Markgraf, V., Hajdas, I., McCulloch, R.D., 2005b. Mid-Holocene strengthening of the Southern Westerlies in South America - Sedimentological evidences from Lago Cardiel, Argentina (49°S). Glob. Planet. Change 49, 75–93.

Gladstone, R.M., Lee, V., Rougier, J., Payne, A.J., Hellmer, H., Le Brocq, A., Shepherd, A., Edwards, T.L., Gregory, J., Cornford, S.L., 2012. Calibrated prediction of Pine Island Glacier retreat during the 21st and 22nd centuries with a coupled flowline model. Earth Planet. Sci. Lett. 333–334, 191–199.

Glasser, N.F., Bennett, M.R., 2004. Glacial erosional landforms: Origins and significance for palaeoglaciology. Prog. Phys. Geogr. 28, 43–75.

Glasser, N.F., Clemmens, S., Schnabel, C., Fenton, C.R., McHargue, L., 2009a. Tropical glacier fluctuations in the Cordillera Blanca, Peru between 12.5 and 7.6 ka from cosmogenic 10 Be dating. Quat. Sci. Rev. 28, 3448–3458.

Glasser, N.F., Ghiglione, M.C., 2009. Structural, tectonic and glaciological controls on the

evolution of fjord landscapes. Geomorphology 105, 291–302.

Glasser, N.F., Hambrey, M.J., 2002. Sedimentary facies and landform genesis at a temperate outlet glacier: Soler glacier, North Patagonian Icefield. Sedimentology 49, 43–64.

Glasser, N.F., Hambrey, M.J., 2001. Styles of sedimentation beneath Svalbard valley glaciers under changing dynamic and thermal regimes. J. Geol. Soc. London. 158, 697–707.

Glasser, N.F., Harrison, S., Jansson, K., 2009b. Topographic controls on glacier sediment-landform associations around the temperate North Patagonian Icefield. Quat. Sci. Rev. 28, 2817–2832.

Glasser, N.F., Harrison, S., Jansson, K.N., Anderson, K., Cowley, A., 2011. Global sea-level contribution from the Patagonian Icefields since the Little Ice Age maximum. Nat. Geosci. 4, 303–307.

Glasser, N.F., Harrison, S., Schnabel, C., Fabel, D., Jansson, K.N., 2012a. Younger Dryas and early Holocene age glacier advances in Patagonia. Quat. Sci. Rev. 58, 7–17.

Glasser, N.F., Hughes, P.D., Fenton, C., Schnabel, C., Rother, H., 2012b. 10Be and 26Al exposure-age dating of bedrock surfaces on the Aran ridge, Wales: evidence for a thick Welsh Ice Cap at the Last Glacial Maximum. J. Quat. Sci. 27, 97–104.

Glasser, N.F., Jansson, K., 2008. The Glacial map of southern South America. J. Maps 4, 175–196.

Glasser, N.F., Jansson, K.N., 2005. Fast-flowing outlet glaciers of the Last Glacial Maximum Patagonian Icefield. Quat. Res. 63, 206–211.

Glasser, N.F., Jansson, K.N., Duller, G.A.T., Singarayer, J., Holloway, M., Harrison, S., 2016. Glacial lake drainage in Patagonia (13-8 kyr) and response of the adjacent Pacific Ocean. Sci. Rep. 6, 21064.

Glasser, N.F., Jansson, K.N., Harrison, S., Kleman, J., 2008. The glacial geomorphology and Pleistocene history of South America between 38°S and 56°S. Quat. Sci. Rev. 27, 365–390.

Glasser, N.F., Jansson, K.N., Harrison, S., Rivera, A., 2005. Geomorphological evidence for variations of the North Patagonian Icefield during the Holocene. Geomorphology 71, 263–277.

Glen, J.W., 1955. The creep of polycrystalline ice. Proc. R. Soc. 228, 519–538.

Golledge, N., Mackintosh, A.N., Anderson, B.M., Buckley, K.M., Doughty, A.M., Barrell, D.J.A., Denton, G.H., Vandergoes, M.J., Andersen, B.G., Schaefer, J.M., 2012. Last Glacial

Maximum climate in New Zealand inferred from a modelled Southern Alps icefield. Quat. Sci. Rev. 46, 30–45.

Golledge, N.R., 2007. An ice cap landsystem for palaeoglaciological reconstructions: characterizing the Younger Dryas in western Scotland. Quat. Sci. Rev. 26, 213–229.

Golledge, N.R., Phillips, E., 2008. Sedimentology and architecture of De Geer moraines in the western Scottish Highlands, and implications for grounding-line glacier dynamics. Sediment. Geol. 208, 1–14.

Golledge, N.R., Thomas, Z.A., Levy, R.H., Gasson, E.G.W., Naish, T.R., McKay, R.M., Kowalewski, D.E., Fogwill, C.J., 2017. Antarctic climate and ice-sheet configuration during the early Pliocene interglacial at 4.23 Ma. Clim. Past 13, 959–975.

Gong, Y., Zwinger, T., Åström, J., Altena, B., Schellenberger, T., Gladstone, R., Moore, J., others, 2018. Simulating the roles of crevasse routing of surface water and basal friction on the surge evolution of Basin 3, Austfonna ice cap. Cryosphere.

González, M.A., Salgado, P.S.A., Sagredo, E.A., Ward, D., 2013. Equilibrium Line Altitudes Since the Last Glacial Termination in Río Tranquilo Valley (47°S), Central Patagonia. Geosur.

Goodchild, J.G., 1875. The Glacial Phenomena of the Eden Valley and the Western Part of the Yorkshire-Dale District. Q. J. Geol. Soc. London 31, 55–99.

Goodsell, B., Hambrey, M.J., Classer, N.F., 2005. Debris transport in a temperate valley glacier: Haut Glacier d'Arolla, Valais, Switzerland. J. Glaciol. 51, 139–146.

Gordon, J.E., Brian Whalley, W., Gellatly, A.F., Vere, D.M., 1992. The formation of glacial flutes: Assessment of models with evidence from Lyngsdalen, North Norway. Quat. Sci. Rev. 11, 709–731.

Gosse, J.C., Phillips, F.M., 2001. Terrestrial in situ cosmogenic nuclides: theory and application. Quat. Sci. Rev. 20, 1475–1560.

Gourlet, P., Rignot, E., Rivera, A., Casassa, G., 2016. Ice thickness of the northern half of the Patagonia Icefields of South America from high-resolution airborne gravity surveys. Geophys. Res. Lett. 43, 241–249.

Graham, D.J., Hambrey, M.J., 2007. Sediments and landforms in an upland glaciated-valley landsystem, upper Ennerdale, English Lake District. Glacial Sediment. Process. Prod. Hambrey, MJ, Christoffersen, P., Glas. NF, Hubbard, B., Eds 235–256.

Greenwood, S., 2007. Formalising an inversion methodology for reconstructing ice-sheet

retreat patterns from meltwater channels: application to the British Ice Sheet. J. Quat. Sci. 22, 637–645.

Greve, R., Blatter, H., 2009. Dynamics of ice sheets and glaciers. Springer.

Greve, R., Saito, F., Abe-Ouchi, A., 2011. Initial results of the SeaRISE numerical experiments with the models SICOPOLIS and IcIES for the Greenland ice sheet. Ann. Glaciol. 52, 23–30.

Guillaume, B., Gautheron, C., Simon-Labric, T., Martinod, J., Roddaz, M., Douville, E., 2013. Dynamic topography control on Patagonian relief evolution as inferred from low temperature thermochronology. Earth Planet. Sci. Lett. 364, 157–167.

Haberzettl, T., Anselmetti, F.S., Bowen, S.W., Fey, M., Mayr, C., Zolitschka, B., Ariztegui, D., Mauz, B., Ohlendorf, C., Kastner, S., Lücke, A., Schäbitz, F., Wille, M., 2009. Late Pleistocene dust deposition in the Patagonian steppe - extending and refining the paleoenvironmental and tephrochronological record from Laguna Potrok Aike back to 55ka. Quat. Sci. Rev. 28, 2927–2939.

Haeberli, W., Hoelzle, M., Paul, F., Zemp, M., 2007. Integrated monitoring of mountain glaciers as key indicators of global climate change: the European Alps. Ann. Glaciol. 46, 150–160.

Hagen, J.O., Liestøl, O., 1990. Long-term glacier mass-balance investigations in Svalbard. Ann. Glaciol. 14, 102–106.

Hagg, W.J., Braun, L.N., Uvarov, V.N., Makarevich, K.G., 2004. A comparison of three methods of mass-balance determination in the Tuyuksu glacier region, Tien Shan, Central Asia. J. Glaciol. 50, 505–510.

Hajdas, I., Bonani, G., Moreno, P.I., Ariztegui, D., 2003. Precise radiocarbon dating of Late-Glacial cooling in mid-latitude South America. Quat. Res. 59, 70–78.

Hall, B.L., 2009. Holocene glacial history of Antarctica and the sub-Antarctic islands. Quat. Sci. Rev. 28, 2213–2230.

Hall, B.L., Lowell, T.V., Bromley, G.R.M., Denton, G.H., Putnam, A.E., 2019. Holocene glacier fluctuations on the northern flank of Cordillera Darwin, southernmost South America. Quat. Sci. Rev. 222, 105904.

Hallet, B., 1976. Deposits formed by subglacial precipitation of CaCO3. Geol. Soc. Am. Bull. 87, 1003.

Hallet, B., Hunter, L., Bogen, J., 1996. Rates of erosion and sediment evacuation by glaciers: A review of field data and their implications. Glob. Planet. Change 12, 213–235.

Hambrey, M.J., Ehrmann, W., 2004. Modification of sediment characteristics during glacial transport in high-alpine catchments: Mount Cook area, New Zealand. Boreas 33, 300–318.

Hambrey, M.J., Glasser, N.F., 2012. Discriminating glacier thermal and dynamic regimes in the sedimentary record. Sediment. Geol. 251, 1–33.

Hambrey, M.J., Quincey, D.J., Glasser, N.F., Reynolds, J.M., Richardson, S.J., Clemmens, S., 2009. Sedimentological, geomorphological and dynamic context of debris-mantled glaciers, Mount Everest (Sagarmatha) region, Nepal. Quat. Sci. Rev. 28, 1084.

Harrison, S., Glasser, N., Winchester, V., Haresign, E., Warren, C., Jansson, K., 2006. A glacial lake outburst flood associated with recent mountain glacier retreat, Patagonian Andes. The Holocene 16, 611–620.

Hastenrath, S., 1984. The glaciers of equatorial East Africa. Springer Science & Business Media.

Hedding, D.W., Brook, M.S., Winkler, S., 2018. Old landscapes, new eyes: Revisiting geomorphological research in the Southern Alps of New Zealand. N. Z. Geog. 74, 109–112.

Hein, A.S., Hulton, N.R.J., Dunai, T.J., Schnabel, C., Kaplan, M.R., Naylor, M., Xu, S., 2009. Middle Pleistocene glaciation in Patagonia dated by cosmogenic-nuclide measurements on outwash gravels. Earth Planet. Sci. Lett. 286, 184–197.

Hein, A.S., Hulton, N.R.J., Dunai, T.J., Sugden, D.E., Kaplan, M.R., Xu, S., 2010. The chronology of the Last Glacial Maximum and deglacial events in central Argentine Patagonia. Quat. Sci. Rev. 29, 1212–1227.

Hobbs, P.V., Mason, B.J., 1964. The sintering and adhesion of ice. Philos. Mag. 9, 181–197.

Hock, R., 2003. Temperature index melt modelling in mountain areas. J. Hydrol. 282, 104–115.

Hodgson, D.A., Graham, A.G.C., Griffiths, H.J., Roberts, S.J., Cofaigh, C.Ó., Bentley, M.J., Evans, D.J.A., 2014. Glacial history of sub-Antarctic South Georgia based on the submarine geomorphology of its fjords. Quat. Sci. Rev. 89, 129–147.

Hooke, R., 1991. Positive feedbacks associated with erosion of glacial cirques and overdeepenings. Geol. Soc. Am. Bull. 103, 1104–1108.

Hooke, R., 1981. Flow Law for Polycrystalline Ice in Glaciers: Comparison of Theoretical Predictions, Labratory Data and Field measurements. Rev. Geophys. Sp. Phys. 19, 664–672.

Hooke, R.L.., 2005. Principles of Glacier Mechanics. Cambridge University Press.

Hooyer, T.S., Iverson, N.R., 2000. Clast-fabric development in a shearing granular material: Implications for subglacial till and fault gouge. Geol. Soc. Am. Bull. 112, 683–692.

Hubbard, A., Hein, A.S., Kaplan, M.R., Hulton, N.R.., Glasser, N.F., 2005. a Modelling Reconstruction of the Last Glacial Maximum Ice Sheet and Its Deglaciation in the Vicinity of the Northern Patagonian Icefield , South America. Geogr. Ann. Ser. A Phys. Geogr. 87, 375–391.

Hughes, P.D., Gibbard, P.L., Ehlers, J., 2013. Timing of glaciation during the last glacial cycle: evaluating the concept of a global 'Last Glacial Maximum' (LGM). Earth-Science Rev. 125, 171–198.

Huss, M., Hock, R., 2018. Global-scale hydrological response to future glacier mass loss. Nat. Clim. Chang. 8, 135–140.

Hutchinson, M.F., Xu, T.B., 2013. Anusplin Version 4.4 User Guide. Aust. Natl. Univ. Fenner Sch. Environ. Soc. Canberra, Aust.

Hutter, K., 1983. Theoretical Glaciology. D. Reidel.

Iglesias, V., Markgraf, V., Whitlock, C., 2016. 17,000 years of vegetation, fire and climate change in the eastern foothills of the Andes (lat. 44°S). Palaeogeogr. Palaeoclimatol. Palaeoecol. 457, 195–208.

Immerzeel, W.W., van Beek, L.P.H., Bierkens, M.F.P., 2010. Climate change will affect the Asian water towers. Science 328, 1382–5.

Inge Svendsen, J., Mangerud, J., 1992. Paleoclimatic inferences from glacial fluctuations on Svalbard during the last 20 000 years. Clim. Dyn. 6, 213–220.

Ingólfsson, Ó., Benediktsson, Í.Ö., Schomacker, A., Kjær, K.H., Brynjólfsson, S., Jónsson, S.A., Korsgaard, N.J., Johnson, M.D., 2016. Glacial geological studies of surge-type glaciers in Iceland - Research status and future challenges. Earth-Science Rev. 152, 37–69.

Internacionales, A.O. de L., 1907. Mapa de la region Patagonica entre los grados 47 y 52 sud. Mapa IX.

International Hydrological Decade, 1970. Combined heat, ice and water balances at selected glacier basins. UNESCO Tech. Pap. Hydrol.

Iturrizaga, L., 2018. Glacial landform assemblages and pedestal moraines in the Cordillera Blanca (Peru). Geomorphology 318, 283–302.

Iverson, N.R., Jansson, P., Hooke, R.L., 1994. In-situ measurement of the strength of deforming subglacial till. J. Glaciol. 40, 497–503.

Ivy-Ochs, S., Briner, J.P., 2014. Dating Disappearing Ice with Cosmogenic Nuclides. Elements 10, 351–356.

Ivy-Ochs, S., Kober, F., 2008. Surface exposure dating with cosmogenic nuclides. Eiszeitalter und Gegenwart Quat. Sci. J. 57, 1–2.

Jacobsen, D., Milner, A.M., Brown, L.E., Dangles, O., 2012. Biodiversity under threat in glacier-fed river systems. Nat. Clim. Chang. 2, 361–364.

Jacquet, J., McCoy, S.W., McGrath, D., Nimick, D.A., Fahey, M., O'kuinghttons, J., Friesen, B.A., Leidich, J., 2017. Hydrologic and geomorphic changes resulting from episodic glacial lake outburst floods: Rio Colonia, Patagonia, Chile. Geophys. Res. Lett. 44, 854–864.

James, W.H.M., Carrivick, J.L., 2016. Automated modelling of spatially-distributed glacier ice thickness and volume. Comput. Geosci. 92, 90–103.

Jamieson, S.S.R., Vieli, A., Livingstone, S.J., Cofaigh, C.Ó., Stokes, C., Hillenbrand, C.D., Dowdeswell, J.A., 2012. Ice-stream stability on a reverse bed slope. Nat. Geosci. 5, 799–802.

Johnsen, T.F., Brennand, T.A., 2006. The environment in and around ice-dammed lakes in the moderately high relief setting of the southern Canadian Cordillera. Boreas 35, 106–125.

Johnsen, T.F., Brennand, T.A., 2004. Late-glacial lakes in the Thompson Basin, British Columbia: paleogeography and evolution. Can. J. Earth Sci. 41, 1367–1383.

Johnson, J.S., Everest, J.D., Leat, P.T., Golledge, N.R., Rood, D.H., Stuart, F.M., 2012. The deglacial history of NW Alexander Island, Antarctica, from surface exposure dating. Quat. Res. 77, 273–280.

Jones, A.P. (Alison P.., Tucker, M.E., Hart, J. (Jane), Quaternary Research Association., 1999. The description & analysis of Quaternary stratigraphic field sections. Quaternary Research Association.

Jones, R., N Mackintosh, A., Norton, K., Golledge, N., Fogwill, C., W Kubik, P., Christl, M., L Greenwood, S., 2015. Rapid Holocene thinning of an East Antarctic outlet glacier driven by marine ice sheet instability. Nat. Commun. 9910.

Jones, R.S., Small, D., Cahill, N., Bentley, M.J., Whitehouse, P.L., 2019. iceTEA: Tools for plotting and analysing cosmogenic-nuclide surface-exposure data from former ice margins. Quat.

Geochronol. 51, 72–86.

Joughin, I., Smith, B.E., Medley, B., 2014. Reports 27.3. Science (80-.). 344, 735–739.

Jouvet, G., Seguinot, J., Ivy-Ochs, S., Funk, M., 2017. Modelling the diversion of erratic boulders by the Valais Glacier during the last glacial maximum. J. Glaciol. 63, 487–498.

Kaiser, J., Lamy, F., Hebbeln, D., 2005. A 70-kyr sea surface temperature record off southern Chile (Ocean Drilling Program Site 1233). Paleoceanography 20, n/a-n/a.

Kamb, B., 1970. Sliding motion of glaciers: Theory and observation. Rev. Geophys. 8, 673.

Kamb, B., LaChapelle, E., 1964. Direct Observation of the Mechanism of Glacier Sliding over Bedrock. J. Glaciol. 5, 159–172.

Kaplan, M.R., Ackert, R.P., Singer, B.S., Douglass, D.C., Kurz, M.D., 2004. Cosmogenic nuclide chronology of millennial-scale glacial advances during O-isotope stage 2 in Patagonia. Geol. Soc. Am. Bull. 116, 308.

Kaplan, M.R., Douglass, D.C., Singer, B.S., Ackert, R.P., Caffee, M.W., 2005. Cosmogenic nuclide chronology of pre-last glacial maximum moraines at Lago Buenos Aires, 46°S, Argentina. Quat. Res. 63, 301–315.

Kaplan, M.R., Schaefer, J.M., Denton, G.H., Barrell, D.J.A., Chinn, T.J.H., Putnam, A.E., Andersen, B.G., Finkel, R.C., Schwartz, R., Doughty, A.M., 2010. Glacier retreat in New Zealand during the Younger Dryas stadial. Nature 467, 194–197.

Kaplan, M.R., Schaefer, J.M., Denton, G.H., Doughty, A.M., Barrell, D.J.A., Chinn, T.J.H., Putnam, A.E., Andersen, B.G., Mackintosh, A., Finkel, R.C., Schwartz, R., Anderson, B., 2013. The anatomy of long-term warming since 15 ka in New Zealand based on net glacier snowline rise. Geology 41, 887–890.

Kaplan, M.R., Schaefer, J.M., Strelin, J.A., Denton, G.H., Anderson, R.F., Vandergoes, M.J., Finkel, R.C., Schwartz, R., Travis, S.G., Garcia, J.L., Martini, M.A., Nielsen, S.H.H., 2016. Patagonian and southern South Atlantic view of Holocene climate. Quat. Sci. Rev. 141, 112–125.

Kaplan, M.R., Strelin, J.A., Schaefer, J.M., Denton, G.H., Finkel, R.C., Schwartz, R., Putnam, A.E., Vandergoes, M.J., Goehring, B.M., Travis, S.G., 2011. In-situ cosmogenic 10Be production rate at Lago Argentino, Patagonia: Implications for late-glacial climate chronology. Earth Planet. Sci. Lett. 309, 21–32.

Kaser, G., Fountain, A., Jansson, P., 2003. A Manual for monitoring the mass balance of

mountain glaciers with particular attention to low latitude characteristics; Technical documents in hydrology. Unesco Paris.

Kaser, G., Grosshauser, M., Marzeion, B., 2010. Contribution potential of glaciers to water availability in different climate regimes. Proc. Natl. Acad. Sci. 107, 20223–20227.

Kelly, M.A., Kubik, P.W., Von Blanckenburg, F., SchlÜchter, C., 2004. Surface exposure dating of the Great Aletsch Glacier Egesen moraine system, western Swiss Alps, using the cosmogenic nuclide10Be. J. Quat. Sci. 19, 431–441.

Kelly, M.A., Lowell, T. V., Hall, B.L., Schaefer, J.M., Finkel, R.C., Goehring, B.M., Alley, R.B., Denton, G.H., 2008. A 10Be chronology of lateglacial and Holocene mountain glaciation in the Scoresby Sund region, east Greenland: implications for seasonality during lateglacial time. Quat. Sci. Rev. 27, 2273–2282.

Kilian, R., Lamy, F., 2012. A review of Glacial and Holocene paleoclimate records from southernmost Patagonia (49-55°S). Quat. Sci. Rev. 53, 1–23.

Kingslake, J., Scherer, R.P., Albrecht, T., Coenen, J., Powell, R.D., Reese, R., Stansell, N.D., Tulaczyk, S., Wearing, M.G., Whitehouse, P.L., 2018. West Antarctic Ice Sheet during the Holocene. Nature.

Kirkbride, M.P., 1993. The temporal significance of transitions from melting to calving termini at glaciers in the central Southern Alps of New Zealand. The Holocene 3, 232–240.

Kjær, K.H., Korsgaard, N.J., 2008. Journal of Maps, 2008, 5-20 5–20.

Kjær, K.H., Korsgaard, N.J., Schomacker, A., 2008. Impact of multiple glacier surges - a geomorphological map from Brúarjökull, East Iceland. J. Maps 4, 5–20.

Klein, J., Middleton, R., Tang, H., 1982. Modifications of an FN tandem for quantitative 10Be measurement. Nucl. Instruments Methods Phys. Res. 193, 601–616.

Kleman, J., Borgstrom, I., 1994. Glacial land forms indicative of a partly frozen bed. J. Glaciol. 40, 255–264.

Kleman, J., Borgström, I., Hättestrand, C., 1994. Evidence for a relict glacial landscape in Quebec-Labrador. Palaeogeogr. Palaeoclimatol. Palaeoecol. 111, 217–228.

Kleman, J., Glasser, N.F., 2007. The subglacial thermal organisation (STO) of ice sheets. Quat. Sci. Rev. 26, 585–597.

Kleman, J., Hattestrand, C., Borgstrom, I., Stroeven, A., 1997. Fennoscandian palaeoglaciology reconstructed using a glacial geological inversion model. J. Glaciol. 43, 283–299.

Kleman, J., Hättestrand, C., Stroeven, A.P., Jansson, K.N., De Angelis, H., Borgström, I., 2006. Reconstruction of Palaeo-Ice Sheets - Inversion of their Glacial Geomorphological Record, in: Glacier Science and Environmental Change. Blackwell Publishing, Malden, MA, USA, pp. 192–198.

Kneisel, C., Kääb, A., 2007. Mountain permafrost dynamics within a recently exposed glacier forefield inferred by a combined geomorphological, geophysical and photogrammetrical approach. Earth Surf. Process. Landforms 32, 1797–1810.

Kong, P., Fink, D., Na, C., Huang, F., 2009. Late Quaternary glaciation of the Tianshan, Central Asia, using cosmogenic 10Be surface exposure dating. Quat. Res. 72, 229–233.

Koppes, M., Conway, H., Rasmussen, L.A., Chernos, M., 2011a. Deriving mass balance and calving variations from reanalysis data and sparse observations, Glaciar San Rafael, northern Patagonia, 1950-2005. Cryosphere 5, 791–808.

Koppes, M., Conway, H., Rasmussen, L.A., Chernos, M., 2011b. Deriving mass balance and calving variations from reanalysis data and sparse observations, Glaciar San Rafael, northern Patagonia, 1950-2005. Cryosphere 5, 791–808.

Korschinek, G., Bergmaier, A., Faestermann, T., Gerstmann, U.C., Knie, K., Rugel, G., Wallner, A., Dillmann, I., Dollinger, G., von Gostomski, C.L., Kossert, K., Maiti, M., Poutivtsev, M., Remmert, A., 2010. A new value for the half-life of 10Be by Heavy-Ion Elastic Recoil Detection and liquid scintillation counting. Nucl. Instruments Methods Phys. Res. Sect. B Beam Interact. with Mater. Atoms 268, 187–191.

Krüger, J., 1995. Origin, chronology and climatological significance of annual-moraine ridges at Myrdalsjökull, Iceland. The Holocene 5, 420–427.

Krumbein, W.C., 2003. Measurement and Geological Significance of Shape and Roundness of Sedimentary Particles. SEPM J. Sediment. Res. Vol. 11, 64–72.

Kubik, P.W., Ivy-Ochs, S., Masarik, J., Frank, M., Schlüchter, C., 1998. 10Be and 26Al production rates deduced from an instantaneous event within the dendro-calibration curve, the landslide of Köfels, Ötz Valley, Austria. Earth Planet. Sci. Lett. 161, 231–241.

Lal, D., 1991. Cosmic ray labeling of erosion surfaces: in situ nuclide production rates and erosion models. Earth Planet. Sci. Lett. 104, 424–439.

Lamy, F., Kilian, R., Arz, H.W., Francois, J.-P., Kaiser, J., Prange, M., Steinke, T., 2010. Holocene changes in the position and intensity of the southern westerly wind belt. Nat. Geosci. 3, 695–699.

Lang, H., 1986. Forecasting Meltwater Runoff from Snow-Covered Areas and from Glacier Basins. Springer, Dordrecht, pp. 99–127.

Lang, H., Braun, L., 1990. On the information content of air temperature in the context of snow melt estimation. Hydrol. Mt. Areas 347–354.

Langen, P.L., Solgaard, A.M., Hvidberg, C.S., 2012. Self-inhibiting growth of the Greenland Ice Sheet 39, 1–5.

Lee, J., 2017. Glacial Lithofacies and Stratigraphy, Past Glacial Environments: Second Edition. Elsevier Ltd.

Lemieux-Dudon, B., Blayo, E., Petit, J.-R., Svensson, A., Ritz, C., Barnola, J.-M., Narcisi, B.M., Parrenin, F., 2010. Consistent dating for Antarctic and Greenland ice cores. Quat. Sci. Rev. 29, 8–20.

Lenaerts, J.T.M., Van Den Broeke, M.R., Van Wessem, J.M., Van De Berg, W.J., Van Meijgaard, E., Van Ulft, L.H., Schaefer, M., 2014. Extreme precipitation and climate gradients in patagonia revealed by high-resolution regional atmospheric climate modeling. J. Clim. 27, 4607–4621.

Lenaerts, J.T.M., van Meijgaard, E., van den Broeke, M.R., Ligtenberg, S.R.M., Horwath, M., Isaksson, E., 2013. Recent snowfall anomalies in Dronning Maud Land, East Antarctica, in a historical and future climate perspective. Geophys. Res. Lett. 40, 2684–2688.

Levermann, A., Schewe, J., Montoya, M., 2007. Lack of bipolar see-saw in response to Southern Ocean wind reduction. Geophys. Res. Lett. 34, L12711.

Li, H., Ng, F., Li, Z., Qin, D., Cheng, G., 2012. An extended “perfect-plasticity” method for estimating ice thickness along the flow line of mountain glaciers. J. Geophys. Res. Earth Surf. 117, 1–11.

Lichtenecker, N., 1938. Die gegenwartige und die eiszeit liche Schneegrenze in den Ostalpen. Verhandlungsband der III. Int. Quartarkonferenz, Wien 1936, 141–147.

Lifton, N., Sato, T., Dunai, T.J., 2014. Scaling in situ cosmogenic nuclide production rates using analytical approximations to atmospheric cosmic-ray fluxes. Earth Planet. Sci. Lett. 386, 149–160.

Lifton, N.A., Bieber, J.W., Clem, J.M., Duldig, M.L., Evenson, P., Humble, J.E., Pyle, R., 2005. Addressing solar modulation and long-term uncertainties in scaling secondary cosmic rays for in situ cosmogenic nuclide applications. Earth Planet. Sci. Lett. 239, 140–161.

Livingstone, S.J., Evans, D.J.A., Cofaigh, C.??, Hopkins, J., 2010. The Brampton kame belt and Pennine escarpment meltwater channel system (Cumbria, UK): Morphology, sedimentology and formation. Proc. Geol. Assoc. 121, 423–443.

Livingstone, S.J., Storrar, R.D., Hillier, J.K., Stokes, C.R., Clark, C.D., Tarasov, L., 2015. An ice-sheet scale comparison of eskers with modelled subglacial drainage routes. Geomorphology 246, 104–112.

Lliboutry, L., Duval, P., 1985. Various isotropic and anisotropic ices found in glaciers and polar ice caps and their corresponding rheologies, in: Annales Geophysicae. pp. 207–224.

Longhitano, S.G., 2008. Sedimentary facies and sequence stratigraphy of coarse-grained Gilbert-type deltas within the Pliocene thrust-top Potenza Basin (Southern Apennines, Italy). Sediment. Geol. 210, 87–110.

Lopez, P., Chevallier, P., Favier, V., Pouyaud, B., Ordenes, F., Oerlemans, J., 2010. A regional view of fluctuations in glacier length in southern South America. Glob. Planet. Change 71, 85–108.

Lorrey, A., Fauchereau, N., Stanton, C., Chappell, P., Phipps, S., Mackintosh, A., Renwick, J., Goodwin, I., Fowler, A., 2014. The Little Ice Age climate of New Zealand reconstructed from Southern Alps cirque glaciers: A synoptic type approach. Clim. Dyn. 42, 3039–3060.

Lowe, J.J., Walker, M.J.C., 2014. Reconstructing quaternary environments, Third edit. ed. London : Routledge.

Lukas, S., 2006. Morphostratigraphic principles in glacier reconstruction - A perspective from the British Younger Dryas. Prog. Phys. Geogr. 30, 719–736.

Lukas, S., Benn, D.I., Boston, C.M., Brook, M., Coray, S., Evans, D.J.A., Graf, A., Kellerer-Pirklbauer, A., Kirkbride, M.P., Krabbendam, M., Lovell, H., Machiedo, M., Mills, S.C., Nye, K., Reinardy, B.T.I., Ross, F.H., Signer, M., 2013. Clast shape analysis and clast transport paths in glacial environments: A critical review of methods and the role of lithology. Earth-Science Rev. 121, 96–116.

Lukas, S., Bradwell, T., 2010. Reconstruction of a lateglacial (Younger Dryas) mountain ice field in Sutherland, northwestern Scotland, and its palaeoclimatic implications. J. Quat. Sci. 25, 567–580.

Luthcke, S.B., Arendt, A.A., Rowlands, D.D., McCarthy, J.J., Larsen, C.F., 2008. Recent glacier mass changes in the Gulf of Alaska region from GRACE mascon solutions. J. Glaciol. 54, 767–777.

Mackintosh, A.N., Anderson, B.M., Pierrehumbert, R.T., 2017. Reconstructing Climate from Glaciers. Annu. Rev. Earth Planet. Sci. 45, annurev-earth-063016-020643.

Maeno, N., Eblnuma, T., 1983. Pressure Sintering of Ice and Its Implication to the Densification of Snow at Polar Glaciers and Ice Sheets. J. Phys. Chem. 169, 4103–4110.

Mager, S., Fitzsimons, S., 2007. Formation of glaciolacustrine Late Pleistocene end moraines in the Tasman Valley, New Zealand. Quat. Sci. Rev. 26, 743–758.

Malecki, J., Lovell, H., Ewertowski, W., Górski, Ł., Kurczaba, T., Latos, B., Miara, M., 2018. The glacial landsystem of a tropical glacier : Charquini Sur , Bolivian Andes.

Mancini, M. V., Paez, M.M., Prieto, A.R., Stutz, S., Tonello, M., Vilanova, I., 2005. Mid-Holocene climatic variability reconstruction from pollen records (32°-52°S, Argentina). Quat. Int. 132, 47–59.

Mansilla, C.A., McCulloch, R.D., Morello, F., 2016. Palaeoenvironmental change in Southern Patagonia during the lateglacial and Holocene: Implications for forest refugia and climate reconstructions. Palaeogeogr. Palaeoclimatol. Palaeoecol.

Marden, C.J., 1997. Late-glacial fluctuations of South Patagonian icefield, Torres del Paine National Park, Southern Chile. Quat. Int. 38–39, 61–68.

Markgraf, V., Whitlock, C., Haberle, S., 2007. Vegetation and fire history during the last 18,000 cal yr B.P. in Southern Patagonia: Mallín Pollux, Coyhaique, Province Aisén (45°41’30” S, 71°50’30” W, 640 m elevation). Palaeogeogr. Palaeoclimatol. Palaeoecol. 254, 492–507.

Marren, P.M., 2005. Magnitude and frequency in proglacial rivers: a geomorphological and sedimentological perspective. Earth-Science Rev. 70, 203–251.

Martin, J.R.V., Davies, B.J., Thorndycraft, V.R., 2019. Glacier dynamics during a phase of Late Quaternary warming in Patagonia reconstructed from sediment-landform associations. Geomorphology 337, 111–133.

Marzeion, B., Jarosch, a. H., Hofer, M., 2012. Past and future sea-level change from the surface mass balance of glaciers. Cryosph. 6, 1295–1322.

Masiokas, M.H., Rivera, A., Espizua, L.E., Villalba, R., Delgado, S., Aravena, J.C., 2009. Glacier fluctuations in extratropical South America during the past 1000 years. Palaeogeogr. Palaeoclimatol. Palaeoecol. 281, 242–268.

Massaferro, J., Larocque-Tobler, I., 2013. Using a newly developed chironomid transfer

function for reconstructing mean annual air temperature at Lake Potrok Aike, Patagonia, Argentina. Ecol. Indic. 24, 201–210.

Massaferro, J., Larocque-Tobler, I., Brooks, S.J., Vandergoes, M., Dieffenbacher-Krall, A., Moreno, P., 2014. Quantifying climate change in Huelmo mire (Chile, Northwestern Patagonia) during the Last Glacial Termination using a newly developed chironomid-based temperature model. Palaeogeogr. Palaeoclimatol. Palaeoecol. 399, 214–224.

Matthews, J.A., Cornish, R., Shakesby, R.A., 1979. "Saw-Tooth" Moraines in Front of Bødalsbreen, Southern Norway. J. Glaciol. 22, 535–546.

Mayo, L.R., Meier, M.F., Tangborn, W.V., 1972. A system to combine stratigraphic and annual mass-balance systems: a contribution to the international hydrological decade. J. Glaciol. 11, 3–14.

Mayr, C., Lücke, A., Wagner, S., Wissel, H., Ohlendorf, C., Haberzettl, T., Oehlerich, M., Schäbitz, F., Wille, M., Zhu, J., Zolitschka, B., 2013. Intensified Southern Hemisphere Westerlies regulated atmospheric CO2 during the last deglaciation. Geology 41, 831–834.

McCabe, G.J., Fountain, A.G., 1995. Relations between Atmospheric Circulation and Mass Balance of South Cascade Glacier, Washington, U.S.A. Arct. Alp. Res. 27, 226.

McCulloch, R.D., Bentley, M.J., Purves, R.S., Hulton, N.R.J., Sugden, D.E., Clapperton, C.M., 2000. Climatic inferences from glacial and palaeoecological evidence at the last glacial termination, southern South America. J. Quat. Sci. 15, 409–417.

Meier, M.F., 1984. Contribution of small glaciers to global sea level. Science 226, 1418–21.

Meier, M.F., Dyurgerov, M.B., Rick, U.K., O'neel, S., Pfeffer, W.T., Anderson, R.S., Anderson, S.P., Glazovsky, A.F., 2007. Glaciers dominate eustatic sea-level rise in the 21st century. Science 317, 1064–7.

Mendelova, M., Hein, A.S., McCulloch, R., Davies, B., 2017. The Last Glacial Maximum and deglaciation in central Patagonia, 44°S–49°S. Cuad. Investig. Geográfica 43, 719.

Menounos, B., Clague, J.J., Osborn, G., Davis, P.T., Ponce, F., Goehring, B., Maurer, M., Rabassa, J., Coronato, A., Marr, R., 2013. Latest Pleistocene and Holocene glacier fluctuations in southernmost Tierra del Fuego, Argentina. Quat. Sci. Rev. 77, 70–79.

Mercanton, P.-L., Heim, A., Held, L., Rütimeyer, L., 1916. Vermessungen am Rhonegletscher: Mensurations au glacier du Rhône. 1874-1915. Zürcher & Furrer.

Mercer, J.H., 1976. Glacial history of southernmost South America. Quat. Res. 6, 125–166.

Mercer, J.H., 1968. Variations of some Patagonian glaciers since the Late-Glacial. Am. J. Sci. 266, 91–109.

Meur, E.L.E., Vincent, C., 2003. A two-dimensional shallow ice-flow model of Glacier de 49.

Miall, A.D., 1992. Alluvial deposits. Facies Model. response to sea Lev. Chang. 119–142.

Miall, A.D., 1985. Architectural-Element Analysis : A New Method of Facies Analysis Applied to Fluvial Deposits. Earth-Science Rev. 22, 261–308.

Millan, R., Rignot, E., Rivera, A., Martineau, V., Mouginot, J., Zamora, R., Uribe, J., Lenzano, G., De Fleurian, B., Li, X., Gim, Y., Kirchner, D., 2019. Ice thickness and bed elevation of the Northern and Southern Patagonian Icefields. Geophys. Res. Lett. 2019GL082485.

Mills, S.C., Grab, S.W., Carr, S.J., 2009. Recognition and palaeoclimatic implications of late Quaternary niche glaciation in eastern Lesotho. J. Quat. Sci. 24, 647–663.

Moller, M., Schneider, C., Kilian, R., 2007. Glacier change and climate forcing in recent decades at Gran Campo Nevado , southernmost Patagonia. Ann. Glaciol. 136–144.

Morano-Büchner, C., Aravena, J.C., 2013. Lichenometric analysis using genus Rhizocarpon, section Rhizocarpon (Lecanorales: Rhizocarpaceae) at Mount San Lorenzo, southern Chile. Rev. Chil. Hist. Nat. 86, 465–473.

Moreno, P.I., 2004a. Millennial-scale climate variability in northwest Patagonia over the last 15 000 yr. J. Quat. Sci. 19, 35–47.

Moreno, P.I., 2004b. Millennial-scale climate variability in northwest Patagonia over the last 15 000 yr. J. Quat. Sci.

Moreno, P.I., Francois, J.P., Moy, C.M., Villa-Martnez, R., 2010. Covariability of the Southern Westerlies and atmospheric CO2 during the Holocene. Geology 38, 727–730.

Moreno, P.I., François, J.P., Villa-Martínez, R.P., Moy, C.M., 2009. Millennial-scale variability in Southern Hemisphere westerly wind activity over the last 5000 years in SW Patagonia. Quat. Sci. Rev. 28, 25–38.

Moreno, P.I., Videla, J., 2016. Centennial and millennial-scale hydroclimate changes in northwestern Patagonia since 16,000 yr BP. Quat. Sci. Rev. 149, 326–337.

Moreno, P.I., Videla, J., Valero-Garcés, B., Alloway, B. V., Heusser, L.E., 2018a. A continuous record of vegetation, fire-regime and climatic changes in northwestern Patagonia spanning the last 25,000 years. Quat. Sci. Rev. 198, 15–36.

Moreno, P.I., Vilanova, I., Villa-Martínez, R., Dunbar, R.B., Mucciarone, D.A., Kaplan, M.R., Garreaud, R.D., Rojas, M., Moy, C.M., De Pol-Holz, R., Lambert, F., 2018b. Onset and Evolution of Southern Annular Mode-Like Changes at Centennial Timescale. Sci. Rep. 8, 3458.

Morlighem, M., Rignot, E., Seroussi, H., Larour, E., Ben Dhia, H., Aubry, D., 2010. Spatial patterns of basal drag inferred using control methods from a full-Stokes and simpler models for Pine Island Glacier, West Antarctica. Geophys. Res. Lett. 37, n/a-n/a.

Moy, C.M., Dunbar, R.B., Moreno, P.I., Francois, J.P., Villa-Mart??nez, R., Mucciarone, D.M., Guilderson, T.P., Garreaud, R.D., 2008. Isotopic evidence for hydrologic change related to the westerlies in SW Patagonia, Chile, during the last millennium. Quat. Sci. Rev. 27, 1335–1349.

Muller, F., 1962. Zonation in the accumulation area od the glaciers of Axel Heiberg Island, N.W.T, Canada. J. Glaciol.

Murray, T., 1997. Assessing the paradigm shift: Deformable glacier beds. Quat. Sci. Rev. 16, 995–1016.

Nielsen, L.T., Adalgeirsdóttir, G., Gkinis, V., Nuterman, R., Hvidberg, C.S., 2018. The effect of a Holocene climatic optimum on the evolution of the Greenland ice sheet during the last 10 kyr. J. Glaciol. 64, 477–488.

Nimick, D.A., McGrath, D., Mahan, S.A., Friesen, B.A., Leidich, J., 2016. Latest Pleistocene and Holocene glacial events in the Colonia valley, Northern Patagonia Icefield, southern Chile. J. Quat. Sci. 31, 551–564.

Nishiizumi, K., Imamura, M., Caffee, M.W., Southon, J.R., Finkel, R.C., McAninch, J., 2007. Absolute calibration of10Be AMS standards. Nucl. Instruments Methods Phys. Res. Sect. B Beam Interact. with Mater. Atoms 258, 403–413.

Nishiizumi, K., Winterer, E.L., Kohl, C.P., Klein, J., Middleton, R., Lal, D., Arnold, J.R., 1989. Cosmic ray production rates of ^{10}Be and ^{26}Al in quartz from glacially polished rocks. J. Geophys. Res. 94, 17907.

Noël, B., Van De Berg, W.J., Van Meijgaard, E., Kuipers Munneke, P., Van De Wal, R.S.W., Van Den Broeke, M.R., 2015. Evaluation of the updated regional climate model RACMO2.3: Summer snowfall impact on the Greenland Ice Sheet. Cryosphere.

Nye, J.F., 1970. Glacier sliding without cavitation in a linear viscous approximation, in: Proceedings of the Royal Society of London A: Mathematical, Physical and Engineering

Sciences. The Royal Society, pp. 381–403.

Nye, J.F., 1969. A calculation on the sliding of ice over a wavy surface using a Newtonian viscous approximation, in: Proceedings of the Royal Society of London A: Mathematical, Physical and Engineering Sciences. The Royal Society, pp. 445–467.

Nye, J.F., 1952. A Method of Calculating the Thicknesses of the Ice-Sheets. Nature 169, 529–530.

Ó Cofaigh, C., Davies, B.J., Livingstone, S.J., Smith, J.A., Johnson, J.S., Hocking, E.P., Hodgson, D.A., Anderson, J.B., Bentley, M.J., Canals, M., Domack, E., Dowdeswell, J.A., Evans, J., Glasser, N.F., Hillenbrand, C.D., Larter, R.D., Roberts, S.J., Simms, A.R., 2014. Reconstruction of ice-sheet changes in the Antarctic Peninsula since the Last Glacial Maximum. Quat. Sci. Rev. 100, 87–110.

Ó Cofaigh, C., Evans, D.J.A., England, J., 2003. Ice-marginal terrestrial landsystems: sub-polar glacier margins of the Canadian and Greenland High Arctic. Glacial Landsystems. Arnold, London 45–64.

Oehlerich, M., Mayr, C., Gussone, N., Hahn, A., Hölzl, S., Lücke, A., Ohlendorf, C., Rummel, S., Teichert, B.M.A., Zolitschka, B., 2015. Lateglacial and Holocene climatic changes in south-eastern Patagonia inferred from carbonate isotope records of Laguna Potrok Aike (Argentina). Quat. Sci. Rev. 114, 189–202.

Oerlemans, J., 2005. Extracting a Climate Signal from 169 Glacier Records. Science (80-.). 308, 675–677.

Oerlemans, J., 2001. Glaciers and Climate Change. Rotterdam. Netherlands.

Oerlemans, J., 1997. A flowline model for Nigardsbreen, Norway: Projection of future glacier length based on dynamic calibration with the historic record. Ann. Glaciol. 24, 382–389.

Oerlemans, J., Fortuin, J.P.F., 1992. Sensitivity of glaciers and small ice caps to greenhouse warming. Science (80-.). 258, 115–117.

Ohmura, A., Kasser, P., Funk, M., 1992. Climate at the Equilibrium Line of Glaciers. J. Glaciol. 38, 397–411.

Osmaston, H., 2005. Estimates of glacier equilibrium line altitudes by the Area × Altitude, the Area × Altitude Balance Ratio and the Area × Altitude Balance Index methods and their validation. Quat. Int. 138–139, 22–31.

Osmaston, H.A., 1975. Models for the estimation of firnlines of present and Pleistocene

glaciers. Peel, RF, Chisholm, MDI Haggett, p.(eds) Process. Phys. Hum. Geogr. Bristol Essays, Univ. Bristol Press. Bristol 218, 245.

Østrem, G., Stanley, A., 1969. Glacier mass-balance measurements: a manual for field and office work. Canadian Department of Energy, Mines and Resources.

Owen, L.A., Finkel, R.C., Barnard, P.L., Haizhou, M., Asahi, K., Caffee, M.W., Derbyshire, E., 2005. Climatic and topographic controls on the style and timing of Late Quaternary glaciation throughout Tibet and the Himalaya defined by 10Be cosmogenic radionuclide surface exposure dating. Quat. Sci. Rev. 24, 1391–1411.

Owen, L.A., Frankel, K.L., Knott, J.R., Reynhout, S., Finkel, R.C., Dolan, J.F., Lee, J., 2011. Beryllium-10 terrestrial cosmogenic nuclide surface exposure dating of Quaternary landforms in Death Valley. Geomorphology 125, 541–557.

Palmer, A.P., Lowe, J.J., 2017. Dynamic landscape changes in Glen Roy and vicinity, west Highland Scotland, during the Younger Dryas and early Holocene: a synthesis. Proc. Geol. Assoc. 128, 2–25.

Palmer, A.P., Rose, J., Lowe, J.J., Walker, M.J.C., 2008. Annually laminated Late Pleistocene sediments from Llangorse Lake, South Wales, UK: a chronology for the pattern of ice wastage. Proc. Geol. Assoc. 119, 245–258.

Parizek, B.R., Alley, R.B., 2004. Ice thickness and isostatic imbalances in the Ross Embayment, West Antarctica: model results. Glob. Planet. Change 42, 265–278.

Paterson, W.S.B., 1994. The physics of glaciers. Butterworth-Heinemann.

Paterson, W.S.B., Budd, W.F., 1982. Flow parameters for ice sheet modeling. Cold Reg. Sci. Technol. 6, 175–177.

Patton, H., Hubbard, A., Andreassen, K., Auriac, A., Whitehouse, P.L., Stroeven, A.P., Shackleton, C., Winsborrow, M., Heyman, J., Hall, A.M., 2017. Deglaciation of the Eurasian ice sheet complex. Quat. Sci. Rev. 169, 148–172.

Peacock, J.D., 1986. Alluvial fans and an outwash fan in upper Glen Roy, Lochaber. Scottish J. Geol. 22, 347–366.

Pedro, J.B., Bostock, H.C., Bitz, C.M., He, F., Vandergoes, M.J., Steig, E.J., Chase, B.M., Krause, C.E., Rasmussen, S.O., Markle, B.R., Cortese, G., 2016. The spatial extent and dynamics of the Antarctic Cold Reversal. Nat. Geosci. 9, 51–55.

Pedro, J.B., Martin, T., Steig, E.J., Jochum, M., Park, W., Rasmussen, S.O., 2016. Southern

Ocean deep convection as a driver of Antarctic warming events. Geophys. Res. Lett. 43, 2192–2199.

Pedro, J.B., van Ommen, T.D., Rasmussen, S.O., Morgan, V.I., Chappellaz, J., Moy, A.D., Masson-Delmotte, V., Delmotte, M., 2011. The last deglaciation: timing the bipolar seesaw. Clim. Past 7, 671–683.

Pellitero, R., Rea, B.R., Spagnolo, M., Bakke, J., Hughes, P., Ivy-Ochs, S., Lukas, S., Ribolini, A., 2015. A GIS tool for automatic calculation of glacier equilibrium-line altitudes. Comput. Geosci. 82, 55–62.

Pellitero, R., Rea, B.R., Spagnolo, M., Bakke, J., Ivy-Ochs, S., Frew, C.R., Hughes, P., Ribolini, A., Lukas, S., Renssen, H., 2016. GlaRe, a GIS tool to reconstruct the 3D surface of palaeoglaciers. Comput. Geosci. 94, 77–85.

Phillips, E., Lipka, E., van der Meer, J.J.M., 2013. Micromorphological evidence of liquefaction, injection and sediment deposition during basal sliding of glaciers. Quat. Sci. Rev. 81, 114–137.

Phillips, E.R., Evans, D.J.A., van der Meer, J.J.M., Lee, J.R., 2018. Microscale evidence of liquefaction and its potential triggers during soft-bed deformation within subglacial traction tills. Quat. Sci. Rev. 181, 123–143.

Piotrowski, J.A., Tulaczyk, S., 1999. Subglacial conditions under the last ice sheet in northwest Germany: Ice-bed separation and enhanced basal sliding? Quat. Sci. Rev. 18, 737–751.

Pollard, D., DeConto, R.M., 2009. Modelling West Antarctic ice sheet growth and collapse through the past five million years. Nature 458, 329–332.

Popovnin, V. V, Danilova, T.A., Petrakov, D.A., 1999. A pioneer mass balance estimate for a Patagonian glacier: Glaciar De los Tres, Argentina. Glob. Planet. Change 22, 255–267.

Porter, P.R., Murray, T., Dowdeswell, J.A., 1997. Sediment deformation and basal dynamics beneath a glacier surge front: Bakaninbreen, Svalbard. Ann. Glaciol. 24, 21–26.

Prest, V.K., 1968. Nomenclature of moraines and ice-flow features as applied to the glacial map of Canada. Department of Energy, Mines and Resources.

Price, R.J., 1963. A glacial meltwater drainage system in Peeblesshire, Scotland. Scott. Geogr. Mag. 79, 133–141.

Punkari, M., 1995. Glacial flow systems in the zone of confluence between the Scandinavian and Novaja Zemlya Ice Sheets. Quat. Sci. Rev. 14, 589–603.

Purdie, A.H.L., Brook, M.S., Fuller, I.C., 2008. Seasonal Variation in Ablation and Surface Velocity on a Temperate Maritime Glacier : Fox Glacier , New Zealand. Arctic, Antarct. Alp. Res. 40, 140–147.

Putkonen, J., Swanson, T., 2003. Accuracy of cosmogenic ages for moraines. Quat. Res. 59, 255–261.

Putnam, A.E., Denton, G.H., Schaefer, J.M., Barrell, D.J.A., Andersen, B.G., Finkel, R.C., Schwartz, R., Doughty, A.M., Kaplan, M.R., Schlüchter, C., 2010. Glacier advance in southern middle-latitudes during the Antarctic Cold Reversal. Nat. Geosci. 3, 700–704.

Putnam, A.E., Schaefer, J.M., Barrell, D.J.A., Vandergoes, M., Denton, G.H., Kaplan, M.R., Finkel, R.C., Schwartz, R., Goehring, B.M., Kelley, S.E., 2010. In situ cosmogenic 10Be production-rate calibration from the Southern Alps, New Zealand. Quat. Geochronol. 5, 392–409.

Putnam, A.E., Schaefer, J.M., Denton, G.H., Barrell, D.J.A., Birkel, S.D., Andersen, B.G., Kaplan, M.R., Finkel, R.C., Schwartz, R., Doughty, A.M., 2013. The Last Glacial Maximum at 44°S documented by a 10Be moraine chronology at Lake Ohau, Southern Alps of New Zealand. Quat. Sci. Rev. 62, 114–141.

Putnam, A.E., Schaefer, J.M., Denton, G.H., Barrell, D.J.A., Finkel, R.C., Andersen, B.G., Schwartz, R., Chinn, T.J.H., Doughty, A.M., 2012. Regional climate control of glaciers in New Zealand and Europe during the pre-industrial Holocene. Nat. Geosci. 5, 627–630.

Quade, J., Kaplan, M.R., 2017. Lake-level stratigraphy and geochronology revisited at Lago (Lake) Cardiel, Argentina, and changes in the Southern Hemispheric Westerlies over the last 25 ka. Quat. Sci. Rev. 177, 173–188.

Ramos, V.A., Niemeyer, H., Skarmeta, J., Muñoz, J., 1982. Magmatic evolution of the Austral Patagonian Andes. Earth Sci. Rev. 18, 411–443.

Rea, B.R., 2009. Defining modern day Area-Altitude Balance Ratios (AABRs) and their use in glacier-climate reconstructions. Quat. Sci. Rev. 28, 237–248.

Rea, B.R., Evans, D.J.A., 2007. Quantifying climate and glacier mass balance in north Norway during the Younger Dryas. Palaeogeogr. Palaeoclimatol. Palaeoecol. 246, 307–330.

Reading, H.G., 1978. Sedimentary environments and facies. Blackwell Oxford.

Repka, J.L., Anderson, R.S., Finkel, R.C., 1997. Cosmogenic dating of fluvial terraces, Fremont River, Utah. Earth Planet. Sci. Lett. 152, 59–73.

Reuther, A., Geiger, C., Urdea, P., Niller, H.-P., Heine, K., 2004. Determining the glacial

equilibrium line altitude (ELA) for the Northern Retezat Mountains, Southern Carpathians and resulting paleoclimatic implications for the last glacial cycle. Analele Univ. Vest din Timișoara, Geogr. XIV, 9–32.

Richardson, S.D., Reynolds, J.M., 2000. An overview of glacial hazards in the Himalayas. Quat. Int. 65, 31–47.

Rignot, E., Rivera, A., Casassa, G., 2003. Contribution of the Patagonia Icefields of South America to sea level rise. Science 302, 434–7.

Ritz, C., Fabre, A., Letréguilly, A., 1996. Sensitivity of a Greenland ice sheet model to ice flow and ablation parameters: consequences for the evolution through the last climatic cycle. Clim. Dyn. 13, 11–23.

Rivera, A., 2004. Mass balance investigations at Glaciar Chico, Southern Patagonia Icefield, Chile. South. Patagon. Icefield, Chile.

Roberts, S.J., Hodgson, D.A., Shelley, S., Royles, J., Griffiths, H.J., Deen, T.J., Thorne, M.A. s., 2010. Establishing lichenometric ages for nineteenth- and twentieth-century glacier fluctuations on south georgia (south atlantic). Geogr. Ann. Ser. A, Phys. Geogr. 92, 125–139.

Rodbell, D.T., Smith, J.A., Mark, B.G., 2009. Glaciation in the Andes during the Lateglacial and Holocene. Quat. Sci. Rev. 28, 2165–2212.

Roering, J.J., Mackey, B.H., Marshall, J.A., Sweeney, K.E., Deligne, N.I., Booth, A.M., Handwerger, A.L., Cerovski-Darriau, C., 2013. 'You are HERE': Connecting the dots with airborne lidar for geomorphic fieldwork. Geomorphology 200, 172–183.

Rose, J., Menzies, J., 1996. Glacial stratigraphy, in: Modern and Past Glacial Environments. pp. 445–473.

Rutt, I.C., Hagdorn, M., Hulton, N.R.J., Payne, A.J., 2009. The glimmer community ice sheet model. J. Geophys. Res. Earth Surf. 114, 1–22.

Ryder, J.M., 1971. The stratigraphy and morphology of para-glacial alluvial fans in south-central British Columbia. Can. J. Earth Sci. 8, 279–298.

Sagredo, Araya, P.S., Lowell, T. V, Aravena, J.C., Kelly, M.A., Schaefer, J.M., 2018. Trans-Pacific glacial response to the Antarctic Cold Reversal in the southern mid- latitudes. Quat. Sci. Rev. 188, 160–166.

Sagredo, E.A., Lowell, T. V., Kelly, M.A., Rupper, S., Aravena, J.C., Ward, D.J., Malone, A.G.,

2017. Equilibrium line altitudes along the Andes during the Last millennium: Paleoclimatic implications. The Holocene 1–15.

Sagredo, E.A., Rupper, S., Lowell, T. V., 2014. Sensitivities of the equilibrium line altitude to temperature and precipitation changes along the Andes. Quat. Res. 81, 355–366.

Sato, A., Takahashi, S., Naruse, R., Wakahama, G., 1984. Ablation and heat balance of the Yukikabe snow patch in the Daisetsu Mountains, Hokkaido, Japan. Ann. Glaciol. 5, 122–126.

Scambos, T., Fahnestock, M., Moon, T., Gardner, A., Klinger, M., 2016. Global Land Ice Velocity Extraction from Landsat 8 (Go-LIVE), Version 1, Boulder, Colorado USA. NSIDC Natl. Snow Ice Data Center, doi 10, N5ZP442B.

Schäbitz, F., Wille, M., Francois, J.-P., Haberzettl, T., Quintana, F., Mayr, C., Lücke, A., Ohlendorf, C., Mancini, V., Paez, M.M., Prieto, A.R., 2013a. Reconstruction of palaeoprecipitation based on pollen transfer functions – the record of the last 16 ka from Laguna Potrok Aike, southern Patagonia. Quat. Sci. Rev. 71, 175–190.

Schäbitz, F., Wille, M., Francois, J.P., Haberzettl, T., Quintana, F., Mayr, C., Lücke, A., Ohlendorf, C., Mancini, V., Paez, M.M., Prieto, A.R., Zolitschka, B., 2013b. Reconstruction of palaeoprecipitation based on pollen transfer functions - the record of the last 16ka from Laguna Potrok Aike, southern Patagonia. Quat. Sci. Rev. 71, 175–190.

Schaefer, J.M., Denton, G.H., Kaplan, M., Putnam, A., Finkel, R.C., Barrell, D.J.A., Andersen, B.G., Schwartz, R., Mackintosh, A., Chinn, T., Schlüchter, C., 2009. High-Frequency Holocene Glacier Fluctuations in New Zealand Differ from the Northern Signature 622–626.

Schaefer, M., Machguth, H., Falvey, M., Casassa, G., 2013a. Modeling past and future surface mass balance of the Northern Patagonia Icefield. J. Geophys. Res. Earth Surf. 118, 571–588.

Schaefer, M., Machguth, H., Falvey, M., Casassa, G., 2013b. Modeling past and future surface mass balance of the Northern Patagonia Icefield. J. Geophys. Res. Earth Surf. 118, 571–588.

Schaefer, M., Machguth, H., Falvey, M., Casassa, G., 2013c. Modeling past and future surface mass balance of the Northern Patagonia Icefield. J. Geophys. Res. Earth Surf. 118, 571–588.

Schaefer, M., MacHguth, H., Falvey, M., Casassa, G., Rignot, E., 2015. Quantifying mass balance

processes on the Southern Patagonia Icefield. Cryosphere 9, 25–35.

Schaefer, M., MacHguth, H., Falvey, M., Casassa, G., Rignot, E., 2015. Quantifying mass balance processes on the Southern Patagonia Icefield. Cryosphere 9, 25–35.

Schlüchter, C., Gander, P., Lowell, T. V, Denton, G.H., 1999. Glacially Folded Outwash Near Lago Llanquihue, southern Lake District, Chile. Geogr. Ann 81, 347–358.

Schmidt, L.S., 2019. Short- and Long-term Model Simulations of the Evolution of Vatnajökull Ice Cap. University of Iceland.

Schneider, C., Glaser, M., Kilian, R., Santana, A., Casassa, G., 2003. Weather observations across the Southern Andes at 53°s. Phys. Geogr. 24, 97–119.

Schneider, C., Kilian, R., Glaser, M., 2007. Energy balance in the ablation zone during the summer season at the Gran Campo Nevado Ice Cap in the Southern Andes. Glob. Planet. Change 59, 175–188.

Schoof, C., 2006. A variational approach to ice stream flow. J. Fluid Mech. 556, 227–251.

Schwikowski, M., Schläppi, M., Santibañez, P., Rivera, A., Casassa, G., 2013. Net accumulation rates derived from ice core stable isotope records of Pío XI glacier, Southern Patagonia Icefield. Cryosph. 7, 1635–1644.

Schytt, V., 1962. Mass balance studies in Kebnekajse. J. Glaciol. 4, 281–288.

Screen, J.A., Gillett, N.P., Stevens, D.P., Marshall, G.J., Roscoe, H.K., Screen, J.A., Gillett, N.P., Stevens, D.P., Marshall, G.J., Roscoe, H.K., 2009. The Role of Eddies in the Southern Ocean Temperature Response to the Southern Annular Mode. J. Clim. 22, 806–818.

Seddik, H., Greve, R., Zwinger, T., Gillet-chaulet, F., Gagliardini, O., 2012. Simulations of the Greenland ice sheet 100 years into the future with the full Stokes model Elmer / Ice 58, 427–440.

Seguinot, J., Ivy-Ochs, S., Jouvet, G., Huss, M., Funk, M., Preusser, F., 2018. Modelling last glacial cycle ice dynamics in the Alps. Cryosph. 12, 3265–3285.

Seligman, G., Douglas, C.K.M., 1936. Snow structure and ski fields. Macmillan, London.

Shulmeister, J., Fink, D., Augustinus, P.C., 2005. A cosmogenic nuclide chronology of the last glacial transition in North-West Nelson, New Zealand—new insights in Southern Hemisphere climate forcing during the last deglaciation. Earth Planet. Sci. Lett. 233, 455–466.

Siani, G., Colin, C., Michel, E., Carel, M., Richter, T., Kissel, C., Dewilde, F., 2010. Late Glacial to Holocene terrigenous sediment record in the Northern Patagonian margin: Paleoclimate implications. Palaeogeogr. Palaeoclimatol. Palaeoecol. 297, 26–36.

Simms, A.R., Ivins, E.R., DeWitt, R., Kouremenos, P., Simkins, L.M., 2012. Timing of the most recent Neoglacial advance and retreat in the South Shetland Islands, Antarctic Peninsula: insights from raised beaches and Holocene uplift rates. Quat. Sci. Rev. 47, 41–55.

Sissons, J.B., 2017. The lateglacial lakes of Glens Roy, Spean and vicinity (Lochaber district, Scottish Highlands). Proc. Geol. Assoc. 128, 32–41.

Smedley, R.K., Chiverrell, R.C., Ballantyne, C.K., Burke, M.J., Clark, C.D., Duller, G.A.T., Fabel, D., McCarroll, D., Scourse, J.D., Small, D., Thomas, G.S.P., 2017. Internal dynamics condition centennial-scale oscillations in marinebased ice-stream retreat. Geology 45, 787–790.

Smedley, R.K., Glasser, N.F., Duller, G.A.T., 2016. Luminescence dating of glacial advances at Lago Buenos Aires (∼46 °S), Patagonia. Quat. Sci. Rev. 134, 59–73.

Smith, M.J., 2011. Geomorphological mapping : methods and applications. Oxford : Elsevier Science, Oxford.

Smith, M.J., Clark, C.D., 2005. Methods for the visualization of digital elevation models for landform mapping. Earth Surf. Process. Landforms 30, 885–900.

Smith, M.J., Rose, J., Booth, S., 2006. Geomorphological mapping of glacial landforms from remotely sensed data: An evaluation of the principal data sources and an assessment of their quality. Geomorphology 76, 148–165.

Smith, N.D., Ashley, G., 1985. Proglacial lacustrine environment, in: Glacial Sedimentary Environments. Special Publications of SEPM.

Sneed, E.D., Folk, R.L., 1958. Pebbles in the lower Colorado River, Texas a study in particle morphogenesis. J. Geol. 66, 114–150.

Solomina, O.N., Bradley, R.S., Hodgson, D.A., Ivy-Ochs, S., Jomelli, V., Mackintosh, A.N., Nesje, A., Owen, L.A., Wanner, H., Wiles, G.C., Young, N.E., 2015. Holocene glacier fluctuations. Quat. Sci. Rev. 111, 9–34.

Soruco, A., Vincent, C., Francou, B., Ribstein, P., Berger, T., Sicart, J.E., Wagnon, P., Arnaud, Y., Favier, V., Lejeune, Y., 2009. Mass balance of Glaciar Zongo, Bolivia, between 1956 and 2006, using glaciological, hydrological and geodetic methods. Ann. Glaciol. 50, 1–8.

Spedding, N., Evans, D.J.A., 2002. Sediments and lanforms at Kvjárjökull, southeast Iceland: a

reappraisal of the galciated valley landsystem. Sediment. Geol. 149, 21–42.

Spencer, C.J., Yakymchuk, C., Ghaznavi, M., 2017. Geoscience Frontiers Visualising data distributions with kernel density estimation and reduced chi-squared statistic. Geosci. Front. 8, 1247–1252.

Stansell, N.D., Polissar, P.J., Abbott, M.B., 2007. Last glacial maximum equilibrium-line altitude and paleo-temperature reconstructions for the Cordillera de Mérida, Venezuelan Andes. Quat. Res. 67, 115–127.

Steger, C.R., Reijmer, C.H., Van Den Broeke, M.R., Wever, N., Forster, R.R., Koenig, L.S., Kuipers Munneke, P., Lehning, M., Lhermitte, S., Ligtenberg, S.R.M., others, 2017. Firn meltwater retention on the Greenland ice sheet: A model comparison. Front. earth Sci. 5, 3.

Stern, C.R., Moreno, P.I., Sagredo, E., Aravena, J.C., 2016. Holocene tephrochronology around Cochrane (~47°S), southern Chile. Andean Geol. 43, 1–19.

Stocker, T.F., Qin, D., Plattner, G.-K., Tignor, M., Allen, S.K., Boschung, J., Nauels, A., Xia, Y., Bex, V., Midgley, P.M., others, 2013. Climate change 2013: The physical science basis.

Stokes, C.R., Clark, C.D., 2002. Are long subglacial bedforms indicative of fast ice flow? Boreas 31, 239–249.

Stokes, C.R., Clark, C.D., 1999. Geomorphological criteria for identifying Pleistocene ice streams. Ann. Glaciol. 28, 67–74.

Stokes, C.R., Tarasov, L., Blomdin, R., Cronin, T.M., Fisher, T.G., Gyllencreutz, R., Hättestrand, C., Heyman, J., Hindmarsh, R.C.A., Hughes, A.L.C., Jakobsson, M., Kirchner, N., Livingstone, S.J., Margold, M., Murton, J.B., Noormets, R., Peltier, W.R., Peteet, D.M., Piper, D.J.W., Preusser, F., Renssen, H., Roberts, D.H., Roche, D.M., Saint-Ange, F., Stroeven, A.P., Teller, J.T., 2015. On the reconstruction of palaeo-ice sheets: Recent advances and future challenges. Quat. Sci. Rev. 125, 15–49.

Stone, J.O., 2000. Air pressure and cosmogenic isotope production. J. Geophys. Res. Solid Earth 105, 23753–23759.

Strelin, J.A., Denton, G.H., Vandergoes, M.J., Ninnemann, U.S., Putnam, A.E., 2011. Radiocarbon chronology of the late-glacial Puerto Bandera moraines, Southern Patagonian Icefield, Argentina. Quat. Sci. Rev. 30, 2551–2569.

Strelin, J.A., Kaplan, M.R., Vandergoes, M.J., Denton, G.H., Schaefer, J.M., 2014. Holocene glacier history of the Lago Argentino basin, Southern Patagonian Icefield. Quat. Sci. Rev.

101, 124–145.

Strelin, J.A., Sone, T., Mori, J., Torielli, C.A., Nakamura, T., 2006. New Data Related to Holocene Landform Development and Climatic Change from James Ross Island, Antarctic Peninsula, in: Antarctica. Springer-Verlag, Berlin/Heidelberg, pp. 455–459.

Stuefer, M., Rott, H., Skvarca, P., 2007. Glaciar Perito Moreno, Patagonia: Climate sensitivities and glacier characteristics preceding the 2003/04 and 2005/06 damming events. J. Glaciol. 53, 3–16.

Sugden, D.E., 1978. Glacial Erosion by the Laurentide Ice Sheet. J. Glaciol. 20, 367–391.

Sugden, D.E., 1970. Landforms of Deglaciation in the Cairngorm Mountains, Scotland. Trans. Inst. Br. Geogr. 201.

Sugiyama, S., Minowa, M., Sakakibara, D., Skvarca, P., Sawagaki, T., Ohashi, Y., Naito, N., Chikita, K., 2016. Thermal structure of proglacial lakes in Patagonia. J. Geophys. Res. Earth Surf. 121, 2270–2286.

Sutherland, J.L., Carrivick, J.L., Evans, D.J.A., Shulmeister, J., Quincey, D.J., 2019. The Tekapo Glacier, New Zealand, during the Last Glacial Maximum: An active temperate glacier influenced by intermittent surge activity. Geomorphology 343, 183–210.

Syverson, K.M., Mickelson, D.M., 2009. Origin and significance of lateral meltwater channels formed along a temperate glacier margin, Glacier Bay, Alaska. Boreas 38, 132–145.

Takeuchi, Y., Naruse, R., Skvarca, P., 1996. Annual air-temperature measurement and ablation estimate at Moreno Glacier, Patagonia. Bull. glacier Res. 14, 23–28.

Tangborn, W. V, Krimmel, R.M., Meier, M.F., 1971. A comparison of glacier mass balance by glaciological, hydrological and mapping methods, South Cascade Glacier, Washington Wendell. Snow Ice-Symposium-Neiges Glaces 185–196.

the PISM authors, 2017. PISM, a Parallel Ice Sheet Model, manual version 1.0.

Thorarinsson, S., 1940. Present Glacier Shrinkage, and Eustatic Changes of Sea-Level. Geogr. Ann. 22, 131.

Thorndycraft, V.R., Bendle, J.M., Benito, G., Davies, B.J., Sancho, C., Palmer, A.P., Fabel, D., Armitage, S., Medealdea, A., Martin, J.R.V., 2019. Glacial lake evolution and Atlantic-Pacific drainage reversals during deglaciation of the Patagonian Ice Sheet. Quat. Sci. Rev. 203, 102–127.

Timmermann, A., Okumura, Y., An, S.-I., Clement, A., Dong, B., Guilyardi, E., Hu, A., Jungclaus,

J.H., Renold, M., Stocker, T.F., Stouffer, R.J., Sutton, R., Xie, S.-P., Yin, J., Timmermann, A., Okumura, Y., An, S.-I., Clement, A., Dong, B., Guilyardi, E., Hu, A., Jungclaus, J.H., Renold, M., Stocker, T.F., Stouffer, R.J., Sutton, R., Xie, S.-P., Yin, J., 2007. The Influence of a Weakening of the Atlantic Meridional Overturning Circulation on ENSO. J. Clim. 20, 4899–4919.

Todd, J., Christoffersen, P., 2014. Are seasonal calving dynamics forced by buttressing from ice mélange or undercutting by melting? Outcomes from full-Stokes simulations of Store Gletscher, West Greenland. Cryosph. Discuss. 8, 3525–3561.

Toggweiler, J.R., 2009. Climate change. Shifting westerlies. Science 323, 1434–1435.

Toggweiler, J.R., Russell, J.L., Carson, S.R., 2006. Midlatitude westerlies, atmospheric CO_2, and climate change during the ice ages. Paleoceanography 21, n/a-n/a.

Tonello, M.S., Mancini, M.V., Seppä, H., 2009. Quantitative reconstruction of Holocene precipitation changes in southern Patagonia. Quat. Res. 72, 410–420.

Tonkin, T.N., Midgley, N.G., Cook, S.J., Graham, D.J., 2016. Ice-cored moraine degradation mapped and quantified using an unmanned aerial vehicle: A case study from a polythermal glacier in Svalbard. Geomorphology 258, 1–10.

Trenberth, K.E., 1991. Storm tracks in the Southern Hemisphere subtropical oceans. J. Geophys. Res. C Ocean.

Turner, K.J., Fogwill, C.J., McCulloch, R.., Sugden, D.E., 2005. Deglaciation of the Eastern Flank of the North Patagonian Icefield and Associated Continental-Scale Lake Diversions. Geogr. Ann. Ser. A Phys. Geogr. 87, 363–374.

Turney, C.S.M., Roberts, R.G., de Jonge, N., Prior, C., Wilmshurst, J.M., McGlone, M.S., Cooper, J., 2007. Redating the advance of the New Zealand Franz Josef Glacier during the Last Termination: evidence for asynchronous climate change. Quat. Sci. Rev. 26, 3037–3042.

Undén, P., Rontu, L., Jarvinen, H., Lynch, P., Calvo Sánchez, F.J., Cats, G., Cuxart, J., Eerola, K., Fortelius, C., Garc\'\ia-Moya, J.A., others, 2002. HIRLAM-5 scientific documentation.

Van Daele, M., Bertrand, S., Meyer, I., Moernaut, J., Vandoorne, W., Siani, G., Tanghe, N., Ghazoui, Z., Pino, M., Urrutia, R., De Batist, M., 2016a. Late Quaternary evolution of Lago Castor (Chile, 45.6S): Timing of the deglaciation in northern Patagonia and evolution of the southern westerlies during the last 17 kyr. Quat. Sci. Rev. 133, 130–146.

Van Daele, M., Bertrand, S., Meyer, I., Moernaut, J., Vandoorne, W., Siani, G., Tanghe, N.,

Ghazoui, Z., Pino, M., Urrutia, R., De Batist, M., 2016b. Late Quaternary evolution of Lago Castor (Chile, 45.6°S): Timing of the deglaciation in northern Patagonia and evolution of the southern westerlies during the last 17 kyr. Quat. Sci. Rev. 133, 130–146.

Van der Woerd, J., Ryerson, F.J., Tapponnier, P., Gaudemer, Y., Finkel, R., Meriaux, A.S., Caffee, M., Guoguang, Z., Qunlu, H., 1998. Holocene left-slip rate determined by cosmogenic surface dating on the Xidatan segment of the Kunlun fault (Qinghai, China). Geology 26, 695.

Van Meijgaard, E., Van Ulft, L.H., Van De Berg, W.J., Bosveld, F.C., Van Den Hurk, B.J.J.M., Lenderink, G., Siebesma, A.P., 2008. The KNMI regional atmospheric climate model RACMO version 2.1.

Van Wessem, J.M., Reijmer, C.H., Morlighem, M., Mouginot, J., Rignot, E., Medley, B., Joughin, I., Wouters, B., Depoorter, M.A., Bamber, J.L., others, 2014. Improved representation of East Antarctic surface mass balance in a regional atmospheric climate model.

Vanneste, H., De Vleeschouwer, F., Martínez-Cortizas, A., von Scheffer, C., Piotrowska, N., Coronato, A., Le Roux, G., 2015. Late-glacial elevated dust deposition linked to westerly wind shifts in southern South America. Sci. Rep. 5, 11670.

Villa-Martínez, R., Moreno, P.I., Valenzuela, M.A., 2012. Deglacial and postglacial vegetation changes on the eastern slopes of the central Patagonian Andes (47°S). Quat. Sci. Rev. 32, 86–99.

Wakahama, G., 1975. The role of meltwater in densification processes of snow and firn. Int. Assoc. Hydrol. Sci. Snow Mech. Symp. (Grindelwald, Switzerland, 1974) 1961, 66–72.

Wake, L.M., Marshall, S.J., 2015. Assessment of current methods of positive degree-day calculation using in situ observations from glaciated regions. J. Glaciol. 61, 329–344.

Waldmann, N., Ariztegui, D., Anselmetti, F.S., Austin, J.A., Moy, C.M., Stern, C., Recasens, C., Dunbar, R.B., 2010. Holocene climatic fluctuations and positioning of the Southern Hemisphere westerlies in Tierra del Fuego (54° S), Patagonia. J. Quat. Sci. 25, 1063–1075.

Walker, R.G., 1992. Facies, facies models and modern stratigraphic concepts. Facies Model. response to sea-level Chang. 1–14.

Warren, C., Aniya, M., 1999. The calving glaciers of southern South America. Glob. Planet. Change 22, 59–77.

Warren, C.R., 1992. Iceberg calving and the glacioclimatic record. Prog. Phys. Geogr. 16, 253–

282.

Warren, C.R., Glasser, N.F., Harrison, S., Winchester, V., Kerr, A.R., Rivera, A., 1995. Characteristics of Tide-Water Calving at Glaciar San-Rafael, Chile. J. Glaciol. 41, 273–289.

Warren, C.R., Rivera, A., 1994. Non-linear climatic response of calving glaciers: a case study of Pio XI glacier, Chilean Patagonia. Rev. Chil. Hist. Nat. 67, 385–394.

Weertman, J., 1957. On the sliding of glaciers. J. Glaciol. 3, 33–38.

Weis, M., Greve, R., Hutter, K., 1999. Theory of shallow ice shelves 15–50.

Wells, S.G., McFadden, L.D., Poths, J., Olinger, C.T., 1995. Cosmogenic 3He surface-exposure dating of stone pavements: Implications for landscape evolution in deserts. Geology 23, 613.

Wenzens, G., 2005. Glacier advances east of the Southern Andes between the Last Glacial Maximum and 5,000 BP compared with lake terraces of the endorrheic Lago Cardiel (49 S, Patagonia, Argentina). Zeitschrift für Geomorphol. 433–454.

Wenzens, G., 2002. The influence of tectonically derived relief and climate on the extent of the last Glaciation east of the Patagonian ice fields (Argentina, Chile). Tectonophysics 345, 329–344.

Whitlock, C., Moreno, P.I., Bartlein, P., 2007. Climatic controls of Holocene fire patterns in southern South America. Quat. Res. 68, 28–36.

Wilkinson, D.S., 1988. A pressure-sintering model for the densification of polar firn and glacier ice. J. Glaciol. 34, 40–45.

Williams, G., 1936. The Geomorphology of Stewart Island, New Zealand. Geogr. J. 87, 328.

Winkelmann, R., Martin, M.A., Haseloff, M., Albrecht, T., Bueler, E., Khroulev, C., Levermann, A., 2011. The Potsdam Parallel Ice Sheet Model (PISM-PIK) - Part 1: Model description. Cryosphere 5, 715–726.

World Glacier Monitoring Service, 2008. Global Glacier Changes : facts and figures 88.

Wright, W.B., 1912. III.—The Drumlin Topography of South Donegal. Geol. Mag. 9, 153.

Wyrwoll, K.-H., 1977. Causes of rock-slope failure in a cold area: Labrador-Ungava. Geol. Soc. Am. Rev. Eng. Geol. 3, 59–67.

Xu, S., Dougans, A.B., Freeman, S.P.H.T., Schnabel, C., Wilcken, K.M., 2010. Improved 10Be and 26Al-AMS with a 5 MV spectrometer. Nucl. Instruments Methods Phys. Res. Sect. B Beam

Interact. with Mater. Atoms 268, 736–738.

Yamada, T., 1987. Glaciological characteristics revealed by 37.6-m deep core drilled at the accumulation area of San Rafael Glacier, the Northern Patagonia Icefield. Bull. glacier Res. 59–67.

Yan, Q., Owen, L.A., Wang, H., Zhang, Z., 2018. Climate Constraints on Glaciation Over High-Mountain Asia During the Last Glacial Maximum. Geophys. Res. Lett. 45, 9024–9033.

Yde, J.C., Paasche, O., 2010. Reconstructing climate change: Not all glaciers suitable. Eos (Washington. DC). 91, 189–191.

Yoon, H. Il, Yoo, K.-C., Park, B.-K., Kim, Y., Khim, B.-K., Kang, C.-Y., 2004. The origin of massive diamicton in Marian and Potter coves, King George Island, West Antarctica. Geosci. J. 8, 1–10.

Zemp, M., Hoelzle, M., Haeberli, W., 2009. Six decades of glacier mass-balance observations: A review of the worldwide monitoring network. Ann. Glaciol. 50, 101–111.

Zemp, M., Huss, M., Thibert, E., Eckert, N., McNabb, R., Huber, J., Barandun, M., Machguth, H., Nussbaumer, S.U., Gärtner-Roer, I., Thomson, L., Paul, F., Maussion, F., Kutuzov, S., Cogley, J.G., 2019. Global glacier mass changes and their contributions to sea-level rise from 1961 to 2016. Nature 568, 382–386.

Ziemen, F.A., Hock, R., Aschwanden, A., Khroulev, C., Kienholz, C., Melkonian, A., Zhang, J., 2016. Modeling the evolution of the Juneau Icefield between 1971 and 2100 using the Parallel Ice Sheet Model (PISM). J. Glaciol. 62, 199–214.

Zwinger, T., Greve, R., Gagliardini, O., Shiraiwa, T., Lyly, M., 2007. A full Stokes-flow thermo-mechanical model for firn and ice applied to the Gorshkov crater glacier, Kamchatka. Ann. Glaciol. 45, 29–37.